

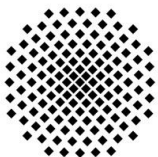


Max Planck Institute  
For Intelligent Systems  
Stuttgart

---

**Deposition and Characterization of Multi-Functional,  
Complex Thin Films Using Atomic Layer Deposition for  
Copper Corrosion Protection**

**Gül Dogan**



**Universität  
Stuttgart**

Dissertation at University of Stuttgart  
Faculty of Chemistry  
Stuttgart

---



# Deposition and Characterization of Multi-Functional, Complex Thin Films Using Atomic Layer Deposition for Copper Corrosion Protection

Von der Fakultät Chemie der Universität Stuttgart  
zur Erlangung der Würde eines Doktors der  
Naturwissenschaften (Dr. rer. nat.) genehmigte Abhandlung

Vorgelegt von  
Gül Dogan  
aus Ankara, Türkei

Supervised by Dr. Kahraman Keskinbora

Hauptberichter: Prof. Dr. Gisela Schütz  
Mitberichter: Prof. Dr. Dr. h.c. Guido Schmitz  
Prüfungsvorsitzender: Prof. Dr. Thomas Schleid

Tag der mündlichen Prüfung: 23. Mai 2022

Max-Planck-Institut für Intelligente Systeme, Stuttgart

2022





# Contents

Declaration of Authorship .....	iii
Publication of Individual Chapters in Scientific Journals .....	v
List of Abbreviations and Symbols .....	vii
1. Introduction .....	1
1.1. Thesis Objectives .....	1
1.2. Thesis Organization .....	2
2. Theoretical Background .....	5
2.1. Atomic Layer Deposition (ALD) .....	5
2.1.1 ALD Equipment .....	11
2.2. The Use of ALD in Corrosion Protection .....	11
2.2.1. ALD Materials for Corrosion Protection.....	12
2.2.2. ALD Protection in Varied Corrosive Environment .....	13
2.2.3. Process Parameters Effect on Corrosion Protection.....	14
2.2.4. ALD Applications for Corrosion Protection .....	15
3. Characterization Techniques.....	17
3.1. Spectroscopic Ellipsometry.....	17
3.2. X-ray Photoelectron Spectroscopy .....	19
3.3. X-ray Diffraction .....	20
3.4. Electron Microscopy.....	21
4. Overview of Thesis .....	25
5. <i>In Situ</i> X-ray Diffraction and Spectro-Microscopic Study of ALD Protected Copper Films .....	47
6. Bayesian Machine Learning for Efficient Minimization of Defects in ALD Passivation Layers..	49
7. Micromachining of Al <sub>2</sub> O <sub>3</sub> Thin Films <i>via</i> Laser Drilling and Plasma Etching for Interfacing Copper.....	51
8. Summary .....	53
9. Zusammenfassung.....	55
10. Acknowledgements .....	57
11. Appendix .....	59
11.1. Supporting Information: <i>In Situ</i> X-ray Diffraction and Spectro-Microscopic Study of ALD Protected Copper Films .....	59
11.2. Supporting Information: Bayesian Machine Learning for Efficient Minimization of Defects in ALD Passivation Layers.....	69
11.3. Supporting Information: Micromachining of Al <sub>2</sub> O <sub>3</sub> Thin Films <i>via</i> Laser Drilling and Plasma Etching for Interfacing Copper .....	81



## **Erklärung über die Eigenständigkeit der Dissertation**

Ich versichere, dass ich die vorliegende Arbeit mit dem Titel

### **Deposition and Characterization of Multi-Functional, Complex Thin Films Using Atomic Layer Deposition for Copper Corrosion Protection**

selbständig verfasst und keine anderen als die angegebenen Quellen und Hilfsmittel benutzt habe; aus fremden Quellen entnommene Passagen und Gedanken sind als solche kenntlich gemacht.

## **Declaration of Authorship**

I hereby certify that the dissertation entitled

### **Deposition and Characterization of Multi-Functional, Complex Thin Films Using Atomic Layer Deposition for Copper Corrosion Protection**

is entirely my own work except where otherwise indicated. Passages and ideas from other sources have been clearly indicated.

Name/Name: \_\_\_\_\_

Unterschrift/Signed: \_\_\_\_\_

Datum/Date: \_\_\_\_\_



## **Publication of Individual Chapters in Scientific Journals**

The present thesis has a cumulative structure. The chapters are the following three papers, which have been published in scientific journals.

### **Publication I. In Situ X-ray Diffraction and Spectro-Microscopic Study of ALD**

**Protected Copper Films**, Gül Dogan, Umut T. Sanli, Kersten Hahn, Lutz Müller, Herbert Gruhn, Christian Silber, Gisela Schütz, Corinne Grévent, and Kahraman Keskinbora, *ACS Applied Materials & Interfaces* **2020** 12 (29), 33377-33385 DOI: 10.1021/acsami.0c06873

### **Publication II. Bayesian Machine Learning for Efficient Minimization of Defects in ALD**

**Passivation Layers**, Gül Dogan, Sinan O. Demir, Rico Gutzler, Herbert Gruhn, Cem B. Dayan, Umut T. Sanli, Christian Silber, Utku Culha, Metin Sitti, Gisela Schütz, Corinne Grévent, and Kahraman Keskinbora, *ACS Applied Materials & Interfaces* **2021** 13 (45), 54503-54515, DOI: 10.1021/acsami.1c1458

### **Publication III. Micromachining of Al<sub>2</sub>O<sub>3</sub> Thin Films via Laser Drilling and Plasma**

**Etching for Interfacing Copper**, Gül Dogan, Frank Chiu, Sam U.H. Chen, Mebil R.T. David, Andreas Michalowski, Michael Schänzel, Christian Silber, Gisela Schütz, Corinne Grévent, Kahraman Keskinbora, *Materials & Design*, **2021** (210), 110114, ISSN 0264-1275, DOI: 10.1016/j.matdes.2021.110114.

## **Contribution Report**

I. Responsible for writing the manuscript and for all experimental work. The co-authors revised the manuscript.

II. Responsible for writing the manuscript and for most of the experimental work. The Bayesian Optimization was performed and explained in the method part by Sinan Özgün Demir. The other co-authors revised the manuscript.

III. Responsible for writing the manuscript and for most of the experimental work. Laser drilling and plasma etching was performed by Frank Chiu and Sam U. H. Chen at ASE Kaohsiung. The co-authors revised the manuscript.



## List of Abbreviations and Symbols

---

ALD	Atomic Layer Deposition
ALE	Atomic Layer Annealing
CMOS	Complementary Metal-Oxide-Semiconductor
DRAM	Dynamic Random Access Memory
GPC	Growth per Cycle
CVD	Chemical Vapor Deposition
PE-ALD	Plasma Enhanced Atomic Layer Deposition
CCP	Capacitively Coupled Plasma
SERS	Surface Enhanced Raman Spectroscopy
SE	Spectroscopic Ellipsometry
XPS	X-ray Photoelectron Spectroscopy
XRD	X-ray Diffraction
GI-XRD	Grazing Incidence X-ray Diffraction
EM	Electron Microscopy
SEM	Scanning Electron Microscopy
EDX	Energy Disperse X-ray Spectroscopy
BF	Bright Field
BSE	Back Scattered Electron
FIB	Focused Ion Beam
TEM	Transmission Electron Microscopy
MSE	Mean Squared Error
BF-TEM	Bright Field Transmission Electron Microscopy
SAED	Selected Area Electron Diffraction
STEM	Scanning Transmission Electron Microscopy
HAADF	High Angle Annular Dark Field
EELS	Electron Energy Loss Spectroscopy
FFT	Fast Fourier Transform
LSV	Linear Sweep Voltammetry
FFD	Fractional Factorial Design
BO	Bayesian Optimization
PCB	Printed Circuit Board

---





## **1.Introduction**

Copper is used for a wide range of applications in plumbing, heat exchangers, interconnect and gate electrodes for microelectronics due to superior electrical and thermal conductivity and good mechanical workability.<sup>1-2</sup> However, the use of copper in these applications is often hampered due to corrosion in oxidative environment such as moisture or elevated temperature. Copper is commonly used as interconnects within many electronic components with steadily increasing density and decreasing line width, where elevated temperatures, above 300 °C, can be reached during the operation and cause the corrosion of copper and the failure of device.

To improve the performance of copper, wide range of techniques has been used for the deposition of protective layers such as chemical vapor deposition, electrodeposition, and plasma treatments.<sup>3-4</sup> Among these techniques, Atomic Layer Deposition (ALD) offers an attractive alternative to achieve high quality protective layers with an accurate thickness control, uniformity in a large surface area, excellent step coverage and composition control.<sup>4-6</sup>

ALD has emerged as an attractive encapsulation, passivation, and protection technique in many application areas,<sup>1-2, 6-10</sup> where several oxide layers have been introduced to protect copper in different corrosive environments. The performance of ALD thin films for corrosion protection is highly dependent on the defect density such as pinholes and structural defects.<sup>1, 4, 11-18</sup> Defects such as pinholes and structural defects allow the transport of reactive species through the barrier film, which lead to the corrosion of copper. Even though ALD is still one of the few techniques that can provide lower defect density compared to other deposition techniques, the corrosion protection performance of ALD materials is highly dependent on process parameters. Therefore, a correct identification and tuning of the process parameters are essential to achieve best protection performance of ALD thin films.

In addition to the best corrosion protection performance of ALD thin films, the micro- and nano-structuring of these layers need to be addressed for many applications such as semiconductor processes to connect bottom copper layer to the top metal layers. Therefore, an ability to selective removal and micromachining of protective films is also required for the future applications of ALD layers.

### **1.1. Thesis Objectives**

This thesis focuses on ALD thin film protection properties against corrosion of copper to develop an understanding of material interface properties and to develop novel thin films

processes. This understanding is then applied to enhance materials with potential use in semiconductor devices. The main research objectives are listed below:

Understanding corrosion protection properties of ALD thin films:

- Development of protective thin films by combining different oxide layers
- To characterize the protection properties at high temperatures and in aggressive environments,
- To understand the interaction of copper and ALD protection layers when exposed to high temperatures,
- Finding the optimum deposition parameters to achieve defect-free thin layers for best corrosion protection

Application of ALD oxide thin films for copper corrosion protection in semiconductor devices:

- Structuring the ALD thin films to make reliable interface for copper-copper interconnects with micromachining methods such as laser drilling and plasma etching
- To remove ALD layers in a localized, selective way without degradation of the underlying copper layer

## 1.2. Thesis Organization

This thesis consists of seven chapters, an introductory chapter, a summary of characterization techniques, overview of the thesis, three articles and one summary chapters. It is organized according to requirements of cumulative thesis, defined by Faculty of Chemistry, University of Stuttgart.

Chapter 2 introduce the technique of atomic layer deposition. The fundamental knowledge and characteristic of the method is described. A literature review is provided with focus on the use of ALD oxide thin films to protect copper against corrosion. Chapter 3 summarizes the most used characterization techniques in this thesis. Chapter 4 gives an overview of the thesis, focusing on the most important findings in this thesis.

Chapter 5 presents the viability of bilayer ALD thin films against the protection of copper from oxidation via *in situ* XRD technique at 350 °C under atmospheric conditions. Further, the interaction of copper with the passivation layers is analyzed *post factum* using detailed spectro-microscopic investigations.

Chapter 6 outlines a systematic study on the improvement of the protective properties of ALD thin films. The minimization of the defects in ALD passivation layers are represented by

process parameters optimization. A hybrid Bayesian Optimization algorithm is used to find the best process parameters in model-based study on ALD- $\text{Al}_2\text{O}_3$  thin films.

Chapter 7 reports the applicability of ALD thin films in copper interconnection fabrication as a potential application. The micromachining methods  $\text{CO}_2$  laser drilling and plasma etching are studied to selectively remove the ALD- $\text{Al}_2\text{O}_3$  films and to provide a clean interface for copper interconnections.

Chapter 8 summarizes the results and contribution of this thesis. Additionally, the future perspectives of the use of ALD materials in corrosion protection of copper are stated.



## 2. Theoretical Background

### 2.1. Atomic Layer Deposition (ALD)

The ALD was first applied to polycrystalline thin films, such as ZnS, for electroluminescent displays in 1970s.<sup>19</sup> The technique was called atomic layer epitaxy (ALE) since the deposition of one atomic layer was possible. During 1980s, the technique was also used to deposit amorphous structures like Al<sub>2</sub>O<sub>3</sub> thin films. The interest of the ALD technique was increased with 1990s due to high demand of thin layers in semiconductor fabrication processes.<sup>20</sup> With early 2000s, the use of ALD method has extended to silicon-based microelectronic industry. In between these times, the technique was also named as atomic layer deposition rather than atomic layer epitaxy.<sup>20-21</sup> The main path for this increased interest was ALD of insulation oxide films for low-leakage high-k dielectrics in Complementary Metal-Oxide-Semiconductor (CMOS) transistors and Dynamic Random Access Memory (DRAM) devices.<sup>21-22</sup> The ALD method is still on high demand for many more application areas due to capability of precise control for growth thin films.

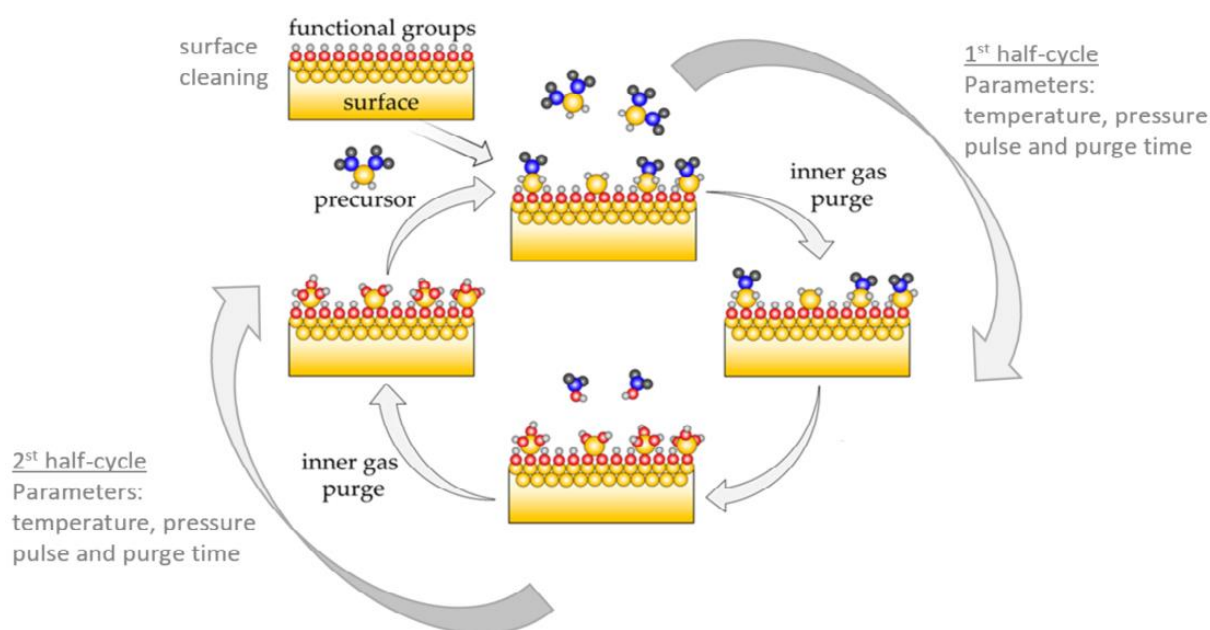
ALD is mainly a sub-group of chemical vapor deposition method based on the sequential self-terminating gas-solid reactions. ALD method provides precise control over the film thickness and improved film conformality over high aspect ratio on complex structures. Most ALD processes involve two reactants and typically is characterized by four steps<sup>23</sup>:

1. Pulse step of first reactant and subsequent self-terminating gas-solid reaction.
2. Purge step to remove excess reactants and gaseous reaction by-products.
3. Pulse step of second reactant and subsequent self-terminating gas-solid reaction.
4. Purge step to remove excess reactants and gaseous reaction by-products.

This sequence is called as a reaction cycle. Step 1 and 2 are first half cycle, and step 3 and 4 are second half cycle.

In the first step, the substrate surface is exposed to a precursor. The first precursor (step 1) chemisorbs in a self-limiting way onto the surface. Once the surface is covered with a monolayer of precursor, no further reactions occur. In the next step, excess precursor's molecules are removed by pumping or purging the reactor. During the third step, a second reactant reacts with the ligands of the chemisorbed precursor in a self-limiting way. In the final fourth step, the excess reactant is also removed and another ALD cycle can begin. A reaction cycle that includes four basic steps is shown in Figure 1. Even though the surface expected to be covered by monolayer in each half cycle, it is experimentally difficult to reach this theoretical

perfect condition. There are several requirements, such as substrate surface functionality, precursor stability, need to be fulfilled.

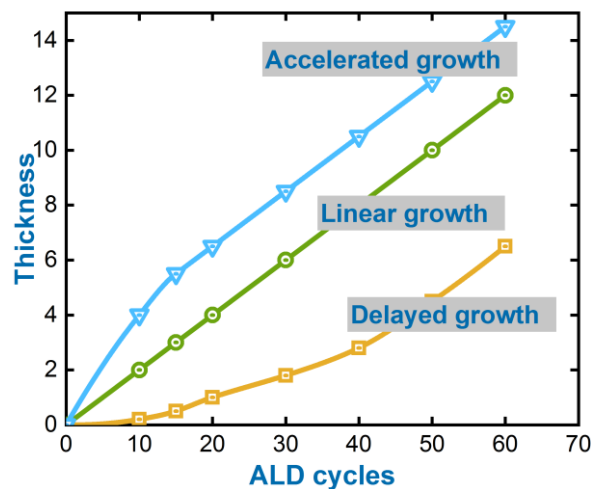


**Figure 1.** Schematic illustration of atomic layer deposition (ALD) growth cycle of two half-cycles (including four steps).<sup>22</sup>

In an ideal ALD, once the surface reactive sites are covered, no further deposition takes place.<sup>22, 24-25</sup> The precursor molecules can diffuse on the surface until they are chemisorbed on reactive sites. As a result, films with a uniform thickness are grown, even on complex three-dimensional (3D) structures. During each reaction cycle, a fixed amount of material is deposited, known as Growth per Cycle (GPC). Due to the self-limiting character of the reactions, corresponding nominal thickness is linearly increased with ALD cycles, given in Figure 2. An intended film thickness can be deposited by setting the number of reaction cycles. As the reactions are self-limiting, no tuning of reactant dose or flux is necessary when the dose is sufficient for the complete saturation of surface sites. Characteristic ALD growth is directly linked to the surface control of extreme precise thickness controllability and uniformity.<sup>22, 24-27</sup>

With the main characteristic behavior of ALD method, self-limiting growth, the linear increase observed with the ALD cycles. However, the experimental observations reveal that the initial film growth occurs likely in a non-linear fashion. The substrate surface functionality, homogeneity of reactive species on substrate surface, reaction of precursors and adsorption processes (surface chemistry) defines the initial growth properties. The substrate material or surface treatments before ALD may lead to a growth delay or growth enhancement in the initial

stage of film growth. However, the effect of the original substrate has loose the impact with continued deposition and steady state growth can be achieved after few ALD cycles.<sup>26, 28</sup>



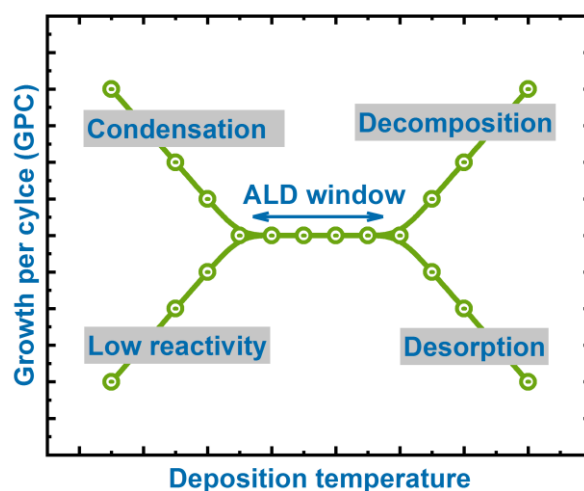
**Figure 2.** The relation between GPC and number of cycles in different types of ALD processes: linear growth, accelerated growth and delayed growth. Typical values for ALD cycles and thicknesses are given in the figure. The growth per cycle (GPC) is defined as the slope of the thickness and number of cycles. The accelerated growth is known as substrate-enhanced growth, and delayed growths is substrate-inhibited growth.

**ALD Growth Initiation:** Following the above statement, different growth mode can be observed in initial state of ALD. Figure 2 schematically shows three possible cases for evolution of GPC during the initial state of growth. For the ideal process, there would be a constant GPC even in the initial state, indicating that the reactive site density on the substrate and film are equal. In the surface-enhanced growth (accelerated growth) indicates that the density of reactive sites on the substrate is higher than on the ALD film. The GPC starts high, and then reaches to a constant value. In the case of surface-inhibited growth, the GPC starts low, and then reaches to a constant value, which is also called delayed growth. The inhibited growth is observed when the deposition starts at a limited number of nucleation sites.

The initial growth mode, dependent on the nucleation of ALD, is important for the deposition of continuous pinhole free films. Non-uniform nucleation sites results in island like grow.<sup>29</sup> While it can be used as an advantage for the deposition of nanoparticles, for continues thin films it may result in increased defect density.

**Temperature Window:** ALD processes have ideally a specific temperature range in which GPC shows no dependency on temperature.<sup>22-26</sup> Figure 3 shows the example of ALD temperature window as a function of temperature. The constant line represents an ideal ALD process.

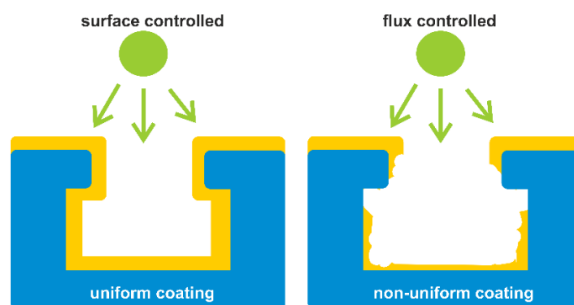
Outside the temperature window, different ALD behavior can be observed based on the chemical and physical processes. If the deposition temperature is too low, some precursors and co-reactants can condense on the substrate surface and lead an increase in GPC. Indeed, at lower temperatures the thermal energy could be limited and results the low reactivity of the precursor with surface species. The low reactivity is then followed by decrease in GPC and prevents the saturation of reactions. If the temperature is too high, the precursors or co-reactants can decompose and lead to a CVD growth with an increase of GPC. Additionally, the film or the reactive surface groups may desorb or etch above a certain temperature and results in a GPC decrease.<sup>25, 30</sup>



**Figure 3.** The idealized temperature window of the ALD process, shown by the GPC as a function of temperature. A condensation at low temperatures, low reactivity due to limited thermal energy, decomposition at high temperatures and desorption.

**Uniformity and Conformality:** Compared to other deposition techniques, the growth mechanism in ALD is unique and different due to the self-limiting reactions.<sup>3, 25, 31-32</sup> With self-saturating ALD half cycles, film conformality is greatly improved. Even on complex surfaces or on three-dimensional structures, the same film thickness is obtained when a sufficient flux reaches all areas. The Figure 4 represents the coverage of surface controlled growth (like in ALD) and compares to other techniques, which have the coverage for flux-controlled growth (like in CVD). The left side of Figure 4 shows the uniformity for all areas, even on three-dimensional structures. The surface controlled species provides the perfect uniformity for an ideal ALD growth. However, the flux controlled species results low conformality, mains varying thickness over the surface.<sup>22, 24-25</sup>





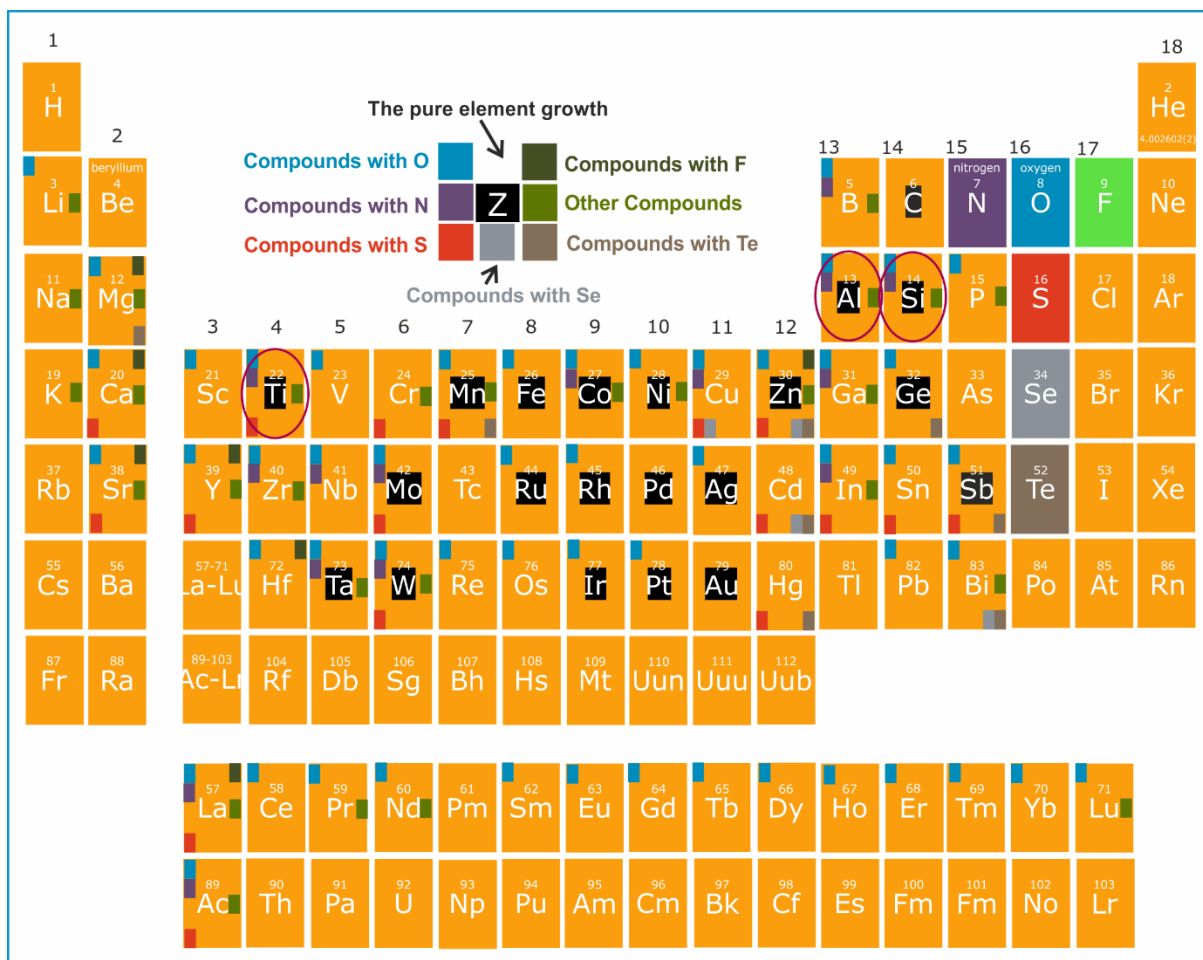
**Figure 4.** Schematic representation of conformality where deposition occurs uniformly on overall surface. While left side describe the uniform coating, the right side illustrates the flux-controlled processes, which could not meet uniformity across the surface.

**Precursors, Co-reactants, and Materials:** For an ideal ALD process there are several physical and chemical conditions need to be fulfilled like precursor stability, reactivity, volatility, and reactor temperature. Among these, the precursor chemistry play an important role and should be stable for the defined deposition temperature, which should be volatile and not decompose at the defined deposition temperature. Furthermore, the precursors should provide the self-terminating reactions without reacting with itself.<sup>33</sup>

Precursor sources are generally metal atoms, surrounded by ligands, i.e. inorganic coordination complexes. The ligands essentially play a key role in determining the characteristic of the precursor. Halide-based precursors such as  $\text{HfCl}_4$ ,  $\text{TiCl}_4$  or alkoxides such as  $\text{Ti}(\text{OPr})_4$  or alkylamides such as  $\text{Ta}(\text{NMe}_2)_5$  can be given as an example for a precursors with common ligand types.<sup>34</sup>

Co-reactant sources are generally nonmetal sources and are all volatile, small molecules, such as elements ( $\text{H}_2$  or  $\text{O}_2$ ), hydrates ( $\text{H}_2\text{O}$ ,  $\text{NH}_3$ ) or alkyl compounds. The main purpose of co-reactants is to react with surface ligands. Therefore, they must be reactive enough at the defined experimental conditions like substrate temperature.<sup>23, 34</sup>

A wide variety of technologically important materials has been deposited using ALD.<sup>22-23, 30, 34-35</sup> Furthermore, the selection of elements have been successfully included to the ALD films. In Figure 5, the periodic table shows main-group elements, transition metals, and lanthanides which have been reported for ALD deposition. ALD processes are most generally available for metal-oxides because of thermodynamic stability of the oxide bonds. However, ALD processes are also available for metal-nitrides, -selenides, -sulphides, -tellurides and additionally for pure metals such as Pt, Ru, W etc.<sup>34, 36</sup>



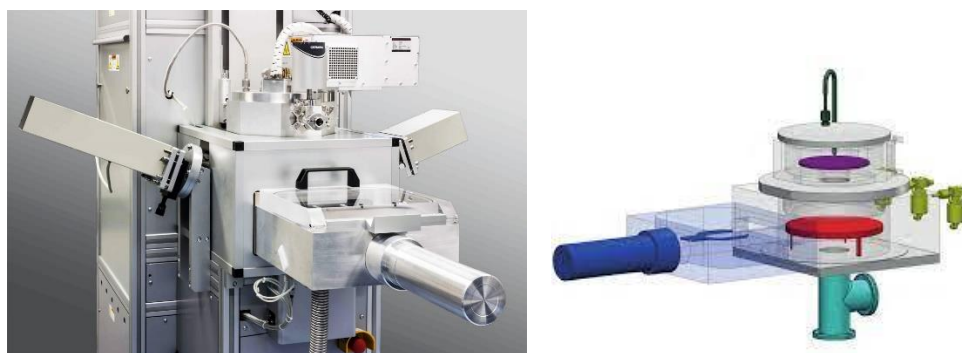
**Figure 5.** Periodic table showing the materials deposited by ALD. The circled elements indicate the studied ALD materials in this work.

**Plasma-Enhanced Atomic Layer Deposition:** To increase the reactivity during ALD deposition, co-reactants with shorter lifetimes can be also used. For instance, plasma species or ozone gases have shorter lifetimes compared to other co-reactants like water. However, due to short lifetime, these co-reactants should be produced *in situ* directly during deposition.<sup>19</sup> ALD processes, involving an extra energy to produce more reactive species, are referred to as energy-enhanced ALD or in the special case of using plasma, plasma enhanced ALD (PE-ALD).

With the application of plasma, more reactive species are obtained such as radicals, ions, photons, electrons.<sup>23</sup> The ions, electrons, and photons can be produced directly with plasma power. The use of plasma provides higher reactivity and prevent the long purge times during deposition.<sup>37,33 29</sup>

### 2.1.1 ALD Equipment

SENTECH LL reactor (Sentech Instruments) is used in this thesis for ALD depositions. A picture of this reactor is shown in Figure 6. The reactor can accommodate wafers with diameter up to 200 mm and it has a load-lock chamber for loading and unloading the samples without the need of venting the main reactor chamber. The main reactor chamber is equipped with a turbo molecular pump and fore-line pump. The base pressure in the reactor chamber is typically in 0.5 Pa at fine vacuum.



**Figure 6.** An overview of ALD reactor chamber, on the left side a view of device and on the right side schematic view of reactor chamber, which shows reactor chamber with substrate electrode (red), precursor cabinet (yellow), gas line (green), vacuum pump system (cyan), single wafer vacuum load lock and CCP source (violet).<sup>38</sup>

The reactor is equipped with a remote Capacitively Coupled Plasma (CCP) generator placed above the main reactor chamber. The CCP source consists of two parallel electrodes where the top electrode, i.e. showerhead, is powered by RF to generate plasma species. The plasma generated in such configuration is usually referred as "remote plasma". The plasma is in direct contact with the substrate which is not involved in the generation of the plasma. For the remote plasma configuration, plasma source is located remotely above the substrate. The plasma conditions can be adjusted independently from the substrate, which provides more control of the plasma properties.<sup>29, 33</sup>

Various gases are available for the generation of the plasma in this setup such as Ar, O<sub>2</sub>, N<sub>2</sub>, H<sub>2</sub>, and NH<sub>3</sub>. However in this thesis, a remote H<sub>2</sub>:N<sub>2</sub> plasma mixture was used as the co-reactant. For a detailed description of the ion flux and energies, photon flux, electron density and temperature, the reader is referred to references.

## 2.2. The Use of ALD in Corrosion Protection

Atomic layer deposition (ALD) is an enabling technology for encapsulating sensitive materials owing to its high quality, conformal coating capability.<sup>6, 9, 39-40</sup> Multiple research groups have addressed the performance of ALD thin films for corrosion protection.<sup>1, 4-5, 11-13, 15-17, 41-49</sup> A

highlight of this section is to review the performance of these thin films against corrosion. The ability of ALD in protection applications are demonstrated with focus on copper as well as other metals. The most common ALD materials are presented with some related details. The most common corrosive environments are then reported from the literature. The section is then continued with the performance of ALD thin films in corrosion protection, the effect of process parameters on protection performance and the common application areas.

### 2.2.1. ALD Materials for Corrosion Protection

Various of ALD oxide layers have introduced to protect copper against corrosion in liquid oxidative environments. However, the most intense research is performed on  $\text{Al}_2\text{O}_3$  layers for corrosion protection due to ease of nucleation on metal surfaces.<sup>1, 4-5, 11-13, 15-18, 41-45, 50-51</sup> The ALD of  $\text{Al}_2\text{O}_3$  is one of the well-known process and the process is almost ideal. The process has a wide deposition temperature range of 25-500 °C, the films are amorphous, and the precursors are relatively cheap.

In the literature, the  $\text{Al}_2\text{O}_3$  thin films are generally deposited by trimethyl aluminium and water precursors. Some research groups have reported the use of  $\text{O}_3$  or PEALD with  $\text{O}_2$  plasma rather than use of water.<sup>22, 24, 33, 50</sup> As owing more reactive species, these processes could result in better film quality, especially at lower deposition temperatures. A better nucleation may be achieved due to higher reactivity of  $\text{O}_3$  and  $\text{O}_2$  plasma. However, the possible damage on the substrate should be considered as an important effect on deposited films. Furthermore, using  $\text{O}_3$  or  $\text{O}_2$  plasma could not reach the same level of conformality in complex surfaces.

Another frequently used ALD material for corrosion protection is  $\text{TiO}_2$ .<sup>43, 45-46, 52</sup> Commonly used precursors are  $\text{TiCl}_4$  and TTIP with  $\text{H}_2\text{O}$ . Sometimes more reactive co-reactants are also used like  $\text{O}_2$  plasma. However, the chlorine impurity with the use of  $\text{TiCl}_4$  is reported in the deposited film. As chlorine is a corrosive gas, the use of TTIP is more beneficial for corrosion protection application. While the deposited films are generally amorphous, several studies are also reported the anatase formation at the temperature range 125-680 °C. Bulk  $\text{TiO}_2$  is chemically more stable than  $\text{Al}_2\text{O}_3$ , and thus expected higher protection performance in aggressive environments. While polycrystalline  $\text{TiO}_2$  showed better resistance against  $\text{H}_2\text{SO}_4$  solution than amorphous  $\text{TiO}_2$ , the grain boundaries in polycrystalline films may act as a defect and preferential route for corrosion in long-term applications. Furthermore, the deposition of  $\text{TiO}_2$  on direct metal surfaces are not favorable due to difficulties of nucleation.

Other common ALD materials for corrosion protection are SiO<sub>2</sub>, Ta<sub>2</sub>O<sub>5</sub>, HfO<sub>2</sub>, ZrO<sub>2</sub> and ZnO.<sup>9, 13, 52-55</sup> Several ALD precursors exist for these ALD processes, but most common are H<sub>2</sub>O with tris(tert-butoxy)silanol ([CH<sub>3</sub>CO]<sub>3</sub>SiOH) for SiO<sub>2</sub>, tantalum pentaethoxide (Ta[OCH<sub>2</sub>CH<sub>3</sub>]<sub>5</sub>) for Ta<sub>2</sub>O<sub>5</sub>, tetrakis(ethylmethylamino)zirconium (Zr[N(CH<sub>3</sub>)(C<sub>2</sub>H<sub>5</sub>)]<sub>4</sub>) for ZrO<sub>2</sub>, diethyl zinc (Zn(C<sub>2</sub>H<sub>5</sub>)<sub>2</sub>) for ZnO, and tetrakis(dimethylamino)hafnium (Hf[N(CH<sub>3</sub>)<sub>2</sub>]<sub>4</sub>) for HfO<sub>2</sub>. While Ta<sub>2</sub>O<sub>5</sub> and SiO<sub>2</sub> films are amorphous, the films of ZrO<sub>2</sub>, ZnO, and HfO<sub>2</sub> can have polycrystalline structures in appropriate conditions.

Several groups have introduced multilayer ALD systems to achieve better corrosion protection performance on copper, and other metal surfaces.<sup>43, 45, 52, 56-57</sup> While Al<sub>2</sub>O<sub>3</sub> layer is used to improve the adhesion/nucleation on the metal surface, following ALD layers are combined to improve the durability of films against corrosion. Due to ease of nucleation on a variety of metal surfaces, ALD-Al<sub>2</sub>O<sub>3</sub> layer is preferred as a first layer on the multilayer systems. Even a very thin Al<sub>2</sub>O<sub>3</sub> layer can therefore provide sufficient nucleation beneath other ALD materials. The most common reported multilayer system is Al<sub>2</sub>O<sub>3</sub>/TiO<sub>2</sub> in the literature.<sup>43, 52</sup> While Al<sub>2</sub>O<sub>3</sub> is used to improve adhesion/nucleation, TiO<sub>2</sub> is used to improve chemical stability in aggressive environment. Other multilayer systems, such as Al<sub>2</sub>O<sub>3</sub>/SiO<sub>2</sub>, Al<sub>2</sub>O<sub>3</sub>/ZnO, Al<sub>2</sub>O<sub>3</sub>/HfO<sub>2</sub>, etc., are also reported in different corrosive environment.<sup>52, 54</sup>

### 2.2.2. ALD Protection in Varied Corrosive Environment

A variety of corrosive liquid environments such as water, NaCl, or NH<sub>4</sub>OH has been used to investigate the protection performance of ALD films.<sup>9, 47-48, 55</sup> Abdulagatov *et al.* studied ALD of Al<sub>2</sub>O<sub>3</sub>, TiO<sub>2</sub>, Al<sub>2</sub>O<sub>3</sub> with capping TiO<sub>2</sub> and Al<sub>2</sub>O<sub>3</sub> with a capping layer ZnO on planar copper to prevent water corrosion at 90 °C.<sup>41</sup> While the Al<sub>2</sub>O<sub>3</sub> with capping ZnO layer protected the copper for 10 days, the Al<sub>2</sub>O<sub>3</sub> with a capping TiO<sub>2</sub> layer protected for 80 days. Daubert *et al.* studied the corrosion protection properties of Al<sub>2</sub>O<sub>3</sub>, TiO<sub>2</sub>, ZnO, HfO<sub>2</sub>, and ZrO<sub>2</sub> in aqueous NaCl solution.<sup>52</sup> In that work, the Al<sub>2</sub>O<sub>3</sub> and HfO<sub>2</sub> films were more preferable for initial corrosion protection, but in longer exposure, the HfO<sub>2</sub> film showed the best stability. Furthermore, other metal surfaces are also reported with similar ALD protection. For instance, pitting corrosion was observed on the stainless steel samples which protected with ALD-TiO<sub>2</sub> layer when exposed to the 1 M HCl solution.<sup>58</sup> Marin *et al.* reported the changes of ALD-TiO<sub>2</sub> stainless steel samples in 0.2 M NaCl solution for 24 h and 500 h exposure.<sup>59</sup> While the samples were stable during 24 h, the slight changes were observed for longer exposure (without dissolution of ALD-TiO<sub>2</sub> layer).

ALD thin films have been investigated against common corrosives in the gas environment, such as O<sub>2</sub> and moisture.<sup>9,55</sup> Under ambient conditions, ALD protected cobalt nanopillars has been shown improved corrosion resistance compared to bare nanopillars. At high temperatures, iron nanoparticles, silver nanoparticles, niobium and copper materials are also showed improved durability with ALD protection.<sup>60-61</sup> However, reported values are limited and shown a huge deviation based on substrate materials and deposition processes. Furthermore, ALD protection performance is generally defined after annealing or storing. Without knowing operation performance, direct conclusion could not be drawn as oxidation may occur without being noticed. Even though it appears that, ALD layers protect the metals by some of degrees, direct comparison between ALD materials are also challenging due to limited number of published papers. Thus, the performance of ALD layers against corrosion in the gas environments or at high temperatures has been lacking in the literature.

### 2.2.3. Process Parameters Effect on Corrosion Protection

The corrosion protection performance of ALD materials outlined above is dependent on several physical properties including substrate surface, deposition temperature, precursor stability, reactor pressure, etc.<sup>1, 11-13, 44, 53, 62-65</sup> The surface adsorption and reaction of precursor to the substrate defines the surface chemistry and the nucleation of ALD. Although the effect of original substrate is lost with continued deposition, the lack of uniform nucleation sites could result pinholes/defects in the deposited film. Micro-particles, heterogeneities on the substrate, or the presence of an interfacial oxide layer between the substrate and passivation layer serve as nucleation sites for defects.<sup>17,44,66</sup> Also, ALD process may lead the formation of defects due to the surface reactions caused by the inaccurate tuning of process parameters like temperature, pulse time. The combination of substrate surface properties, ALD process parameters and the imperfections of the ALD process can create intrinsic and extrinsic defects, which trigger and accelerate the corrosion process locally. As defects act as a pathway for the transport of reactive species, the defect density on which the corrosion protection performance depends has to be strictly controlled and minimized.

Several groups have been investigated the performance of ALD thin films in corrosion protection based on the defect density.<sup>1, 4-5, 9, 12-18, 42, 44, 46-48, 51-52, 54, 66-73</sup> The most intense research is performed on Al<sub>2</sub>O<sub>3</sub> layers due to the good adhesion to many metal surfaces. Vanhaberbeke *et al.* studied the defect density of 20 nm thick ALD-Al<sub>2</sub>O<sub>3</sub> layers on copper with using copper electroplating and copper wet etching techniques and reported the defect density as  $3.14 \times 10^{-6}$  area %.<sup>48</sup> Zhang *et al* showed the defect density of ALD-Al<sub>2</sub>O<sub>3</sub> layers on copper

was reduced orders of magnitude ( $90/\text{cm}^2$ ) by appropriate substrate surface treatment and efficient nucleation of ALD- $\text{Al}_2\text{O}_3$ .<sup>4</sup> The presence of interfacial oxide layer between substrate and passivation layer is intensively reported as a key role in the corrosion protection.<sup>16-17, 66</sup> Mirhashemihaghighi *et al.* studied the necessity for the control of the interface to optimize the corrosion protection of ALD ultrathin films.<sup>17</sup> It was shown that modifying the interfacial native oxide layer by pre-treatment of the copper substrate is beneficial to the corrosion resistance since less channel defects were found by presence of freshly regrown native oxide. Furthermore, the best protective properties of ALD  $\text{Al}_2\text{O}_3$  thin films on low alloy steel were achieved by pre-treatment of the substrate, according to Harkönen *et al.*<sup>68</sup> A few studies have also investigated the ALD process parameters effect on defect density.<sup>14, 68-69</sup> Chang *et al.* reported that the intrinsic defects nucleate as residual OH ligands originating from the incomplete reactions in the first ALD cycles with respect to the substrate surface properties.<sup>15</sup> To achieve the best corrosion protection with reduced defect density, there are many parameters to be tuned like pre-treatments for substrate surface properties, deposition temperature, ALD pulse time for saturation, etc. Even though several studies in the literature focused on the defect structure of ALD- $\text{Al}_2\text{O}_3$  and substrate surface properties, the systemic optimization process along from substrate surface properties to ALD process parameters with detailed discussions has not been reported.

#### 2.2.4. ALD Applications for Corrosion Protection

ALD is still one of the few techniques that can provide lower defect density compared to other deposition techniques with accurate thickness control, uniformity over a large area, and excellent step coverage.<sup>24-25, 37</sup> As materials become more complex and move into the nano-scale, these properties become increasingly demanding. As a result, ALD has emerged as an attractive encapsulation, passivation and protection technique in many application areas. Several applications used ALD films as a protection layer in the literature. For example, ALD protective layers were used for copper rollers in hot emboss components, molybdenum walls in a microreactor, plasmonic silver and copper nanostructures in biosensors, surface-enhanced Raman scattering (SERS) and femtosecond laser excitation, and copper nanowires for transparent electrodes. The most studied protective material is  $\text{Al}_2\text{O}_3$  but also  $\text{TiO}_2$ ,  $\text{SiO}_2$  and  $\text{HfO}_2$  single layers,  $\text{Al}_2\text{O}_3$ - $\text{ZnS}$  and  $\text{AlN-TiO}_2$  nanolaminates and  $\text{Al}_2\text{O}_3$  doped  $\text{ZnO}$  have been considered. As wide range of applications are available in the literature, the general requirements or restriction of ALD protection properties could not be listed. However, the most common desired properties is the protection of the underlying metals, in other words, the

protective film should be stable with less defect density to prevent etching of metals through the defects by reactive species.



### 3. Characterization Techniques

In this section, the characterization techniques with focus on the ALD film properties are reviewed. The main interest of the section is to give an overview about the characterization techniques which mostly used for ALD thin film structures. Several techniques are capable to image and quantitatively analyze the ALD materials on different length scales. From a variety of techniques, spectroscopic ellipsometry (SE), X-ray spectroscopy (XPS), X-ray diffraction (XRD) and electron microscopy are applied complementary on the thin film surfaces during this thesis. A short introduction of these techniques, data evaluation and interpretation are given in the following.

#### 3.1. Spectroscopic Ellipsometry

Spectroscopic Ellipsometry (SE) measures the change in polarization that occurs when a light beam is reflected from or transmitted through a sample.<sup>74</sup> For reflected light, this change in polarization,  $\rho$ , is often described with two values,  $\Psi$  and  $\Delta$ ;

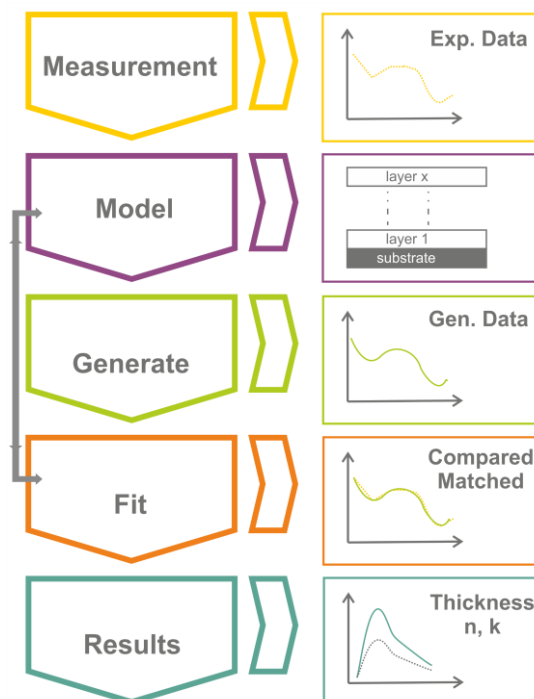
$$\rho = \tan(\Psi) e^{-i\Delta} = \frac{\bar{R}_p}{\bar{R}_s} \quad 1$$

where  $\Psi$  is the ratio of reflected amplitudes and  $\Delta$  is the phase difference between p- and s-polarizations. Polarization changes arise from the reflectivity difference between electric field components oriented parallel (p-) and perpendicular (s-) to the plane of incidence. Measurements generally occur at an oblique angle of incidence  $\phi$ , defined as the angle between the incident light beam and sample surface normal. The incident light is linearly polarized with electric field components in both p- and s-planes. The light reflection produces a change in amplitude ratio and phase difference between the p- and s-components. SE measures this ‘change’ in polarization to help determine the sample properties. Basic ellipsometry measurements produce two quantities, typically expressed as  $\Psi$  and  $\Delta$ .<sup>75</sup>

While SE measurements are used to determine optical constants and film thickness, they are not a direct measurement. In a few simplified cases, the equations can be inverted to calculate optical constants or film thickness from measured  $\Psi$ ,  $\Delta$  data.<sup>76</sup>

**Data analysis:** Regression analysis is commonly used to determine the best-fit results considering all measured and simulated data.<sup>76</sup> Figure 7 summarizes the process of ellipsometry analysis.

The first step is to collect SE data on the sample. The ellipsometer shines light with known polarization onto the sample and then the light reflects or transmits into the receiver head which determines the new reflected or transmitted polarization state.



**Figure 7.** Data analysis flowchart for Spectroscopic Ellipsometry measurements. Regression analysis helps determine unknown parameters of the optical model such as film thickness and optical constants.

In step 2, the sample is described with using optical model, which gives layer thicknesses and optical constants for each material. The model-generated data is calculated based on Fresnel equations. For known sample properties, reference optical constant values for many materials are available in the literature. For unknown sample properties, initial estimates are also given at this step. In Step 3, regression analysis is used. The unknown model parameters are varied to improve the match between model-generated curves and collected data. The fitting is based on minimizing the difference between curves as described by a comparator function, such as mean squared error (MSE).

The model can be modified, as shown in Step 4 of Figure 7, to improve the match between model predicted and measurement data. As a rule, the best sample description is often the one produced by the simplest model. The model provides information about the unknown sample properties, as shown in Step 5. SE measurements are commonly used to determine thin film thickness and optical constants.<sup>77-78</sup> However, many additional material properties can be determined through their effect on material optical constants: crystallinity, conductivity, composition, porosity, strain, and surface roughness.<sup>79</sup>

## SE Analysis in This Work

A spectroscopic ellipsometry was used to analyze the growth characteristic of ALD thin films via *in situ*. During ALD growth, the deposition was stopped, and the deposited film thickness was measured at regular intervals. The native oxide of copper before the deposition was also controlled via *in situ* SE measurements. The deposited ALD film thicknesses were further measured via *in situ* and *ex situ* SE. While Drude modelling was mostly used for ALD thin film's thickness measurements, Drude Lorentz model was also used to measure copper native oxide layer.

## 3.2. X-ray Photoelectron Spectroscopy

X-ray Photoelectron Spectroscopy (XPS) is a surface-sensitive characterization technique for quantitative elemental composition and chemical analysis.<sup>80</sup> It is based on the photoelectric effect, where an X-ray photon is absorbed by a core or valence electron. If the incident photon energy is larger than the binding energy of the electron, the electron will be emitted. The binding energy is specific to the orbital and the atom from which the electron is emitted. Therefore, it is possible to determine the elemental composition of a sample. Moreover, quantitative analysis can be performed since the number of detected electrons for a certain binding energy is proportional to the amount present from a certain element in the sample. The binding energy of the emitted electrons is dependent on the chemical environment and on the oxidation state. Therefore, with XPS it is also possible to distinguish between different compounds representing different chemical environments.<sup>81</sup> This quantification gives the relative intensities of the detected elements (i.e. atomic percentages).

In addition to conventional XPS, depth profiling can be obtained to determine the elemental composition throughout the film. The main method to obtain the depth profile is etching for instance with argon ions where surface layers are removed by sputtering while XPS spectra are obtained step by step during the removal of surface layers.

## XPS Analysis in This Work

X-ray photoelectron spectroscopy was used to analyze the chemistry of copper and ALD thin films. According to specific binding energies, quantitative atomic concentration and chemical state of the detected elements was found for both copper and deposited ALD thin films (for details please see chapter 5).

### 3.3. X-ray Diffraction

X-ray diffraction (XRD) is a characterization technique used to determine the crystalline structure of a sample. This technique is based on the detection of constructive interference of X-rays scattered from a sample. When a sample is exposed to X-ray radiation, it results in a diffraction pattern with enhanced intensities in specific directions associated with its crystal structure.<sup>82-83</sup> By moving X-ray detector, it is possible to determine the directions of the diffracted beams and their intensities.<sup>84</sup>

An X-ray beam hits the sample with an incident angle. The difference between the distances covered by the two X-rays gives  $2d \sin \theta$ , where  $\theta$  is the angle of incidence of the X-ray beam and  $d$  is the spacing between the two lattice planes. If this difference in distance is equal to a multiple of the wavelength of the X-ray radiation (1.54 Å when using a Cu K- $\alpha$  source), constructive interference between the two X-rays will occur.

This condition is referred to Bragg's law<sup>85</sup> and is described by the following equation:

$$n\lambda = 2d \sin \theta \quad 2$$

In  $\theta/2\theta$  scan measurements, both the incident X-ray beam and the detector make an angle  $\theta$  with respect to the sample surface. By scanning over a range of  $2\theta$  values, various sets of lattice planes can produce constructive interference. In this measurement configuration, only the planes oriented parallel to the surface will contribute to the diffraction spectra. Since the penetration depth of Cu K- $\alpha$  X-rays is usually around 10  $\mu\text{m}$ , for thin films with thicknesses in the nanometer range a strong contribution of the substrate on the diffraction spectra is usually an issue.<sup>84</sup> For this reason another measurement configuration should be employed to gain more information on the crystalline structure of a thin film by minimizing the substrate contribution. This configuration, called Grazing Incidence XRD (GI-XRD).

In GI-XRD the X-ray beam hits the sample with a constant incident angle,  $\omega$  (usually  $< 2^\circ$ ).<sup>84</sup> The angle of incidence beam is fixed and a diffraction spectrum is collected by moving the detector along the  $2\theta$  circle.<sup>84</sup>

The bisector between the incident and reflected X-ray is not perpendicular to the sample surface as in the case of  $\theta/2\theta$  scan. In the GI-XRD configuration, the direction of the bisector is constantly changing due to the fixed incidence angle. Therefore, by scanning over the  $2\theta$  range, lattice planes having different orientations with respect to the surface normal are taken into diffraction conditions.

## **XRD Analysis in This Work**

X-ray diffraction was used to analyze the crystal structure of ALD thin films. With application of GI-XRD technique, the crystal structure of ALD thin films were obtained with small contribution of the substrate, copper. Additionally, ALD thin films were characterized via *in situ* XRD at high temperatures to observe the performance of protection properties against copper corrosion (for details please see chapter 5).

### **3.4. Electron Microscopy**

Electron microscopy (EM) is a standard technique to characterize materials on a micro- and nanometer scale.<sup>86</sup> With an electron beam the specimens are irradiated and numerous signals are generated by the interaction of the beam and specimen. The signals facilitate the image of specimen; characterize the material structure and composition. In material science, EM is one of the most used technique due to a versatile capability.<sup>87</sup> There are two main different types of electron microscope, the scanning electron microscope (SEM) and the transmission electron microscope (TEM). The image is obtained with the reflected or backscattered electrons in the SEM, while the transmitted electrons are used for imaging in the TEM. In both microscopes, the electron beam is generated by an electron gun and controlled by electromagnetic, electrostatic lenses and apertures.

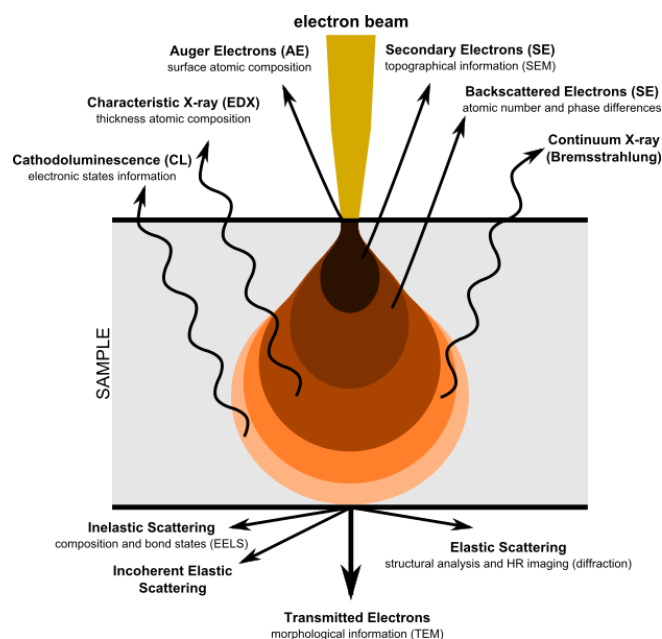
#### **3.4.1. Scanning Electron Microscopy**

SEM characterization allows the imaging of non-electron-transparent samples.<sup>87-88</sup> The surface of the sample is scanned by the electron beam. The electron beam interacts with the large volume of specimen. The depth of the interaction volume is dependent on the secondary ion radiations, the mean free path of the radiation in the sample. A variety of signals (secondary, backscattered and Auger electrons, continuum and characteristic X-rays and fluorescence) are generated by the primary beam and sample interaction illustrated in Figure 8.<sup>88</sup> Secondary and Auger electrons provide topographical and compositional information of the surface due to short mean free path by emitted electrons from near surface region. The detected electron' intensity is mapped to the beam position for imaging. The backscattered electrons are used to determine the elemental variations of the surface from deeper area as compared to secondary electrons due to longer mean free path. While the heavier elements have higher scattering efficiency, the lower ones have lower scattering efficiency. Therefore, the surface areas with heavier elements appear brighter (Z contrast), while the lighter are darker in SEM images.<sup>89</sup>

The SEM instrument is generally equipped by EDX for enabling qualitative and quantitative elemental analysis.

### SEM Analysis in This Work

A scanning electron microscopy was used to characterize the surface of ALD thin films. By using of secondary electron images, topographical features of ALD thin films were represented. Backscattered electron images were used to analyze the contrast differences based on atomic numbers. The use of SEM in this work was mainly focused on the ALD thin film surface properties for before and after features.



**Figure 8.** Electron-matter interactions, the different types of signals generated.<sup>90</sup>

### 3.4.2. Transmission Electron Microscopy

In TEM, a hot filament or field emission gun inside a high vacuum column produces the electrons, which are accelerated and focused on the sample by electromagnetic lenses.<sup>87, 89, 91</sup> In bright-field transmission electron microscopy (BF-TEM), a thin ( $\leq 200$  nm) samples are required as electrons must be transmitted through the sample. With the electron beam interaction of the sample, absorption, diffraction, and scattering can occur. The image is then obtained by projected beam on a fluorescent screen, image plate detector or CCD camera to analyze the morphological properties.<sup>91</sup> Indeed, the structural information (crystallographic) can be also obtained by direct imaging of crystal lattice spacing or by selected-area electron diffraction (SAED). In the case of SAED, the diffraction pattern in reciprocal space is collected from the crystalline domains of the sample.

## **HAADF-STEM**

The scanning transmission electron microscopy (STEM) provides narrower electron beam to scan through the specified sample area rather than the entire specimen.<sup>87-88</sup> STEM provides the images which are not visible, weakly absorbed/scattered in BF-TEM. The image is obtained on the illuminating area by detection of scattered electrons and mapping their intensities. The resolution of the image is dependent on the beam diameter, accuracy of position and interaction volume. There are several detection geometries available; however, for the thin film characterization the high angle annular dark field (HAADF-STEM) is mostly preferred.<sup>92</sup> As electrons are scattered at high angles involving heavier elements, the elemental composition of the sample can be derived HAADF-STEM and images can be obtained at atomic scale.

## **Elemental Analysis Techniques**

Electron energy loss spectroscopy (EELS) uses the energy distribution of electrons (typically high-energy electrons, 60-300 kV), which electrons can interact either elastically or inelastically with the sample.<sup>91-92</sup> A typical energy loss spectrum includes several regions. The first peak, the most intense for a very thin specimen, occurs at 0 eV loss (equal to the primary beam energy) and is therefore called the zero-loss peak. It represents electrons that did not undergo inelastic scattering but may have been scattered elastically or with an energy loss too small to measure. EELS data can be used to determine the atomic structure and chemical properties of a specimen, including the type and quantity of atoms present, chemical state of atoms and the collective interactions of atoms with their neighbors.

## **TEM Analysis in This Work**

Transmission electron microscopy was used to analyze the structural changes of ALD thin films and copper. After exposure of corrosive environments, the thin film stability was studied via bright field (BF) images to understand even the nanoscale changes in the structures. High angle annular dark field images were further used for chemical analysis. The crystallinity of the thin films was also demonstrated by use of fast Fourier transform (FFT).





## 4. Overview of Thesis

This thesis is mainly focused on the investigation of ALD based corrosion protection of copper by series of experiments. This work paves a path for future ALD layer applications in the protection of copper and other metals in important fields of technology like semiconductor fabrication processes.

### ***In Situ* X-ray Diffraction and Spectro-Microscopic Study of ALD Protected Copper Films**

#### **Publication I: Technological and Scientific Context**

As shown before, various ALD oxide layers have been introduced to protect copper against corrosion in liquid environments. The most studied protective material is  $\text{Al}_2\text{O}_3$  but also  $\text{TiO}_2$ ,  $\text{SiO}_2$  and  $\text{HfO}_2$  single layers,  $\text{Al}_2\text{O}_3$ -ZnS,  $\text{Al}_2\text{O}_3$ - $\text{SiO}_2$  and  $\text{Al}_2\text{O}_3$ - $\text{TiO}_2$  bilayers have been considered to protect copper against corrosion in a variety of chemical environments such as NaCl, water, or  $\text{NH}_4\text{OH}$  (references in Section 2.2). However, the performance of ALD oxide layers at elevated temperatures, along with a detailed discussion of the microstructural evaluation of the layer stack has been not reported. The protection of copper is essential for these elevated temperatures (up to  $350\text{ }^\circ\text{C}$ ) in many applications such as semiconductor devices, PCB, etc. Therefore, within this thesis, the corrosion protection of Cu using  $\text{Al}_2\text{O}_3/\text{TiO}_2$  and  $\text{Al}_2\text{O}_3/\text{SiO}_2$  bilayer at  $350\text{ }^\circ\text{C}$  was investigated in the first step using *in situ* X-ray diffraction (XRD). The surface of ALD protected Cu were evaluated in the second step using X-ray photoelectron spectroscopy (XPS) and scanning electron microscopy (SEM). The composition and structure of the ALD bilayers were further studied using a scanning transmission electron microscopy with an electron energy-loss spectrometer. The cross-sections were prepared by a focused ion beam.

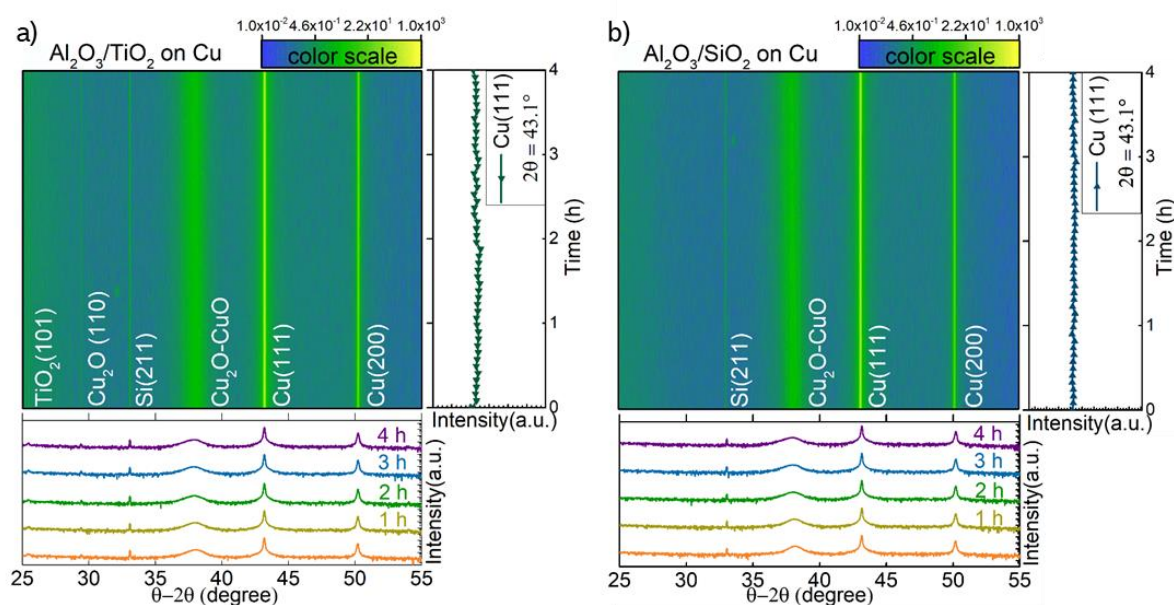
#### **Publication I: Results**

The prepared bilayers were composed of 10 nm  $\text{Al}_2\text{O}_3$  as a seed layer and 40 nm of protective layer structures on  $1.5\text{ }\mu\text{m}$  thick Cu layer. The thickness of the layers was measured by *in situ* and *ex situ* spectroscopic ellipsometry on Cu layer as well as on Si layer as reference. According to GI-XRD spectra, ALD layers were amorphous, and no additional phases were detected. The protected copper diffraction peaks were found at around  $43.1^\circ$  and  $50.2^\circ$  corresponding to (111) and (200) reflection planes, respectively. Additionally, the broad peak was observed at around  $37.8^\circ$ , attributed to a mixture of oxide phases.

The corrosion protection performance of the ALD bilayers were tested by *in situ* XRD analysis, which allows direct observation and overview of the evaluation of solid-state phases over time

and in response to changing temperature. We evaluated the Cu (111) peak intensity in bare- and protected-Cu metal as a function of time for 4 hours. During first measurements, XRD pattern started to change in a decrease of Cu diffraction peaks and an increase of oxide phases. The Cu (111) peak dropped to 70% of its initial intensity in one hour. After 4 h exposure to 350 °C, Cu diffraction peaks almost disappeared and were converted into a mixture of oxide phases, including mainly CuO.

In contrast, ALD covered copper films showed “excellent” protection against corrosion. Figure 9a,b shows  $\text{Al}_2\text{O}_3/\text{TiO}_2$  and  $\text{Al}_2\text{O}_3/\text{SiO}_2$  diffraction data in which copper peaks stayed same during 4 h at 350 °C. Although there were no changes observed for Cu peaks, the tiny anatase phase at 25.4° peak was observed at 25.4° that exhibits only small amount crystallinity for 40 nm thick  $\text{TiO}_2$  during annealing.

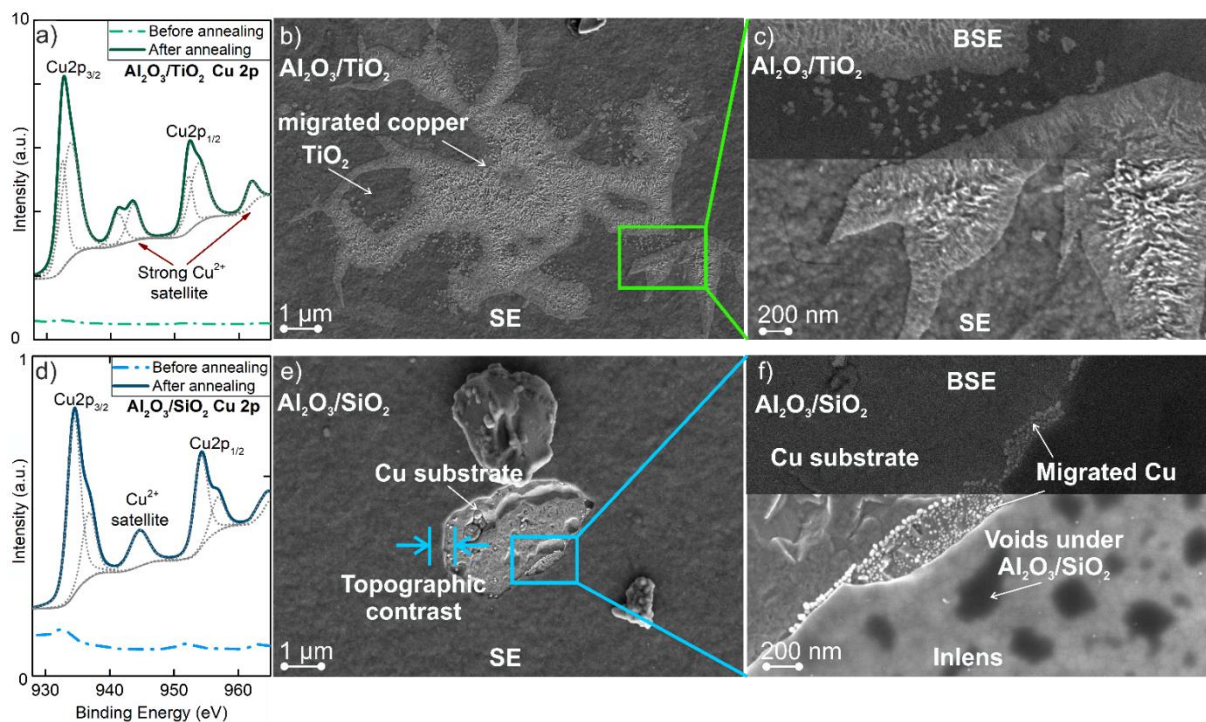


**Figure 9.** *In situ* XRD analysis at 350 °C for 4 h under atmospheric conditions. The density plot represents overall XRD pattern during annealing; the right-hand side gives the change of Cu (111) peak intensity over the time, and the lower part gives the XRD pattern for specified annealing times for (a)  $\text{Al}_2\text{O}_3/\text{TiO}_2$  on Cu, and (b)  $\text{Al}_2\text{O}_3/\text{SiO}_2$  on Cu.

To get better insight in two underlying microscopic processes, *post factum* spectro-microscopic investigations were studied for the interactions of the copper with ALD protection layers. While an overview of the morphology was studied by detailed scanning electron microscopy (SEM), additional X-ray photoelectron spectroscopy (XPS) measurements provided insights in the chemical nature of the process.

The effect of annealing on the morphology of  $\text{Al}_2\text{O}_3/\text{TiO}_2$  layer is presented in Figure 10a-c. According to XPS survey spectra, copper was detected on the surface with a 5 at.% coverage by the single element analysis, showing Cu 2p metal peaks and additionally strong  $\text{Cu}^{2+}$  satellite

peaks. The findings showed that Cu atoms moved to surface and oxidized on the surface (Figure 10a). SEM analysis indicated the presence of two different phases, supporting the XPS findings. As shown in Figure 10b,c, presence of copper on the surface was detected by using back scattered electron (BSE) imaging. The brighter areas detected by BSE were attributed to copper due to higher atomic number.

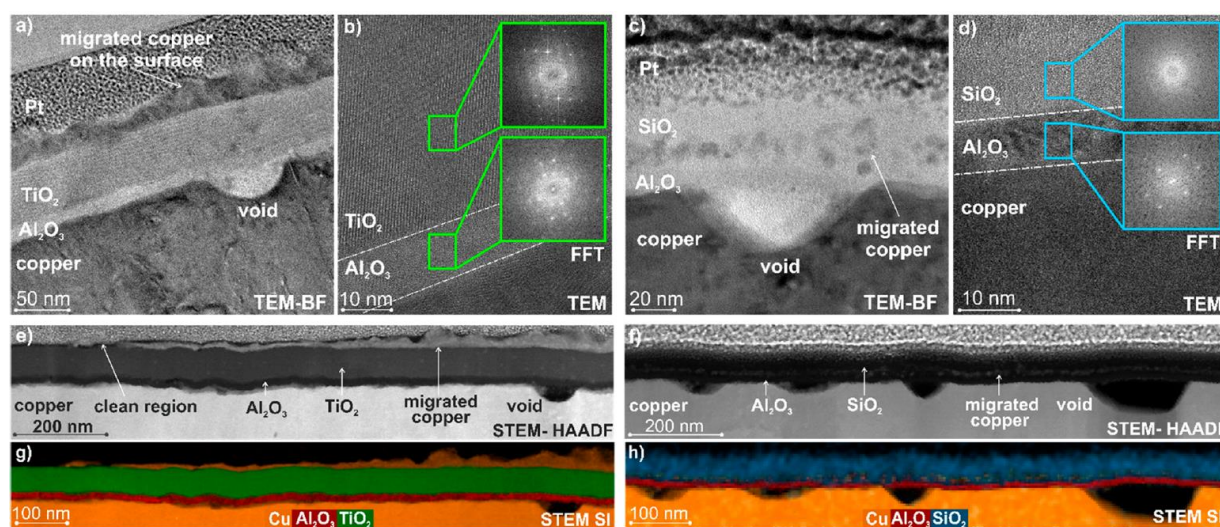


**Figure 10.** Post factum surface analyses of the film stacks following the *in situ* XRD. (a) XPS of copper peaks from the surface of the  $\text{Al}_2\text{O}_3/\text{TiO}_2$ . (b) A secondary electron signal from SEM. (c) Side by side comparison of backscattered and secondary electron signals. (d) The presence of copper species on the surface for  $\text{Al}_2\text{O}_3/\text{SiO}_2$  films. (e) An SEM image of a fracture surface (f) A close-up image of the fracture surface taken using the in-lens detector.

In the case of  $\text{Al}_2\text{O}_3/\text{SiO}_2$  layer, the copper, found on the surface, strongly reduced to 0.7 at.% coverage. The single elemental analysis showed Cu 2p metal peaks, and a rather weak  $\text{Cu}^{2+}$  peak (Figure 10d). The SEM analysis, in figure 10e,f, was carried out on the fractured region that includes  $\text{SiO}_2$  layer, Cu substrate and the interface with diffused Cu. The topographical contrast is given to represent height differences on the fractured region. BSE imaging was again used to label the copper and  $\text{SiO}_2$  layer. By using Inlens imaging, the subsurface information was additionally collected. The void structures were observed under the ALD layer and further supported by the calculation of the penetration depth of electrons.

The composition and structure of ALD thin films after annealing were evaluated using transmission electron microscopy (TEM) in combination with an electron energy-loss spectrometer (EELS) after cross-section preparation with focused ion beam (FIB). Figure 11a

shows the bright field image of the  $\text{Al}_2\text{O}_3/\text{TiO}_2$  layer which includes the void structure and migrated copper on the surface. A fast Fourier transform (FFT) of the TEM image, given in Figure 11b, showed the formation of crystallites in the  $\text{TiO}_2$  layer as supported by XRD measurements. The high-angle annular dark-field (HAADF) images of annealed  $\text{Al}_2\text{O}_3/\text{TiO}_2$  is given in Figure 11e and the elemental maps, extracted from electron energy-loss spectra, are given in Figure 11g for  $\text{Al}_2\text{O}_3/\text{TiO}_2$  based on Cu-Al-Ti-O elements, where the element oxygen was not included to ease the data interpretation. The copper was found on the surface of  $\text{Al}_2\text{O}_3/\text{TiO}_2$  lamella at significant amounts in agreement with XPS and SEM analyses.



**Figure 11.** Bright-field (BF) images of annealed (a)  $\text{Al}_2\text{O}_3/\text{TiO}_2$  and (c)  $\text{Al}_2\text{O}_3/\text{SiO}_2$  bilayers. High-angle annular dark-field (HAADF) images of annealed (e)  $\text{Al}_2\text{O}_3/\text{TiO}_2$  and (f)  $\text{Al}_2\text{O}_3/\text{SiO}_2$  were given corresponding to (g) Cu-Al-O-Ti and (h) Cu-Al-O-Si elemental maps extracted from the electron energy-loss spectrum image.

In the case of  $\text{Al}_2\text{O}_3/\text{SiO}_2$ , more void structures were observed and migrated copper was detected inside the layer, given in Figure 11c. The FFT of the  $\text{SiO}_2$  layer showed the scattering characteristic of amorphous phase, shown in Figure 11d. The high-angle annular dark-field (HAADF) images of annealed  $\text{Al}_2\text{O}_3/\text{SiO}_2$  are given in Figure 11f.

The elemental maps, extracted from electron energy-loss spectra, are given in Figure 11h for  $\text{Al}_2\text{O}_3/\text{SiO}_2$  based on Cu-Al-Si-O elements, where the element oxygen was not included to ease the data interpretation. The copper was not present on the surface of  $\text{Al}_2\text{O}_3/\text{SiO}_2$  bilayer and the bulk of the copper atoms seem to have been captured within the  $\text{SiO}_2$  layer, near the  $\text{Al}_2\text{O}_3/\text{SiO}_2$  interface, according to the high-resolution HAADF-STEM images and elemental mapping using EELS, which is shown in Figure 11h.

According to cross-section analysis, migration channels could not be detected in the ALD bilayers. However, voids in the copper forming near the interface of both  $\text{Al}_2\text{O}_3/\text{SiO}_2$  and  $\text{Al}_2\text{O}_3/\text{TiO}_2$  were observed.



### **Publication I: Discussions**

In the case of  $\text{Al}_2\text{O}_3/\text{TiO}_2$ , copper was found to migrate through pinholes and defects and reached the topmost layer (5.2 at.% on the surface). As no copper was found inside the ALD layers, mass diffusion of copper during annealing could be excluded. The presence of defects inside ALD layers were attributed to the several mechanisms such as ALD process imperfections, Cu substrate surface properties or the recrystallization of  $\text{TiO}_2$ .

In the case of  $\text{Al}_2\text{O}_3/\text{SiO}_2$ , copper migrated through the  $\text{Al}_2\text{O}_3$  layer and stopped on around interface but did not reach the surface at large amounts (0.7 at.% on the surface). The hindered copper movement was attributed the higher density of  $\text{SiO}_2$  layer and its structural stability in its amorphous phase. Additionally, the drive through diffusion within  $\text{SiO}_2$  could be the mechanism of copper migration.

The important overall results were that Cu was migrated to the surface and/or interface of the ALD layers with using temperature as a driving force. Structural relaxations, recombination of point defects or formation of grain boundaries with the crystallization of layer might strongly affect the migration of copper. In addition, the defects inside ALD layers, so called pinholes, play an important role in creating pathways for copper movement. The structural defects or Cu substrate imperfections can serve as a nucleation sites for pinholes and defects inside ALD layer. Furthermore, mass diffusion within the ALD layer might be another mechanism for copper migration. The copper migration, therefore, strongly depends on the layer stack.

### **Publication I: Conclusions**

The ALD bilayers successfully functioned as aimed in protection the underlying copper. Although copper migration was observed on both film stack, the layers could be improved by substrate cleaning and optimization of ALD parameters to reduce the number of overall defects and pinholes which should block the copper migration to a substantial degree if not altogether. These investigations demonstrated that the defect density is the most important parameter and must be strictly controlled and minimized for better corrosion protection performance, especially such a thin layer. These observations reveal that the correct identification and the tuning of principal ALD parameters are essential to achieve the best corrosion protection with ALD thin films.

## **Bayesian Machine Learning for Efficient Minimization of Defects in ALD Passivation Layers**

### **Publication II: Technological/ Scientific Context**

The main challenge for deposition of high quality thin films for corrosion protection is eliminating defects, such as pinholes and structural defects that allow the transport of reactive species into the films. The heterogeneities on the substrate surface, microparticles, or presence of interfacial oxide layer between the substrate and passivation layer serve as a nucleation point for defects. Additionally, ALD process may lead to defects according to undesired surface reactions due to inaccurate tuning of process parameters. These combinations may create intrinsic and extrinsic defects, which accelerate locally the corrosion process. Therefore, the systematic optimization process along from substrate surface properties to ALD process parameters is essential to achieve the best corrosion protection performance.

There are various methods to reduce the number of experiments while identifying the critical parameters. Among them, the two-level fractional factorial design (FFD) is one of the widely used design of experimental method to screen the primary factors that control the process. It is mainly used to determine whether the parameters have an effect on the result (like defect density) and to estimate the magnitude of the parameter on the result. The important parameters are identified using two-level FFD analysis to focus on the optimization process with further experiments. The other optimization methods based on mathematical models aim to obtain the most extensive possible information about the produced results with the smallest possible number of experiments. For example, Taguchi or response surface methodology are used to build a model for the relation between the parameters and output results, which is further used for optimization purposes. However, the main disadvantage of these optimization methods is that the experimental parameters must be defined before the optimization process and cannot adopt the features that appear during the experiments. In other words, it would be necessary to extend the parameter space repeatedly to build an acceptable model and perform optimization if the mathematical model is not verified by the defined design method.

Machine learning methods to optimizing selected parameters using small number of experiments has made great progresses in recent years. Among these, the Bayesian optimization (BO) method can employ a probabilistic model to represent unknown function. Bayesian optimization is a sequential design strategy for global optimization of black-box functions that does not assume any functional forms. The BO uses a model-based approach which is updating at each iteration using new results and generating new candidate parameters with probability

distribution of promising solutions. The sequential design is achieved by balancing two criteria. Firstly, BO explore the unknown regions based on the parameters limit and a priori knowledge. Secondly, it focuses on a specific region where interesting behavior is observed such as rapid change or non-linearity. The single iteration of BO, used in this work, can be summarized as following:

- a. BO selects a new parameter set based on the model prediction
- b. A physical experiment is conducted with the selected parameters and the results is obtained (defect density is measured)
- c. The model is updated with newly collected data from the experiment for the next iterations of BO (new parameters are selected again accordingly)

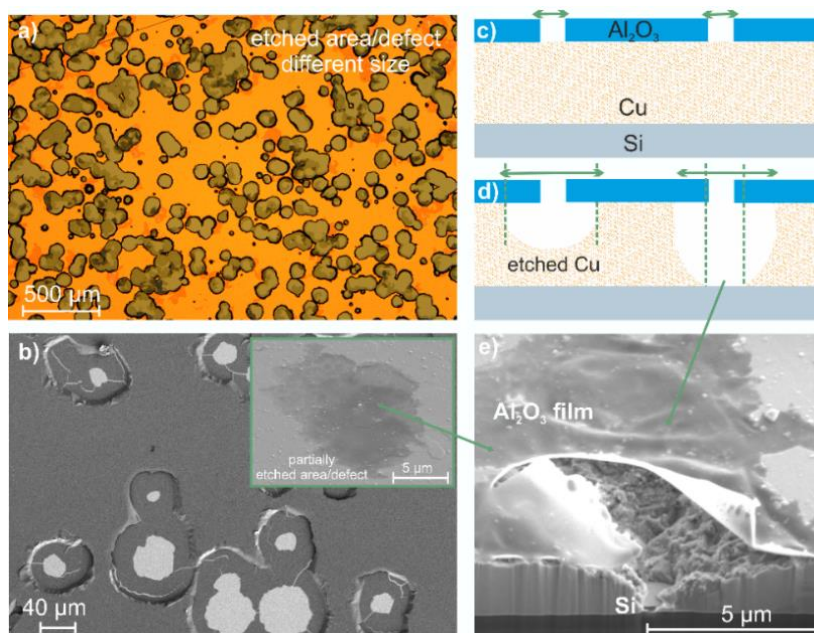
The BO achieves good balance between the modelling difficulty and parameter optimization efficiency. There are many optimization problems are solved using BO approach. However, its application to the optimization of ALD film properties have not been reported. Therefore, within this thesis, the effect of ALD process parameters and copper surface properties on corrosion protection performance with a model-based study of ALD- $\text{Al}_2\text{O}_3$  thin films are investigated by using a hybrid approach. In this hybrid approach, a two-level FFD method is used to rapidly identify the main parameters that effect the defect density. Then, BO approach is applied to find the optimum values for the selected process parameters.

The properties of the fabricated ALD films are studied by different techniques. The growth properties and the final thickness of the layers were analyzed using *in situ* spectroscopic ellipsometry. The defect density of the layers was utilized by wet etching technique. The layers were immersed to nitric acid solution for 30 min. The etched area percentage was used as an indicator of the defect density. Samples after wet etching were analyzed by XPS and SEM.

## **Publication II: Results**

The  $\text{Al}_2\text{O}_3$  thin films were deposited for 500 cycles using different process parameters and the final thickness of the deposited films was measured between 27 nm and 40 nm based on the process parameters.

The reference  $\text{Al}_2\text{O}_3$  films, deposited with standard parameters, immersed the nitric acid solution for 30 min. After the acid solution reached the copper surface through the defects, the etching reaction occurred. The typical etched pattern is shown in Figure 12a and 12b. The proposed sketch of major steps for the wet etching process is given in Figure 12c,d. The cross-section of a single etch pit is also shown in Figure 12e.



**Figure 12.** The 30 min etching of Al<sub>2</sub>O<sub>3</sub>-protected Cu. (a) Optical microscope images from the middle of the area. (b) SEM images from the larger vias. (c) and (d) Proposed sketch for major steps. (e) Cross-section images of the presented area that focuses on smaller vias.

The reference sample deposition is repeated three times to determine the repeatability of the process. Accordingly, the overall mean etched area for three batches was found extremely large ( $44.94 \pm 27.32\%$ ). The substantial deviation of the etched area percentage is attributed to the unoptimized process.

**Table 1.** Process parameters that could affect the defect density of ALD thin films.

Pretreatment	Ar-H <sub>2</sub> Plasma O <sub>2</sub> Plasma
ALD Process	Temperature (for 1 <sup>st</sup> and 2 <sup>nd</sup> half-cycle) Pulse Time (for 1 <sup>st</sup> half-cycle)
Parameters	Atomic Layer Annealing (ALA- end of each cycle) Pressure (for 1 <sup>st</sup> and 2 <sup>nd</sup> half-cycle)

The optimization process started with the application of two level FFD analysis to identify the main parameters for further optimization study. A total six parameters, as given in Table 1, were screened. With two level FFD analysis, 8 experimental runs were performed for the upper and lower limit of the parameters in the defined experimental matrix. The main contribution of each parameter was calculated according to etched area percentage, given in Table 2. The experimental matrix, etched area percentages and calculated contributions are given with details in Chapter 6. Accordingly, Ar/H<sub>2</sub> plasma pretreatment, deposition temperature and pulse time were selected as the main influencing parameters on ALD deposition quality. Hence, the number of parameters is reduced from 6 to 3 by two level FFD analysis.



The optimization process is continued with selected three parameters. The Al<sub>2</sub>O<sub>3</sub> thin films were deposited iteratively using the process parameter values suggested by BO method. The duration of Ar/H<sub>2</sub> plasma was defined between 0 min and 15 min, the deposition temperature varied between 150 °C and 350 °C, and the pulse time was limited to 20 ms and 80 ms. Their values were varied until the etched area percentage reached the target value of 0.03% which was selected based on the best-performing run during FFD analysis. The optimization was started with 10 parallel runs, in which seven of the runs were randomly chosen and the remaining with known-outcome conditions from previous experiments. Table 3 summarizes the result of experiments for three of the independent runs.

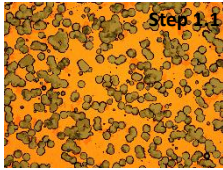
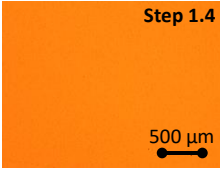



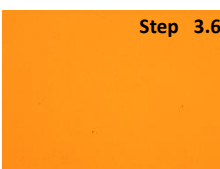
**Table 2.** Process variables based on the two-level FFD with the final film thickness, growth per cycle (GPC), and etched area percentages. The etched area percentage was defined as the response of the system. The contribution to the response (etched area) was calculated and given for each parameter.

	Pre-treatment		ALD process parameters				Thickness (nm)	GPC (nm/cycle)	Etched Area (%)
	Ar-H <sub>2</sub> plasma (min)	O <sub>2</sub> plasma (min)	Temperature (°C)	Pressure (Pa)	Pulse time (ms)	ALA (ms)			
Run 0	0	0	150	6	20	0	27.3	0.05	45.00%
Run 1	15	5	350	20	80	40	51.2	0.103	47.00%
Run 2	0	5	350	6	80	0	44.2	0.075	13.63%
Run 3	15	0	350	20	20	0	48.4	0.092	0.03%
Run 4	0	0	150	20	80	0	46.1	0.095	1.03%
Run 5	0	0	350	6	20	40	54.2	0.103	0.08%
Run 6	0	5	150	20	20	40	56.1	0.106	1.77%
Run 7	15	0	150	6	80	40	56.7	0.107	0.29%
Run 8	15	5	150	6	20	0	26.7	0.048	30.70%
Effect	15.80	23.32	7.13	1.32	7.42	1.30			
SS	499.41	1087.8	101.55	3.46	110.24	3.40			
<b>Contribution</b>	<b>21.65%</b>	<b>47.17%</b>	<b>4.40%</b>	<b>0.15%</b>	<b>4.78%</b>	<b>0.15%</b>			

The etched area percentage as a function of number of iterations is given in Figure 13a. All of the optimization runs reached the target etched area percentage in the second or third iteration of the optimization process. To continually search the optimal state and gain more information about the process, additional experiments were performed on the first three optimization runs. The local minimum points were prioritized in these additional runs. Figure 13b illustrates the additional experiments. For the first run, the etched area percentage improved in the first iteration. However, the second and third runs showed the improvement in the following iterations.

By application of BO, the etched area percentage of the optimized ALD layers was improved at least four orders or magnitude compared to reference state. The reliability of the optimized layers were evaluated repeating the process 3 times under the same condition. For three batches, the mean etched area was found  $0.003 \pm 0.001\%$ , demonstrating the successful application of BO approach.

**Table 3.** Experimental parameters and results of 3 parallel optimization runs for achieving the defect density target (all runs are given in Chapter 6). Each optimization step is labeled by the identifier of the optimization run and the corresponding iteration of the BO (*e.g.*, Step 1.2). The table shows the experimental parameters at each step, the final ALD thickness of the Al<sub>2</sub>O<sub>3</sub> thin film, the growth rate GPC, and the etched area percentage. The selected optical microscope images are given for the best and worst observed etched area percentages. Step 1.1 shows the reference sample.

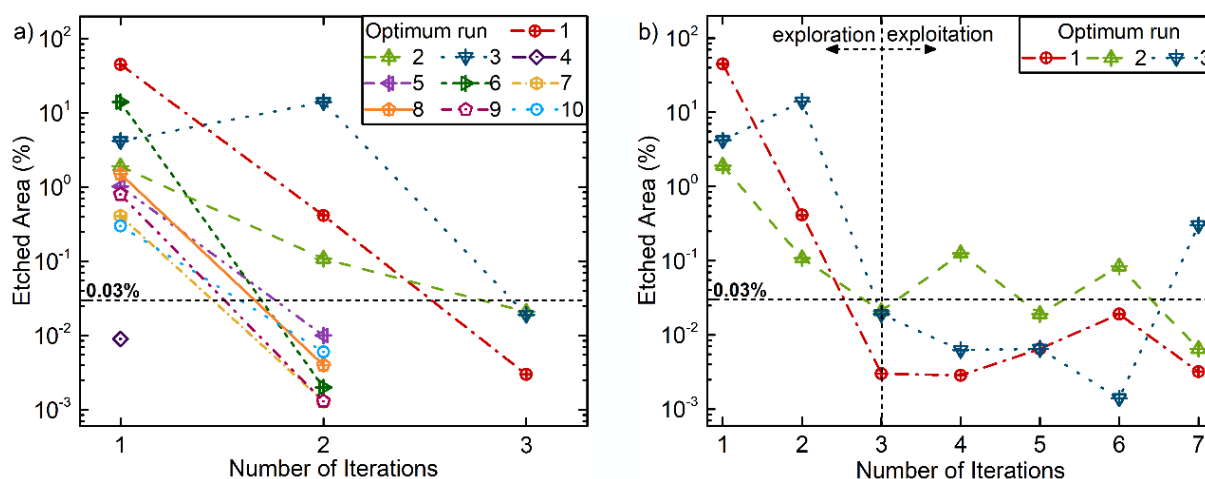
Optimum Run	Pre-treatment	ALD process parameters		Thickness (nm)	GPC (nm/cycle)	Etched Area (%)	Selected Optical Microscopy Images	
	Ar-H <sub>2</sub> plasma (min)	Temperature (°C)	Pulse time (ms)					
Step 1.1	0	150	20	27.26	0.056	44.935		
Step 1.2	0	250	80	39.25	0.080	0.414		
Step 1.3	7.5	350	60	41.01	0.084	0.018		
<b>Step 1.4</b>	<b>5</b>	<b>250</b>	<b>40</b>	<b>34.96</b>	<b>0.073</b>	<b>0.003</b>		
Step 1.5	5	300	50	38.49	0.081	0.007		
Step 1.6	5	250	50	35.2	0.074	0.019		
Step 1.7	7.5	300	50	39.14	0.079	0.003		
Step 2.1	0	350	20	35.9	0.075	1.911		
Step 2.2	0	350	50	40.73	0.084	0.108		
Step 2.3	7.5	250	50	35.54	0.075	0.021		
Step 2.4	0	350	40	39.71	0.082	0.126		
Step 2.5	5	250	50	35.2	0.074	0.019		
Step 2.6	2.5	300	50	36.18	0.076	0.084		
<b>Step 2.7</b>	<b>5</b>	<b>300</b>	<b>50</b>	<b>38.49</b>	<b>0.081</b>	<b>0.007</b>		
Step 3.1	0	150	80	33.22	0.069	4.189		
Step 3.2	0	150	20	27.26	0.056	44.935		
Step 3.3	5	250	50	35.2	0.074	0.019		
Step 3.4	5	350	60	40.64	0.084	0.006		
Step 3.5	5	300	50	38.49	0.081	0.007		
<b>Step 3.6</b>	<b>5</b>	<b>300</b>	<b>60</b>	<b>39.88</b>	<b>0.082</b>	<b>0.001</b>		
Step 3.7	2.5	250	50	35.18	0.075	0.070		

## Publication II: Discussions

The process parameters effect on defect density, so called etched area percentage, was studied with collected experimental data from BO runs. Accordingly, the Ar/H<sub>2</sub> plasma pretreatment had the most significant effect on defect density with an optimum at around 5 min application. The effect of plasma pretreatment on defect density was attributed to the difference in interface between Cu and Al<sub>2</sub>O<sub>3</sub> film. While Cu samples were etched by acetic acid before the deposition, the native oxide layer is still found due to sample transfer process and instillation of ALD chamber. By applying the plasma pretreatment, the air-formed oxide layer is removed and allow the controlled oxide layer formation inside ALD chamber.

The influence of the deposition temperature and pulse time on the corrosion protection properties of Al<sub>2</sub>O<sub>3</sub> is discussed in two parts. While the first part focuses on the correlation between temperature and pulse time without the effect of plasma pre-treatment ( $\leq 2.5$  min), the second part focuses on the combination of temperature and pulse time with plasma pre-treatment ( $\geq 5$  min). When the plasma pretreatment was less than or equal to 2.5 min, the higher temperature and longer pulse time was found beneficial for reducing the defect density. However, the optimization target is only achieved for the deposition temperature above 150 °C

and longer pulse time duration (5 min and longer). Among pulse time and temperature, the temperature was therefore identified to have a more significant influence than the pulse time on the corrosion protection properties. The effect of temperature on defect density was attributed to the type of reactive sides and the effect of temperature on the preferred reaction mechanism. A lower defect density with increased temperature may be related to the higher reactivity of the species.



**Figure 13.** The BO process showing the minimization of the etched area percentage for each iteration. (a) 10 parallel optimization runs with exploration orientation until the etched area percentage reached the target value, 0.03% pointing to a significant decrease of the defect density. (b) Following experiments with exploitation orientation with three parallel optimization runs to seek better performances for lower defect density in the system.

## Publication II: Conclusions

The hybrid approach, two level FFD and BO, was successfully deployed to find best process parameters for depositing ALD- $\text{Al}_2\text{O}_3$  layers on copper. The defect density of  $\text{Al}_2\text{O}_3$  film was significantly decreased, and the corrosion protection properties of the layer were considerably improved.

Using two level FFD method, the process parameters were reduced from 6 to 3 to be considered in optimization step, which are plasma pretreatment, deposition temperature and pulse time. BO was for the first time applied to maximize the corrosion protection performance of ALD layers. The optimal parameters were found in only a few iterations. The optimization process repeated 10 times independently to demonstrate the efficiency and efficacy of the BO approach. Compared to reference  $\text{Al}_2\text{O}_3$  film, the etched area percentage was decreased from  $45 \pm 27$  to  $0.03 \pm 0.001\%$  by optimizing the process parameters. According to optimization process, once the temperature was increased above  $250\text{ }^\circ\text{C}$ , and plasma pretreatment was applied for 5 min, the optimization target is achieved independent from the pulse time.

The importance of the optimization process parameters for the maximize corrosion protection performance was demonstrated on ALD- $\text{Al}_2\text{O}_3$  films. Through the BO approach, we have showed efficient optimization methodology for the large number of spaces in complex systems such as manufacturing processes in material science applications.

## **Micromachining of ALD- $\text{Al}_2\text{O}_3$ Films *via* Laser Drilling and Plasma Etching for Interfacing Copper**

### **Publication III: Technological/ Scientific Context**

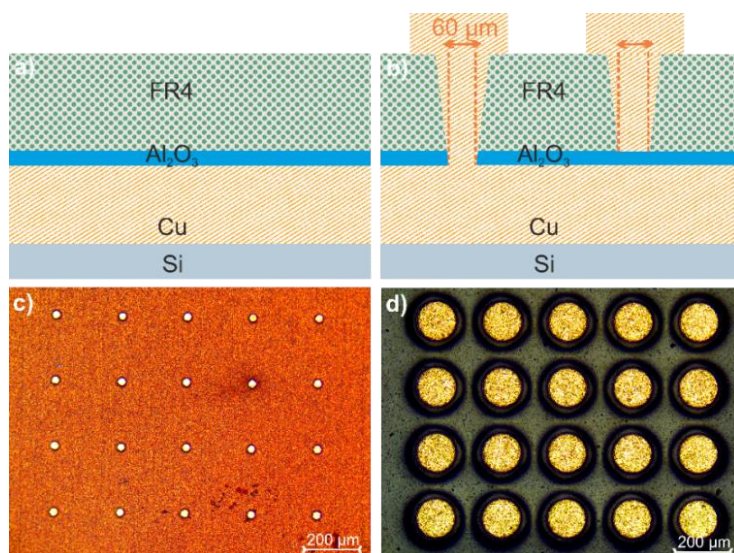
To influence of the ALD thin films for copper corrosion protection on the micro- and nano-structuring of the layer performance and possibilities need to be addressed for many applications such as semiconductor processes, microwells, etc. For example, as hole drilling structuring through micromachining is necessary to make contacts through the passivation layer to connect the top copper layer to the metal layers below. The copper passivation layer must be removed in a localized, selective way without degradation of underlying copper and then filled the obtained structures with copper to create electrical connection between two different copper layers. Especially in semiconductor technology, ALD thin films offer an attractive route in passivation of copper with thinner and conformal layers by structuring 3D finer complex interconnects. Therefore, micromachining properties by common methods play an important role for future applications of ALD materials.

Among several methods to structure the layers for copper-copper interconnection,  $\text{CO}_2$  laser drilling and etching are the most common two methods. Therefore, within this thesis, the micromachining of ALD passivation layers was studied using laser drilling and plasma etching. The applicability of ALD layers was studied on Cu- $\text{Al}_2\text{O}_3$ -FR4 (FR4: glass fiber reinforced epoxy) structures, which typically encountered in PCBs or electronic packaging. The process was investigated with the focus on the quality of the formed microvias and copper-copper interface in the device. Electrical contact test was conducted on copper microvias (copper structures, after removing the passivation layer the vias filled by copper) using four-point-probe measurements. Based on the measured current and reference copper samples. Furthermore, the cross-section of the copper-copper interconnection was studied with SEM, after metallographic cross-section preparation.

### **Publication III: Results**

The Cu substrate was cleaned with acetic acid for 1 min.  $\text{Al}_2\text{O}_3$  films were deposited on these substrates with 5 nm and 100 nm thickness and followed by 40  $\mu\text{m}$  FR4 layer coating. The Cu-

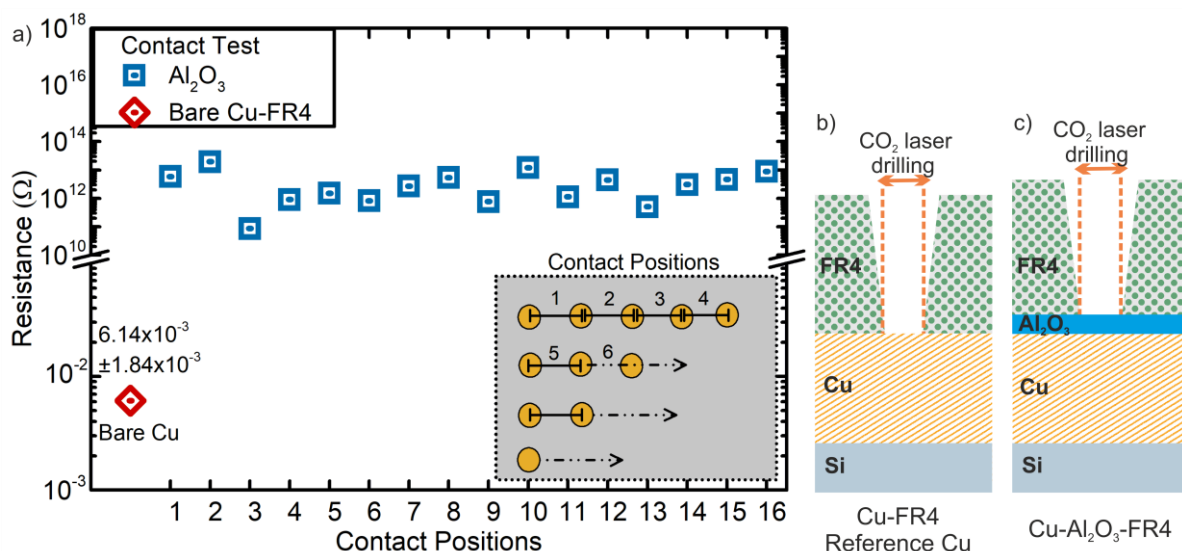
$\text{Al}_2\text{O}_3$ -FR4 layer stack was structured firstly by  $\text{CO}_2$  laser drilling. The  $\text{CO}_2$  laser power at 10.6  $\mu\text{m}$  wavelength was set to 1.1 mJ for one shot with 60  $\mu\text{m}$  spot size. Total power of 3.3 mJ was used for three shots with 4  $\mu\text{s}$  pulse duration. Figure 16 represent the layer stack (14a), schematic cross-section (14b), and obtained structure after laser drilling (14c), and following copper filling of the vias (14d).



**Figure 14.** The  $\text{CO}_2$  laser drilling details. (a) Schematic representation of Cu- $\text{Al}_2\text{O}_3$ -FR4 layers on silicon file-layer, where FR4 is the glass fiber reinforced epoxy. (b) Schematic presentation of micromachining: The  $\text{CO}_2$  laser removes the FR4 layer and reaches the surface of  $\text{Al}_2\text{O}_3$  with two possibilities; successful removing of the ALD layer as indicated on the left side or unsuccessful as on the right side. (c) Optical microscope image of the structured microarrays. (d) Optical microscope image after copper filling of structured microarrays.

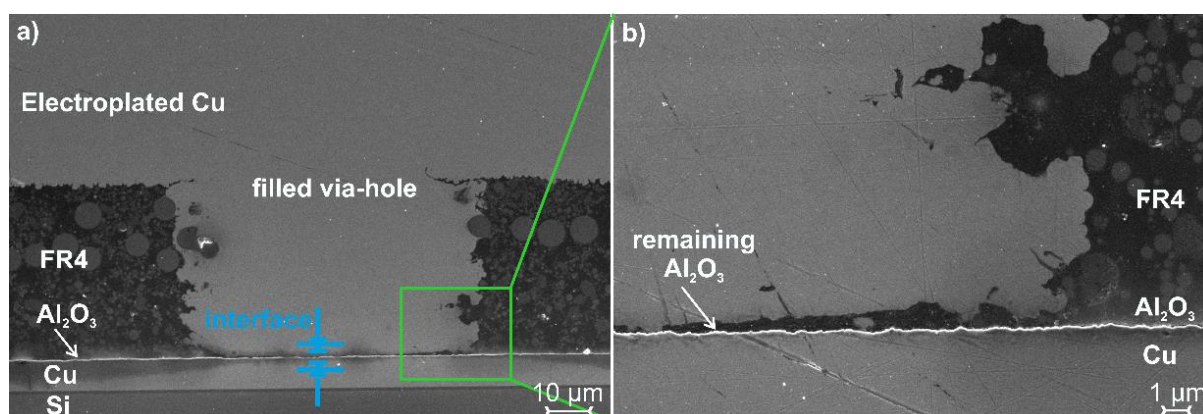
The electrical resistance of the samples was used as an indicator for the success of micromachining. As FR4 is well-known layer that can be removed by  $\text{CO}_2$  laser, the electrical resistance was used directly as an indicator for the ALD layer. The resistance results for 100 nm thick  $\text{Al}_2\text{O}_3$  film are given in Figure 15, which also includes schematic explanation for high and low resistance values. The bare copper sample (Cu-FR4) without ALD layer is also showed in the Figure 15 as a reference state.

According to electrical measurements, the  $\text{Al}_2\text{O}_3$  protected copper layer showed high resistance in comparison to bare copper. Electrical resistance for all pads was found to be more than  $10^{11} \Omega$ , indicating the process was not sufficient for a reliable electrical interconnection. The  $\text{CO}_2$  laser drilling could not successfully remove the ALD layer, which act as a passivation layer on the interface of the copper-copper connection. Cross-section SEM analysis verified the presence of  $\text{Al}_2\text{O}_3$  layer at the interface. The cross-section image for one of the copper pads is given in Figure 16. The remaining copper is highlighted on the interface of copper-copper interconnect.



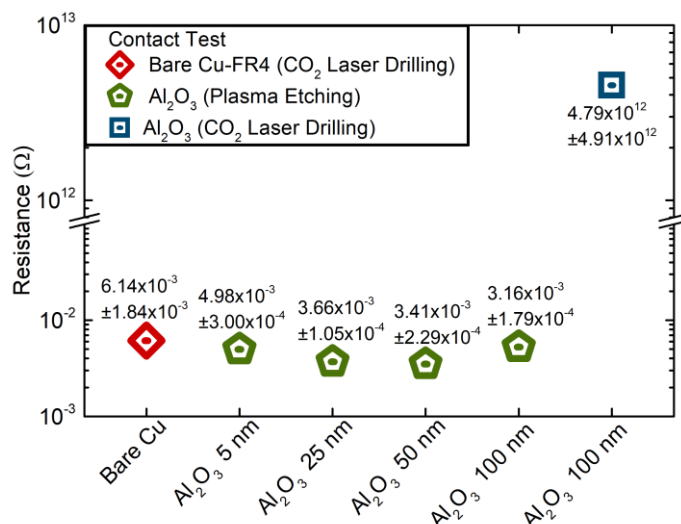
**Figure 15.** (a) The electrical resistance of copper vias through CO<sub>2</sub> laser-drilled microarray. Electrical resistance is given according to the measured position on the microarray. The bare copper (Cu-FR4 layer) resistance result is used as the reference of good contact (low resistance) to indicate successful structuring of Al<sub>2</sub>O<sub>3</sub> thin film. (b) Schematic representation of Si-Cu-FR4 layers, used as reference copper sample (c) Schematic representation of Si-Cu-Al<sub>2</sub>O<sub>3</sub>-FR4 layers.

Plasma etching was in the following applied on the Cu-Al<sub>2</sub>O<sub>3</sub>-FR4 layer system using CF<sub>4</sub>/O<sub>2</sub> microwave plasma at 2500 W with 150 sccm CF<sub>4</sub> and O<sub>2</sub> 1000 sccm gas flows. The micromachining of the Al<sub>2</sub>O<sub>3</sub> layer was investigated using the methods described in the previous section. After removing the FR4 layer by CO<sub>2</sub> laser following, the CF<sub>4</sub>/O<sub>2</sub> plasma etching was performed by microwave plasma source on Al<sub>2</sub>O<sub>3</sub> films. The electrical resistance of copper-copper connection is given in Figure 17. The resistance values were given as an average of 16 pads, which bare copper and laser-drilled samples were added for overall comparison.



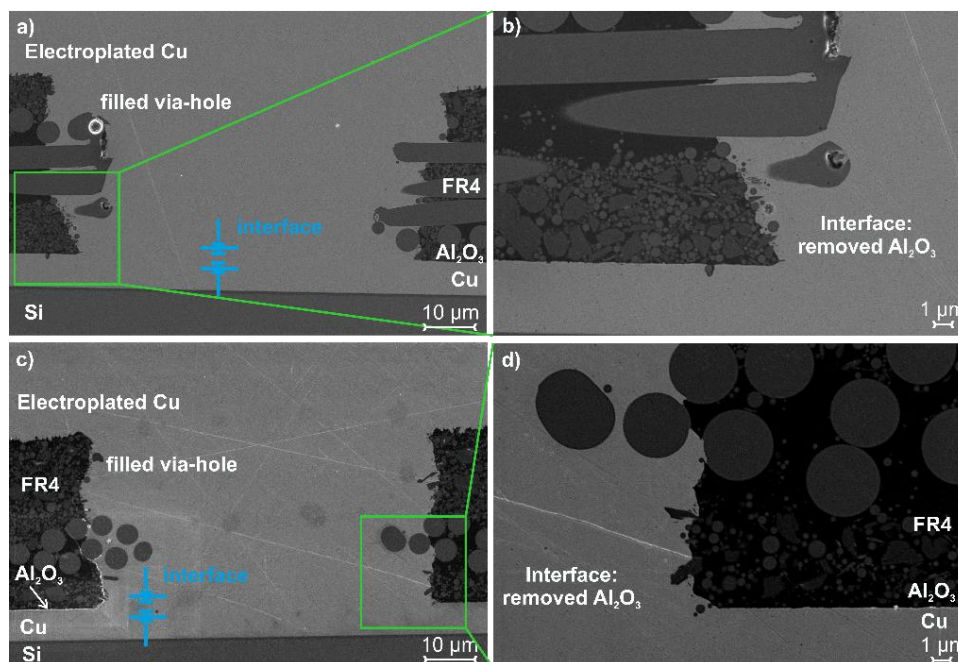
**Figure 16.** SEM images of copper-copper connection formed in Cu-Al<sub>2</sub>O<sub>3</sub>-FR4 multilayers by CO<sub>2</sub> laser drilling. (a) Cross-section of the copper pad (filled via) (b) with higher magnification. The interface of copper and electroplated copper indicates the presence of Al<sub>2</sub>O<sub>3</sub> thin films, which could not be removed by CO<sub>2</sub> laser.





**Figure 17.** The electrical resistance of copper vias, drilled by CO<sub>2</sub> laser and etched by plasma. FR4 layer was removed by CO<sub>2</sub> laser drilling, and Al<sub>2</sub>O<sub>3</sub> thin film was removed by plasma etching. Electrical resistance is given as an average for 16 pads of the microarray. The bare copper (Cu-FR4 layer) resistance result is used to reference good contact (low resistance). The CO<sub>2</sub> laser drilling result for 100-nm Al<sub>2</sub>O<sub>3</sub> film is added for a better comparison of structuring methods.

Plasma etching of Al<sub>2</sub>O<sub>3</sub> films results in similar contact resistance in the range of  $10^{-3}$  Ω for all thicknesses. The Al<sub>2</sub>O<sub>3</sub> layer was entirely removed from the interface of copper. The clean interface of the copper-copper connection, without the residual of Al<sub>2</sub>O<sub>3</sub> film, was also observed on the cross-section analysis as given for 5 nm Al<sub>2</sub>O<sub>3</sub> film and 100 nm Al<sub>2</sub>O<sub>3</sub> film in Figure 18a and 18b.

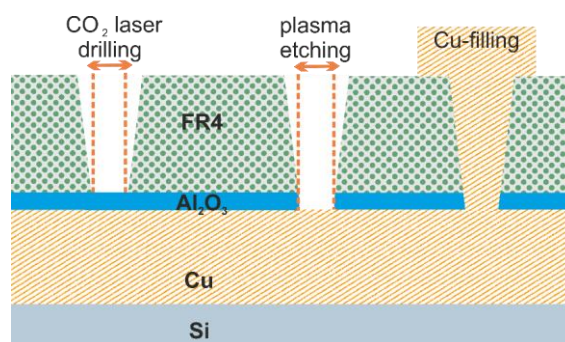


**Figure 18.** SEM images of copper-copper connection formed in Cu-Al<sub>2</sub>O<sub>3</sub>-FR4 multilayers by CO<sub>2</sub> laser drilling and plasma etching. (a) The cross-section of copper via for 5-nm thick Al<sub>2</sub>O<sub>3</sub> film (b) with higher magnification. (c) The cross-section of copper via for 100-nm thick Al<sub>2</sub>O<sub>3</sub> film (d) with higher magnification. The interface between copper and electroplated copper indicates that Al<sub>2</sub>O<sub>3</sub> thin films were successfully etched by microwave plasma.

### Publication III: Discussions

The experimental results showed that CO<sub>2</sub> laser drilling alone could not remove the Al<sub>2</sub>O<sub>3</sub> film, while plasma etching successfully removed for structuring microarrays. Furthermore, the underlying copper was protected during the micromachining of the passivation layer.

The plasma etching of Cu-Al<sub>2</sub>O<sub>3</sub>-FR4 multilayers was able to structure selectively without using an etching mask. The top layer, FR4, was selectively removed by laser drilling process, and obtained microarray structures act as a mask for plasma etching to remove Al<sub>2</sub>O<sub>3</sub> film, which provides solvent-free structuring. The schematic representation of the impact of laser drilling and plasma etching on micromachining is given in Figure 19. After CO<sub>2</sub> laser drilling, plasma etching was performed and followed by copper filling, allowing multilevel interconnections as used for microvias in PCB manufacturing.



**Figure 19.** Schematic representation of structuring approach for Cu-Al<sub>2</sub>O<sub>3</sub>-FR4 layers on silicon file layer. The CO<sub>2</sub> laser drilling is used to remove the FR4 layer, and solvent-free plasma etching (without mask) is used to remove the Al<sub>2</sub>O<sub>3</sub> thin films. The via-holes are then filled by copper electroplating, which provides a reliable copper-copper connection.

### Publication III: Conclusions

The micromachining of ALD-Al<sub>2</sub>O<sub>3</sub> passivation layers were studied using CO<sub>2</sub> laser drilling and plasma etching to establish a reliable interface for copper-copper interconnects on Cu-Al<sub>2</sub>O<sub>3</sub>-FR4 layer system, which was adopted from PCB technology.

According to contact test results and cross-section analysis, CO<sub>2</sub> laser drilling alone is not capable of removing the ALD-Al<sub>2</sub>O<sub>3</sub> thin films without damaging the underlying copper films. Plasma etching was found to be effective in the removing the Al<sub>2</sub>O<sub>3</sub> layers even for 100 nm thickness. A reliable copper-copper connection was shown by electrical contact test and cross-section analysis. The described CO<sub>2</sub> laser drilling followed by plasma etching on the Cu-Al<sub>2</sub>O<sub>3</sub> (ALD)-FR4 multilayer system successfully removed the encapsulation layer. The FR4 layer was removed by CO<sub>2</sub> laser drilling and Al<sub>2</sub>O<sub>3</sub> layer by following plasma etching.



## References

1. Cremers, V.; Rampelberg, G.; Baert, K.; Abrahami, S.; Claes, N.; de Oliveira, T. M.; Terryn, H.; Bals, S.; Dendooven, J.; Detavernier, C., Corrosion Protection of Cu by Atomic Layer Deposition. *Journal of Vacuum Science & Technology A* **2019**, *37* (6), 060902.
2. Friederich, P.; Fediai, A.; Kaiser, S.; Konrad, M.; Jung, N.; Wenzel, W., Toward Design of Novel Materials for Organic Electronics. *Adv Mater* **2019**, *31* (26), e1808256.
3. Fischer, R. A., Chemical Vapor Deposition: Principles and Applications. *Angewandte Chemie* **1994**, *106* (9), 1062-1063.
4. Zhang, Y.; Seghete, D.; Abdulagatov, A.; Gibbs, Z.; Cavanagh, A.; Yang, R.; George, S.; Lee, Y.-C., Investigation of the Defect Density in Ultra-thin Al<sub>2</sub>O<sub>3</sub> Films Grown Using Atomic Layer Deposition. *Surface and Coatings Technology* **2011**, *205* (10), 3334-3339.
5. Chai, Z.; Liu, Y.; Li, J.; Lu, X.; He, D., Ultra-thin Al<sub>2</sub>O<sub>3</sub> Films Grown by Atomic Layer Deposition for Corrosion Protection of Copper. *RSC Adv.* **2014**, *4* (92), 50503-50509.
6. Pinna, N.; Knez, M., *Atomic Layer Deposition of Nanostructured Materials*. Wiley-VCH: Weinheim, 2012.
7. Jung, Y. S.; Cavanagh, A. S.; Riley, L. A.; Kang, S. H.; Dillon, A. C.; Groner, M. D.; George, S. M.; Lee, S. H., Ultrathin Direct Atomic Layer Deposition on Composite Electrodes for Highly Durable and Safe Li-ion Batteries. *Adv Mater* **2010**, *22* (19), 2172-6.
8. Liu, Y., Li, S., Zhang, J., Liu, J., Han, Z., Ren, L., Corrosion Inhibition of Biomimetic Superhydrophobic Electrodeposition Coatings on Copper Substrate. *Corrosion Science* **2015**, *94*, 190-196.
9. Singh, A. K.; Adstedt, K.; Brown, B.; Singh, P. M.; Graham, S., Development of ALD Coatings for Harsh Environment Applications. *ACS Appl Mater Interfaces* **2019**, *11* (7), 7498-7509.
10. Zhang, F.-Y.; Prasad, A. K.; Advani, S. G., Investigation of a Copper Etching Technique to Fabricate Metallic Gas Diffusion Media. *Journal of Micromechanics and Microengineering* **2006**, *16* (11), N23-N27.
11. Alers, G. B. L., X.; Sukamto, J. H.; Kailasam, S. K.; Reid, J.; Harm, G., Influence of Copper Purity on Microstructure and Electromigration. *IEEE* **2004**, (0-7803-8308).
12. Bahari, H. S.; Savaloni, H., Surface Analysis of Cu Coated With ALD Al<sub>2</sub>O<sub>3</sub> and its Corrosion Protection Enhancement in NaCl Solution: EIS and Polarization. *Materials Research Express* **2019**, *6* (8), 865-870.
13. Chai, Z.; Li, J.; Lu, X.; He, D., Use of Electrochemical Measurements to Investigate the Porosity of Ultra-thin Al<sub>2</sub>O<sub>3</sub> Films Prepared by Atomic Layer Deposition. *RSC Adv.* **2014**, *4* (74), 39365-39371.
14. Kolkovsky, V.; Stübner, R., Hydrogen-Related Defects in Al<sub>2</sub>O<sub>3</sub> Layers Grown on n-type Si by the Atomic Layer Deposition Technique. *Physica B: Condensed Matter* **2018**, *535*, 171-174.
15. M.L. Changa, L. C. W., H.C. Lina, M.J. Chena, K.M. Linb, Investigation of Defects in Ultra-thin Al<sub>2</sub>O<sub>3</sub> Films Deposited on Pure Copper by the Atomic Layer Deposition Technique. *Applied Surface Science* **2015**, *359*, 533-542.
16. Mirhashemihaghighi, S.; Światowska, J.; Maurice, V.; Seyeux, A.; Klein, L. H.; Salmi, E.; Ritala, M.; Marcus, P., The Role of Surface Preparation in Corrosion Protection of Copper with Nanometer-thick ALD Alumina Coatings. *Applied Surface Science* **2016**, *387*, 1054-1061.
17. Mirhashemihaghighi, S.; Światowska, J.; Maurice, V.; Seyeux, A.; Klein, L. H.; Salmi, E.; Ritala, M.; Marcus, P., Interfacial Native Oxide Effects on the Corrosion Protection of Copper Coated with ALD Alumina. *Electrochimica Acta* **2016**, *193*, 7-15.
18. Zhang, Y.; Zhang, Y.-Z.; Miller, D. C.; Bertrand, J. A.; Jen, S.-H.; Yang, R.; Dunn, M. L.; George, S. M.; Lee, Y. C., Fluorescent Tags to Visualize Defects in Al<sub>2</sub>O<sub>3</sub> Thin Films Grown Using Atomic Layer Deposition. *Thin Solid Films* **2009**, *517* (24), 6794-6797.
19. Parsons, G. N., Elam, J. W., S. M. George, S. Haukka, H. Jeon, W. M. M. E. Kessels, M. Leskelä, P. Poodt, M. Ritala, and S. M. Rossnagel, , History of Atomic Layer Deposition and its Relationship with the American Vacuum Society. *Journal of Vacuum Science & Technology A: Vacuum, Surfaces, and Films*, **2013**, *31* (5), 050818.
20. Suntola, T., Atomic Layer Epitaxy. *Materials Science Reports* **1989**, *4* (5), 261-312.

21. Gregory, N. P.; Jeffrey, W. E.; Steven, M. G.; Suvi, H.; Hyeongtag, J.; Kessels, W. M. M.; Markku, L.; Paul, P.; Mikko, R.; Steven, M. R., History of atomic layer deposition and its relationship with the American Vacuum Society. *Journal of Vacuum Science & Technology A: Vacuum, Surfaces, and Films* **2013**, *31* (5), 050818.
22. Knoops, H. C. M., Potts, S.E., A.A. Bol, W.M.M. Kessels, *Atomic Layer Deposition*. Second Edition ed.; 2015; p 1101-1134.
23. Leskelä M., a. R., M. , Atomic layer Deposition (ALD): From Precursors to Thin Flm Structures. *Thin Solid Films* **2002**, *409* (04), 138-146.
24. Leskelä, M.; Ritala, M., Atomic Layer Deposition ( ALD ): From Precursors to Thin Film Structures. **2002**, *409*, 138-146.
25. George, S. M., Atomic Layer Deposition: An Overview. *Chemical Reviews* **2010**, *110* (1), 111-131.
26. Riikka, L. P., Surface Chemistry of Atomic Layer Deposition: A Case Study for the Trimethylaluminum/Water Process. *Journal of Applied Physics* **2005**, *97* (12), 121301.
27. Tiznado, H.; Zaera, F., Surface Chemistry in the Atomic Layer Deposition of TiN Films from TiCl<sub>4</sub> and Ammonia. *The Journal of Physical Chemistry B* **2006**, *110* (27), 13491-13498.
28. Riikka, L. P.; Wilfried, V., Island Growth as a Growth Mode in Atomic Layer Deposition: A Phenomenological Model. *Journal of Applied Physics* **2004**, *96* (12), 7686-7695.
29. Knez, M.; Nielsch, K.; Niinistö, L., Synthesis and Surface Engineering of Complex Nanostructures by Atomic Layer Deposition. *Advanced Materials* **2007**, *19* (21), 3425-3438.
30. Puurunen, R. L.; Saarihahti, J.; Kattelus, H., Implementing ALD Layers in MEMS Processing. *ECS Transactions* **2007**, *11* (7), 3-14.
31. Elam, J. W.; George, S. M., Growth of ZnO Al<sub>2</sub>O<sub>3</sub> Alloy Films Using Atomic Layer Deposition Techniques. *Chemistry of Materials* **2003**, *15* (4), 1020-1028.
32. Elam, J. W., Schuisky, M., Ferguson, J. D., George S. M., Surface Chemistry and Film Growth during TiN Atomic Layer Deposition using TDMAT and NH<sub>3</sub>. *Thin Solid Films* **2003**, *436* (2), 145-156.
33. Pyymäki Perros C. A. Thermal and Plasma-Enhanced Atomic Layer Deposition: The Study of Employment in Various Nanotechnology Applications. Aalto University, Aalto-yliopisto, 2015.
34. Ville, M.; Markku, L. a.; Mikko, R.; Riikka, L. P., Crystallinity of Inorganic Films Grown by Atomic Layer Deposition: Overview and General Trends. *Journal of Applied Physics* **2013**, *113* (2), 021301.
35. Nicotra, G., Ramasse, Q. M.,, *Material Science in Semiconductor Processing*. Elsevier Ltd.: 2017; Vol. 65.
36. Hämäläinen, J.; Ritala, M.; Leskelä, M., Atomic Layer Deposition of Noble Metals and Their Oxides. *Chemistry of Materials* **2014**, *26* (1), 786-801.
37. Musschoot, J. Advantages and Challenges of Plasma Enhanced Atomic Layer Deposition. Ghent University, Ghent, 2011.
38. GbmH, S. I., PEALD System for Thermal and Plasma Based Processes *ALD Brochures* **2020**, 3.
39. Marichy, C.; Bechelany, M.; Pinna, N., Atomic Layer Deposition of Nanostructured Materials for Energy and Environmental Applications. *Adv Mater* **2012**, *24* (8), 1017-32.
40. Zaera, H. T. a. F., Surface Chemistry in the Atomic Layer Deposition of TiN Films from TiCl<sub>4</sub> and Ammonia. *J. Phys. Chem. B* **2006**, *110* (13491-13498), 13491-13498.
41. Abdulagatov, A. I.; Yan, Y.; Cooper, J. R.; Zhang, Y.; Gibbs, Z. M.; Cavanagh, A. S.; Yang, R. G.; Lee, Y. C.; George, S. M., Al<sub>2</sub>O<sub>3</sub> and TiO<sub>2</sub> Atomic Layer Deposition on Copper for Water Corrosion Resistance. *ACS Appl Mater Interfaces* **2011**, *3* (12), 4593-4601.
42. Correa, G. C.; Bao, B.; Strandwitz, N. C., Chemical Stability of Titania and Alumina Thin Films Formed by Atomic Layer Deposition. *ACS Appl Mater Interfaces* **2015**, *7* (27), 14816-14821.
43. Dias, V. M.; Chiappim, W.; Fraga, M. A.; Maciel, H. S.; Marciano, F. R.; Pessoa, R. S., Atomic Layer Deposition of TiO<sub>2</sub> and Al<sub>2</sub>O<sub>3</sub> Thin Films for the Electrochemical Study of Corrosion Potection in Alluminum Alloy Cans Used in Beverage. *Materials Research Express* **2020**, *7* (7).
44. Díaz, B.; Härkönen, E.; Światowska, J.; Maurice, V.; Seyeux, A.; Marcus, P.; Ritala, M., Low-Temperature Atomic Layer Deposition of Al<sub>2</sub>O<sub>3</sub> Thin Coatings for Corrosion Protection of Steel: Surface and Electrochemical Analysis. *Corrosion Science* **2011**, *53* (6), 2168-2175.

45. Fusco, M. A.; Oldham, C. J.; Parsons, G. N., Investigation of the Corrosion Behavior of Atomic Layer Deposited Al<sub>2</sub>O<sub>3</sub>/TiO<sub>2</sub> Nanolaminate Thin Films on Copper in 0.1 M NaCl. *Materials (Basel)* **2019**, *12* (4).
46. Moehl, T.; Suh, J.; Severy, L.; Wick-Joliat, R.; Tilley, S. D., Investigation of (Leaky) ALD TiO<sub>2</sub> Protection Layers for Water-Splitting Photoelectrodes. *ACS Appl Mater Interfaces* **2017**, *9* (50), 43614-43622.
47. Shadi Mirhashemihaghighi, J. S., Vincent Maurice, Antoine Seyeux, Lorena, H. Klein, Emma Harkonen, Mikko Ritala, and Philippe Marcus, Electrochemical and Surface Analysis of the Corrosion Protection of Copper by Nanometer-Thick Alumina Coatings Prepared by Atomic Layer Deposition. *Journal of The Electrochemical Society* **2015**, *162* (8) (C377-C384).
48. Vanhaverbeke, C.; Cauwe, M.; Stockman, A.; Op de Beeck, M.; De Smet, H., Comparison of Copper Electroplating, Copper Wet Etching and Linear Sweep Voltammetry as Techniques to Investigate the Porosity of Atomic Layer Deposited Al<sub>2</sub>O<sub>3</sub>. *Thin Solid Films* **2019**, *686*, 137424.
49. Yersak, A. S.; Lewis, R. J.; Tran, J.; Lee, Y. C., Characterization of Thin Film Dissolution in Water with *in-situ* Monitoring of Film Thickness Using Reflectometry. *ACS Appl Mater Interfaces* **2016**, *8* (27), 17622-30.
50. Puurunen, R. L., Surface Chemistry of Atomic Layer Deposition: A Case Study for the Trimethylaluminum/Water Process. *Journal of Applied Physics* **2005**, *97* (12), 121301.
51. Spahr, H.; Bülow, T.; Nowak, C.; Hirschberg, F.; Reinker, J.; Hamwi, S.; Johannes, H.-H.; Kowalsky, W., Impact of Morphological Defects on the Electrical Breakdown of Ultra Thin Atomic Layer Deposition Processed Al<sub>2</sub>O<sub>3</sub> Layers. *Thin Solid Films* **2013**, *534*, 172-176.
52. Daubert, J. S.; Hill, G. T.; Gotsch, H. N.; Gremaud, A. P.; Ovental, J. S.; Williams, P. S.; Oldham, C. J.; Parsons, G. N., Corrosion Protection of Copper Using Al<sub>2</sub>O<sub>3</sub>, TiO<sub>2</sub>, ZnO, HfO<sub>2</sub>, and ZrO<sub>2</sub> Atomic Layer Deposition. *ACS Appl Mater Interfaces* **2017**, *9* (4), 4192-4201.
53. Chang, C.-C.; Pan, F.-M.; Chen, C.-W., Effect of Surface Reduction Treatments of Plasma-Enhanced Atomic Layer Chemical Vapor Deposited TaN<sub>x</sub> on Adhesion with Copper. *Journal of The Electrochemical Society* **2010**, *157* (2), G62.
54. Nehm, F.; Klumbies, H.; Richter, C.; Singh, A.; Schroeder, U.; Mikolajick, T.; Monch, T.; Hossbach, C.; Albert, M.; Bartha, J. W.; Leo, K.; Muller-Meskamp, L., Breakdown and Protection of ALD Moisture Barrier Thin Films. *ACS Appl Mater Interfaces* **2015**, *7* (40), 22121-22127.
55. Vargas, I. T.; Fischer, D. A.; Alsina, M. A.; Pavissich, J. P.; Pasten, P. A.; Pizarro, G. E., Copper Corrosion and Biocorrosion Events in Premise Plumbing. *Materials (Basel)* **2017**, *10* (9).
56. Dogan, G.; Sanli, U. T.; Hahn, K.; Muller, L.; Gruhn, H.; Silber, C.; Schutz, G.; Grevent, C.; Keskinbora, K., In Situ X-ray Diffraction and Spectro-Microscopic Study of ALD Protected Copper Films. *ACS Appl Mater Interfaces* **2020**, *12* (29), 33377-33385.
57. Eigenfeld, N. T.; Gray, J. M.; Brown, J. J.; Skidmore, G. D.; George, S. M.; Bright, V. M., Ultra-thin 3D Nano-devices from Atomic Layer Deposition on Polyimide. *Adv Mater* **2014**, *26* (23), 3962-7.
58. Matero, R., Ritala, M., M. Leskelä, T. Salo, J. Aromaa and O. Forsen, Atomic Layer Deposited Thin Films for Corrosion Protection. *J. Phys. IV France* **1999**, *9*, Pr8-493–Pr8-499.
59. Marin, E., Lanzutti A., L. Paussa, L. Guzman and L. Fedrizzi, Long Term Performance of Atomic Layer Deposition Coatings for Corrosion Protection of Stainless Steel *Mater. Corros.* **2015**, *66*, 907-914.
60. Im H., Wittenberg, N.J., N. C. Lindquist, S. H. Oh, Atomic Layer Deposition: A Versatile Technique for Plasmonics and Nanobiotechnology. *J. Mater. Res.* **2012**, *27*, 663-671.
61. King D. M., S. J. A., Liang X., Hakim L. F., Weimer A. W., Atomic Layer Deposition on Particles Using a Fluidized Bed Reactor with in situ Mass Spectrometry. *Surf. Coat. Technol.* **2007**, *201*, 9163-9171.
62. Batra, N.; Gope, J.; Vandana; Panigrahi, J.; Singh, R.; Singh, P. K., Influence of Deposition Temperature of Thermal ALD Deposited Al<sub>2</sub>O<sub>3</sub> Films on Silicon Surface Passivation. *AIP Advances* **2015**, *5* (6).
63. Bordihn, S.; Kiesow, I.; Mertens, V.; Engelhart, P.; M $\ddot{Y}$ ller, J. W.; Kessels, W. M. M., Impact of the Deposition and Annealing Temperature on the Silicon Surface Passivation of ALD Al<sub>2</sub>O<sub>3</sub> Films. *Energy Procedia* **2012**, *27*, 396-401.

64. Chavez, K. L.; Hess, D. W., A Novel Method of Etching Copper Oxide Using Acetic Acid. *Journal of The Electrochemical Society* **2001**, *148* (11), G640.
65. Deng, Z.; He, W.; Duan, C.; Shan, B.; Chen, R., Atomic Layer Deposition Process Optimization by Computational Fluid Dynamics. *Vacuum* **2016**, *123*, 103-110.
66. Härkönen, E.; Tervakangas, S.; Kolehmainen, J.; Díaz, B.; Światowska, J.; Maurice, V.; Seyeux, A.; Marcus, P.; Fenker, M.; Tóth, L.; Radnóczy, G.; Ritala, M., Interface Control of Atomic Layer Deposited Oxide Coatings by Filtered Cathodic Arc Deposited Sublayers for Improved Corrosion Protection. *Materials Chemistry and Physics* **2014**, *147* (3), 895-907.
67. Belousov, I. V., Grib, A. G., Kuznetsov, G. V., The Influence of Surface Defects on the Pinhole Formation in Silicide Thin Film. *Semiconductor Physics, Quantum Electronics & Optoelectronics* **2006**, *9* (3), 29-34.
68. Härkönen, E.; Potts, S. E.; Kessels, W. M. M.; Díaz, B.; Seyeux, A.; Światowska, J.; Maurice, V.; Marcus, P.; Radnóczy, G.; Tóth, L.; Kariniemi, M.; Niinistö, J.; Ritala, M., Hydrogen–Argon Plasma Pre-treatment for Improving the Anti-Corrosion Properties of Thin Al<sub>2</sub>O<sub>3</sub> Films Deposited Using Atomic Layer Deposition on Steel. *Thin Solid Films* **2013**, *534*, 384-393.
69. Kim, H. G.; Lee, J. G.; Kim, S. S., Self-Assembled Monolayers as a Defect Sealant of Al<sub>2</sub>O<sub>3</sub> Barrier Layers Grown by Atomic Layer Deposition. *Organic Electronics* **2018**, *52*, 98-102.
70. Neizvestny, I. G.; Shwartz, N. L.; Yanovitskaja, Z. S.; Zverev, A. V., Simulation of Surface Relief Effect on ALD Process. *Computational Materials Science* **2006**, *36* (1-2), 36-41.
71. Yersak, A. S.; Lee, Y.-C., Probabilistic Distributions of Pinhole Defects in Atomic Layer Deposited Films on Polymeric Substrates. *J Vac Sci Technol A* **2016**, *34* (1), 01A149.
72. Potts, S. E.; Schmalz, L.; Fenker, M.; Diaz, B.; Swiatowska, J.; Maurice, V.; Seyeux, A.; Marcus, P.; Radnóczy, G.; Toth, L.; Kessels, W. M. M., Ultra-Thin Aluminium Oxide Films Deposited by Plasma-Enhanced Atomic Layer Deposition for Corrosion Protection. *Journal of the Electrochemical Society* **2011**, *158* (5), C132-C138.
73. Yersak, A. S.; Lewis, R. J.; Tran, J.; Lee, Y. C., Characterization of Thin Film Dissolution in Water with in Situ Monitoring of Film Thickness Using Reflectometry. *ACS Appl Mater Interfaces* **2016**, *8* (27), 17622-30.
74. Furchner, A., Kratz C., Gkogkou D., Ketelsen H., Hinrichs, K., *Infrared-spectroscopic Single-shot Laser Mapping Ellipsometry: Proof of Concept for Fast Investigations of Structured Surfaces and Interactions in Organic Thin Films*. Elsevier Ltd.: 2016; Vol. 421- Part B.
75. Spectroscopic Ellipsometry SE 800. **2004**.
76. Johs, B.; A. Woollam, J.; M. Herzinger, C.; Hilfiker, J.; A. Synowicki, R.; Bungay, C., Overview of Variable-angle Spectroscopic Ellipsometry ( VASE ): II Advanced Applications. **1999**, *1*, 29-58.
77. Langereis, E., Heil, S. B. S., M. C. M., van de Sanden, W. M. M. Kessels, In situ Spectroscopic Ellipsometry Study on the Growth of Ultrathin TiN Films by Plasma-Assisted Atomic Layer Deposition. *Journal of Applied Physics* **2006**, *100* (2), 023534.
78. Hilfiker, J. N., *In situ Spectroscopic Ellipsometry for Characterization of Thin Film Growth*. "" ed.; Woodhead Publishing Limited: 2011; p 99-151.
79. Langereis, E.; Heil, S. B. S.; Sanden, M. C. M. v. d.; Kessels, W. M. M., \textit{In situ} spectroscopic ellipsometry study on the growth of ultrathin TiN films by plasma-assisted atomic layer deposition. *Journal of Applied Physics* **2006**, *100* (2), 023534.
80. Bluhm, H., *X-ray Photoelectron Spectroscopy for in situ Characterization of Thin Film Growth*. 2011; p 75-98.
81. Briggs, D., Handbook of X-ray Photoelectron Spectroscopy. *Surface and Interface Analysis* **1981**, *3* (4).
82. Bob, H., BRUKER AXS B8-Discover DaVinci.
83. X-Ray Interactions: Photoabsorption, Scattering, Transmission, and Reflection. *Atomic Data and Nuclear Data Tables* **1993**, *54* (2), 181-342.
84. Birkholz, M., Principles of X-ray Diffraction. **2006**, 1-40.
85. Chemical Resistance Chart. In *Resistance Tables*, AG, S., Ed. Siemens Flow Instruments: 2008.
86. Cao, G., Wang, Y., *Nanostructures and Nanomaterials*. World Scientific: Singapore, 2011.

87. Lewis, S., L., Agg, K., M., Ross, P., *FORENSIC SCIENCES | Gunshot Residues*. Elsevier: 2005; Vol. Second Edition.
88. Szyrkowska, I., *MICROSCOPY TECHNIQUES: Scanning Electron Microscopy*. Elsevier: 2005; Vol. Second Edition.
89. Geert Cornelis, J. T., Manuel Montaña, Stephan Wagner, Julian A. Gallego-Urrea, Karin Mattsson, Andreas Gondikas,, *Challenges and Current Approaches Toward Environmental Monitoring of Nanomaterials*. Elsevier: 2021; Vol. 4, p 73-108.
90. Claudionico~commonswiki, Electron Interaction In *Matter.svg*, Matter.svg, E. I. w., Ed. Wikimedia, 2013; Vol. 654 × 631 pixels.
91. Senthil K. P., G. P. K., Naushad, M., *Chapter 4 - Characterization Techniques for Nanomaterials*. Elsevier: 2019.
92. Maria Kaliva, M. V., *Chapter 17 - Nanomaterials Characterization*. Elsevier: 2020.
93. Choudhary, S.; Sarma, J. V. N.; Pande, S.; Ababou-Girard, S.; Turban, P.; Lepine, B.; Gangopadhyay, S., Oxidation Mechanism of Thin Cu Films: A Gateway Towards the Formation of Single Oxide Phase. *AIP Advances* **2018**, *8* (5), 055114.
94. Wang, J.-P.; Cho, W., Oxidation Behavior of Pure Copper in Oxygen and/or Water Vapor at Intermediate Temperature. *Isij International - ISIJ INT* **2009**, *49*, 1926-1931.
95. Rao, Z. M.; Xiao, X. B.; He, Z. F., Simulation of Drilling Micro-Hole by a Dual CO<sub>2</sub> Laser Beam Irradiated Sticking Plaster. *Applied Mechanics and Materials* **2012**, *203*, 519-522.
96. Bharatish, A.; Narasimha Murthy, H. N.; Anand, B.; Madhusoodana, C. D.; Praveena, G. S.; Krishna, M., Characterization of Hole Circularity and Heat Affected Zone in Pulsed CO<sub>2</sub> Laser Drilling of Alumina Ceramics. *Optics & Laser Technology* **2013**, *53*, 22-32.
97. Kim, J. W.; Kim, Y. C.; Lee, W. J., Reactive Ion Etching Mechanism of Plasma Enhanced Chemically Vapor Deposited Aluminum Oxide Film in CF<sub>4</sub>/O<sub>2</sub> plasma. *Journal of Applied Physics* **1995**, *78* (3), 2045-2049.
98. Pinos, J.; Mikmekova, S.; Frank, L., About the Information Depth of Backscattered Electron Imaging. *J Microsc* **2017**, *266* (3), 335-342.
99. Krstulović, N.; Shannon, S.; Stefanuik, R.; Fanara, C., Underwater-Laser Drilling of Aluminum. *The International Journal of Advanced Manufacturing Technology* **2013**, *69* (5-8), 1765-1773.
100. Ma, H. P.; Yang, J. H.; Yang, J. G.; Zhu, L. Y.; Huang, W.; Yuan, G. J.; Feng, J. J.; Jen, T. C.; Lu, H. L., Systematic Study of the SiO<sub>x</sub> Film with Different Stoichiometry by Plasma-Enhanced Atomic Layer Deposition and Its Application in SiO<sub>x</sub>/SiO<sub>2</sub> Super-Lattice. *Nanomaterials (Basel)* **2019**, *9* (1).
101. Logan, M. A., Sheet Resistivity Measurements on Rectangular Surfaces: General Solution for Four Point Probe Conversion Factors. *The Bell System Technical Journal* **1967**, *46* (10), 2277-2322.



## 5. *In Situ* X-ray Diffraction and Spectro-Microscopic Study of ALD Protected Copper Films

(Reprinted with the permission of the American Chemical Society)

Gül Dogan, Umut T. Sanli, Kersten Hahn, Lutz Müller, Herbert Gruhn, Christian Silber, Gisela Schütz, Corinne Grévent, and Kahraman Keskinbora

### Abstract

In many applications of copper in industry and research, copper migration and degradation of metallic copper to its oxides is a common problem. There are numerous ways to overcome this degradation with varying success. Atomic layer deposition (ALD) based encapsulation and passivation of the metallic copper recently emerged as a serious route to success owing to the conformality and density of the ALD films. So far, the majority of the studies have been focused on corrosion protection of copper in a variety of chemical environments, mostly at ambient temperature. An investigation of the stability of the ALD film stacks and copper's interaction with them at elevated temperatures has been lacking. Here, we study the mitigation of copper oxidation and migration in 50 nm thick  $\text{Al}_2\text{O}_3/\text{TiO}_2$  and  $\text{Al}_2\text{O}_3/\text{SiO}_2$  bilayer ALD stacks. First, the corrosion dynamics were investigated *via in situ* X-ray diffraction (XRD) at 350 °C under atmospheric conditions, and second, the interaction of copper with the passivation layers have been examined *post factum* using detailed spectro-microscopic investigations. According to the XRD results, both ALD films exhibited excellent oxidation protection. In contrast, bare Cu immediately started to oxidize at 350 °C and transformed entirely to its known oxide phases in 4 h. Spectro-microscopic studies revealed that there are structural and chemical changes on the top surface and within the film stacks. The  $\text{TiO}_2$  layer was crystallized during annealing, while the  $\text{SiO}_2$  layer stayed in the amorphous phase, which was analyzed by grazing incidence XRD and transmission electron microscopy. According to scanning electron microscopy and X-ray photoelectron spectroscopy analysis, copper was detected on the surface with a higher amount in  $\text{Al}_2\text{O}_3/\text{TiO}_2$  than  $\text{Al}_2\text{O}_3/\text{SiO}_2$ , 5.2 at.% and 0.7 at.%, respectively. Based on the surface and cross-sectional analysis, copper migration was observed on both layers, albeit more substantially in  $\text{Al}_2\text{O}_3/\text{TiO}_2$ . In the case of  $\text{Al}_2\text{O}_3/\text{SiO}_2$ , the bulk of the copper was captured at the interface of the two oxides.





# In Situ X-ray Diffraction and Spectro-Microscopic Study of ALD Protected Copper Films

Gül Dogan,\* Umut T. Sanli, Kersten Hahn, Lutz Müller, Herbert Gruhn, Christian Silber, Gisela Schütz, Corinne Grévent,\* and Kahraman Keskinbora\*



Cite This: *ACS Appl. Mater. Interfaces* 2020, 12, 33377–33385



Read Online

ACCESS |



Metrics & More



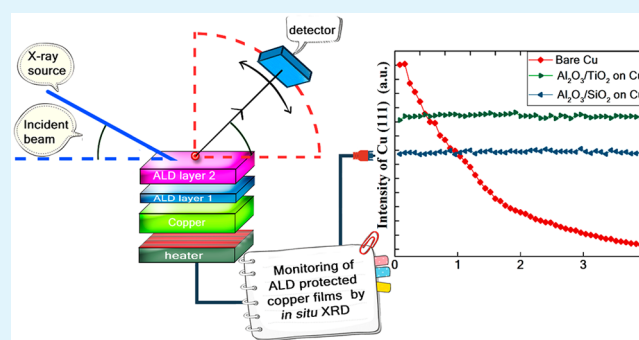
Article Recommendations



Supporting Information

**ABSTRACT:** In many applications of copper in industry and research, copper migration and degradation of metallic copper to its oxides is a common problem. There are numerous ways to overcome this degradation with varying success. Atomic layer deposition (ALD) based encapsulation and passivation of the metallic copper recently emerged as a serious route to success owing to the conformality and density of the ALD films. So far, the majority of the studies have been focused on corrosion protection of copper in a variety of chemical environments, mostly at ambient temperature. An investigation of the stability of the ALD film stacks and copper's interaction with them at elevated temperatures has been lacking. Here, we study the mitigation of copper oxidation and migration in 50 nm thick  $\text{Al}_2\text{O}_3/\text{TiO}_2$  and  $\text{Al}_2\text{O}_3/\text{SiO}_2$  bilayer ALD stacks. First, the corrosion dynamics were investigated *via in situ* X-ray diffraction (XRD) at 350 °C under atmospheric conditions, and second, the interaction of copper with the passivation layers have been examined *post factum* using detailed spectro-microscopic investigations. According to the XRD results, both ALD films exhibited excellent oxidation protection. In contrast, bare Cu immediately started to oxidize at 350 °C and transformed entirely to its known oxide phases in 4 h. Spectro-microscopic studies revealed that there are structural and chemical changes on the top surface and within the film stacks. The  $\text{TiO}_2$  layer was crystallized during annealing, while the  $\text{SiO}_2$  layer stayed in the amorphous phase, which was analyzed by grazing incidence XRD and transmission electron microscopy. According to scanning electron microscopy and X-ray photoelectron spectroscopy analysis, copper was detected on the surface with a higher amount in  $\text{Al}_2\text{O}_3/\text{TiO}_2$  than  $\text{Al}_2\text{O}_3/\text{SiO}_2$ , 5.2 at.% and 0.7 at.%, respectively. Based on the surface and cross-sectional analysis, copper migration was observed on both layers, albeit more substantially in  $\text{Al}_2\text{O}_3/\text{TiO}_2$ . In the case of  $\text{Al}_2\text{O}_3/\text{SiO}_2$ , the bulk of the copper was captured at the interface of the two oxides.

**KEYWORDS:** ALD, copper, oxidation, corrosion protection, *in situ* XRD



## 1. INTRODUCTION

Applications of copper are ubiquitous in modern technology, where it is used for a wide range of applications such as in heat exchangers, interconnects, and gate electrodes for micro-electronics due to its superior thermal conductivity, electrical conductivity, and excellent mechanical workability.<sup>1–5</sup> Although these advantages make the use of copper attractive, corrosion in an oxidative environment remains a serious problem.<sup>6,7</sup> For example, in copper interconnects, a larger grain size is in demand to have lower electrical resistance and therefore better circuit performance. While the annealing of copper was typically carried out at 100 °C, with the protective coating of copper interconnect, the annealing temperature has been increased up to 300 °C.<sup>8</sup> The protective coatings are often used to prolong the performance of copper under harsh conditions.<sup>7,9</sup> A wide range of techniques has been used for the deposition of protective layers, such as chemical vapor deposition, electrodeposition, and plasma treatments.<sup>9,10</sup>

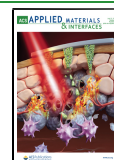
Within these techniques, atomic layer deposition (ALD) offers an attractive route to achieve high-quality protective layers with an accurate thickness control, uniformity over a large area, excellent step coverage, and composition control.<sup>7,11–13</sup>

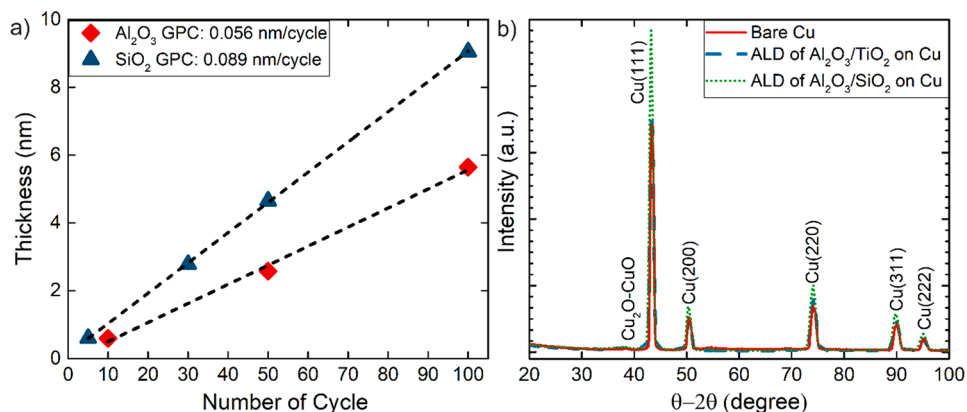
ALD is a subgroup of chemical vapor deposition techniques (CVD), in which the reaction is separated into two self-limiting surface reactions. The self-limiting growth of the film ensures the deposition of a partial or monolayer of atoms per cycle.<sup>11,12,14</sup> In each cycle, approximately the same thickness of the material is deposited. The film thickness, therefore, can be controlled accurately by the number of deposition cycles.

Received: April 14, 2020

Accepted: June 17, 2020

Published: June 17, 2020





**Figure 1.** ALD film growth and structural properties: (a) film thickness as a function of the number of cycles for Al<sub>2</sub>O<sub>3</sub> and SiO<sub>2</sub>, (b) GI-XRD spectra of Al<sub>2</sub>O<sub>3</sub>/SiO<sub>2</sub> and Al<sub>2</sub>O<sub>3</sub>/TiO<sub>2</sub> protective layers as-deposited with bare Cu, which ALD layers were an amorphous structure.

Additionally, the self-limiting growth allows uniformity over a large area, even in 3D complex structures.<sup>15,16</sup>

Several groups have introduced ALD of various oxide layers to protect copper against corrosion in liquid oxidative environments. The most intense research is performed on Al<sub>2</sub>O<sub>3</sub> layers for corrosion protection due to ease of nucleation on metal surfaces.<sup>17–19</sup> When Al<sub>2</sub>O<sub>3</sub> protected copper is exposed to a NaCl solution, the corrosion rate is decreased compared to bare Cu.<sup>1,18,20–24</sup> However, Al<sub>2</sub>O<sub>3</sub> dissolves in the long term when directly exposed to an aqueous solution.<sup>22,25</sup> Several other ALD layers have been reported that provide sufficient corrosion protection of Cu, such as TiO<sub>2</sub>, SiO<sub>2</sub>, HfO<sub>2</sub>, ZnO, ZrO<sub>2</sub>, Nb<sub>2</sub>O<sub>5</sub>, and Ta<sub>2</sub>O<sub>5</sub>.<sup>18,20–23,25–29</sup> Abdulgatov et al. studied ALD of Al<sub>2</sub>O<sub>3</sub>, TiO<sub>2</sub>, Al<sub>2</sub>O<sub>3</sub> with capping TiO<sub>2</sub> and Al<sub>2</sub>O<sub>3</sub> with a capping layer ZnO on planar copper to prevent water corrosion at 90 °C. While the Al<sub>2</sub>O<sub>3</sub> with capping ZnO layer protected the copper for 10 days, the Al<sub>2</sub>O<sub>3</sub> with a capping TiO<sub>2</sub> layer protected for 80 days.<sup>25</sup> Daubert et al. studied the corrosion protection properties of Al<sub>2</sub>O<sub>3</sub>, TiO<sub>2</sub>, ZnO, HfO<sub>2</sub>, and ZrO<sub>2</sub> in aqueous NaCl solution. In that work, the Al<sub>2</sub>O<sub>3</sub> and HfO<sub>2</sub> films were more preferable for initial corrosion protection, but in longer exposure, the HfO<sub>2</sub> film showed the best stability.<sup>20</sup> In the literature, a variety of chemical environments such as water, NaCl, or NH<sub>4</sub>OH have been used for investigation of protection of ALD films.<sup>1,18,20–23,25,27,28,30–32</sup> However, the performance of ALD layers at elevated temperatures, along with a detailed discussion of the microstructural evolution of the layer stack has not been reported.

In this study, the corrosion protection of Cu using Al<sub>2</sub>O<sub>3</sub>/SiO<sub>2</sub> and Al<sub>2</sub>O<sub>3</sub>/TiO<sub>2</sub> bilayers at 350 °C is reported by using *in situ* X-ray diffraction (XRD), which allows direct observation and overview of the evolution of solid-state phases over time and in response to changing temperature. The oxidation protection performance of the layers was measured by the evolution of the Cu (111) peak intensity in bare- and protected-Cu metal as a function of time. Furthermore, *post factum* spectro-microscopic investigations revealed the rich nature of interactions of the copper with its protection layers, which were not fully captured by the *in situ* measurements. Using scanning electron microscopy (SEM), X-ray photoelectron spectroscopy (XPS), transmission electron microscopy (TEM) in combination with electron energy-loss spectroscopy (EELS), the structural and compositional changes were studied in detail.

## 2. EXPERIMENTAL SECTION

Copper (Cu) samples (99.999% purity) were electrodeposited on p-type Si (100) with 1.5 μm thickness and 6 nm surface roughness. All samples were cut to 2 cm × 2 cm and rinsed with acetic acid for 1 min to remove oxide layers from the surface of Cu. The ALD devices from Sentech Instruments GmbH and Oxford Instruments were used for deposition with constant nitrogen flow as a carrier gas. Precursors were pulsed using direct vapor drawing from stainless steel bubblers.

Al<sub>2</sub>O<sub>3</sub>/TiO<sub>2</sub> bilayers were deposited using ALD (Oxford Instruments) at 150 °C. For Al<sub>2</sub>O<sub>3</sub> deposition, the precursors were used at room temperature (RT). TMA (C<sub>6</sub>H<sub>18</sub>Al<sub>2</sub>) and H<sub>2</sub>O were pulsed for 30 ms and purged for 15 s. During TiO<sub>2</sub> deposition, TDMAT (C<sub>8</sub>H<sub>24</sub>N<sub>4</sub>Ti) was heated to 75 °C, pulsed for 100 ms and purged for 15 s, followed by 15 ms H<sub>2</sub>O pulse and 10 s purge. Al<sub>2</sub>O<sub>3</sub>/SiO<sub>2</sub> bilayers were deposited using ALD (Sentech Instruments GmbH) at 150 °C. After depositing Al<sub>2</sub>O<sub>3</sub> with 20 ms pulse and 1980 ms purge time, SiO<sub>2</sub> layers were deposited using SAM (C<sub>8</sub>H<sub>22</sub>N<sub>2</sub>Si) which was heated to 80 °C and an O<sub>2</sub> plasma. SAM was pulsed into the chamber for 140 ms and purged for 1980 ms. The O<sub>2</sub> plasma was pulsed for 1 s at 200 W and purged for 1 s.

The bilayers are composed of 10 nm Al<sub>2</sub>O<sub>3</sub> as a seed layer and 40 nm of protective layer structures. The thickness of the layers and ALD growth properties were analyzed using *in situ* spectroscopic ellipsometry (SE, SENresearch 4.0, Sentech, Germany), on Cu and Si reference wafers that were placed in the reactor during deposition. The final thickness of the layers and homogeneity of the depositions were determined using *ex situ* SE with mapping options from 49 points on Si and as well as Cu samples. The amorphous ALD films were identified with grazing incidence-XRD (GI-XRD) in 2θ range 20–100° with Cu-K<sub>α</sub> radiation using the Bruker AX8 device.

*In situ* XRD measurements were conducted at 350 °C under atmospheric conditions for 4 h in which each measurement takes 5 min. The diffractometer (Bruker axs-D8) was used with Cu-K<sub>α</sub> radiation. After inserting the sample, the chamber was heated to 350 °C with the rate, 0.2 °C/s. During heating, intermittent measurements were conducted at 30 °C, 100 °C, and 200 °C to analyze the effect of temperature. At 350 °C, regular θ–2θ scans were carried between 25° and 55° with 0.1 s/step. The sequential XRD scans were programmed by DIFFRAC plus XRD software during 4 h. The number of XRD scans were determined according to complete oxidation of copper at 350 °C.

The surface of Cu and ALD protected Cu were evaluated using X-ray photoelectron spectroscopy (XPS), Theta Probe Instrument, and scanning electron microscopy (SEM, Zeiss Gemini, Germany). The composition and structure of the ALD films after annealing were evaluated using a scanning transmission electron microscope (JEOL ARM200CF) in combination with an electron energy-loss spectrometer (Gatan GIF Quantum ERS). The cross sections were prepared using a focused ion beam (Dualbeam, FEI Nova Nanolab 600, The Netherlands).

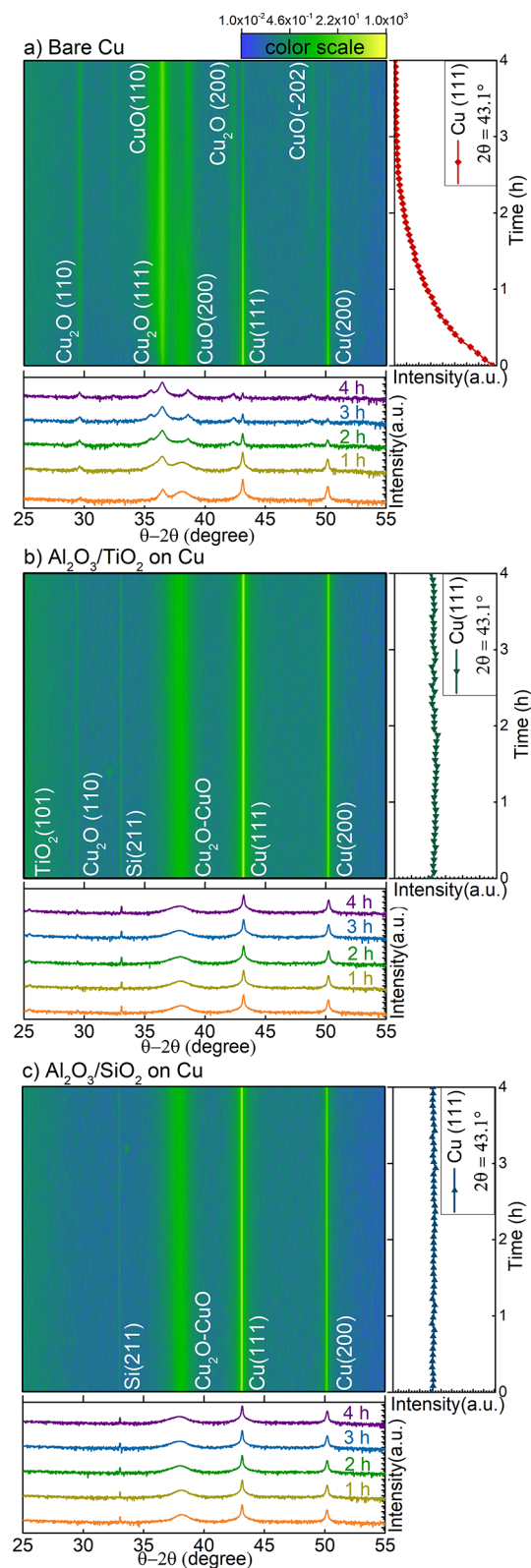
### 3. RESULTS AND DISCUSSION

**ALD Film Growth and Structural Properties.** The 10 nm thick  $\text{Al}_2\text{O}_3$  followed by either the 40 nm thick  $\text{SiO}_2$  or  $\text{TiO}_2$  films were deposited on copper-coated silicon wafers with 2.4 nm thick native oxide ( $\text{CuO}$ ), measured by SE. The sputtered copper layer thickness was 1.5  $\mu\text{m}$ . Both  $\text{Al}_2\text{O}_3/\text{SiO}_2$  and  $\text{Al}_2\text{O}_3/\text{TiO}_2$  processes showed a characteristic ALD growth mechanism where the film thickness increases linearly with the number of cycles. Figure 1a depicts the growth per cycle for  $\text{Al}_2\text{O}_3$  and  $\text{SiO}_2$  for 10 nm thin films, deposited at 150  $^\circ\text{C}$  on Cu and measured by *in situ* SE. The growth rates were calculated from the slope of the fit and were found to be 0.056 and 0.089 nm/cycle for  $\text{Al}_2\text{O}_3/\text{SiO}_2$  and 0.090 and 0.080 nm/cycle for  $\text{Al}_2\text{O}_3/\text{TiO}_2$  layers, respectively. The GI-XRD spectra after the deposition show that the films were amorphous. The curves for bare Cu, Cu coated with  $\text{Al}_2\text{O}_3/\text{SiO}_2$ , and Cu coated with  $\text{Al}_2\text{O}_3/\text{TiO}_2$  are given in Figure 1b. Compared to the polycrystalline structure of Cu, no additional phases were detected within the ALD protection layer. The SEM images showing the morphology of ALD bilayers are given in Figure S1, Supporting Information.

**In Situ XRD Measurements.** The stability of the ALD layers was tested using *in situ* XRD at 350  $^\circ\text{C}$  for 4 h at atmospheric conditions. During heating, set-point control measurements were taken at 30  $^\circ\text{C}$ , 100  $^\circ\text{C}$ , and 200  $^\circ\text{C}$  (Figure S2, Supporting Information). The diffraction data of the ALD layers were compared with bare copper to analyze the protection properties of ALD layers against degradation at an elevated temperature. The diffraction data for the measurements was labeled according to the JCPDS database and represented in the text with  $2\theta$  values.<sup>33</sup>

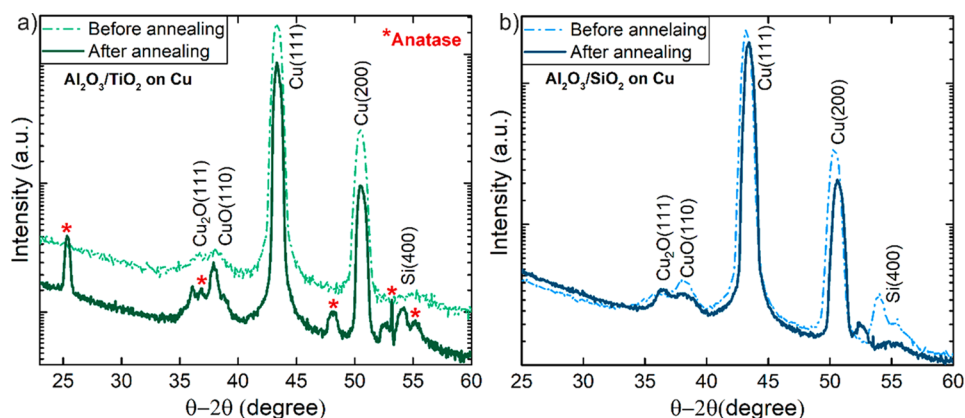
Figure 2a shows the XRD patterns of bare Cu at 350  $^\circ\text{C}$  for 4 h. During the first measurements, bare Cu showed sharp diffraction peaks centered at around 43.1 $^\circ$  and 50.2 $^\circ$  corresponding to the (111) and (200) reflection planes, respectively. Additionally, the broad peak was observed at around 37.8 $^\circ$ , attributed to a mixture of oxide phases of CuO (110) and  $\text{Cu}_2\text{O}$  (111). With the continuation of the annealing process, the XRD pattern started to change in a decrease of Cu diffraction peaks and an increase of oxide phases. The Cu (111) peak dropped to 70% of its initial intensity in 1 h. In addition to the splitting of the oxide peak at around 37.8 $^\circ$ , new phases have appeared at 35.6 $^\circ$  and 42.3 $^\circ$ , labeled as CuO (-111) and  $\text{Cu}_2\text{O}$  (200), respectively. After 4 h exposure to 350  $^\circ\text{C}$ , Cu diffraction peaks almost disappeared and were converted into a mixture of oxide phases, including mainly CuO, which is further supported by GI-XRD measurements (Figure S3, Supporting Information). The surface properties of oxidized copper are given in Figure S4, Supporting Information.

In contrast to bare Cu, ALD films showed “excellent” protection against corrosion. Figure 2b,c show the  $\text{Al}_2\text{O}_3/\text{SiO}_2$  and  $\text{Al}_2\text{O}_3/\text{TiO}_2$  diffraction data in which copper peaks stayed the same for 4 h at 350  $^\circ\text{C}$  using *in situ* XRD measurements. With metallic copper peaks at 43.1 $^\circ$  and 50.2 $^\circ$ , the broad copper oxide peak was observed at around 37.8 $^\circ$ . Besides the observed oxide peak at room temperature (RT), an indication of further oxide phase formation was not detected with increasing exposure time (Figure S2, Supporting Information). Indeed, neither the Cu (111) peak intensity nor oxide peak intensity show a trace of change in the XRD pattern for both

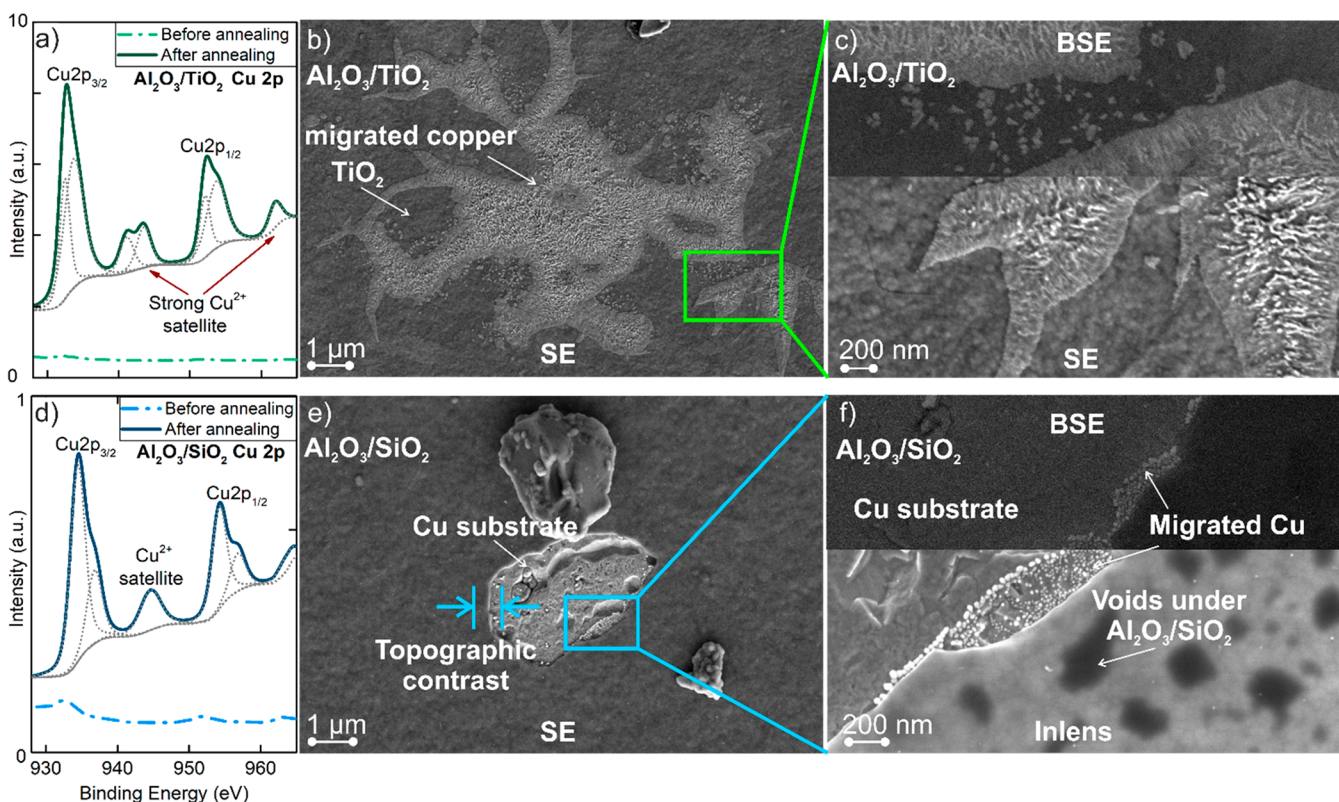


**Figure 2.** *In situ* XRD analysis at 350  $^\circ\text{C}$  for 4 h under atmospheric conditions. The density plot represents overall XRD pattern during annealing; the right-hand side gives the change of Cu (111) peak intensity over the time, and the lower part gives the XRD pattern for specified annealing times for (a) bare Cu and (b)  $\text{Al}_2\text{O}_3/\text{TiO}_2$  on Cu and (c)  $\text{Al}_2\text{O}_3/\text{SiO}_2$  on Cu (intensities are in log 10 scale).





**Figure 3.** GI-XRD of (a)  $\text{Al}_2\text{O}_3/\text{TiO}_2$  and (b)  $\text{Al}_2\text{O}_3/\text{SiO}_2$  bilayers after annealing at 350 °C for 4 h under atmospheric conditions (intensities are in log 10 scale). The  $\text{Al}_2\text{O}_3/\text{TiO}_2$  spectra showed the amorphous  $\text{TiO}_2$  layer transformed to anatase phase; whereas, the  $\text{Al}_2\text{O}_3/\text{SiO}_2$  spectra remained the same during annealing.

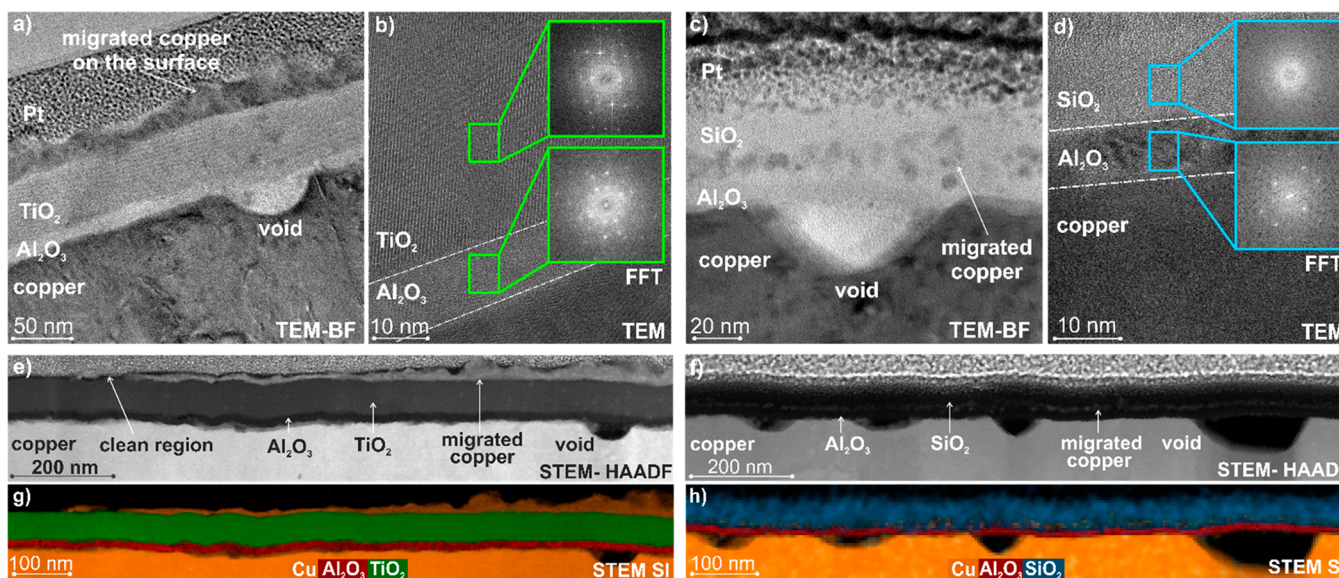


**Figure 4.** Post factum surface analyses of the film stacks following the *in situ* XRD. (a) XPS of copper peaks from the surface of the  $\text{Al}_2\text{O}_3/\text{TiO}_2$  shows the presence of metallic copper and copper oxide formation. (b) A secondary electron signal from SEM shows significant spread of the migrated copper on the film surface. (c) Side by side comparison of backscattered and secondary electron signals with increased intensity in the formations correlate well with the higher atomic number of copper. In the case of  $\text{Al}_2\text{O}_3/\text{SiO}_2$  films, the presence of copper species on the surface is much more limited as XPS intensity in the figure in part d indicates. An SEM image of a fracture surface in part e provides insight into the restructuring in the stack. The underlying copper film, an intermediate layer, and the passivation layers can be seen together. In part f, a close-up image of the fracture surface taken using the in-lens detector showed dark spots that were attributed to the formation of voids in the copper film near the interface. Also, migrated copper particles can be identified.

layers, which successfully include the protection properties of ALD layers on copper.

**Effect of Annealing on the Structure.** The  $\text{Al}_2\text{O}_3/\text{TiO}_2$  diffraction data in Figure 2b revealed the anatase phase at 25.4° that exhibits the crystallization of 40 nm thick  $\text{TiO}_2$  during annealing. According to set-point control measurements, amorphous  $\text{TiO}_2$  starts to transform into the anatase phase at 350 °C with primary peak growth (101) (Figure S2,

Supporting Information). This is supported by the postannealing GI-XRD results as indicated in Figure 3a, where not only the (101) peak but also (004) at 37.8°, (200) at 48°, (105) at 53.9°, and (211) at 55° peaks of anatase were labeled. While *in situ* XRD results show the existence of the anatase phase with poor crystallinity, the GI-XRD demonstrates the improvement of the crystalline structure during annealing at 350 °C. The  $\text{TiO}_2$  exists in three different crystalline phases, which are



**Figure 5.** Bright-field (BF) images of annealed (a)  $\text{Al}_2\text{O}_3/\text{TiO}_2$  and (c)  $\text{Al}_2\text{O}_3/\text{SiO}_2$  bilayers. The migrated copper and void structures were represented. The FFT generated patterns are shown in parts b and d with green and blue insets. While the  $\text{SiO}_2$  was amorphous,  $\text{Al}_2\text{O}_3$  and  $\text{TiO}_2$  showed crystalline reflections. High-angle annular dark-field (HAADF) images of annealed (e)  $\text{Al}_2\text{O}_3/\text{TiO}_2$  and (f)  $\text{Al}_2\text{O}_3/\text{SiO}_2$  were given corresponding to (g) Cu–Al–O–Ti and (h) Cu–Al–O–Si elemental maps extracted from the electron energy-loss spectrum image. The void structures were observed in both samples. While copper migrated to the surface in  $\text{Al}_2\text{O}_3/\text{TiO}_2$ , the movement was hindered, and copper stayed inside the layers in  $\text{Al}_2\text{O}_3/\text{SiO}_2$ .

anatase, rutile, and brookite. Among these, rutile is the stable phase at all temperatures and pressures,<sup>34</sup> which has been confirmed by thermodynamic studies.<sup>35–37</sup> The anatase phase is generally favorable for temperatures below 600 °C in solution-phase preparation methods, and it is transformed into the rutile phase around 800 °C, which is varying with its composition, deposition method, and purity.<sup>38</sup>

In comparison with as-annealed GI-XRD diffraction data, the 40 nm-thick  $\text{SiO}_2$  layer remained amorphous even after for 4 h of exposure to 350 °C. The GI-XRD data in Figure 3b showed no change for the  $\text{Al}_2\text{O}_3/\text{SiO}_2$  bilayer after annealing. The change in Si (400) peak that comes from the substrate depends on the relative in-plane orientation of the substrate with respect to the measurement direction. It does not signify a crystallographic change in the substrate.

**Effect of Annealing on the Morphology.** Although the ALD layers were stable and hindered the oxidation of copper en masse during annealing, copper was detected on the surface of both samples to varying degrees. If ALD layers did not protect copper, the copper oxide film would have grown and be detected by XRD, as in the case of bare copper. It, therefore, brings a related question of whether copper atoms migrated through the channels using the temperature as a driving force. Thus, further analyses were studied on the surfaces and interfaces by SEM, XPS, and TEM.

The morphological changes on the surface by the migration of copper to the top layer of the  $\text{Al}_2\text{O}_3/\text{TiO}_2$  films presented in Figure 4a–c. According to XPS survey spectra, copper was detected on the surface with 5.2 at.% based on the overall 50  $\text{nm}^2$  scanned area. The survey spectra also showed Ti and O elements with a contribution of adventitious carbon from the environment (Figure S5a, Supporting Information). Moreover, the single element analysis of copper depicts the Cu 2p binding energies in Figure 4a, where metallic copper peaks were labeled at 834.5 and 954.2 eV and strong  $\text{Cu}^{2+}$  satellite peaks at 944.7 and 963 eV.<sup>39</sup> This additionally indicates that copper atoms

moved through migration channels and then oxidized on the surface. Figure 4b represents the migrated copper on the surface using the secondary electron (SE) signal of SEM. Besides, the presence of copper was analyzed by back scattered electron (BSE) imaging, in which two phases were detected on the surface, as shown in Figure 4c. As copper has a higher atomic number than both Ti and O, the brighter areas detected by BSE are attributed to the copper, which could be migrated to the surface during annealing.

According to XPS analysis, Cu was detected on the  $\text{Al}_2\text{O}_3/\text{SiO}_2$  surface with 0.7 at.% (Figure S5b, Supporting Information). Compared to the  $\text{Al}_2\text{O}_3/\text{TiO}_2$  bilayer, a markedly smaller amount of copper was found on the surface. The elemental analysis showed metallic copper peaks at 834.5 and 954.2 eV and a single weak peak of the  $\text{Cu}^{2+}$  satellite at 944.7 eV, given in Figure 4d.

The SEM analysis, in Figure 4e,f, was carried out for  $\text{Al}_2\text{O}_3/\text{SiO}_2$  bilayer on the fractured region that includes  $\text{SiO}_2$  layer, Cu substrate, and the interface with diffused Cu. The fractured region was presented by topographical contrast based on the height difference between the Cu substrate and the  $\text{SiO}_2$  layer. The image was taken by using the SE detector, as shown in Figure 4e. The presence of the Cu phase and the  $\text{SiO}_2$  layer was further supported by BSE imaging with dark and bright areas. Indeed, void structures were seen on the surface by using the InLens detector, as shown in Figure 4f.

The SE detector did not capture the void structures in the  $\text{Al}_2\text{O}_3/\text{SiO}_2$  films as secondary electrons have lower energy (<50 eV) and consequently shallow escape depths. However, the void structures appeared in images which were recorded using the InLens detector. Since the InLens detector is placed directly above the sample, it receives a substantial contribution from the backscattered electrons, and it was, therefore, possible to observe the subsurface structures beneath the ALD protection film, clearly showing the void structures. This indication was further supported by the calculation of the



penetration depth of electrons (Equation S1, Supporting Information). The SEM images in agreement with the calculations revealed that the void structures were at least 46 nm below the surface, which indicates the copper substrate rather than the ALD layer (see Table S1 and Figure S6, Supporting Information). Moreover, the void structures might be related to the transport mechanism of copper, and the movement of copper atoms leads to voids on the substrate. Even though annealing at 350 °C leads to morphological changes, the annealing at lower temperatures such as 200 °C, the whole film stack in both Al<sub>2</sub>O<sub>3</sub>/TiO<sub>2</sub> and Al<sub>2</sub>O<sub>3</sub>/SiO<sub>2</sub> seems to be much more stable based on the SEM analysis (Figure S7, Supporting Information).

Cross-sectional TEM lamellae were prepared from the region (Figure S8, Supporting Information) that includes copper on the surface in the Al<sub>2</sub>O<sub>3</sub>/TiO<sub>2</sub> sample and voids in the Al<sub>2</sub>O<sub>3</sub>/SiO<sub>2</sub> sample. According to TEM analyses, the oxide components of the ALD layers in both samples were structurally stable during annealing without any intermixing of phases at the interfaces. Figure 5a shows the bright field image of the Al<sub>2</sub>O<sub>3</sub>/TiO<sub>2</sub> layer which includes the void structure and migrated copper on the surface. A fast Fourier transform (FFT) of the TEM image, given in Figure 5b, showed the formation of crystallites in the TiO<sub>2</sub> layer as supported by XRD measurements. In comparison with Al<sub>2</sub>O<sub>3</sub>/TiO<sub>2</sub>, more void structures were observed and migrated copper was detected inside the layer of Al<sub>2</sub>O<sub>3</sub>/SiO<sub>2</sub>, given in Figure 5c. The FFT of the SiO<sub>2</sub> layer showed the scattering characteristic of amorphous phase, shown in Figure 5d. The high-angle annular dark-field (HAADF) images of annealed Al<sub>2</sub>O<sub>3</sub>/TiO<sub>2</sub> and Al<sub>2</sub>O<sub>3</sub>/SiO<sub>2</sub> are given in Figure 5e,f. According to cross-section analysis, migration channels could not be detected in the ALD bilayers. However, voids in the copper forming near the interface of both Al<sub>2</sub>O<sub>3</sub>/SiO<sub>2</sub> and Al<sub>2</sub>O<sub>3</sub>/TiO<sub>2</sub> were observed.

The elemental maps, extracted from electron energy-loss spectra, are given in Figure 5g for Al<sub>2</sub>O<sub>3</sub>/TiO<sub>2</sub> based on the Cu–Al–Ti–O elements and in Figure 5h for Al<sub>2</sub>O<sub>3</sub>/SiO<sub>2</sub> based on Cu–Al–Si–O elements, where the element oxygen was not included to ease the data interpretation. While copper was found on the surface of Al<sub>2</sub>O<sub>3</sub>/TiO<sub>2</sub> lamella at significant amounts in agreement with XPS and SEM analyses, it was not present on the surface of Al<sub>2</sub>O<sub>3</sub>/SiO<sub>2</sub> bilayers. In the case of Al<sub>2</sub>O<sub>3</sub>/SiO<sub>2</sub>, the bulk of the copper atoms seem to have been captured within the SiO<sub>2</sub> layer, near the Al<sub>2</sub>O<sub>3</sub>/SiO<sub>2</sub> interface, according to the high-resolution HAADF-STEM images and elemental mapping using EELS, which is shown in Figure 5f,h.

Moreover, the Al<sub>2</sub>O<sub>3</sub> layers in both samples showed crystallinity via FFT analysis that were not detected via the *in situ* XRD measurements (Figure 5b,d). The recrystallization temperature of amorphous Al<sub>2</sub>O<sub>3</sub> is usually reported to be around 600 °C in the literature.<sup>40,41</sup> However, several factors could have led to the observed crystallization. Indeed, it is known that electron–atom and electron–electron interactions lead to beam damage during TEM analysis.<sup>42,43</sup> Alternatively, the transformation could have happened during the *in situ* XRD measurements due to extended exposure to high temperatures. At the same time, the technique might not be sensitive enough to detect structural changes within a 10 nm thick Al<sub>2</sub>O<sub>3</sub> layer. If that is indeed the case, the lower recrystallization temperature can be explained by the thickness of the film, which is in the range of 10 nm.

Although microstructural changes were observed on both film stacks, a four-point probe electrical measurement of the films shows that the conductivity (sheet resistance) of the passivated copper films did not change after annealing at 350 °C (Table S2, Supporting Information). This demonstrates that the ALD bilayers functioned as intended in protecting the underlying copper.

**Migration of Copper.** During annealing, temperature serves as a driving force for the migration of copper within ALD layers, which is directly facilitated by defect structure.<sup>44</sup> Structural relaxations, recombination of point defects, or formation of grain boundaries with the crystallization of layers might strongly influence the migration of copper.<sup>45,46</sup> Furthermore, the pinholes inside the ALD layers play an important role in creating pathways for copper migration. The structural defects or surface contamination, in turn, can serve as nucleation sites for pinhole and defect formation.<sup>44–46</sup> Additionally, mass diffusion within the ALD layers is another possible mechanism to explain the copper migration.<sup>47,48</sup> From the detailed microscopic investigations in this work, we observed that the mode of copper migration depends strongly on the layer stack of Al<sub>2</sub>O<sub>3</sub>/TiO<sub>2</sub> and Al<sub>2</sub>O<sub>3</sub>/SiO<sub>2</sub>.

In the case of Al<sub>2</sub>O<sub>3</sub>/TiO<sub>2</sub>, copper appears to have migrated through pinholes and defects and reached the topmost layer of the film during annealing at 350 °C. Indeed, the migrated copper was detected only at the surface and not within the ALD layers. This indicates that the copper migrated mainly through the pinholes and local defects and not via a mass diffusion through the bulk of the TiO<sub>2</sub> layer. The presence of defects in TiO<sub>2</sub> are attributed to the several mechanisms such as creation of defects and pinholes in a typical nonideal ALD deposition and nucleation processes<sup>49</sup> and by surface contamination. Finally, the creation of defects such as formation of grain boundaries and pinholes can also be due to the recrystallization process, which was specifically observed in TiO<sub>2</sub>.

In contrast, in the Al<sub>2</sub>O<sub>3</sub>/SiO<sub>2</sub> bilayer, copper migrated through the Al<sub>2</sub>O<sub>3</sub> layer and penetrated for a short distance (~10 nm) inside the 50 nm thick SiO<sub>2</sub> layer but did not reach the surface at large amounts. The successful blocking of the copper migration within the SiO<sub>2</sub> layer is attributed mainly to the higher density of the SiO<sub>2</sub> film<sup>50</sup> and its structural stability in its amorphous phase. The presence of copper inside the SiO<sub>2</sub> layer can be accredited to both sealed line pinholes and defects.<sup>49</sup> Indeed, it might not be the only mechanism for diffusion in the case of the Al<sub>2</sub>O<sub>3</sub>/SiO<sub>2</sub> bilayer. It appears that the drive through diffusion within the amorphous SiO<sub>2</sub> could also be the mechanism of copper migration, albeit at much lower transport rates compared to the defect mediated migration in the Al<sub>2</sub>O<sub>3</sub>/TiO<sub>2</sub> layer stack. This further explains the XPS survey spectra results in which only a small amount of copper was found on the surface for Al<sub>2</sub>O<sub>3</sub>/SiO<sub>2</sub> bilayers.

While defects created by the recrystallization of TiO<sub>2</sub> are characteristic of the material properties at this temperature and cannot be avoided, the density of pinholes in ALD layers correlates with the density of structural defects on the substrate, nucleation mechanism in the first ALD cycles, process temperature, and other process parameters and could be optimized.<sup>26,51</sup> The improvement of surface properties of copper could be one of the vital solutions for decreasing the pinhole density. Mirhashemighighi et al. showed that a pretreated substrate with enhanced surface properties showed the improved corrosion protection of copper in one order of

magnitude with respect to polarization resistance.<sup>51</sup> Even though an ideal ALD process shows the linear increase of thickness with the number of deposition cycles, the growth is not entirely constant during the first few cycles for the real ALD process, as a substrate is not wholly covered with deposited material and leads to a less nucleation rate at the first several cycles in metals.<sup>45,46</sup>

The combination of imperfections of ALD growth and surface properties of the substrate and postprocessing induces intrinsic and extrinsic defects, which serve as enabling factors for the copper migration. While both ALD bilayers were protecting copper against oxidation at high temperature, the layers could be improved by substrate cleaning and optimization of ALD parameters to reduce the number of overall defects and pinholes which should block the copper migration to a substantial degree if not altogether.

#### 4. CONCLUSIONS

In this work, we have studied the viability of Al<sub>2</sub>O<sub>3</sub>/TiO<sub>2</sub> and Al<sub>2</sub>O<sub>3</sub>/SiO<sub>2</sub> bilayer thin film stacks against the protection of copper from oxidation *via in situ* XRD at 350 °C under atmospheric conditions. Further, an in-depth evaluation of the microstructural evolution using spectro-microscopy showed critical differences between the behaviors of the two-layer stacks.

During *in situ* monitoring, XRD showed that bare copper started to oxidize within a few minutes, as observed by a substantial decrease of Cu (111) peak intensity with complete oxidation of the film at the end of the experiment. On the contrary, both ALD bilayers protected the underlying copper layer to a large degree against oxidation, as evidenced by a constant Cu (111) peak intensity and we conclude the excellent protection of both ALD layers against oxidation at 350 °C.

On the other hand, other types of microstructural transformations were observed within both the bilayers and the copper films. According to GI-XRD and STEM analysis, the amorphous TiO<sub>2</sub> layer transformed into the anatase phase during annealing. Despite the excellent antioxidation performance of the ALD layers, some morphological changes at the surface level were observed. Detailed SEM and XPS analyses also showed the presence of copper on the surface, while the ALD bilayers remained in the same chemical composition. Detailed analytical STEM studies via STEM-EELS revealed the copper on the surface for Al<sub>2</sub>O<sub>3</sub>/TiO<sub>2</sub> layers, where it was again oxidized according to the XPS results. In the case of Al<sub>2</sub>O<sub>3</sub>/SiO<sub>2</sub> bilayers, copper was mainly stopped at the bilayer interface, with mass diffusion into the SiO<sub>2</sub> layer, as observed via STEM-EELS. Copper was found on the surface again according to the XPS, albeit at much lower quantities. Therefore, Al<sub>2</sub>O<sub>3</sub>/SiO<sub>2</sub> bilayers act both as a diffusion barrier for copper and against oxidation of the underlying films, emerging as the more promising candidate for a dual-purpose encapsulation/passivation layer. The optimization of the ALD process parameters are expected to decrease the pinhole density in all stack elements and further improve the already promising antioxidative and diffusion barrier properties.

#### ■ ASSOCIATED CONTENT

##### SI Supporting Information

The Supporting Information is available free of charge at <https://pubs.acs.org/doi/10.1021/acsami.0c06873>.

As-deposited SEM images, *in situ* XRD measurements during heating, GI-XRD measurement and SEM images for annealed bare copper, XPS survey spectra for before and after annealing, the penetration depth calculations and SEM images of Al<sub>2</sub>O<sub>3</sub>/SiO<sub>2</sub> bilayer, SEM images of the as-annealed ALD bilayers for 4 h at 200 °C, TEM sample preparation details, and sheet resistance measurements (PDF)

#### ■ AUTHOR INFORMATION

##### Corresponding Authors

**Gül Dogan** – Robert Bosch GmbH, Automotive Electronics, 72703 Reutlingen, Germany; Max Planck Institute for Intelligent Systems, 70569 Stuttgart, Germany; [orcid.org/0000-0002-6121-0242](https://orcid.org/0000-0002-6121-0242); Email: [guel.dogan@de.bosch.com](mailto:guel.dogan@de.bosch.com)

**Corinne Grévent** – Robert Bosch GmbH, Automotive Electronics, 72703 Reutlingen, Germany; Email: [corinne.grevent@de.bosch.com](mailto:corinne.grevent@de.bosch.com)

**Kahraman Keskinbora** – Max Planck Institute for Intelligent Systems, 70569 Stuttgart, Germany; Email: [keskinbora@is.mpg.de](mailto:keskinbora@is.mpg.de)

##### Authors

**Umut T. Sanli** – Max Planck Institute for Intelligent Systems, 70569 Stuttgart, Germany

**Kersten Hahn** – Max Planck Institute for Solid State Research, 70569 Stuttgart, Germany

**Lutz Müller** – Robert Bosch GmbH, Automotive Electronics, 72703 Reutlingen, Germany

**Herbert Gruhn** – Robert Bosch GmbH, Corporate Sector Research and Advance Engineering, 71272 Stuttgart, Germany

**Christian Silber** – Robert Bosch GmbH, Automotive Electronics, 72703 Reutlingen, Germany

**Gisela Schütz** – Max Planck Institute for Intelligent Systems, 70569 Stuttgart, Germany

Complete contact information is available at:

<https://pubs.acs.org/10.1021/acsami.0c06873>

##### Notes

The authors declare no competing financial interest.

#### ■ ACKNOWLEDGMENTS

The authors thank F. Adam and R. Dinnebier for *in situ* XRD measurements, V. Mankowski for providing wafers, T. Reindl, M. Hagel, and J. Weis for the Al<sub>2</sub>O<sub>3</sub>/TiO<sub>2</sub> films, G. Maier, P. Schützendübe, and G. Richter for the GI-XRD and XPS analyses, U. Eigenthaler for the TEM sample preparation and C. Ozsoy Keskinbora for the TEM and SEM discussions. Last but not least, B. Ludescher, H. David, Y. Unutulmazsoy, Y. Chen, K. Son, A. Bauder, S. Klein, M. Ost, A. Mann, F. Dietz, I. Henkel, and G. Ernst are gratefully acknowledged for their kind support. The Stuttgart Center for Electron Microscopy group has received funding from the European Union's Horizon 2020 research and innovation program under Grant Agreement No. 823717–ESTEEM3. Three of the authors, C.G., C.S., and L.M., hold a patent application (DE102017216453A) on the application of ALD films described in this work.

#### ■ REFERENCES

(1) Mirhashemihaghighi, S.; Swiatowska, J.; Maurice, V.; Seyeux, A.; Klein, L. H.; Harkonen, E.; Ritala, M.; Marcus, P. Electrochemical and

Surface Analysis of the Corrosion Protection of Copper by Nanometer-Thick Alumina Coatings Prepared by Atomic Layer Deposition. *J. Electrochem. Soc.* **2015**, *162* (8), C377–C384.

(2) Vargas, I. T.; Fischer, D. A.; Alsina, M. A.; Pavissich, J. P.; Pasten, P. A.; Pizarro, G. E. Copper Corrosion and Biocorrosion Events in Premise Plumbing. *Materials* **2017**, *10* (9), 1036.

(3) Morgan, B.; Waits, C. M.; Krizmanic, J.; Ghodssi, R. Development of a Deep Silicon Phase Fresnel Lens Using gray-scale Lithography and Deep Reactive Ion Etching. *J. Microelectromech. Syst.* **2004**, *13* (1), 113–120.

(4) Chang, C.-C.; Pan, F.-M.; Chen, C.-W. Effect of Surface Reduction Treatments of Plasma-Enhanced Atomic Layer Chemical Vapor Deposited TaN<sub>x</sub> on Adhesion with Copper. *J. Electrochem. Soc.* **2010**, *157* (2), G62.

(5) Alers, G. B. L., X.; Sukamto, J. H.; Kailasam, S. K.; Reid, J.; Harm, G. Influence of Copper Purity on Microstructure and Electromigration. In *International Interconnect Technology*; IEEE Electron Devices Society, 2004; pp 45–47, DOI: 10.1109/IITC.2004.1345679.

(6) Fortunato, E.; Barquinha, P.; Martins, R. Oxide Semiconductor Thin-film Transistors: A Review of Recent Advances. *Adv. Mater.* **2012**, *24* (22), 2945–2986.

(7) Cremers, V.; Rampelberg, G.; Baert, K.; Abrahami, S.; Claes, N.; de Oliveira, T. M.; Terryn, H.; Bals, S.; Dendooven, J.; Detavernier, C. Corrosion Protection of Cu by Atomic Layer Deposition. *J. Vac. Sci. Technol., A* **2019**, *37* (6), No. 060902.

(8) Yang, C. C.; Witt, C.; Wang, P. C.; Edelstein, D.; Rosenberg, R. Stress Control During Thermal Annealing of Copper Interconnects. *Appl. Phys. Lett.* **2011**, *98* (5), No. 051911.

(9) Liu, Y.; Li, S.; Zhang, J.; Liu, J.; Han, Z.; Ren, L. Corrosion Inhibition of Biomimetic Super-hydrophobic Electrodeposition Coatings on Copper Substrate. *Corros. Sci.* **2015**, *94*, 190–196.

(10) He, G.; Lu, S.; Xu, W.; Szunerits, S.; Boukherroub, R.; Zhang, H. Controllable Growth of Durable Superhydrophobic Coatings on a Copper Substrate via Electrodeposition. *Phys. Chem. Chem. Phys.* **2015**, *17* (16), 10871–10880.

(11) Leskela, M.; Ritala, M. Atomic Layer Deposition Chemistry: Recent Developments and Future Challenges. *Angew. Chem., Int. Ed.* **2003**, *42* (45), 5548–5554.

(12) Tiznado, H.; Zaera, F. Surface Chemistry in the Atomic Layer Deposition of TiN Films from TiCl<sub>4</sub> and Ammonia. *J. Phys. Chem. B* **2006**, *110*, 13491–13498.

(13) Sanli, U. T.; Jiao, C.; Baluktsian, M.; Grevent, C.; Hahn, K.; Wang, Y.; Srot, V.; Richter, G.; Bykova, I.; Weigand, M.; Schutz, G.; Keskinbora, K. 3D Nanofabrication of High-Resolution Multilayer Fresnel Zone Plates. *Advanced Science* **2018**, *5* (9), 1800346.

(14) Ritala, M.; Asikainen, T.; Leskela, M.; Jokinen, J.; Lappalainen, R.; Utriainen, M.; Niinisto, L.; Ristolainen, E. Effects of Intermediate Zinc Pulses on Properties Of Tin and Nbn Films Deposited by Atomic Layer Epitaxy. *Appl. Surf. Sci.* **1997**, *120* (3-4), 199–212.

(15) George, S. M. Atomic Layer Deposition: An Overview. *Chem. Rev.* **2010**, *110*, 111–131.

(16) Puurunen, R. L. Surface Chemistry of Atomic Layer Deposition: A Case Study for the Trimethylaluminum/water Process. *J. Appl. Phys.* **2005**, *97* (12), 121301.

(17) Potts, S. E.; Schmalz, L.; Fenker, M.; Diaz, B.; Swiatowska, J.; Maurice, V.; Seyeux, A.; Marcus, P.; Radnoczi, G.; Toth, L.; Kessels, W. M. M. Ultra-Thin Aluminium Oxide Films Deposited by Plasma-Enhanced Atomic Layer Deposition for Corrosion Protection. *J. Electrochem. Soc.* **2011**, *158* (5), C132–C138.

(18) Diaz, B.; Światowska, J.; Maurice, V.; Seyeux, A.; Normand, B.; Härkönen, E.; Ritala, M.; Marcus, P. Electrochemical and Time-of-flight Secondary Ion Mass Spectrometry Analysis of Ultra-thin Metal Oxide (Al<sub>2</sub>O<sub>3</sub> and Ta<sub>2</sub>O<sub>5</sub>) Coatings Deposited by Atomic Layer Deposition on Stainless Steel. *Electrochim. Acta* **2011**, *56* (28), 10516–10523.

(19) Vanhaverbeke, C.; Cauwe, M.; Stockman, A.; Op de Beeck, M.; De Smet, H. Comparison of Copper Electroplating, Copper Wet Etching and Linear Sweep Voltammetry as Techniques to Investigate

the Porosity of Atomic Layer Deposited Al<sub>2</sub>O<sub>3</sub>. *Thin Solid Films* **2019**, *686*, 137424.

(20) Daubert, J. S.; Hill, G. T.; Gotsch, H. N.; Gremaud, A. P.; Ovental, J. S.; Williams, P. S.; Oldham, C. J.; Parsons, G. N. Corrosion Protection of Copper Using Al<sub>2</sub>O<sub>3</sub>, TiO<sub>2</sub>, ZnO, HfO<sub>2</sub>, and ZrO<sub>2</sub> Atomic Layer Deposition. *ACS Appl. Mater. Interfaces* **2017**, *9* (4), 4192–4201.

(21) Chai, Z.; Liu, Y.; Li, J.; Lu, X.; He, D. Ultra-thin Al<sub>2</sub>O<sub>3</sub> Films Grown by Atomic Layer Deposition for Corrosion Protection of Copper. *RSC Adv.* **2014**, *4* (92), 50503–50509.

(22) Correa, G. C.; Bao, B.; Strandwitz, N. C. Chemical Stability of Titania and Alumina Thin Films Formed by Atomic Layer Deposition. *ACS Appl. Mater. Interfaces* **2015**, *7* (27), 14816–14821.

(23) Chai, Z.; Li, J.; Lu, X.; He, D. Use of Electrochemical Measurements to Investigate the Porosity of Ultra-thin Al<sub>2</sub>O<sub>3</sub> Films Prepared by Atomic Layer Deposition. *RSC Adv.* **2014**, *4* (74), 39365–39371.

(24) Bahari, H. S.; Savaloni, H. Surface Analysis of Cu Coated With ALD Al<sub>2</sub>O<sub>3</sub> and its Corrosion Protection Enhancement in NaCl Solution: EIS and Polarization. *Mater. Res. Express* **2019**, *6* (8), No. 086570.

(25) Abdulgatov, A. I.; Yan, Y.; Cooper, J. R.; Zhang, Y.; Gibbs, Z. M.; Cavanagh, A. S.; Yang, R. G.; Lee, Y. C.; George, S. M. Al<sub>2</sub>O<sub>3</sub> and TiO<sub>2</sub> Atomic Layer Deposition on Copper for Water Corrosion Resistance. *ACS Appl. Mater. Interfaces* **2011**, *3* (12), 4593–4601.

(26) Mirhashemihaghighi, S.; Światowska, J.; Maurice, V.; Seyeux, A.; Klein, L. H.; Salmi, E.; Ritala, M.; Marcus, P. The Role of Surface Preparation in Corrosion Protection of Copper with Nanometer-thick ALD Alumina Coatings. *Appl. Surf. Sci.* **2016**, *387*, 1054–1061.

(27) Singh, A. K.; Adstedt, K.; Brown, B.; Singh, P. M.; Graham, S. Development of ALD Coatings for Harsh Environment Applications. *ACS Appl. Mater. Interfaces* **2019**, *11* (7), 7498–7509.

(28) Anderson, M. D.; Aitchison, B.; Johnson, D. C. Corrosion Resistance of Atomic Layer Deposition-Generated Amorphous Thin Films. *ACS Appl. Mater. Interfaces* **2016**, *8* (44), 30644–30648.

(29) Fusco, M. A.; Oldham, C. J.; Parsons, G. N. Investigation of the Corrosion Behavior of Atomic Layer Deposited Al<sub>2</sub>O<sub>3</sub>/TiO<sub>2</sub> Nanolaminate Thin Films on Copper in 0.1 M NaCl. *Materials (Basel)* **2019**, *12* (4), 672.

(30) Hoffmann, L.; Theirich, D.; Pack, S.; Kocak, F.; Schlamm, D.; Hasselmann, T.; Fahl, H.; Raupke, A.; Gargouri, H.; Riedl, T. Gas Diffusion Barriers Prepared by Spatial Atmospheric Pressure Plasma Enhanced ALD. *ACS Appl. Mater. Interfaces* **2017**, *9* (4), 4171–4176.

(31) Moehl, T.; Suh, J.; Severy, L.; Wick-Joliat, R.; Tilley, S. D. Investigation of (Leaky) ALD TiO<sub>2</sub> Protection Layers for Water-Splitting Photoelectrodes. *ACS Appl. Mater. Interfaces* **2017**, *9* (50), 43614–43622.

(32) Nehm, F.; Klumbies, H.; Richter, C.; Singh, A.; Schroeder, U.; Mikolajick, T.; Monch, T.; Hossbach, C.; Albert, M.; Bartha, J. W.; Leo, K.; Muller-Meskamp, L. Breakdown and Protection of ALD Moisture Barrier Thin Films. *ACS Appl. Mater. Interfaces* **2015**, *7* (40), 22121–22127.

(33) Degen, T.; Sadki, M.; Bron, E.; König, U.; Nénert, G. *The HighScore Suite, Powder Diffraction*; December 2014; Vol. 29, Supplement S2, pp S13–S18.

(34) Reyes-Coronado, D.; Rodriguez-Gattorno, G.; Espinosa-Pesqueira, M. E.; Cab, C.; de Coss, R.; Oskam, G. Phase-pure TiO<sub>2</sub> Nanoparticles: Anatase, Brookite and Rutile. *Nanotechnology* **2008**, *19* (14), 145605.

(35) Hanaor, D. A. H.; Sorrell, C. C. Review of the Anatase to Rutile Phase Transformation. *J. Mater. Sci.* **2011**, *46* (4), 855–874.

(36) Muscat, J.; Swamy, V.; Harrison, N. M. First-principles Calculations of the Phase Stability of TiO<sub>2</sub>. *Phys. Rev. B: Condens. Matter Mater. Phys.* **2002**, *65* (22), 224112.

(37) Tatchyn, R.; Csonka, P. L.; Lindau, I. Maximum-efficiency Transmission Grating Profiles for Metals in the Soft X-ray Range. *Nucl. Instrum. Methods Phys. Res.* **1983**, *208* (1–3), 237–243.

(38) Bakri, A. S.; Sahdan, M. Z.; Adriyanto, F.; Raship, N. A.; Said, N. D. M.; Abdullah, S. A.; Rahim, M. S. Effect of Annealing



Temperature of Titanium-dioxide Thin Films on Structural and Electrical Properties. *AIP Conf. Proc.* **2016**, 1788, No. 030030.

(39) NIST Standard Reference Database Number 20. In *NIST X-ray Photoelectron Spectroscopy Database*; National Institute of Standards and Technology: Gaithersburg, MD, 2000; 20899.

(40) Barros, C.; Blanc-Pelissier, D.; Fave, A.; Blanquet, E.; Crisci, A.; Fourmond, E.; Albertini, D.; Sabac, A.; Ayadi, K.; Girard, P.; Lemiti, M. Characterization of Al<sub>2</sub>O<sub>3</sub> Thin Films Prepared by Thermal ALD. *Energy Procedia* **2015**, 77, 558–564.

(41) Zhang, L.; Jiang, H. C.; Liu, C.; Dong, J. W.; Chow, P. Annealing of Al<sub>2</sub>O<sub>3</sub> Thin Films Prepared by Atomic Layer Deposition. *J. Phys. D: Appl. Phys.* **2007**, 40 (12), 3707–3713.

(42) Jiang, N. Electron Beam Damage in Oxides: A Review. *Rep. Prog. Phys.* **2016**, 79 (1), No. 016501.

(43) Nakamura, R.; Ishimaru, M.; Yasuda, H.; Nakajima, H. Atomic Rearrangements in Amorphous Al<sub>2</sub>O<sub>3</sub> under Electron-beam Irradiation. *J. Appl. Phys.* **2013**, 113 (6), No. 064312.

(44) Schneider, C.; Schichtel, P.; Mogwitz, B.; Rohnke, M.; Janek, J. Chemical Diffusion of Copper in Lead Telluride. *Solid State Ionics* **2017**, 303, 119–125.

(45) Yersak, A. S.; Lee, Y.-C. Probabilistic Distributions of Pinhole Defects in Atomic Layer Deposited Films on Polymeric Substrates. *J. Vac. Sci. Technol., A* **2016**, 34 (1), No. 01A149.

(46) Neizvestny, I. G.; Shwartz, N. L.; Yanovitskaja, Z. S.; Zverev, A. V. Simulation of Surface Relief Effect on ALD Process. *Comput. Mater. Sci.* **2006**, 36 (1–2), 36–41.

(47) Istratov, A. A.; Weber, E. R. Physics of Copper in Silicon. *J. Electrochem. Soc.* **2002**, 149 (1), G21.

(48) Shen, J.; Giergiel, J.; Schmid, A.K.; Kirschner, J. Surface Alloying and Pinhole Formation in Ultra-thin Fe/Cu(100) Films. *Surf. Sci.* **1995**, 328, 32–46.

(49) Chang, M. L.; Wang, L. C.; Lin, H. C.; Chen, M. J.; Lin, K. M. Investigation of Defects in Ultra-Thin Al<sub>2</sub>O<sub>3</sub> Films Deposited on Pure Copper by the Atomic Layer Deposition Technique. *Appl. Surf. Sci.* **2015**, 359, 533–542.

(50) Pfeiffer, K.; Shestaeva, S.; Bingel, A.; Munzert, P.; Ghazaryan, L.; van Helvoirt, C.; Kessels, W. M. M.; Sanli, U. T.; Grévent, C.; Schütz, G.; Putkonen, M.; Buchanan, I.; Jensen, L.; Ristau, D.; Tünnermann, A.; Szeghalmi, A. Comparative Study of ALD SiO<sub>2</sub> Thin Films for Optical Applications. *Opt. Mater. Express* **2016**, 6 (2), 660.

(51) Mirhashemihaghighi, S.; Światowska, J.; Maurice, V.; Seyeux, A.; Klein, L. H.; Salmi, E.; Ritala, M.; Marcus, P. Interfacial Native Oxide Effects on the Corrosion Protection of Copper Coated with ALD Alumina. *Electrochim. Acta* **2016**, 193, 7–15.

## ■ NOTE ADDED AFTER ASAP PUBLICATION

This paper was published ASAP on July 7, 2020, with an error to an author's surname. The corrected version was reposted on July 8, 2020.



## 6. Bayesian Machine Learning for Efficient Minimization of Defects in ALD Passivation Layers

(Reprinted with the permission of the American Chemical Society)

Gül Dogan, Sinan O. Demir, Rico Gutzler, Herbert Gruhn, Cem B. Dayan, Umut T. Sanli, Christian Silber, Utku Culha, Metin Sitti, Gisela Schütz, Corinne Grévent, and Kahraman Keskinbora

### Abstract

Atomic layer deposition (ALD) is an enabling technology for encapsulating sensitive materials owing to its high-quality, conformal coating capability. Finding the optimum deposition parameters is vital to achieving defect-free layers; however, the high dimensionality of the parameter space makes a systematic study on the improvement of the protective properties of ALD films challenging. Machine-learning (ML) methods are gaining credibility in materials science applications by efficiently addressing these challenges and outperforming conventional techniques. Accordingly, this study reports the ML-based minimization of defects in an ALD- $\text{Al}_2\text{O}_3$  passivation layer for the corrosion protection of metallic copper using Bayesian optimization (BO). In all experiments, BO consistently minimizes the layer defect density by finding the optimum deposition parameters in less than three trials. Electrochemical tests show that the optimized layers have virtually zero film porosity and achieve five orders of magnitude reduction in corrosion current as compared to control samples. Optimized parameters of surface pretreatment using Ar/ $\text{H}_2$  plasma, the deposition temperature above 200 °C, and 60 ms pulse time quadruple the corrosion resistance. The significant optimization of ALD layers presented in this study demonstrates the effectiveness of BO and its potential outreach to a broader audience, focusing on different materials and processes in materials science applications.



# Bayesian Machine Learning for Efficient Minimization of Defects in ALD Passivation Layers

Gül Dogan,\* Sinan O. Demir, Rico Gutzler, Herbert Gruhn, Cem B. Dayan, Umut T. Sanli, Christian Silber, Utku Culha,\* Metin Sitti, Gisela Schütz, Corinne Grévent, and Kahraman Keskinbora\*



Cite This: *ACS Appl. Mater. Interfaces* 2021, 13, 54503–54515



Read Online

ACCESS |



Metrics & More



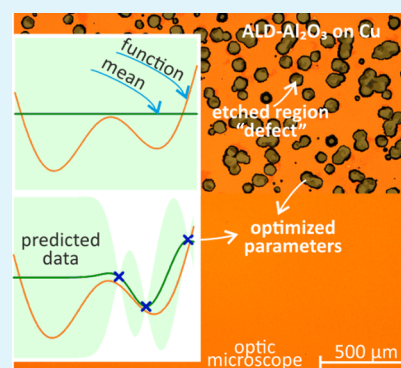
Article Recommendations



Supporting Information

**ABSTRACT:** Atomic layer deposition (ALD) is an enabling technology for encapsulating sensitive materials owing to its high-quality, conformal coating capability. Finding the optimum deposition parameters is vital to achieving defect-free layers; however, the high dimensionality of the parameter space makes a systematic study on the improvement of the protective properties of ALD films challenging. Machine-learning (ML) methods are gaining credibility in materials science applications by efficiently addressing these challenges and outperforming conventional techniques. Accordingly, this study reports the ML-based minimization of defects in an ALD- $\text{Al}_2\text{O}_3$  passivation layer for the corrosion protection of metallic copper using Bayesian optimization (BO). In all experiments, BO consistently minimizes the layer defect density by finding the optimum deposition parameters in less than three trials. Electrochemical tests show that the optimized layers have virtually zero film porosity and achieve five orders of magnitude reduction in corrosion current as compared to control samples. Optimized parameters of surface pretreatment using  $\text{Ar}/\text{H}_2$  plasma, the deposition temperature above  $200\text{ }^\circ\text{C}$ , and 60 ms pulse time quadruple the corrosion resistance. The significant optimization of ALD layers presented in this study demonstrates the effectiveness of BO and its potential outreach to a broader audience, focusing on different materials and processes in materials science applications.

**KEYWORDS:** atomic layer deposition, copper, defect density, wet etching, Bayesian optimization



## INTRODUCTION

The utilization of machine-learning (ML)-based approaches has recently gained significant momentum in addressing the challenging problems in materials science and engineering.<sup>1</sup> Their computational power is now outperforming the conventional optimization and simulation tools and allowing the improvement of complex processes in materials science.<sup>2</sup> From these processes, the discovery of novel materials and the prediction of material properties have been the most active fields of research.<sup>3,4</sup> In these application areas, ML methods efficiently employ the existing data to test new parameters that may yield novel material designs and properties. However, materials science applications can further take advantage of ML methods. In addition to the exploration of new materials, complex material fabrication processes (e.g., thin-film deposition) that depend on a careful selection of fabrication parameters can benefit from the ML methods, which can generate optimum results in a time- and cost-effective fashion. Here, such an ML-based optimization approach was applied to a technologically very relevant problem: the encapsulation of copper against chemical attacks from a harsh environment.

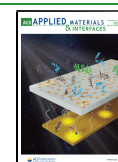
The surface passivation of copper is often used in corrosion protection in various applications such as microelectronics, photovoltaics, heat exchangers, gate electrodes, and inter-

connects.<sup>5–9</sup> The deposition of thin films is one of the most preferred methods for applying protective coatings.<sup>10–12</sup> The main challenge for depositing thin films for corrosion protection is eliminating the defects, such as pinholes and structural defects that allow the transport of reactive species in films.<sup>13–16</sup> Among all the available deposition techniques, atomic layer deposition (ALD) stands out owing to its high-quality thin films with excellent uniformity and conformity. ALD is also often cited for having lower defect densities.<sup>17–21</sup> However, the defect density on which the corrosion-protection performance depends has to be strictly controlled and minimized for wide-scale applications.<sup>22</sup> Microparticles, heterogeneities on the substrate, or the presence of an interfacial oxide layer between the substrate and the passivation layer serve as nucleation sites for defects.<sup>23–25</sup> Also, an inaccurate tuning of ALD process parameters may lead to defects due to undesired surface reactions.<sup>26,27</sup> Thus,

**Received:** August 1, 2021

**Accepted:** October 7, 2021

**Published:** November 4, 2021



both intrinsic and extrinsic defects can trigger and accelerate the corrosion process locally.<sup>23,27–29</sup>

The performance of ALD thin films for corrosion protection based on the defect density has been addressed by multiple research groups.<sup>8,10,13–16,22–28,30–45</sup> Among these, the most extensive research is performed on  $\text{Al}_2\text{O}_3$  layers, thanks to their excellent adhesion to many metal surfaces.<sup>38,46</sup> Zhang et al. showed that the defect density of ALD- $\text{Al}_2\text{O}_3$  layers on copper determined by copper electroplating was reduced by orders of magnitude (from  $\sim 1.2 \times 10^5 \text{ cm}^{-2}$  to  $\sim 90 \text{ cm}^{-2}$ ) with appropriate substrate surface treatment for efficient nucleation of ALD- $\text{Al}_2\text{O}_3$ .<sup>15</sup> Vanhaberbeke et al. studied the porosity of 20 nm thick ALD- $\text{Al}_2\text{O}_3$  layers on copper. They reported the number of pinholes as  $50 \text{ cm}^{-2}$  to  $100 \text{ cm}^{-2}$  by copper electroplating and the porosity as  $8.04 \times 10^{-2}\%$  to  $3.23 \times 10^{-3}\%$  by linear sweep voltammetry (LSV).<sup>34</sup> In our previous study performed on copper substrates, we also investigated the corrosion protection of  $\text{Al}_2\text{O}_3/\text{TiO}_2$  and  $\text{Al}_2\text{O}_3/\text{SiO}_2$  bilayers at elevated temperatures.<sup>47</sup> Even though the ALD layers showed excellent corrosion protection at elevated temperatures, the detailed spectromicroscopic study revealed copper on the surface of the ALD layer. The transport of copper was attributed to the defect structure of the layers, which created the pathway through the film. Some other studies investigated the ALD process parameter effect on the defect density.<sup>28,32,33</sup> Chang et al. reported that the intrinsic defects nucleate on residual OH ligands originating from the incomplete reactions in the first ALD cycles because of the substrate surface properties.<sup>13</sup> Even though several studies in the literature have focused on the defect structure of ALD- $\text{Al}_2\text{O}_3$  and substrate surface properties,<sup>15,22,27</sup> systematic optimization involving substrate surface properties and ALD process parameters has not been reported. These studies reveal that the correct identification and the tuning of principal parameters are essential in improving the design of experiments and achieving the best corrosion protection with ALD thin films. However, these parameters exist in a continuous and high-dimensional search space, which may require an impractical number of experiments to identify and optimize using manual tuning or exhaustive search methods. In addition, ALD is a relatively slow deposition method, which further complicates manual optimization approaches. That is why alternative methods would be desirable for achieving higher efficiency in terms of experimentation.

Various methods can be applied to multiparameter optimization problems, such as ALD thin film fabrication. Optimization methods based on mathematical models are proposed to reduce the number of experiments while identifying the principal parameters that define a process.<sup>48–50</sup> One of the most widely used methods is the statistical design of experiment (DOE), aiming at obtaining the most extensive possible information about the produced results with the smallest possible number of experiments.<sup>48,49</sup> The two-level fractional factorial design (FFD) is used to screen the designs to identify the primary factors that control a process.<sup>49,51</sup> For the linear regression model, higher than first-order equations are used to identify both individual effects and the interaction effect of input parameters on the results.<sup>48,51,52</sup> The response surface methodology or the Taguchi method is used to build a model for the relation between input parameters and output results.<sup>48,53–56</sup> This established model can be used for optimization purposes.<sup>48,55,56</sup> However, it could be necessary to extend the parameter space repeatedly to build an

acceptable model and perform optimization if the mathematical model is not verified by the defined DOE design.<sup>50,57</sup>

Therefore, DOE methods do not explain the relationship between input parameters and output results in all application scenarios. In some cases, they might require more trials to discover proper parameter space to make them applicable and explain relations between input parameters and output results.

There are emerging examples of applying ML methods to optimizing selected parameters using a small number of experiments.<sup>50,58–62</sup> Among these, the Bayesian optimization (BO) method can employ a probabilistic model (i.e., typically Gaussian processes (GPs)<sup>63</sup>) to represent an unknown function. It sequentially updates this representation by suggesting and testing new data points in that function's parameter space.<sup>64,65</sup> BO can be configured to explore the unknown regions in the parameter space of this target function or focus on a specific region of interest in the case of optimization tasks. Therefore, BO has significant advantages compared to optimization methods that require predefined models of the target processes. The ability to operate by testing a small set of data points and using a probabilistic model that can approximate unknown inherent variances in a physical process render BO an attractive method for optimization problems in materials science.<sup>50,66–70</sup> For example, Yuan et al. studied the optimization of Pb-free  $\text{BaTiO}_3$ -based piezoelectric with large electrostrain.<sup>71</sup> It has also been applied for the optimization of metal oxide' grain boundary structures for efficient identification,<sup>72</sup> optimization of high-quality nanofibers,<sup>73</sup> optimizations of both the alloy composition and associated heat treatment process for the performance of Al-7xxx series alloys,<sup>74</sup> optimization of low-hysteresis Ni-Ti-based shape memory alloys  $\text{BaTiO}_3$ -based piezoelectric with large electrostrains,<sup>57</sup> and optimization of nanostructures for optimal phonon transport.<sup>75</sup> Although BO is increasingly used in various fields related to materials science, its applications to the optimization of ALD film properties have not been reported.

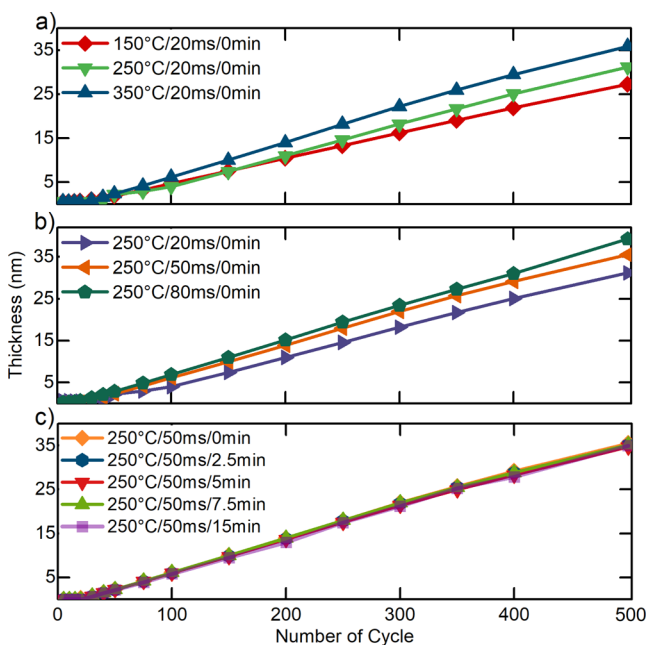
In this study, we used the ALD process to deposit  $\text{Al}_2\text{O}_3$  thin films for copper corrosion protection. We proposed a hybrid approach to improve the experimental design process by identifying the principal parameters and optimizing these specified parameters to minimize the ALD films' defect density for maximum corrosion-protection performance. In our hybrid approach, we first employed a two-level FFD method to rapidly identify the main parameters that affect the defect density. Then, we utilized BO to find the optimum values for the selected process parameters, which is reported for the first time for rapid and adaptive optimization of the defect density of ALD- $\text{Al}_2\text{O}_3$  films. We studied the properties of the fabricated thin films using wet-chemical etching, X-ray photoelectron spectroscopy (XPS), scanning electron microscopy (SEM), focused ion beam (FIB), and LSV methods. The experimental results showed that the optimization of the identified parameters substantially improved our films' protective properties against corrosion under harsh conditions. We believe that this hybrid approach will have wide-ranging implications for optimization work in materials science.

## RESULTS AND DISCUSSION

**ALD Film Growth.** The  $\text{Al}_2\text{O}_3$  films were deposited for 500 cycles using different process conditions defined in the following section. The film thickness and growth properties were monitored by in situ spectroscopic ellipsometry (SE) measurements. Independent from the process parameters, all



Al<sub>2</sub>O<sub>3</sub> films showed a substrate-inhibited growth mode during the first ALD reaction cycles. ALD depositions showed a linear increase in thickness with the number of cycles. The final thicknesses at 500 cycles were measured between 27 and 40 nm because the growth per cycle (GPC) was changed according to the process parameters. Figure 1a–c shows the



**Figure 1.** Thickness of the Al<sub>2</sub>O<sub>3</sub> thin films as a function of the number of ALD cycles for different (a) deposition temperatures, (b) pulse times, and (c) Ar/H<sub>2</sub> plasma pretreatment. One parameter was varied, while the other two were chosen to be constant for each subfigure.

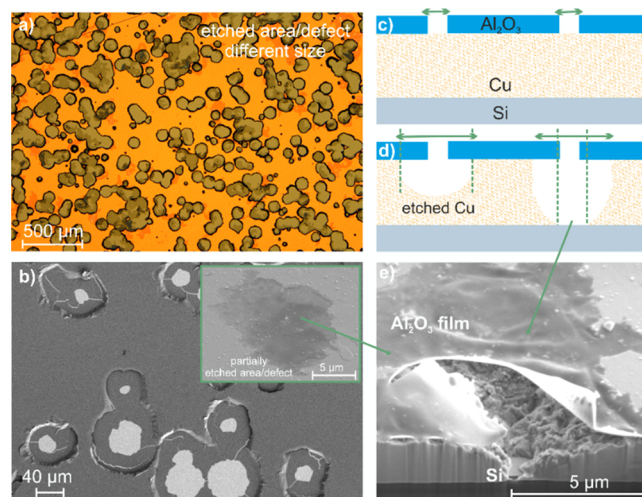
growth behavior of Al<sub>2</sub>O<sub>3</sub> thin films for different values of the deposition temperature, pulse time, and Ar/H<sub>2</sub> plasma pretreatment conditions, respectively. One of the parameters was varied in each part (Figure 1), while the other two were kept constant. The GPC increased with increasing temperature and pulse time, with a maximum of 0.08 nm/cycle. As indicated in Figure 1c, the GPC remained the same with different Ar/H<sub>2</sub> plasma pretreatment durations.

According to the GI-XRD analysis, Al<sub>2</sub>O<sub>3</sub> films were amorphous at all deposition temperatures, as shown in Figure S1, Supporting Information. From the XPS survey spectra, the stoichiometry ([Al]:[O]) ratio was found to be 0.6, which indicates the Al<sub>2</sub>O<sub>3</sub> composition (Figure S2, Supporting Information). The surface properties of Al<sub>2</sub>O<sub>3</sub> films according to SEM and optical microscopy are given in Figure S3, Supporting Information.

**Copper Wet Etching.** The ALD-Al<sub>2</sub>O<sub>3</sub>-protected copper samples were etched in a nitric acid (40 vol %) solution at room temperature for a duration between 1 and 30 min (Figure S4, Supporting Information). The etching process, which was monitored by optical microscopy, started with small punctiform dots that indicate defects. The number of dots and the dimensions of etched areas were related to the etching duration. An increase in the etching duration also increased the etched area and overlapped the etched areas. It was assumed that longer exposure to acid allowed all kinds of defects such as line defects, sealed line defects, vacancies, and pinholes to be revealed.<sup>34</sup> Therefore, considering our applications and

optimization process, the study here focused on longer acid exposure durations, namely, 30 min, to reveal all defect types. At these long etching durations, the individual etched regions starting off of a single defect started to coalesce. Therefore, counting individual pinholes for longer etching processes was not practical. In this study, we defined the total etched area percentage of copper as an indicator of the initial defect density and the quality of deposition in terms of corrosion protection.

**Reference Al<sub>2</sub>O<sub>3</sub> Sample.** The reference Al<sub>2</sub>O<sub>3</sub> films, before the optimization described in this work, were deposited at 150 °C with 20 ms pulse time and 1980 ms purge time for both precursors TMA and H<sub>2</sub>O without any plasma pretreatment.<sup>35,36,76</sup> ALD deposition using these standard process parameters was referred to as “reference samples” in the following. These samples were exposed to the nitric acid (40 vol %) etching solution for 30 min. After the acid/water solution reached the copper surface through the defects, the etching reaction took place and generated gaseous and soluble byproducts.<sup>77</sup> According to Zang et al., the etchant removed copper at the same rate in all directions during the etching process and produced a hemispherical trench.<sup>78</sup> After 30 min of etching in nitric acid (40 vol %) solution, the typical etched pattern was obtained, which is shown in Figure 2. While Figure



**Figure 2.** Etching (30 min) of Al<sub>2</sub>O<sub>3</sub>-protected Cu. (a) Optical microscope images from the middle of the area (according to three different samples and five different regions on each sample, 45% of the total area was etched). (b) SEM images from the larger vias. (c) and (d) Proposed sketch for major steps for wet etching, in which the etchant reached the copper surface through the defect, and copper was dissolved below the ALD film. (e) Cross-section images of the presented area that focuses on smaller vias. The standard deposition parameters were used for the reference Al<sub>2</sub>O<sub>3</sub> film.

2a,b shows the optical microscope and SEM images, Figure 2c,d shows the proposed sketch of major steps for the wet etching process. The cross-section of a single etch pit is given in Figure 2e, which is in good agreement with the proposed sketch of the trench formation originating from a point-like defect in the ALD layer such as pinholes and progressing until copper is completely removed.<sup>34</sup> The remaining free-standing film was usually torn in the course of stress relaxation.

The reference sample deposition and wet etching process were repeated three times to determine the batch-to-batch deviation. Additionally, three samples were deposited for each

Table 1. Process Variables Based on the Two-Level FFD with the Final Film Thickness, GPC, and Etched Area Percentages<sup>a</sup>

	pretreatment		ALD process parameters				thickness (nm)	GPC (nm/cycle)	etched area (%)
	Ar-H <sub>2</sub> plasma (min)	O <sub>2</sub> plasma (min)	temperature (°C)	pressure (Pa)	pulse time (ms)	ALA (ms)			
run 0	0	0	150	6	20	0	27.3	0.05	45.00%
run 1	15	5	350	20	80	40	51.2	0.103	47.00%
run 2	0	5	350	6	80	0	44.2	0.075	13.63%
run 3	15	0	350	20	20	0	48.4	0.092	0.03%
run 4	0	0	150	20	80	0	46.1	0.095	1.03%
run 5	0	0	350	6	20	40	54.2	0.103	0.08%
run 6	0	5	150	20	20	40	56.1	0.106	1.77%
run 7	15	0	150	6	80	40	56.7	0.107	0.29%
run 8	15	5	150	6	20	0	26.7	0.048	30.70%
effect	15.80	23.32	7.13	1.32	7.42	1.30			
SS	499.41	1087.8	101.55	3.46	110.24	3.40			
contribution	21.65%	47.17%	4.40%	0.15%	4.78%	0.15%			

<sup>a</sup>The etched area percentage was defined as the response of the system. The contribution to the response (etched area) was calculated and given for each parameter

batch to evaluate sample-to-sample deviation (Figure S5, Supporting Information). While the average etched area from three samples was found to be  $39.35 \pm 10.51\%$  for batch 1, they were  $17.54 \pm 2.02$  and  $77.92 \pm 13.62\%$  for batch 2 and 3, respectively. The overall mean etched area for three batches was then  $44.94 \pm 27.32\%$ , calculated by averaging the values with error propagation analysis. The substantial deviation of the etched area percentage and the lack of reproducibility from sample to sample and from batch to batch were attributed to an unoptimized process that leads to an undesired behavior. The significant differences between the samples were a sign that the defects were randomly affected by all steps and not controllable in the complex system as the deposition parameters were not optimized.

**Applications of the FFD.** A total of six parameters: O<sub>2</sub> plasma pretreatment, Ar/H<sub>2</sub> plasma pretreatment, process temperature, pulse time, atomic layer annealing (ALA), and pressure were screened to identify the key parameters that have a main effect on the defect density for maximum corrosion-protection performance. While Ar/H<sub>2</sub> plasma and O<sub>2</sub> plasma pretreatments were applied before the ALD deposition, pulse time, ALA, and pressure were changed during deposition. According to Shih et al., the ALA treatment was defined layer-by-layer as in situ plasma treatment between each ALD cycle.<sup>79</sup>

With a two-level FFD, eight experimental runs were performed (see Methods).<sup>49,80,81</sup> The high and low levels (two-level) for each parameter were determined in reference to the original deposition parameters (reference sample), which was called "Run 0." According to the experimental design, O<sub>2</sub> plasma was applied for 0 and 5 min, and the Ar/H<sub>2</sub> plasma was for 0 and 15 min. The temperature was set to 150 and 350 °C, and pulse time for 20 and 80 ms. The ALA was defined to 0 and 40 ms, and pressure to 6 and 20 Pa. The etched area percentage was used as the output response. The experimental matrix, which was defined by two-level FFD, corresponding responses, and the main contribution effect of parameters are given in Table 1. The response of each experimental run was calculated for three samples and used as the mean etched area percentage after 30 min wet etching. For each parameter, the contribution (Table 1) was calculated as the ratio of its sum of the square over the total sum of squares.<sup>51,82</sup> The main effect plot is given in Figure S6, Supporting Information. The optical

microscopy images of the Al<sub>2</sub>O<sub>3</sub> films after wet etching are presented in Figure S7, Supporting Information.

According to Table 1, the O<sub>2</sub> plasma had the highest contribution, calculated as 47.17%, followed by the Ar/H<sub>2</sub> plasma with 21.65%. The deposition temperature and pulse time contributions were found to be relatively high and had approximately the same magnitude of effect on the etched area with 4.40 and 4.78%, respectively. The effects of the ALA and pressure were observed to be even lower with only 0.15% contribution.

Based on the two-level FFD results, the parameters of the ALA and pressure were not considered for the following optimization step because of their low influence on the corrosion-protection performance. According to Shih et al., the ALA process was applied to enhance adatom migration and remove the ligands by energy transformation from Ar plasma.<sup>79</sup> However, the ALA process showed no improvement in the protection performance of Al<sub>2</sub>O<sub>3</sub> films based on two-level FFD analysis. On the other hand, even though the O<sub>2</sub> plasma pretreatment had the highest contribution based on the FFD results, the etched area percentage dramatically increased when the O<sub>2</sub> plasma-pretreated samples were immersed in the acid solution for 30 min. This negative impact of the O<sub>2</sub> plasma pretreatment was attributed to the formation of a Cu<sub>2</sub>O film on copper (The thickness of the Cu<sub>2</sub>O film was measured up to 300 nm by in situ SE, and surface properties were analyzed by XPS, as shown in Figure S8, Supporting Information). In conclusion, the O<sub>2</sub> plasma pretreatment was entirely omitted from the optimization step because of its adverse effect on the protection properties of the deposited Al<sub>2</sub>O<sub>3</sub> film.

The remaining parameters, Ar/H<sub>2</sub> plasma pretreatment, temperature, and pulse time, were selected as the influencing parameters on ALD deposition quality. Hence, the two-level FFD analysis allowed us to reduce the number of parameters from 6 to 3 to be considered for the BO step.

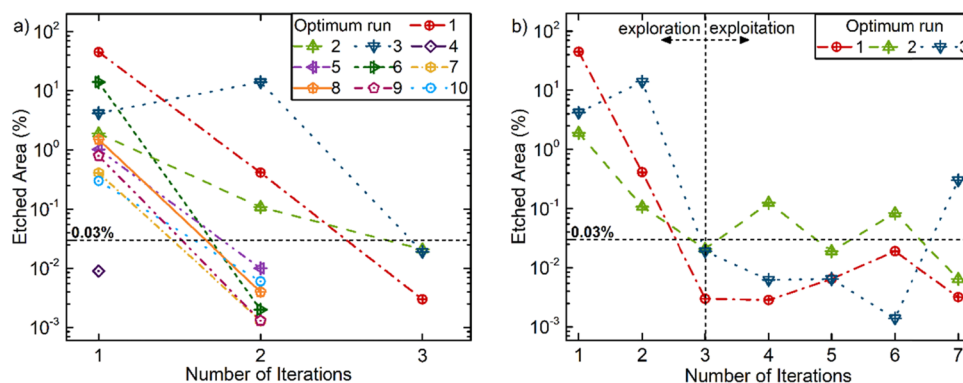
**Applications of the BO Design.** To minimize the etched area percentage, the Al<sub>2</sub>O<sub>3</sub> films were deposited iteratively using the process parameter values suggested using the BO method (see Methods). Their values were varied until the etched area percentage reached the target value of 0.03%, which was selected based on the best-performing run (i.e., run 3 in Table 1) achieved during the FFD analysis. The duration of Ar/H<sub>2</sub> was defined between 0 and 15 min, the deposition



Table 2. Experimental Parameters and Results of 10 Parallel Optimization Run for Achieving the Defect Density Target<sup>a</sup>

Optimum Run	Pre-treatment	ALD process parameters		Thickness (nm)	GPC (nm/cycle)	Etched Area (%)	Selected Optical Microscopy Images	
	Ar-H <sub>2</sub> plasma (min)	Temperature (°C)	Pulse time (ms)					
Step 1.1	0	150	20	27.26	0.056	44.935		
Step 1.2	0	250	80	39.25	0.080	0.414		
Step 1.3	7.5	350	60	41.01	0.084	0.018		
<b>Step 1.4</b>	<b>5</b>	<b>250</b>	<b>40</b>	<b>34.96</b>	<b>0.073</b>	<b>0.003</b>		
Step 1.5	5	300	50	38.49	0.081	0.007		
Step 1.6	5	250	50	35.2	0.074	0.019		
Step 1.7	7.5	300	50	39.14	0.079	0.003		
Step 2.1	0	350	20	35.9	0.075	1.911		
Step 2.2	0	350	50	40.73	0.084	0.108		
Step 2.3	7.5	250	50	35.54	0.075	0.021		
Step 2.4	0	350	40	39.71	0.082	0.126		
Step 2.5	5	250	50	35.2	0.074	0.019		
Step 2.6	2.5	300	50	36.18	0.076	0.084		
<b>Step 2.7</b>	<b>5</b>	<b>300</b>	<b>50</b>	<b>38.49</b>	<b>0.081</b>	<b>0.007</b>		
Step 3.1	0	150	80	33.22	0.069	4.189		
Step 3.2	0	150	20	27.26	0.056	44.935		
Step 3.3	5	250	50	35.2	0.074	0.019		
Step 3.4	5	350	60	40.64	0.084	0.006		
Step 3.5	5	300	50	38.49	0.081	0.007		
<b>Step 3.6</b>	<b>5</b>	<b>300</b>	<b>60</b>	<b>39.88</b>	<b>0.082</b>	<b>0.001</b>		
Step 3.7	2.5	250	50	35.18	0.075	0.070		
Step 4.1	15	250	50	35.21	0.075	0.009		
Step 5.1	0	150	50	32.69	0.068	1.024		
Step 5.2	7.5	200	60	33.9	0.071	0.010		
Step 6.1	0	250	20	31.18	0.064	14.005		
Step 6.2	5	350	40	36.12	0.078	0.002		
Step 7.1	0	250	80	39.25	0.080	0.414		
Step 7.2	7.5	300	60	39.38	0.081	0.001		
Step 8.1	0	200	50	30.64	0.065	1.550		
Step 8.2	7.5	250	40	34.66	0.073	0.004		
Step 9.1	2.5	250	50	35.18	0.075	0.070		
Step 9.2	7.5	300	60	39.38	0.081	0.001		
Step 10.1	0	250	50	35.53	0.075	0.800		
Step 10.2	7.5	250	20	32.11	0.068	0.006		

<sup>a</sup>Each optimization step is labeled by the identifier of the optimization run and the corresponding iteration of the BO (e.g., Step 1.2). The table shows the experimental parameters at each step, the final ALD thickness of the Al<sub>2</sub>O<sub>3</sub> thin film, the growth rate GPC, and the etched area percentage. The selected optical microscope images are given for the best and worst observed etched area percentages. Step 1.1 shows the reference sample



**Figure 3.** BO process showing the minimization of the etched area percentage for each iteration. (a) 10 parallel optimization runs with exploration orientation until the etched area percentage reached the target value, 0.03%, pointing to a significant decrease in the defect density. (b) Following experiments with exploitation orientation with three parallel optimization runs to seek better performances for lower defect density in the system.

temperature,  $T$ , varied between  $T_{\min} = 150$  °C and  $T_{\max} = 350$  °C, and the pulse time  $t_{\text{pulse}}$  was limited to [20–80 ms]. The step sizes were set to 2.5 min and 50 °C for Ar/H<sub>2</sub> and  $T$ , respectively. The parameter set for  $t_{\text{pulse}}$  was defined as

{20,40,50,60,80} ms using a nonfixed step size. The range of values for the investigated parameters with the given step sizes yielded a total number of 125 distinct parameter sets in  $\Theta$  in our experiments.

The hyperparameters for the GP and BO were listed as the prior mean  $\mu(\theta)$ , noise in the collected data  $\sigma_n^2$ , signal variance  $\sigma_f^2$ , length scale  $l_c$  for each dimension of the parameter space  $R^d$ , and exploration-exploitation tradeoff constant  $\xi$ . Considering the etched area could have a value in the range of [0–100%],  $\mu(\theta)$  and  $\sigma_f$  were selected as 50% and 25%, respectively, to contain the actual defect density function inside the 95% confidence interval of the prior. The standard deviation of the noise in the collected data  $\sigma_n$  was set to 0.01%, selected based on the two-level FFD experimental results near the optimization goal. The length scales were set to one-fourth of the total range of each corresponding parameter.<sup>83</sup> Lastly,  $\xi$  was chosen as 0.9 to balance the exploration-exploitation tradeoff.

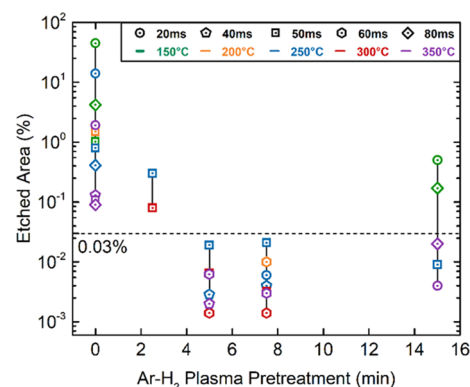
The optimization was started with 10 parallel runs of independently selected sets of parameters, seven of which were randomly chosen and the remaining with known-outcome conditions from previous experiments. In these optimization runs, the expected improvement (EI) was selected as the acquisition function. Each optimization run was stopped when the target threshold, 0.03%, was achieved in the etched area percentage. Table 2 summarizes the results of experiments for these 10 independent optimization runs. The table additionally lists the tested parameter sets, corresponding etched area percentages, and selected optical microscope images for low and high defect densities. Figure 3a shows the obtained etched area percentage values at each step of the optimization runs. All of the optimization runs reached the target threshold in the second or third iteration of the optimization process, which underlines the success of this optimization approach in minimizing the total number of experiments.

To continually search the optimal state through the iterative process and gain more information about the system, additional experiments have been performed on the first three optimization runs (i.e., shown as optimum run 1–3 in Figure 3a). To prioritize exploitation, the probability of improvement (PI) was chosen as the acquisition function in BO throughout these additional experiments. Within the subsequent four iterations of the first optimization run, the etched area percentage improved in the first iteration. However, the second and third optimization runs achieved the lowest defect densities in the following iterations. Figure 3b illustrates these three optimization runs, including the exploration-oriented steps (first three iterations) and exploitation-oriented follow-up steps (subsequent four iterations) of the BO.

The presented results demonstrate the applicability of BO for the optimization of the ALD thin film fabrication process with the given objective function. At least four orders of magnitude improved the etched area percentage of the optimized  $\text{Al}_2\text{O}_3$  layers compared to the reference state. The optimal parameters were found in less than three iteration steps out of the complete set of 125 parameter triplets. The reliability of the optimal parameters was evaluated by repeating the procedure shown in the optimal run 3.6. The  $\text{Al}_2\text{O}_3$  deposition was repeated three times under the same conditions for three samples for each deposition (Figure S9 Supporting Information). The mean etched area was found to be  $0.0027 \pm 0.0012$ ,  $0.0032 \pm 0.0003$ , and  $0.0037 \pm 0.0017\%$  for the three batches, respectively, and it was  $0.0014 \pm 0.0007\%$  for the optimal run 3.6. Compared to the reference  $\text{Al}_2\text{O}_3$  sample, the mean etched area percentage was decreased from  $45 \pm 27$  to  $0.003 \pm 0.001\%$  with the optimization of process parameters

(Table S1, Supporting Information). While some batch-to-batch differences were still observed, the overall etched area remained well below the target value of 0.03%, demonstrating the successful application of the BO approach.

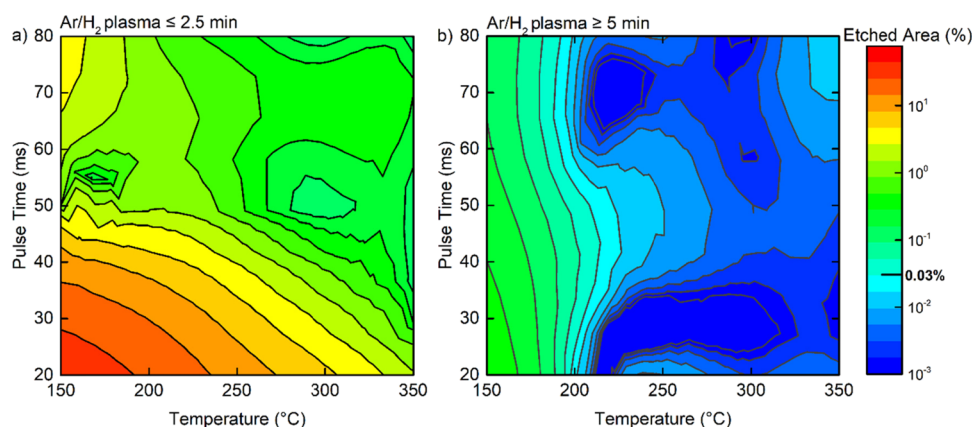
**Effect of the Ar/H<sub>2</sub> Plasma Pretreatment on the Defect Density.** The Ar/H<sub>2</sub> plasma pretreatment influence on the corrosion-protection properties of  $\text{Al}_2\text{O}_3$  was studied with a remote plasma configuration inside an ALD chamber. The pretreatment time was varied from 0 to 15 min with 2.5, 5, and 7.5 min interval steps. After the pretreatment, the ALD process was immediately started for 500 cycles of  $\text{Al}_2\text{O}_3$  deposition. The plasma pretreatment effect on the etched area percentage, given in Figure 4, is a projection of four-



**Figure 4.** Effect of the Ar/H<sub>2</sub> plasma pretreatment on the etched area percentage (defect density) of  $\text{Al}_2\text{O}_3$  thin films. The data were collected based on the plasma pretreatment time at different deposition temperatures and pulse time to highlight the main effect of the plasma pretreatment. The pulse time steps are represented by different symbols and the temperature by color codes. The 0.03% etched area was labeled as the optimization target of BO.

dimensional experimental data into a two-dimensional space. The experimental data are collected from the BO runs (Table 2) and from the data obtained by four additional experiments collected during parameter limit search (Table 2, Supporting Information).

The resulting etched area percentage was found to be between 45 and 0.09% without plasma pretreatment (0 min) and decreased to a minimum of 0.07% with the application of 2.5 min plasma pretreatment. However, both cases could not reach the optimization target value of 0.03%. The defect density was improved with increasing plasma pulse time from 2.5 min to 5 min and reached the target value for a range of different ALD process parameters. The lowest etched area percentage was found to be 0.001% with 5 min plasma pretreatment. For a longer duration of plasma pretreatment, similar etched area percentage values (below 0.03%) were obtained except for the two experiments deposited at 150 °C. Longer exposure to plasma species did not further improve the corrosion-protection performance of the  $\text{Al}_2\text{O}_3$  film. Therefore, the plasma pretreatment duration was found to be optimum at around 5 min of application. These results indicate that the plasma pretreatment had the most significant effect on defect density, which agrees with two-level FFD results. Despite the significant improvement of the defect density with the plasma pretreatment, the results of the 15 min pretreatment showed that it is still not enough to reach the defect density goal below the target value on its own.



**Figure 5.** Effect of temperature and pulse time on the defect density. The data were organized based on temperature and pulse time for (a) shorter ( $\leq 2.5$  min) and (b) longer ( $\geq 5$  min) plasma pretreatment after interpolation. The pulse times were indicated on the y-axis and temperature on the x-axis. The 0.03% etched area was labeled on the color scale as the optimization target of BO. The etched area percentages are shown on the same color scale.

The effect of the plasma pretreatment was attributed to the difference in interface between Cu and  $\text{Al}_2\text{O}_3$  film. At first, Cu samples were cleaned using acetic acid to remove the native oxide and residuals from the copper surface. The  $\text{Cu}_2\text{O}$  thickness after this cleaning process was measured to be 2.5 nm by in situ SE before the plasma pretreatment. This thin oxide layer was attributed to the formation of native oxide during a few minutes of the sample transfer and the installation into the ALD chamber, according to work by Chavez et al.<sup>84</sup> The  $\text{Al}_2\text{O}_3$  films would be deposited on this air-formed oxide layer if there was no plasma pretreatment application in the designed experiment. By applying the plasma pretreatment, the air-formed oxide layer is removed according to the in situ SE data (Figure S10, Supporting Information). However, according to Mirhashemihaghighi et al., the  $\text{Cu}_2\text{O}$  layer can regrow on copper because of water vapor exposure until full coverage of the surface by the  $\text{Al}_2\text{O}_3$  film.<sup>14,25</sup> Inside the ALD chamber, the well-controlled conditions lead to a homogeneously regrown  $\text{Cu}_2\text{O}$  layer. Therefore, the improvement of the corrosion-protection properties with the plasma pretreatment was attributed to the homogeneously grown, clean copper oxide layer rather than the air-formed native oxide, which was in good agreement with the study by Harkönen et al.<sup>32</sup> Moreover, homogeneously grown oxide layers lead to decreased channel defects and hence significantly improve the corrosion-protection properties, according to Mirhashemihaghighi et al.<sup>24</sup> While wet etching is often used to remove the native copper oxide layer before ALD deposition,<sup>25</sup> our results show that an in situ  $\text{Ar}/\text{H}_2$  pretreatment was additionally necessary to control the interface and significantly improve the quality of the corrosion protection of copper by ALD- $\text{Al}_2\text{O}_3$  films.

**Effect of ALD Process Parameters on the Defect Density.** The influence of the deposition temperature and pulse time on the corrosion-protection properties of  $\text{Al}_2\text{O}_3$  is discussed in two parts. While the first part focuses on the correlation between temperature and pulse time without the effect of plasma pretreatment ( $\leq 2.5$  min), the second part focuses on the combination of temperature and pulse time with plasma pretreatment ( $\geq 5$  min). They are illustrated in Figure 5a,b, respectively. The temperature was varied between 150 and 300  $^{\circ}\text{C}$ , and the pulse time, between 20 and 80 ms.

The lowest temperature (150  $^{\circ}\text{C}$ ) and the shortest pulse time (20 ms) result in 45% of the copper film being etched

during acid immersion. On the other hand, the highest temperature (350  $^{\circ}\text{C}$ ) and the longest pulse time (80 ms) resulted in the etching of 0.09% of the total copper area. Therefore, higher temperature and longer pulse time were found to be beneficial for reducing the defect density when the plasma pretreatment was less than or equal to 2.5 min (Figure 5a). When the plasma pretreatment was more than or equal to 5 min, the optimization target of 0.03% was achieved for all pulse times as long as the deposition temperature was above 200  $^{\circ}\text{C}$  (Figure 5b). Among the two parameters, the temperature was therefore identified to have a more significant influence than the pulse time on the corrosion-protection properties of  $\text{Al}_2\text{O}_3$  thin films.

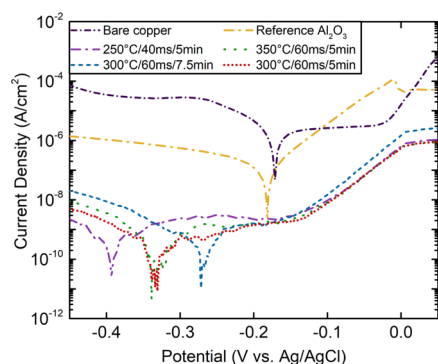
The effect of temperature on the defect density can be attributed to the type of reactive sites and the effect of temperature on the preferred reaction mechanism.<sup>85</sup> The reactive surface sites affect the amount and the type of chemisorbed species. A lower defect density with increased temperature may be related to the higher reactivity of the species. Furthermore, higher temperatures do likely provide sufficient thermal energy to drive new reactions that do not occur at lower temperatures.<sup>86</sup>

The optimized conditions determined by the BO indicate that copper samples should be treated with the  $\text{Ar}/\text{H}_2$  plasma for 5 min. While shorter plasma pretreatment was not enough, the longer pretreatment did not significantly improve the defect density and could even be detrimental. The deposition temperature should be above 200 or 250  $^{\circ}\text{C}$  for even better results. For  $\text{Ar}/\text{H}_2$  plasma above 5 min, the pulse time's impact on defect density was less significant overall. Even with the shortest pulse time (20 ms), the target value of 0.03% could be achieved. In general, a shorter pulse time is advantageous and desired as it reduces the deposition time, conserves precursors, and hence reduces the associated production costs. The layer thickness was not significantly crucial for the defect density, as shown in Figure 1 and Table 2. While the thickest layers (40 nm) were obtained at 350  $^{\circ}\text{C}$ , the optimized defect density ( $<0.03\%$ ) was achieved even in 32 nm thick  $\text{Al}_2\text{O}_3$  layers with plasma pretreatment at 250  $^{\circ}\text{C}$ . Figure S11, Supporting Information, represents the relation between the deposited thickness and etched area percentages.

**Electrochemical Corrosion-Protection Properties of Optimized Layers.** Finally, we studied the electrochemical



response of the optimized layers using LSV. The polarization curves for bare copper, the reference  $\text{Al}_2\text{O}_3$  layer, and selected optimized- $\text{Al}_2\text{O}_3$  layers are shown in Figure 6. The polarization



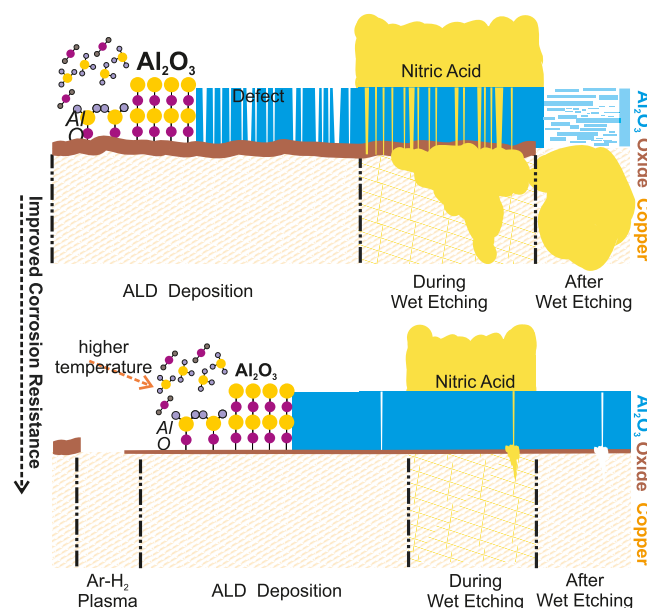
**Figure 6.** Polarization curves of bare copper, reference  $\text{Al}_2\text{O}_3$  film, and selected optimized  $\text{Al}_2\text{O}_3$  films.

curves, analyzed using the Tafel fit, were used to calculate the corrosion current, polarization resistance, and electrochemical porosity.<sup>25,87,88</sup> The calculated values are given in Table 3. The corrosion potential of bare copper shifts toward negative values with  $\text{Al}_2\text{O}_3$  deposition, indicating improved corrosion resistance. The corrosion current density was found to be  $1.5 \times 10^{-5} \text{ A cm}^{-2}$  for bare Cu and dropped to  $9.9 \times 10^{-7} \text{ A cm}^{-2}$  with the presence of reference  $\text{Al}_2\text{O}_3$  films. While the presence of reference ALD- $\text{Al}_2\text{O}_3$  film leads to a general decrease in the current density, the selected optimized  $\text{Al}_2\text{O}_3$  films show a marked reduction in the corrosion current density with approximately five orders of magnitude compared to bare Cu. Even though different process parameters were used for the deposition of the optimized  $\text{Al}_2\text{O}_3$  films, similarly reduced corrosion current densities were obtained between  $3.2 \times 10^{-10}$  and  $9.0 \times 10^{-11} \text{ A cm}^{-2}$ , which indicates the successful optimization process by BO.

The electrochemical porosity for reference  $\text{Al}_2\text{O}_3$  films was found to be 6.58%, according to the calculations defined in the Methods Section. With the optimization of the process parameters, the electrochemical porosity dropped from 6.58% to the values of 0.02 and 0.0007%. Even though the etched area percentages (from wet etching analysis) and porosity (from LSV analysis) showed similar values, the mechanism behind the two measurement techniques was different. The etched areas were formed when the etching solution was in direct contact with the copper surface. In the LSV method, the porosity was defined based on the measured current with contribution from charge transport, Poole-Frenkel effects, and trap-assisted tunneling phenomena.<sup>34</sup> Therefore,

the direct comparison of the results is not possible. However, a positive correlation between the two can be expected.

The improved corrosion-protection properties of optimized ALD- $\text{Al}_2\text{O}_3$  films were exhibited using wet etching and LSV techniques. Moreover, the following sketch (Figure 7)



**Figure 7.** Schematic representation of the corrosion-protection performance of ALD thin films before and after optimization. While the top side of the figure describes the process without optimization, the bottom side describes the improvement. With the optimization process, the applications of plasma cleaning (before ALD deposition) and increased temperature were found to be the most important parameters to achieve higher resistance against corrosion.

illustrates how corrosion-protection performance was improved by process optimization. According to Table 3, similar corrosion current densities and electrochemical porosities were further obtained for process parameters, which indicates once more the necessities of process optimization. In the literature, different corrosion current densities were reported.<sup>31,89,90</sup> For example, corrosion current densities of  $8.3 \times 10^{-7} \text{ A cm}^{-2}$  and  $3 \times 10^{-8} \text{ A cm}^{-2}$  were found for 29 nm thick  $\text{Al}_2\text{O}_3$  films on copper by Daubert et al. and Chai et al., respectively.<sup>36,38</sup> Indeed, Mirhashemighighi et al. reported a current density of  $8 \times 10^{-11} \text{ A cm}^{-2}$  for 50 nm thick  $\text{Al}_2\text{O}_3$  on electropolished and cleaned copper.<sup>8</sup> We report a current density as low as  $9 \times 10^{-11} \text{ A cm}^{-2}$  even for 32 nm thick  $\text{Al}_2\text{O}_3$  on copper in the present study.

**Table 3.** Corrosion Current ( $I_{\text{corr}}$ ), Polarization Resistance ( $R_p$ ), and Porosity<sup>a</sup>

	sample run	$I_{\text{corr}}$ ( $\text{A cm}^{-2}$ )	$R_p$ ( $\Omega$ )	porosity (%)
bare Cu		$1.50 \times 10^{-5}$		
reference $\text{Al}_2\text{O}_3$	Step 1.1	$9.87 \times 10^{-7}$	$1.2 \times 10^5$	6.58
250 °C/40 ms/5 min	Step 1.4	$3.02 \times 10^{-10}$	$3.0 \times 10^7$	0.02
300 °C/60 ms/5 min	Step 3.6	$9.00 \times 10^{-11}$	$8.2 \times 10^7$	0.0007
350 °C/60 ms/5 min	Step 3.4	$1.95 \times 10^{-10}$	$5.5 \times 10^7$	0.0013
300 °C/60 ms/7.5 min	Step 7.2	$2.42 \times 10^{-10}$	$4.5 \times 10^7$	0.0016

<sup>a</sup>The polarization curve was used to calculate the values.

## ■ CONCLUSIONS

The microscopic mechanisms of idealized ALD processes are fairly well understood. However, in practice, the deposition process deviates from this idealistic view. Actual samples deposited in real chambers often exhibit intrabatch and interbatch variability, which can be attributed, among other things, to local variations on sample surfaces or differences in chamber designs, respectively. Therefore, processes usually need to be optimized from scratch when significant changes are made, such as changing the substrate or the deposition chamber. Exhaustive searches to find global optimum can be prohibitively impractical and expensive. The remaining choices are either a theory-guided heuristic search, which can get stuck in a local optimum or a design-of-experiment approach such as the FFD or Taguchi method or some variations. Such methods still require tens of different experiments to generate a response surface.

In this work, we successfully deployed a hybrid BO algorithm to find the best process parameters for depositing  $\text{Al}_2\text{O}_3$  thin films toward reliable encapsulation of the copper metal. As a result, the defect density of the  $\text{Al}_2\text{O}_3$  film was significantly decreased, and the corrosion-protection properties of the layer were considerably improved.

The main process parameters that affect the defect density were identified using a two-level FFD method. Ar/ $\text{H}_2$  plasma pretreatment, temperature, and pulse time were selected from six process parameters according to their higher impact on the corrosion-protection performance. The two-level FFD analysis allowed us to reduce the number of parameters from six to three to be considered for the BO step.

BO was successfully applied for the first time to maximize the corrosion-protection performance of ALD- $\text{Al}_2\text{O}_3$  thin films. The BO was capable of finding optimal parameters in only a few iterations. The efficiency and efficacy of the BO were demonstrated by repeating the optimization 10 times independently and finding the target value of 0.03% etched area in less than three iterations. A repeatability analysis showed the mean etched area to be  $0.003 \pm 0.001\%$  for three batches. Compared to the reference  $\text{Al}_2\text{O}_3$  film, the etched area was decreased from  $45 \pm 27$  to  $0.003 \pm 0.001\%$  by optimizing process parameters. We demonstrated how BO could be efficiently applied to optimize the ALD processes and their parameters.

The Ar/ $\text{H}_2$  plasma pretreatment and temperature were found to impact the corrosion-protection performance significantly. The plasma pretreatment duration of 5 min was enough to increase the corrosion-protection performance of  $\text{Al}_2\text{O}_3$  films significantly. After 2.5 min long plasma pretreatment, a deposition temperature above  $200\text{ }^\circ\text{C}$  and a pulse time of more than 60 ms were required to reach the optimization target. Once the temperature was increased above  $250\text{ }^\circ\text{C}$  and the plasma pretreatment was applied for 5 min, the optimization goal was achieved independent of the pulse time.

Compared to a bare copper sample, the optimized layers showed improved corrosion protection by more than five orders of magnitude with a corrosion current density of  $9 \times 10^{-11}\text{ A cm}^{-2}$ , one of the lowest reported in the literature for ALD- $\text{Al}_2\text{O}_3$  films. The improvement of the current density demonstrated the importance of the optimization process for the corrosion-protection performance.

Here, we demonstrated that BO, an algorithm to find the global optimum for a given objective and cost function, can

efficiently reach the target optimization goal for an ALD process with a fair number of parameters in only a few steps. Therefore, this study aimed at finding an efficient optimization route for the desired function of being resistant to harsh environments. Knowing that we can easily transfer ALD processes in between different chambers and onto other substrates with this method, attention can be focused on the stack or device design. Furthermore, this approach will allow us to utilize the insights into this research to further studies where the material stack is more complex or multiple functions have to be fulfilled at the same time.

## ■ METHODS

Copper (Cu) samples (99.999% purity) were electrodeposited on p-type Si (100), with  $\sim 1.5\text{ }\mu\text{m}$  Cu thickness,  $\sim 3\text{ nm}$  native oxide, and  $\sim 6\text{ nm}$  surface roughness. Before ALD deposition, all samples were rinsed with acetic acid for 1 min to remove residuals and oxide layers from the Cu surface. The  $\text{Al}_2\text{O}_3$  films were deposited using an ALD system with a plasma source attachment (Sentech GmbH, Germany). For the deposition of  $\text{Al}_2\text{O}_3$ , trimethylaluminum (TMA) and ultrapure  $\text{H}_2\text{O}$  were used as precursors under constant nitrogen flow. The reference 30 nm thick  $\text{Al}_2\text{O}_3$  films (nonoptimized) were deposited with precursor pulse for 20 ms and purge of 1980 ms during 500 cycles at  $150\text{ }^\circ\text{C}$ . The growth properties and final thickness of  $\text{Al}_2\text{O}_3$  on copper were analyzed using in situ spectroscopic ellipsometry (SE, SENresearch 4.0., Sentech, Germany).

Ar/ $\text{H}_2$  plasma pretreatment,  $\text{O}_2$  plasma pretreatment, deposition temperature, pulse time, ALA, and pressure were selected as possible parameters that influence the defect density of ALD films. While Ar/ $\text{H}_2$  plasma and  $\text{O}_2$  plasma pretreatments were varied before the deposition starts, pulse time, ALA, and pressure were varied during ALD deposition. The plasma pretreatments were applied under 20 Pa, with 200 sccm gas flow and 200 W plasma power. Ar plasma was pulsed in between each ALD cycle for 40 ms with 200 sccm gas flow and 200 W plasma power for the ALA process. The purge time was extended to 5 s for all the processes to ensure the self-limiting ALD growth based on different pulse time parameters. All  $\text{Al}_2\text{O}_3$  layers were deposited for a constant 500 cycles as the GPC is dependent on the process parameters. The final thickness varied accordingly. The resulting thicknesses were reported in the results part. The two-level FFD design was applied to identify the main parameters for maximum corrosion-protection performance rapidly. The BO approach was then implemented to find the optimum values for the selected process parameters.

The Cu- $\text{Al}_2\text{O}_3$  samples were etched for 30 min in a nitric acid etching solution (40 vol %) at room temperature. While Cu was dissolved immediately in a nitric acid solution,  $\text{Al}_2\text{O}_3$  was found to be resistive.<sup>91</sup> The Cu- $\text{Al}_2\text{O}_3$  samples' etching started with small punctiform dots that increased in size and number over-etching time. Because of the difficulty of identifying individual defects, the defect density was assumed to correlate positively with the total etched area of copper. Therefore, for wet-chemical etching tests, the ratio of the etched area was utilized to the whole area, that is, the etched area percentage, as an indirect indicator of the defect density. The etched areas were analyzed by optical microscopy and Fiji-ImageJ software. Three samples were etched in fresh nitric acid solutions for each experiment. Five different regions were inspected from each sample.

A Gamry corrosion cell was used with a  $1\text{ cm}^2$  working electrode, platinum mesh counter electrode, and 0.1 M sodium chloride (NaCl) electrolyte to perform LSV. The cell was allowed to reach equilibrium at an open-circuit potential (OCP) before LSV measurements were taken. The LSV data were collected using an Autolab potentiostat (Ecochemie Inc., model PGSTST 302 N) at a rate of  $0.1\text{ mV s}^{-1}$  from  $-0.6$  to  $0.5\text{ V}$  versus an Ag/AgCl reference electrode. The corrosion potential, corrosion current, polarization resistance, and porosity were calculated from the polarization curves obtained using LSV and Tafel

analysis.<sup>87</sup> The electrochemical porosity ( $P$ ) was calculated according to the methodology developed by Tato et al. (eq 1).<sup>32,88</sup>

$$P = \frac{i_{\text{corr}}}{i_{\text{corr}}^0} \times 100\% \quad (1)$$

where  $i_{\text{corr}}^0$  and  $i_{\text{corr}}$  are the corrosion current densities of the uncoated and coated copper samples, respectively.

**Two-Level FFD.** In this study, a two-level FFD was used to select the main parameters (factors) from six factors potentially influencing the ALD deposition quality. The two-level FFD is helpful when used at the beginning of an experimental study to determine more influencing parameters with a few experiments.

A two-level FFD is defined by  $2^{k-p}$ , where  $k$  is the number of experimental parameters designated as factors, and  $p$  is the fraction of the factorial design (resolution III, 1/8).<sup>48,80</sup> To evaluate the main effects of six parameters on the etched area percentage, 1/8 fraction was used to decrease the number of experiments. Instead of a full-factorial design ( $2^6$ ), only eight experimental runs were performed in the design of two-level FFD with resolution III ( $2_{\text{III}}^{6-3}$ ).<sup>49,81</sup> Because of selecting a two-level design, the first-order polynomial equation was used for the linear regression model.

For the design of the experiment (DOE), each independent variable was set as the upper and lower limit, which corresponded to high and low levels in the two-level FFD. The experimental sequence was randomized to minimize systematic errors. The contribution of the parameters was analyzed using the Minitab R17 software.

**GP and BO.** This study aimed at minimizing the ALD film's defect density to improve the corrosion protection of the ALD-protected copper samples. Therefore, the BO was applied on the following cost function, which was defined as

$$J: \Theta \rightarrow \mathbb{R} \quad (2)$$

which mapped the parameter set to a scalar cost value, which was the etched area percentage (as a proxy for the defect density) in our case. Using this definition, the global optimization problem was defined and formulated as

$$\theta^* = \underset{\theta \in \Theta}{\text{argmin}} J(\theta), \quad (3)$$

where  $\Theta$  denotes the complete search space,  $\theta$  the process parameters, and  $J(\theta)$  the defect density for a given  $\theta$ .

Because of the nonlinear response of the ALD process to the parameter changes and the lack of an accurate analytic model of the system, the cost function shown in eq 3 was approximated using the data collected from physical experiments. However, the observed experimental results had inherent uncertainty because of the noise in the measurements and variations during the experiments. To include these uncertainties in the approximated model, to overcome the sparsity in the data, and to make probabilistic predictions for the unobserved design parameter sets, the cost function  $J(\theta)$  was modeled using GPs following a previous study:<sup>83</sup>

$$J(\theta) \sim \text{GP}(\mu(\theta), k(\theta, \theta')) \quad (4)$$

Here, the objective cost function  $J(\theta)$  can only be measured with noise, so the experimentally observed defect density  $\hat{J}(\theta)$  was defined as

$$\hat{J}(\theta) = J(\theta) + \mathcal{N}(0, \sigma_n^2), \quad (5)$$

where  $\mathcal{N}$  represents the inherited noise in the experimental measurement of the defect density with a Gaussian distribution with zero mean and variance  $\sigma_n^2$ .

As a nonparametric model, GP was defined by its prior mean  $\mu(\theta)$  and covariance function  $k(\theta, \theta')$  that represented the covariance between the data points in  $\theta$ , that is, parameter sets in our experiments. Here,  $k$  is the kernel function, which describes this covariance between the data points using the squared exponential method as follows:

$$k_{\text{SE}}(\theta, \theta') = \sigma_f^2 \exp(-(\theta - \theta')^2 / 2l_c^2) \quad (6)$$

where  $l_c$  is the length scale that defined the rate of variation in the modeled function for each dimension of the parameter space. In other words, the length scale defined the distance between the two data points where they could significantly influence each other. That is why short-length scales are used to model quickly varying functions, whereas long-length scales are used to model slowly varying functions.<sup>63</sup> The signal variance  $\sigma_f^2$  described the width of distribution, for example, high  $\sigma_f^2$  means higher uncertainty in the predictions of the unobserved  $\theta$ .

BO is a sequential optimization method that updates its model prediction with every step in a finite number of  $N$  experiments. Throughout a single step of BO, the posterior distribution of this GP model,  $J_{\text{post}}(\theta)$ , is updated based on the observed experimental data  $D = \{\theta_i, \hat{J}(\theta_i)\}_{i=1}^N$ , and then, the defect density for a new  $\theta$  is predicted using the posterior mean and variance as follows.

$$J_{\text{post}}(\theta) | D \sim N(\mu_{\text{post}}(\theta), \sigma_{\text{post}}^2(\theta)), \text{ where} \quad (7)$$

$$\mu_{\text{post}}(\theta) = \mu(\theta) + k^T(\theta)K^{-1}y \quad (8)$$

$$\sigma_{\text{post}}^2(\theta) = k(\theta, \theta) - k^T(\theta)K^{-1}k(\theta) \quad (9)$$

where  $k(\theta)$  and  $y \in \mathbb{R}^N$  are described as  $k(\theta) = k(\theta, \theta_{1:n})$  and  $y = \hat{J}(\theta_{1:n}) - \mu(\theta_{1:n})$  for  $\theta_{1:n} \in D$ , and  $K \in \mathbb{R}^{N \times N}$  is the covariance matrix for all observed data points with  $K_{i,j} = k(\theta_i, \theta_j) + \delta_{i,j}\sigma_n^2$  and  $i, j \in \{1, 2, \dots, N\}$ , respectively.  $\delta_{i,j}$  is the Kronecker delta and  $\sigma_n^2$  is the noise in the collected data set.

The BO was utilized throughout the physical experiments to select the following parameter set to be tested,  $\theta_{\text{next}}$  which maximized the acquisition function  $\alpha_{\text{acq}}(\theta)$ . In this study, two different acquisition functions were used: the PI<sup>92</sup> and EI.<sup>93</sup> The PI focuses on the probability of possible cost values below some threshold  $\xi J^*$ , where  $J^*$  is the lowest cost function value observed so far, and  $\xi$  is the constant controlling the balance between exploration and exploitation.<sup>92</sup> EI also considers the expected magnitude of such an improvement by considering the variance in the prediction.<sup>92,93</sup> Therefore, EI was used throughout the first stage of the optimization for exploration and exploitation purposes, and PI was used in the second stage for exploitation only.<sup>94</sup>

A single iteration of the BO with GP was run following the steps given below:

1. BO selected a new parameter set  $\theta$  maximizing the acquisition function based on the GP model prediction.
2. A physical experiment was conducted with the selected  $\theta$ , and defect density  $\hat{J}(\theta)$  was measured.
3. The GP model was updated with the newly collected data from the experiment for the next iterations of BO.

## ■ ASSOCIATED CONTENT

### SI Supporting Information

The Supporting Information is available free of charge at <https://pubs.acs.org/doi/10.1021/acsami.1c14586>.

ALD- $\text{Al}_2\text{O}_3$  film properties by GI-XRD, XPS survey scan and SEM/optical microscope images, reference state defect density based on the exposure time and its repeatability, two-level FFD analysis, Cu- $\text{Al}_2\text{O}_3$  interface differences by XPS for  $\text{O}_2$  plasma pretreatment, repeatability analysis of optimized  $\text{Al}_2\text{O}_3$  films, additional experimental details, in situ SE analysis for Ar/ $\text{H}_2$  plasma pretreatment, and etched area percentage according to thickness (PDF)

## ■ AUTHOR INFORMATION

### Corresponding Authors

Gül Dogan – Robert Bosch GmbH, Automotive Electronics, 72703 Reutlingen, Germany; Max Planck Institute for



Intelligent Systems, 70569 Stuttgart, Germany;  
Email: [guel.dogan@de.bosch.com](mailto:guel.dogan@de.bosch.com)

**Utku Culha** – Max Planck Institute for Intelligent Systems, 70569 Stuttgart, Germany; Present Address: Munich School of Robotics and Machine Intelligence, Technical University of Munich, 80797 Munich, Germany (U.C.); Email: [utku.culha@tum.de](mailto:utku.culha@tum.de)

**Kahraman Keskinbora** – Max Planck Institute for Intelligent Systems, 70569 Stuttgart, Germany; Present Address: Massachusetts Institute of Technology, 77 Mass Avenue, Cambridge, Massachusetts 02139, United States (K.K.); Email: [kahraman@mit.edu](mailto:kahraman@mit.edu)

## Authors

**Sinan O. Demir** – Max Planck Institute for Intelligent Systems, 70569 Stuttgart, Germany

**Rico Gutzler** – Max Planck Institute for Solid State Research, 70569 Stuttgart, Germany

**Herbert Gruhn** – Robert Bosch GmbH, Corporate Sector Research and Advance Engineering, 71272 Stuttgart, Germany

**Cem B. Dayan** – Max Planck Institute for Intelligent Systems, 70569 Stuttgart, Germany

**Umut T. Sanli** – Max Planck Institute for Intelligent Systems, 70569 Stuttgart, Germany

**Christian Silber** – Robert Bosch GmbH, Automotive Electronics, 72703 Reutlingen, Germany

**Metin Sitti** – Max Planck Institute for Intelligent Systems, 70569 Stuttgart, Germany; [orcid.org/0000-0001-8249-3854](https://orcid.org/0000-0001-8249-3854)

**Gisela Schütz** – Max Planck Institute for Intelligent Systems, 70569 Stuttgart, Germany

**Corinne Grévent** – Robert Bosch GmbH, Automotive Electronics, 72703 Reutlingen, Germany

Complete contact information is available at:  
<https://pubs.acs.org/10.1021/acsami.1c14586>

## Funding

Open access funded by Max Planck Society.

## Notes

The authors declare no competing financial interest.

## ACKNOWLEDGMENTS

Authors thank Sebastian Trimpe for Gaussian Process and Bayesian Optimization discussions, Franz Dietz for general defect structure discussion, Volker Mankowski for providing wafers, Barzani Baravan for the sawing process, Bernd Ludescher for wet etching holder preparation, Gerd Maier, Peter Schützendübe, and Gunter Richter for GI-XRD and XPS analysis, and Ulrike Eigenthaler for FIB cross-section sample preparation. Last but not least, Stefan Klein, Pinar Kaya, Lutz Müller, Ingo Henkel, and Gabriele Ernst are gratefully acknowledged for their kind support. Sinan Özgün Demir thanks the Ministry of National Education of the Republic of Turkey for the Doctoral Scholarship. This study was partly funded by the European Research Council (ERC) Advanced Grant “SoMMoR” Project with Grant No: 834531.

## REFERENCES

(1) Butler, K. T.; Davies, D. W.; Cartwright, H.; Isayev, O.; Walsh, A. Machine Learning for Molecular and Materials Science. *Nature* **2018**, *559*, 547–555.

(2) Morgan, D.; Jacobs, R. Opportunities and Challenges for Machine Learning in Materials Science. *Annu. Rev. Mat. Res.* **2020**, *50*, 71–103.

(3) Gubernatis, J. E.; Lookman, T. Machine Learning in Materials Design and Discovery: Examples from the Present and Suggestions for the Future. *Phys. Rev. Mater.* **2018**, *2*, No. 120301.

(4) Chibani, S.; Coudert, F.-X. Machine Learning Approaches for the Prediction of Materials Properties. *APL Mater.* **2020**, *8*, No. 080701.

(5) Morgan, B.; Waits, C. M.; Krizmanic, J.; Ghodssi, R. Development of a Deep Silicon Phase Fresnel Lens Using gray-scale Lithography and Deep Reactive Ion Etching. *J. Microelectromech. S.* **2004**, *13*, 113–120.

(6) Chang, C.-C.; Pan, F.-M.; Chen, C.-W. Effect of Surface Reduction Treatments of Plasma-Enhanced Atomic Layer Chemical Vapor Deposited TaN<sub>x</sub> on Adhesion with Copper. *J. Electrochem. Soc.* **2010**, *157*, G62.

(7) Vargas, I. T.; Fischer, D. A.; Alsina, M. A.; Pavissich, J. P.; Pasten, P. A.; Pizarro, G. E. Copper Corrosion and Biocorrosion Events in Premise Plumbing. *Materials (Basel)* **2017**, *10*, 36.

(8) Shadi Mirhashemihaghighi, J. S.; Maurice, V.; Seyeux, A.; Lorena, H. K.; Harkonen, E.; Ritala, M.; Marcus, P. Electrochemical and Surface Analysis of the Corrosion Protection of Copper by Nanometer-Thick Alumina Coatings Prepared by Atomic Layer Deposition. *J. Electrochem. Soc.* **2015**, *162*, C377–C384.

(9) Alers, G. B. L.; Sukamto, J. H.; Kailasam, S. K.; Reid, J.; Harm, G. Influence of Copper Purity on Microstructure and Electromigration. *IEEE* **2004**, 7803–8308.

(10) Cremers, V.; Rampelberg, G.; Baert, K.; Abrahami, S.; Claes, N.; de Oliveira, T. M.; Terry, H.; Bals, S.; Dendooven, J.; Detavernier, C. Corrosion Protection of Cu by Atomic Layer Deposition. *J. Vacuum Sci. Technol. A* **2019**, *37*, No. 060902.

(11) Liu, Y.; Li, S.; Zhang, J.; Liu, J.; Han, Z.; Ren, L. Corrosion Inhibition of Biomimetic Super-Hydrophobic Electrodeposition Coatings on Copper Substrate. *Corros. Sci.* **2015**, *94*, 190–196.

(12) Fakhri, M.; Babin, N.; Behrendt, A.; Jakob, T.; Gorn, P.; Riedl, T. Facile Encapsulation of Oxide Based Thin Film Transistors by Atomic Layer Deposition Based on Ozone. *Adv. Mater.* **2013**, *25*, 2821–2825.

(13) Changa, M. L.; Lina, H. C.; Chena, M. J.; Linb, K. M. Investigation of Defects in Ultra-Thin Al<sub>2</sub>O<sub>3</sub> Films Deposited on Pure Copper by the Atomic Layer Deposition Technique. *Appl. Surf. Sci.* **2015**, *359*, 533–542.

(14) Mirhashemihaghighi, S.; Światowska, J.; Maurice, V.; Seyeux, A.; Klein, L. H.; Salmi, E.; Ritala, M.; Marcus, P. The Role of Surface Preparation in Corrosion Protection of Copper with Nanometer-Thick ALD Alumina Coatings. *Appl. Surf. Sci.* **2016**, *387*, 1054–1061.

(15) Zhang, Y.; Seghete, D.; Abdulgatov, A.; Gibbs, Z.; Cavanagh, A.; Yang, R.; George, S.; Lee, Y.-C. Investigation of the Defect Density in Ultra-Thin Al<sub>2</sub>O<sub>3</sub> Films Grown Using Atomic Layer Deposition. *Surf. Coat. Technol.* **2011**, *205*, 3334–3339.

(16) Zhang, Y.; Zhang, Y.-Z.; Miller, D. C.; Bertrand, J. A.; Jen, S.-H.; Yang, R.; Dunn, M. L.; George, S. M.; Lee, Y. C. Fluorescent Tags to Visualize Defects in Al<sub>2</sub>O<sub>3</sub> Thin Films Grown Using Atomic Layer Deposition. *Thin Solid Films* **2009**, *517*, 6794–6797.

(17) Leskela, M.; Ritala, M. Atomic Layer Deposition Chemistry: Recent Developments and Future Challenges. *Angew. Chem. Int. Ed. Engl.* **2003**, *42*, 5548–5554.

(18) Zaera, H. T. A. F. Surface Chemistry in the Atomic Layer Deposition of TiN Films from TiCl<sub>4</sub> and Ammonia. *J. Phys. Chem. B* **2006**, *110*, 13491–13498.

(19) He, G.; Lu, S.; Xu, W.; Szunerits, S.; Boukherroub, R.; Zhang, H. Controllable Growth of Durable Superhydrophobic Coatings on a Copper Substrate via Electrodeposition. *Phys. Chem. Chem. Phys.* **2015**, *17*, 10871–10880.

(20) Eigenfeld, N. T.; Gray, J. M.; Brown, J. J.; Skidmore, G. D.; George, S. M.; Bright, V. M. Ultra-thin 3D Nano-Devices from Atomic Layer Deposition on Polyimide. *Adv. Mater.* **2014**, *26*, 3962–3967.

- (21) Marichy, C.; Bechelany, M.; Pinna, N. Atomic Layer Deposition of Nanostructured Materials for Energy and Environmental Applications. *Adv. Mater.* **2012**, *24*, 1017–1032.
- (22) Spahr, H.; Bülow, T.; Nowak, C.; Hirschberg, F.; Reinker, J.; Hamwi, S.; Johannes, H.-H.; Kowalsky, W. Impact of Morphological Defects on the Electrical Breakdown of Ultra Thin Atomic Layer Deposition Processed Al<sub>2</sub>O<sub>3</sub> Layers. *Thin Solid Films* **2013**, *534*, 172–176.
- (23) Díaz, B.; Härkönen, E.; Światowska, J.; Maurice, V.; Seyeux, A.; Marcus, P.; Ritala, M. Low-Temperature Atomic Layer Deposition of Al<sub>2</sub>O<sub>3</sub> Thin Coatings for Corrosion Protection of Steel: Surface and Electrochemical Analysis. *Corros. Sci.* **2011**, *53*, 2168–2175.
- (24) Härkönen, E.; Tervakangas, S.; Kolehmainen, J.; Díaz, B.; Światowska, J.; Maurice, V.; Seyeux, A.; Marcus, P.; Fenker, M.; Tóth, L.; Radnóczy, G.; Ritala, M. Interface Control of Atomic Layer Deposited Oxide Coatings by Filtered Cathodic Arc Deposited Sublayers for Improved Corrosion Protection. *Mater. Chem. Phys.* **2014**, *147*, 895–907.
- (25) Mirhashemihaghighi, S.; Światowska, J.; Maurice, V.; Seyeux, A.; Klein, L. H.; Salmi, E.; Ritala, M.; Marcus, P. Interfacial Native Oxide Effects on the Corrosion Protection of Copper Coated with ALD Alumina. *Electrochim. Acta* **2016**, *193*, 7–15.
- (26) Neizvestny, I. G.; Shwartz, N. L.; Yanovitskaja, Z. S.; Zverev, A. V. Simulation of Surface Relief Effect on ALD Process. *Comput. Mater. Sci.* **2006**, *36*, 36–41.
- (27) Yersak, A. S.; Lee, Y.-C. Probabilistic Distributions of Pinhole Defects in Atomic Layer Deposited Films on Polymeric Substrates. *J. Vac. Sci. Technol. A* **2016**, *34*, 01A149.
- (28) Kolkovsky, V.; Stübner, R. Hydrogen-Related Defects in Al<sub>2</sub>O<sub>3</sub> Layers Grown on n-type Si by the Atomic Layer Deposition Technique. *Phys. B* **2018**, *535*, 171–174.
- (29) Deng, Z.; He, W.; Duan, C.; Shan, B.; Chen, R. Atomic Layer Deposition Process Optimization by Computational Fluid Dynamics. *Vacuum* **2016**, *123*, 103–110.
- (30) MatWeb <http://www.matweb.com>.
- (31) Bahari, H. S.; Savaloni, H. Surface Analysis of Cu Coated With ALD Al<sub>2</sub>O<sub>3</sub> and its Corrosion Protection Enhancement in NaCl Solution: EIS and Polarization. *Mater. Res. Exp.* **2019**, *6*, 865–870.
- (32) Härkönen, E.; Potts, S. E.; Kessels, W. M. M.; Díaz, B.; Seyeux, A.; Światowska, J.; Maurice, V.; Marcus, P.; Radnóczy, G.; Tóth, L.; Kariniemi, M.; Niinistö, J.; Ritala, M. Hydrogen–Argon Plasma Pretreatment for Improving the Anti-Corrosion Properties of Thin Al<sub>2</sub>O<sub>3</sub> Films Deposited Using Atomic Layer Deposition on Steel. *Thin Solid Films* **2013**, *534*, 384–393.
- (33) Kim, H. G.; Lee, J. G.; Kim, S. S. Self-Assembled Monolayers as a Defect Sealant of Al<sub>2</sub>O<sub>3</sub> Barrier Layers Grown by Atomic Layer Deposition. *Org. Electron.* **2018**, *52*, 98–102.
- (34) Vanhaverbeke, C.; Cauwe, M.; Stockman, A.; Op de Beeck, M.; De Smet, H. Comparison of Copper Electroplating, Copper Wet Etching and Linear Sweep Voltammetry as Techniques to Investigate the Porosity of Atomic Layer Deposited Al<sub>2</sub>O<sub>3</sub>. *Thin Solid Films* **2019**, *686*, 137424.
- (35) Chai, Z.; Li, J.; Lu, X.; He, D. Use of Electrochemical Measurements to Investigate the Porosity of Ultra-Thin Al<sub>2</sub>O<sub>3</sub> Films Prepared by Atomic Layer Deposition. *RSC Adv.* **2014**, *4*, 39365–39371.
- (36) Chai, Z.; Liu, Y.; Li, J.; Lu, X.; He, D. Ultra-thin Al<sub>2</sub>O<sub>3</sub> Films Grown by Atomic Layer Deposition for Corrosion Protection of Copper. *RSC Adv.* **2014**, *4*, 50503–50509.
- (37) Correa, G. C.; Bao, B.; Strandwitz, N. C. Chemical Stability of Titania and Alumina Thin Films Formed by Atomic Layer Deposition. *ACS Appl. Mater. Interfaces* **2015**, *7*, 14816–14821.
- (38) Daubert, J. S.; Hill, G. T.; Gotsch, H. N.; Gremaud, A. P.; Ovental, J. S.; Williams, P. S.; Oldham, C. J.; Parsons, G. N. Corrosion Protection of Copper Using Al<sub>2</sub>O<sub>3</sub>, TiO<sub>2</sub>, ZnO, HfO<sub>2</sub>, and ZrO<sub>2</sub> Atomic Layer Deposition. *ACS Appl. Mater. Interfaces* **2017**, *9*, 4192–4201.
- (39) Moehl, T.; Suh, J.; Severy, L.; Wick-Joliat, R.; Tilley, S. D. Investigation of (Leaky) ALD TiO<sub>2</sub> Protection Layers for Water-Splitting Photoelectrodes. *ACS Appl. Mater. Interfaces* **2017**, *9*, 43614–43622.
- (40) Nehm, F.; Klumbies, H.; Richter, C.; Singh, A.; Schroeder, U.; Mikolajick, T.; Monch, T.; Hossbach, C.; Albert, M.; Bartha, J. W.; Leo, K.; Müller-Meskamp, L. Breakdown and Protection of ALD Moisture Barrier Thin Films. *ACS Appl. Mater. Interfaces* **2015**, *7*, 22121–22127.
- (41) Potts, S. E.; Schmalz, L.; Fenker, M.; Diaz, B.; Światowska, J.; Maurice, V.; Seyeux, A.; Marcus, P.; Radnóczy, G.; Toth, L.; Kessels, W. M. M. Ultra-Thin Aluminium Oxide Films Deposited by Plasma-Enhanced Atomic Layer Deposition for Corrosion Protection. *J. Electrochem. Soc.* **2011**, *158*, C132–C138.
- (42) Singh, A. K.; Adstedt, K.; Brown, B.; Singh, P. M.; Graham, S. Development of ALD Coatings for Harsh Environment Applications. *ACS Appl. Mater. Interfaces* **2019**, *11*, 7498–7509.
- (43) Yersak, A. S.; Lewis, R. J.; Tran, J.; Lee, Y. C. Characterization of Thin Film Dissolution in Water with *in-situ* Monitoring of Film Thickness Using Reflectometry. *ACS Appl. Mater. Interfaces* **2016**, *8*, 17622–17630.
- (44) Lange, T.; Reichenberger, S.; Rohe, M.; Bartsch, M.; Kampermann, L.; Klein, J.; Strunk, J.; Bacher, G.; Schlögl, R.; Barcikowski, S. Alumina-Protected, Durable and Photostable Zinc Sulfide Particles from Scalable Atomic Layer Deposition. *Adv. Funct. Mater.* **2021**, No. 2009323.
- (45) Jung, Y. S.; Cavanagh, A. S.; Riley, L. A.; Kang, S. H.; Dillon, A. C.; Groner, M. D.; George, S. M.; Lee, S. H. Ultrathin Direct Atomic Layer Deposition on Composite Electrodes for Highly Durable and Safe Li-ion Batteries. *Adv. Mater.* **2010**, *22*, 2172–2176.
- (46) Poodt, P.; Lankhorst, A.; Roozeboom, F.; Spee, K.; Maas, D.; Vermeer, A. High-Speed Spatial Atomic-Layer Deposition of Aluminum Oxide Layers for Solar Cell Passivation. *Adv. Mater.* **2010**, *22*, 3564–3567.
- (47) Dogan, G.; Sanli, U. T.; Hahn, K.; Müller, L.; Gruhn, H.; Silber, C.; Schutz, G.; Grevent, C.; Keskinbora, K. In Situ X-ray Diffraction and Spectro-Microscopic Study of ALD Protected Copper Films. *ACS Appl. Mater. Interfaces* **2020**, *12*, 33377–33385.
- (48) Dayan, C. B.; Afghah, F.; Okan, B. S.; Yildiz, M.; Menciloglu, Y.; Culha, M.; Koc, B. Modeling 3D Melt Electrospinning Writing by Response Surface Methodology. *Mater. Des.* **2018**, *148*, 87–95.
- (49) Cole, M. T.; Mann, M.; Teo, K. B. K.; Milne, W. I. Engineered Carbon Nanotube Field Emission Devices. *Micro Nano Technol.* **2015**, *125*–186.
- (50) Greenhill, S.; Rana, S.; Gupta, S.; Vellanki, P.; Venkatesh, S. Bayesian Optimization for Adaptive Experimental Design: A Review. *IEEE Access* **2020**, *8*, 13937–13948.
- (51) Nourbakhsh, A.; Ganjipour, B.; Zahedifar, M.; Arzi, E. Morphology Optimization of CCVD-Synthesized Multiwall Carbon Nanotubes, Using Statistical Design of Experiments. *Nanotechnology* **2007**, *18*, No. 115715.
- (52) Pashaei, H.; Ghaemi, A.; Nasiri, M.; Karami, B. Experimental Modeling and Optimization of CO<sub>2</sub> Absorption into Piperazine Solutions Using RSM-CCD Methodology. *ACS Omega* **2020**, *5*, 8432–8448.
- (53) Akhgar, B. N.; Pazouki, M.; Ranjbar, M.; Hosseinnia, A.; Salarian, R. Application of Taguchi Method for Optimization of Synthetic Rutile Nano Powder Preparation from Ilmenite Concentrate. *Chem. Eng. Res. Des.* **2012**, *90*, 220–228.
- (54) Asiltürk, İ.; Akkuş, H. Determining the Effect of Cutting Parameters on Surface Roughness in Hard Turning Using the Taguchi Method. *Measurement* **2011**, DOI: 10.1016/j.measurement.2011.07.003.
- (55) Hou, T.-H.; Su, C.-H.; Liu, W.-L. Parameters Optimization of a Nano-Particle Wet Milling Process Using the Taguchi Method, Response Surface Method and Genetic Algorithm. *Powder Technol.* **2007**, *173*, 153–162.
- (56) Liu, Y.; Liu, C.; Liu, W.; Ma, Y.; Tang, S.; Liang, C.; Cai, Q.; Zhang, C. Optimization of Parameters in Laser Powder Deposition AlSi10Mg Alloy Using Taguchi Method. *Opt. Laser Technol.* **2019**, *111*, 470–480.



- (57) Xue, D.; Balachandran, P. V.; Hogden, J.; Theiler, J.; Xue, D.; Lookman, T. Accelerated Search for Materials with Targeted Properties by Adaptive Design. *Nat. Commun.* **2016**, *7*, No. 11241.
- (58) Freiesleben, J.; Keim, J.; Grutsch, M. Machine Learning and Design of Experiments: Alternative Approaches or Complementary Methodologies for Quality Improvement? *Qual. Reliab. Engineer. Int.* **2020**, *36*, 1837–1848.
- (59) Deringer, V. L.; Caro, M. A.; Csanyi, G. Machine Learning Interatomic Potentials as Emerging Tools for Materials Science. *Adv. Mater.* **2019**, *31*, No. e1902765.
- (60) Friederich, P.; Fediai, A.; Kaiser, S.; Konrad, M.; Jung, N.; Wenzel, W. Toward Design of Novel Materials for Organic Electronics. *Adv. Mater.* **2019**, *31*, No. e1808256.
- (61) Gu, G. H.; Choi, C.; Lee, Y.; Situmorang, A. B.; Noh, J.; Kim, Y. H.; Jung, Y. Progress in Computational and Machine-Learning Methods for Heterogeneous Small-Molecule Activation. *Adv. Mater.* **2020**, *32*, No. e1907865.
- (62) Zhang, Z.; Mansouri Tehrani, A.; Oliynyk, A. O.; Day, B.; Brgoch, J. Finding the Next Superhard Material Through Ensemble Learning. *Adv. Mater.* **2021**, *33*, No. 2005112.
- (63) Rasmussen, C. E. Gaussian Processes in Machine Learning. In *Advanced Lectures on Machine Learning: ML Summer Schools 2003, Canberra, Australia, February 2–14, 2003, Tübingen, Germany, August 4–16, 2003, Revised Lectures*, Bousquet, O.; von Luxburg, U.; Rätsch, G., Eds. Springer Berlin Heidelberg: Berlin, Heidelberg, 2004; 63–71.
- (64) Mockus, J.; Tiesis, V.; Zilinskas, A. The Application of Bayesian Methods for Seeking the Extremum. *Toward Global Optimizat.* **1978**, *3176*, 117–129.
- (65) Shahriari, B.; Swersky, K.; Wang, Z.; Adams, R. P.; de Freitas, N. Taking the Human Out of the Loop: A Review of Bayesian Optimization. *Proc. IEEE* **2016**, *104*, 148–175.
- (66) Stanev, V.; Oses, C.; Kusne, A. G.; Rodriguez, E.; Paglione, J.; Curtarolo, S.; Takeuchi, I. Machine Learning Modeling of Superconducting Critical Temperature. *npj Comput. Mater.* **2018**, *4*, 29.
- (67) Dieb, T. M., Machine Learning-Based Experimental Design in Materials Science. In *Nanoinformatics*, Tanaka, I., Ed. Nanoinformatics, Springer: Singapore, 2018; 65–74.
- (68) Bessa, M. A.; Glowacki, P.; Houlder, M. Bayesian Machine Learning in Metamaterial Design: Fragile Becomes Supercompressible. *Adv. Mater.* **2019**, *31*, No. e1904845.
- (69) Lu, S.; Zhou, Q.; Guo, Y.; Zhang, Y.; Wu, Y.; Wang, J. Coupling a Crystal Graph Multilayer Descriptor to Active Learning for Rapid Discovery of 2D Ferromagnetic Semiconductors/Half-Metals/Metals. *Adv. Mater.* **2020**, *32*, No. e2002658.
- (70) Tu, K. H.; Huang, H.; Lee, S.; Sun, Z.; Alexander-Katz, A.; Ross, C. A. Machine Learning Predictions of Block Copolymer Self-Assembly. *Adv. Mater.* **2020**, *32*, No. e2005713.
- (71) Yuan, R.; Liu, Z.; Balachandran, P. V.; Xue, D.; Zhou, Y.; Ding, X.; Sun, J.; Xue, D.; Lookman, T. Accelerated Discovery of Large Electrostrains in BaTiO<sub>3</sub>-Based Piezoelectrics Using Active Learning. *Adv. Mater.* **2018**, *30*, No. 1702884.
- (72) Kikuchi, S.; Oda, H.; Kiyohara, S.; Mizoguchi, T. Bayesian Optimization for Efficient Determination of Metal Oxide Grain Boundary Structures. *Phys. B* **2018**, *532*, 24–28.
- (73) Li, C.; Rubin de Celis Leal, D.; Rana, S.; Gupta, S.; Sutti, A.; Greenhill, S.; Slezak, T.; Height, M.; Venkatesh, S. Rapid Bayesian Optimisation for Synthesis of Short Polymer Fiber Materials. *Sci. Rep.* **2017**, *7*, No. 5683.
- (74) Vahid, A.; Rana, S.; Gupta, S.; Vellanki, P.; Venkatesh, S.; Dorin, T. New Bayesian-Optimization-Based Design of High-Strength 7xxx-Series Alloys from Recycled Aluminum. *Jom* **2018**, *70*, 2704–2709.
- (75) Ju, S.; Shiga, T.; Feng, L.; Hou, Z.; Tsuda, K.; Shiomi, J. Designing Nanostructures for Phonon Transport via Bayesian Optimization. *Phys. Rev. X* **2017**, *7*, No. 021024.
- (76) Abdulagatov, A. I.; Yan, Y.; Cooper, J. R.; Zhang, Y.; Gibbs, Z. M.; Cavanagh, A. S.; Yang, R. G.; Lee, Y. C.; George, S. M. Al<sub>2</sub>O<sub>3</sub> and TiO<sub>2</sub> Atomic Layer Deposition on Copper for Water Corrosion Resistance. *ACS Appl. Mater. Interfaces* **2011**, *3*, 4593–4601.
- (77) Windholz, M. *The Merck Index*. 10th ed.; Merck & Co. Inc.: Rahway, NJ, 1983; 2052.
- (78) Zhang, F.-Y.; Prasad, A. K.; Advani, S. G. Investigation of a Copper Etching Technique to Fabricate Metallic Gas Diffusion Media. *J. Micromech. Microeng.* **2006**, *16*, N23–N27.
- (79) Shih, H. Y.; Lee, W. H.; Kao, W. C.; Chuang, Y. C.; Lin, R. M.; Lin, H. C.; Shiojiri, M.; Chen, M. J. Low-Temperature Atomic Layer Epitaxy of AlN Ultrathin Films by Layer-by-Layer, in-situ Atomic Layer Annealing. *Sci. Rep.* **2017**, *7*, No. 39717.
- (80) Benredouane, S.; Berrama, T.; Doufene, N. Strategy of Screening and Optimization of Process Parameters Using Experimental Design: Application to Amoxicillin Elimination by Adsorption on Activated Carbon. *Chemom. Intel. Lab. Syst.* **2016**, *155*, 128–137.
- (81) Reason, M.; Mark, F. Z. Application of Two-Level Full Factorial Design and Response Surface Methodology in the Optimization of Inductively Coupled Plasma-Optical Emission Spectrometry (IC-POES) Instrumental Parameters for the Determination of Platinum. *J. Geol. Min. Res.* **2017**, *9*, 43–53.
- (82) Kukovec, A.; Méhn, D.; Nemes-Nagy, E.; Szabó, R.; Kiricsi, I. Optimization of CCVD Synthesis Conditions for Single-Wall Carbon Nanotubes by Statistical Design of Experiments (DoE). *Carbon* **2005**, *43*, 2842–2849.
- (83) Culha, U. D. S.; Trimpe, S.; Sitti, M. Learning of Sub-Optimal Gait Controllers for Magnetic Walking Soft Millirobots. In: *Proceedings of Robotics: Science and Systems (RSS); Robot Sci Syst.* **2020**.
- (84) Chavez, K. L.; Hess, D. W. A Novel Method of Etching Copper Oxide Using Acetic Acid. *J. Electrochem. Soc.* **2001**, *148*, No. G640.
- (85) Pinna, N.; Knez, M. *Atomic Layer Deposition of Nanostructured Materials*. Wiley-VCH: Weinheim, 2012.
- (86) Puurunen, R. L. Surface Chemistry of Atomic Layer Deposition: A Case Study for the Trimethylaluminum/Water Process. *J. Appl. Phys.* **2005**, *97*, No. 121301.
- (87) Buchanan, R. A.; Stansbury, E. E., Electrochemical Corrosion. *Handbook of Environmental Degradation of Materials* 2005, 81–103.
- (88) Tato, W.; Landolt, D. Electrochemical Determination of the Porosity of Single and Duplex PVD Coatings of Titanium and Titanium Nitride on Brass. *J. Electrochem. Soc.* **1998**, *145*, 4173–4181.
- (89) Dias, V. M.; Chiappim, W.; Fraga, M. A.; Maciel, H. S.; Marciano, F. R.; Pessoa, R. S. Atomic Layer Deposition of TiO<sub>2</sub> and Al<sub>2</sub>O<sub>3</sub> Thin Films for the Electrochemical Study of Corrosion Protection in Aluminum Alloy Cans Used in Beverage. *Mater. Res. Exp.* **2020**, *7*, No. 557.
- (90) Fusco, M. A.; Oldham, C. J.; Parsons, G. N. Investigation of the Corrosion Behavior of Atomic Layer Deposited Al<sub>2</sub>O<sub>3</sub>/TiO<sub>2</sub> Nanolaminate Thin Films on Copper in 0.1 M NaCl. *Materials (Basel)* **2019**, *12*, No. 672.
- (91) Chemical Resistance Chart. In *Resistance Tables*, Siemens AG, Siemens Flow Instruments: Germany, 2008.
- (92) Lizotte, D. J. *Practical Bayesian Optimization*; University of Alberta, Department of Computing Science, Edmonton, Canada, 2008, 163.
- (93) Jones, D. R. Efficient Global Optimization of Expensive Black-Box Functions. *J. Global Optimizat.* **1998**, *13*, 445–492.
- (94) Snoek, J.; Larochelle, H.; Adams, R. P. Practical Bayesian Optimization of Machine Learning Algorithms. *Adv. Neur. Info. Process. Syst.* **2012**, *25*, 2951–2959.



## 7. Micromachining of Al<sub>2</sub>O<sub>3</sub> Thin Films *via* Laser Drilling and Plasma Etching for Interfacing Copper

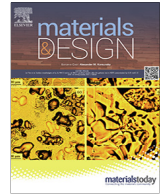
(Reprinted with the permission of the Elsevier Ltd.)

Gül Dogan, Frank Chiu, Sam U.H. Chen, Mebil R.T. David, Andreas Michalowski, Michael Schänzel, Christian Silber, Gisela Schütz, Corinne Grévent, Kahraman Keskinbora

### Abstract

Due to their chemical inertness and high-temperature stability, atomic layer deposited (ALD) oxide thin films emerged as an attractive copper encapsulation, passivation, and protection technology. Several types of high-k dielectrics, which are robust insulators, can be deposited by ALD. Hence, a successful encapsulation process electrically isolates the underlying film and active elements from the environment, as a side effect. To electrically interface such encapsulated structures, a reliable method that selectively and locally removes the encapsulation film is required. Here, the study focused on the effectiveness of laser drilling and plasma etching of Al<sub>2</sub>O<sub>3</sub> thin films deposited *via* ALD, both *in silico* and experimentally. Results have shown that the CO<sub>2</sub> laser drilling alone is insufficient to remove the Al<sub>2</sub>O<sub>3</sub> thin films. However, plasma etching successfully removes the encapsulation layer, providing a clean interface for conductive vias. Results are essential for future ALD layer applications in the encapsulation of copper and other critical components in semiconductor fabrication processes.





# Micromachining of Al<sub>2</sub>O<sub>3</sub> thin films *via* laser drilling and plasma etching for interfacing copper

Gül Dogan<sup>a,b,\*</sup>, Frank Chiu<sup>c</sup>, Sam U.H. Chen<sup>c</sup>, Mebil R.T. David<sup>a</sup>, Andreas Michalowski<sup>d</sup>, Michael Schänzel<sup>d</sup>, Christian Silber<sup>a</sup>, Gisela Schütz<sup>b</sup>, Corinne Grévent<sup>a,\*</sup>, Kahraman Keskinbora<sup>b,e,\*</sup>

<sup>a</sup> Robert Bosch GmbH, Automotive Electronics, Postfach 13 42, 72703 Reutlingen, Germany

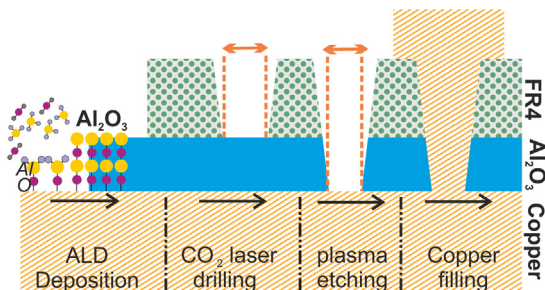
<sup>b</sup> Max-Planck-Institute for Intelligent Systems, Heisenbergstr 3, 70569 Stuttgart, Germany

<sup>c</sup> Advanced Semiconductor Engineering Inc., No.26, Chin 3rd Rd, N.E.P.Z, Nantze, Kaohsiung, Taiwan

<sup>d</sup> Robert Bosch GmbH, Corporate Sector Research and Advance Engineering, Robert-Bosch-Campus1, 71272 Stuttgart, Germany

<sup>e</sup> Massachusetts Institute of Technology, 77 Mass Avenue, Cambridge, MA 02139, USA

## GRAPHICAL ABSTRACT



## ARTICLE INFO

### Article history:

Received 26 May 2021

Revised 8 September 2021

Accepted 13 September 2021

Available online 14 September 2021

### Keywords:

Atomic layer deposition

Micromachining

CO<sub>2</sub> laser drilling

Plasma etching

Copper via Fabrication

## ABSTRACT

Due to their chemical inertness and high-temperature stability, atomic layer deposited (ALD) oxide thin films emerged as an attractive copper encapsulation, passivation, and protection technology. Several types of high-k dielectrics, which are robust insulators, can be deposited by ALD. Hence, a successful encapsulation process electrically isolates the underlying film and active elements from the environment, as a side effect. To electrically interface such encapsulated structures, a reliable method that selectively and locally removes the encapsulation film is required. Here, the study focused on the effectiveness of laser drilling and plasma etching of Al<sub>2</sub>O<sub>3</sub> thin films deposited *via* ALD, both *in silico* and experimentally. Results have shown that the CO<sub>2</sub> laser drilling alone is insufficient to remove the Al<sub>2</sub>O<sub>3</sub> thin films. However, plasma etching successfully removes the encapsulation layer, providing a clean interface for conductive vias. Results are essential for future ALD layer applications in the encapsulation of copper and other critical components in semiconductor fabrication processes.

© 2021 The Authors. Published by Elsevier Ltd. This is an open access article under the CC BY license (<http://creativecommons.org/licenses/by/4.0/>).

\* Corresponding authors at: Robert Bosch GmbH, Automotive Electronics, Postfach 13 42, 72703 Reutlingen, Germany (G. Dogan and C. Grévent) and Massachusetts Institute of Technology, 77 Mass Avenue, Cambridge, MA 02139, USA (K. Keskinbora).

E-mail addresses: [guel.dogan@de.bosch.com](mailto:guel.dogan@de.bosch.com) (G. Dogan), [corinne.grevent@de.bosch.com](mailto:corinne.grevent@de.bosch.com) (C. Grévent), [kahraman@mit.edu](mailto:kahraman@mit.edu) (K. Keskinbora).

<https://doi.org/10.1016/j.matdes.2021.110114>

0264-1275/© 2021 The Authors. Published by Elsevier Ltd.

This is an open access article under the CC BY license (<http://creativecommons.org/licenses/by/4.0/>).

## 1. Introduction

Atomic layer deposited (ALD) oxide thin films have gained increasing attention in copper corrosion protection for several years for electronic, optical, biological, and mechanical applica-

tions [1–3]. ALD offers an attractive route to achieve high-quality protective layers with accurate thickness control, uniformity over a large area, excellent step coverage, and composition control [4–7]. The corrosion protection performance of ALD thin films has been introduced by several research groups [3,8–17]. The most comprehensive research is performed on Al<sub>2</sub>O<sub>3</sub> thin layers due to their better adhesion to metal surfaces [12,18,19]. Our previous work showed the viability of Al<sub>2</sub>O<sub>3</sub>/TiO<sub>2</sub> and Al<sub>2</sub>O<sub>3</sub>/SiO<sub>2</sub> bilayer thin film stacks against the protection of copper at high temperatures [20]. Moreover, we have additionally shown that the protection properties of ALD-Al<sub>2</sub>O<sub>3</sub> thin films under an acidic environment were improved by four orders of magnitude with process optimization and proper surface treatment (to be published elsewhere). Even though several other studies mainly focus on how to fabricate ALD thin films on copper with good corrosion performance, the micro- and nano-structuring of these ALD layers need to be addressed for many applications such as printed circuit board (PCB), electronic packaging, silicon integrated fabric (Si-IF), flexible organic devices, microwells, microneedle arrays, polymer waveguides [21–32].

Structuring through micromachining is necessary to make contacts through the passivation layer to connect the top copper layer to the layers below [33,34]. The structuring is followed by filling the patterned hole with a conductive material to form interconnection (via-hole), which creates an electrical connection between two copper in different layers [21,35]. To achieve this, the ALD layers need to be removed in a localized, selective way without degradation of the underlying copper layer for a reliable electrical connection. Therefore, not only the corrosion protection properties of the ALD layers are crucial, but also the micromachining of these protective layers plays an important role, especially for the future of finer and complex 3D interconnections on semiconductor devices [21,36–38].

Several methods are commonly used to structure the layers for copper–copper interconnection, such as photolithography, direct laser writing, laser drilling, inkjet printing, hot-embossing, dry and wet etching [24,27,36,39–46]. Among these methods, etching and laser drilling are widely studied methods [36]. While wet etching has limits with highly sloped sidewalls and large feature dimensions [47], dry etching using reactive ion plasma shows higher potential in the application of interconnects. Several groups study the structuring of polymers on copper by plasma etching [48–55]. Even though plasma etching was used in making interconnections in copper structures, the ALD-Al<sub>2</sub>O<sub>3</sub> layers have not been reported. Laser drilling, another structuring method, is selective according to the laser wavelength, pulse duration, and incident laser energy, allowing precise removal of the target area with limited detrimental effects on surrounding layers [21]. The CO<sub>2</sub> laser is one of the most widely used lasers with a relatively low cost and high processing speed, advantageous from the deployment point of view [56–58]. Hu *et al.* studied the CO<sub>2</sub> laser drilling process parameters for high density interconnect (HDI) micro via fabrication in which glass fiber reinforced epoxy (FR4) with 200 μm thickness on copper were successfully structured [59]. Okada *et al.* also showed that 50-μm thick glass fiber epoxy reinforced were selectively removed by CO<sub>2</sub> laser for copper–copper connection in printed wiring boards (PRW) [60]. CO<sub>2</sub> lasers were also used to micromachine ceramics [61–68]. Moorhouse *et al.* worked on the 0.63-mm thick Al<sub>2</sub>O<sub>3</sub> ceramics using CO<sub>2</sub> laser [65]. Even though the laser drilling was used to contact the copper metals and Al<sub>2</sub>O<sub>3</sub> bulk layers, the ALD thin films with less than 100 nm thickness have not been reported in the literature. Especially in semiconductor technology with a strong miniaturization trend, ALD thin films offer an attractive route in the passivation of copper with thinner and conformal layers by structuring 3D finer complex interconnects, and therefore

micromachining properties by common methods play an important role for future applications of ALD materials.

This study presents the first detailed account on the micromachining of ALD passivation layers using laser drilling and plasma etching. The applicability of microvia fabrication in a Cu-Al<sub>2</sub>O<sub>3</sub>-FR4 structure is showed to form copper–copper interconnects, which are typically encountered in PCBs or electronic packaging. The CO<sub>2</sub> laser ablation of the ALD layer on Cu was studied *in silico* by numerical simulation in the Abaqus environment. Further, laser drilling was experimentally investigated, focusing on the quality of the formed microvias and copper–copper interface in the Cu-Al<sub>2</sub>O<sub>3</sub>-FR4 reference structure. Using electrical contact tests and cross-section analysis with the combination of the scanning electron microscope (SEM), the overall design was studied in detail with a focus on the copper–copper interface. For plasma etching, similar investigations were performed on the structure, while initial plasma etching experiments were reported on Cu-Al<sub>2</sub>O<sub>3</sub> structures by X-ray photoelectron spectroscopy (XPS), SEM, and profilometer.

## 2. Methods

### 2.1. ALD deposition

Electroplated copper with the 8-μm thickness on silicon substrate was used for ALD depositions. Before the deposition, all Cu samples were rinsed with acetic acid for 1 min to remove residuals and oxide layer from the Cu surface. The Al<sub>2</sub>O<sub>3</sub> films were deposited using an ALD system (Sentech Instruments GmbH, Germany). Trimethylaluminum (TMA) and ultra-pure H<sub>2</sub>O were used at room temperature for the Al<sub>2</sub>O<sub>3</sub> deposition. The precursors were pulsed for 20 ms and purged for 1980 ms at 150 °C substrate/chamber temperature under constant nitrogen flow. The thickness of the layers and ALD growth properties were monitored using *in situ* spectroscopic ellipsometry (SE SENresearch 4.0, Sentech, Germany) on Cu. The final thickness of Al<sub>2</sub>O<sub>3</sub> films was measured by *ex-situ* SE (SENresearch 4.0, Sentech, Germany) and varied between 5 nm and 100 nm. The structure of ALD films was determined by Grazing Incidence XRD (GI-XRD) in the 2θ range 20–100° with Cu-K<sub>α</sub> radiation using the Bruker AX8 device. The surface of ALD protected Cu was evaluated using X-ray photoelectron spectroscopy (XPS, Theta Probe Instrument, Thermo Fisher Scientific, Germany) and Scanning Electron Microscopy (SEM, Zeiss Gemini, Germany).

### 2.2. Numerical analysis

Simulations were used to investigate whether the CO<sub>2</sub> laser process can remove the Al<sub>2</sub>O<sub>3</sub> layer from the copper. A numerical model was constructed with 200-μm silicon (Si) as substrate and copper on the top with 8-μm thickness. The ALD-Al<sub>2</sub>O<sub>3</sub> thin film thickness was chosen to be 100 nm and placed on the top of the model. By neglecting the FR4 layer, it was studied whether it is possible to remove the ALD-Al<sub>2</sub>O<sub>3</sub> layer with the process parameters applied. The model width was 150 μm with a beam diameter of 60 μm and semi-finite modeling during the simulation.

The power absorbed locally in the Al<sub>2</sub>O<sub>3</sub> layer due to the incident laser radiation with Gaussian intensity distribution is given by

$$q = \frac{2AP}{\pi w^2} \exp\left(\frac{-2r^2}{w^2}\right). \quad (1)$$

where P is the overall irradiated power of the laser source, A is the absorbance of Al<sub>2</sub>O<sub>3</sub>, w is the laser beam radius (1/e<sup>2</sup>), and r is the distance from the symmetry axis. The optical penetration depth of the laser wavelength in Al<sub>2</sub>O<sub>3</sub> of about 1.9 μm exceeds the film thickness by more than one order of magnitude. The radiation



passed through the layer is almost entirely reflected at the copper interface and passed back through the layer. In total, about 9.2% of the locally irradiated power is almost homogeneously absorbed in the layer.

The material data used for the numerical calculations are summarized in Table 1. The density, thermal conductivity, and specific heat capacity of Al<sub>2</sub>O<sub>3</sub> were taken at room temperature of 25 °C. The refraction index of Al<sub>2</sub>O<sub>3</sub> is taken at 10.6 μm wavelength according to the CO<sub>2</sub> laser. The time- and spatially-resolved calculations of the temperature distribution within the model system were performed with the commercial software package ABAQUS. An axially symmetrical model was chosen for the calculations, which is advantageous concerning memory requirements and computing time compared to 3D calculations. The calculated temperatures were investigated whether removing the layer by evaporation is possible with the process parameters used.

### 2.3. Formation of Cu-Al<sub>2</sub>O<sub>3</sub>-FR4 layer stack

A ~ 40-μm thick glass fiber reinforced epoxy (FR4) layer was coated on the Cu-Al<sub>2</sub>O<sub>3</sub> structure and cured at 200 °C for 2 h.

### 2.4. Experimental laser drilling

CO<sub>2</sub> laser drilling was performed on Cu-Al<sub>2</sub>O<sub>3</sub>-FR4 layers. The CO<sub>2</sub> laser power at 10.6 μm wavelength was set to 1.1 mJ for one shot with 60 μm spot size. Total power of 3.3 mJ was used for three shots with 4 μs pulse duration with 4 μs dwell time between each pulse.

### 2.5. Experimental plasma etching

Two different plasma sources, CHF<sub>3</sub>/O<sub>2</sub> plasma at radio frequency (RF) and CF<sub>4</sub>/O<sub>2</sub> plasma at microwave frequency, were studied for plasma etching. RF plasma, 13.56 MHz frequency, was used at 300 W and 3x10<sup>-2</sup> mbar pressure with 15-sccm gas flow under DC bias 160 V on Cu-Al<sub>2</sub>O<sub>3</sub> layers. A chromium stencil mask was used to provide selective etching. The microwave plasma, 2.45 GHz frequency, was used at 2500 W with 150 sccm and 1000 sccm CF<sub>4</sub> and O<sub>2</sub> gas flow, respectively, on Cu-Al<sub>2</sub>O<sub>3</sub>-FR4 layers. For the analysis of etching properties, X-ray photoelectron spectroscopy (XPS, Theta Probe Instrument, Germany), Scanning Electron Microscopy (SEM, Zeiss Gemini, Germany), and Bruker Dektak Profilometer were used.

### 2.6. Copper electroplating

After micromachining of Cu-Al<sub>2</sub>O<sub>3</sub>-FR4 structures with laser drilling, plasma etching, or a combination of both, a seed layer of copper was deposited on the bottom and sidewalls of the vias. Then, copper electroplating was applied to fill the vias with applied voltage difference in the CuSO<sub>4</sub>-H<sub>2</sub>O solution and annealed at 175 °C for 2 h.

**Table 1**  
Material properties of the Al<sub>2</sub>O<sub>3</sub> layer for CO<sub>2</sub> laser drilling simulations [69,70].

Material Properties	
Density	3.9x10 <sup>-15</sup> (kg/μm <sup>3</sup> )
Thermal conductivity	3.72 x10 <sup>-5</sup> (W/ μm K)
Specific heat capacity	782.218 (J/kg K)
Young's Modulus	370 (G pa)
Poisson's Ratio	0.22
Melting point	2072 (°C)
Boiling point	2977 (°C)
Latent heat of fusion	1093x10 <sup>3</sup> (J/kg)
Heat of evaporation	1938x10 <sup>4</sup> (J/kg)
Index of Refraction @10.6 μm	0.706 + i0.441

### 2.7. Electrical contact test

An electrical contact test was performed as a four-point probe (FPP) measurement on the electroplated samples. From the four probes, the two external probes were utilized for supply current, and the two internal probes were used for finding the resulting voltage drop over the surface of the substrate. Voltage was applied in this case as a source varying from 0 to 300 mV. A current flow occurred due to the voltage supply, resulting in a voltage drop between the two inner probes. Based on the voltage drop, the resistance between the two pads was measured based on Ohm's law, indicating the removal or non-removal of the isolating ALD Layers.

### 2.8. Cross-Section preparation

The metallographic cross-sections were prepared by first cutting the area of interest by wire-saw and mounted to mechanically support the samples with resin and curing agent at room temperature. The auto grinding was used with abrasive papers from coarse to fine. As a final step, diamond polishing was used to eliminate the scratches and imperfections on the surface. The prepared cross-sections were controlled by optical microscopy, and no mechanical damage was observed.

## 3. Results and discussion

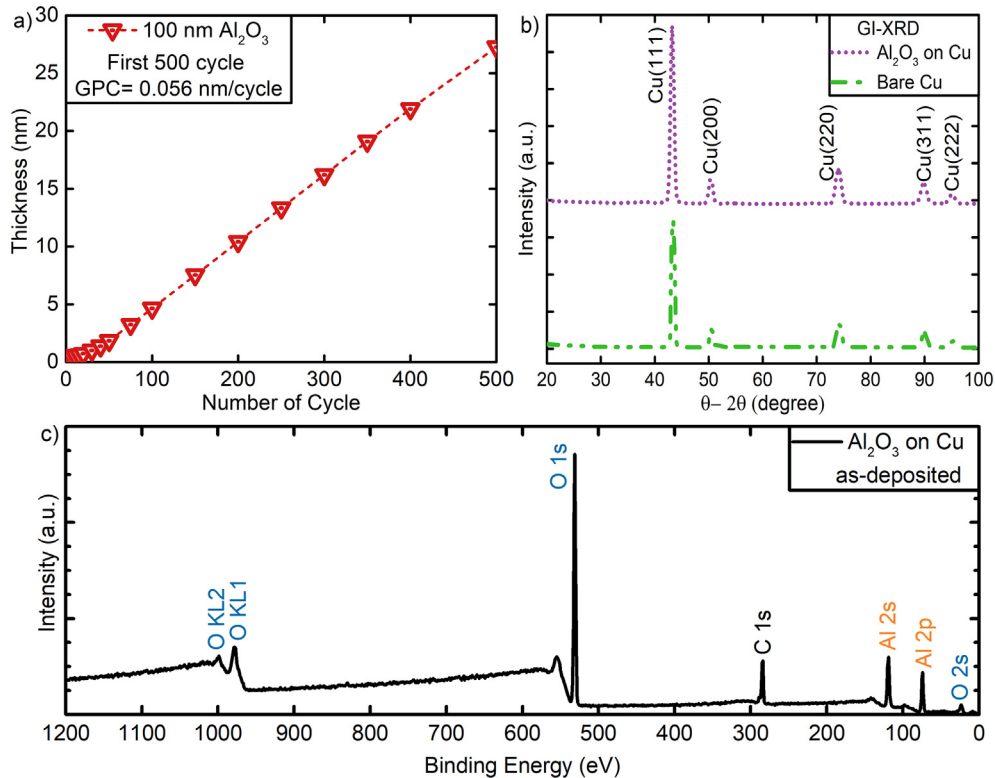
### 3.1. ALD growth and film properties

100-nm thick Al<sub>2</sub>O<sub>3</sub> films were deposited on copper-coated silicon wafers. The 2.4-nm thick native copper oxide layer was measured on 8-μm thick copper by *in situ* spectroscopic ellipsometry (SE). A linear increase in thickness with the number of cycles was observed during the deposition, which is the characteristic growth of ALD. Fig. 1a depicts the growth per cycle for Al<sub>2</sub>O<sub>3</sub> thin films, deposited at 150 °C on Cu and measured by *in situ* SE. The growth rate was calculated from the slope of the fit and was found to be 0.056 nm/cycle. The GI-XRD spectra for bare Cu and Cu-Al<sub>2</sub>O<sub>3</sub> are given in Fig. 1b. Compared to the polycrystalline structure of Cu, no additional phases were detected within the ALD-Al<sub>2</sub>O<sub>3</sub> thin film, which indicates an amorphous film structure. According to XPS survey spectra represented in Fig. 1c, Al and O atoms were detected on the surface, and C atoms came from the environment. Oxygen was found at 47.6 at.%, and aluminum was 33.25 at.%, indicating the formation of Al<sub>2</sub>O<sub>3</sub> with [Al:O]: 0.66 atomic ratios. The surface analysis of the Cu-Al<sub>2</sub>O<sub>3</sub> layer with optic microscopy and SEM is given in Figure S1, Supporting Information.

### 3.2. Al<sub>2</sub>O<sub>3</sub>-CO<sub>2</sub> laser Interaction: Numerical analysis

An *in silico* study was carried out in the Si-Cu-Al<sub>2</sub>O<sub>3</sub> model system, with 100-nm thick Al<sub>2</sub>O<sub>3</sub> deposited on copper, given in Fig. 2a. The micromachining of Al<sub>2</sub>O<sub>3</sub> thin films was analyzed with a CO<sub>2</sub> laser drilling process simulation at 10.6 μm wavelength. It was assumed that the layer would not be removed unless the temperature in the layer reaches the evaporation temperature, which is 2972 °C for Al<sub>2</sub>O<sub>3</sub> [62].

The axial symmetric simulation area had an extension of 208.1 μm in an axial direction and 150 μm in a radial direction. The ambient temperature was assumed to be 25 °C. Three laser pulses with the pulse duration of 4 μs, the energy of 1.1 mJ each, and a time spacing between the pulses of 4 μs each were applied. The laser heat source had a radial extent of 30 μm (60-μm laser beam diameter). Fig. 2b shows an exemplary result of calculated heat distribution, in which the temperature distribution for the model, Al<sub>2</sub>O<sub>3</sub>, Cu, and Si, is given. The time-resolved surface tem-



**Fig. 1.** Thin-film growth, structural and chemical properties of ALD- $\text{Al}_2\text{O}_3$  (a) film thickness as a function of the number of ALD cycles. (b) GI-XRD spectra of ALD- $\text{Al}_2\text{O}_3$  layer as-deposited and comparison with bare Cu (c) XPS survey spectra for as-deposited  $\text{Al}_2\text{O}_3$  layer.

perature of the  $\text{Al}_2\text{O}_3$ , Cu, and Si films is shown in Fig. 2c. Fig. 2d to 2f show the radial distribution of the  $\text{Al}_2\text{O}_3$  surface temperature after each laser pulse. The numerical stability of the calculations was ensured using plausibility considerations (Figure S2, Supporting Information). The most essential applied criteria were the total present energy in the model, which must correspond to the total absorbed laser energy.

According to simulation results, the highest temperature was found at the center of the irradiation region for each pulse (Gaussian beam irradiation). At a given laser power, the temperature on the surface was increased from 25 °C to 850 °C, 900 °C, and 977.3 °C, respectively for first laser pulse, second laser pulse, and third laser pulse. The temperature rises to a high value for each laser pulse during the 4  $\mu\text{s}$  pulse duration and then drops down again due to heat dissipation, as shown in Fig. 2c. The maximum temperature on the surface was achieved at 977.3 °C, below the  $\text{Al}_2\text{O}_3$  vaporization temperature, 2972 °C. Therefore, the simulation result indicates that  $\text{CO}_2$  laser drilling at 1.1 mJ and three pulses (total energy 3.3 mJ) could not melt the ALD- $\text{Al}_2\text{O}_3$  layer for structuring. On the copper layer, the highest temperature was reached 857 °C. As the temperature is below the copper melting temperature, 1050 °C, the copper layer is assumed durable during the laser process.

The more laser power and the higher number of laser pulses would increase the surface temperature and reach the melting temperature of  $\text{Al}_2\text{O}_3$ . Further numerical analyses were therefore studied. Fig. 3 represents the temperature distribution of the  $\text{Al}_2\text{O}_3$  surface and the interface between Cu and  $\text{Al}_2\text{O}_3$  for six additional  $\text{CO}_2$  laser pulses. At the 8th laser pulse (8.8 mJ total power), the temperature on the  $\text{Al}_2\text{O}_3$  surface was calculated around 1100 °C and for Cu surface was around 1050 °C. Although the temperature on the  $\text{Al}_2\text{O}_3$  surface was not enough to remove the layer (the melting point of  $\text{Al}_2\text{O}_3$  is 2972 °C), the copper surface has

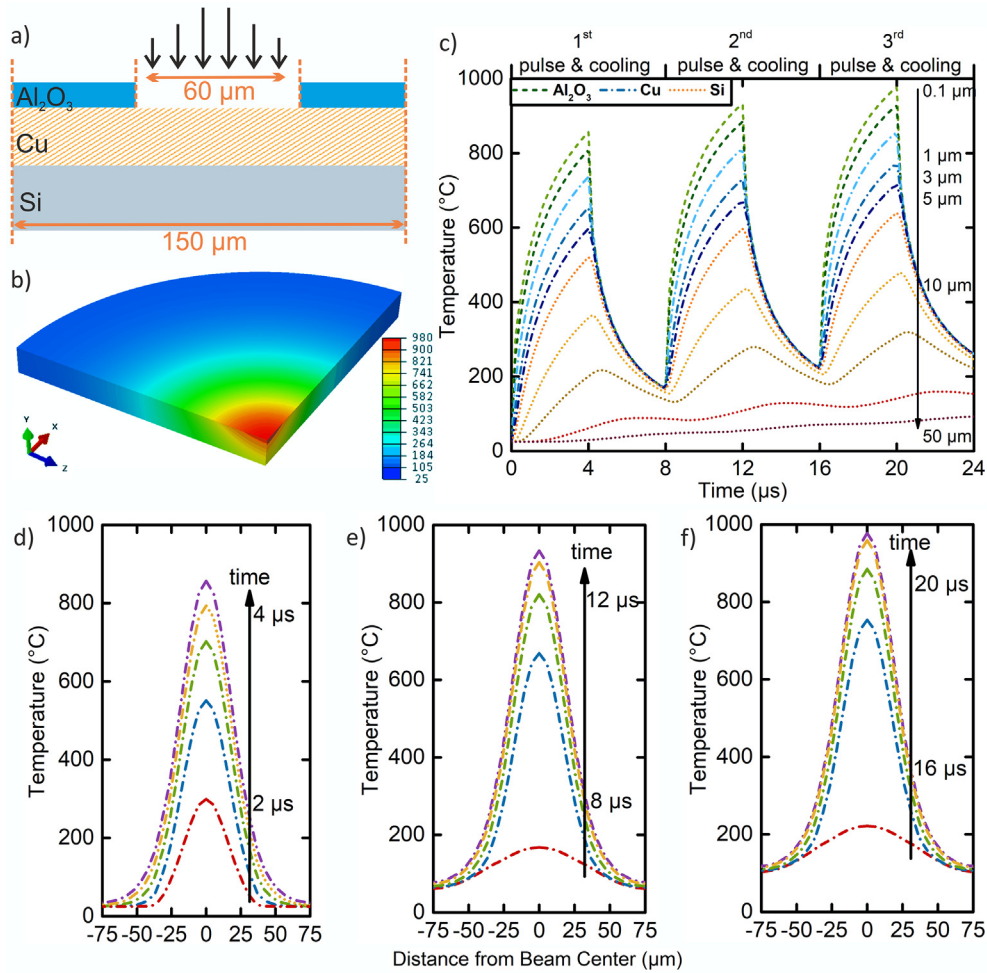
already reached the melting point of 1050 °C. The results showed that more pulse is required to remove the  $\text{Al}_2\text{O}_3$  thin layer. However, more pulses would cause the melting of copper before structuring the  $\text{Al}_2\text{O}_3$  thin layer. According to the numerical analyses, the micromachining of the Cu- $\text{Al}_2\text{O}_3$  layers is not possible using a  $\text{CO}_2$  laser process without melting the Cu layer.

### 3.3. Micromachining of $\text{Al}_2\text{O}_3$ by $\text{CO}_2$ laser drilling

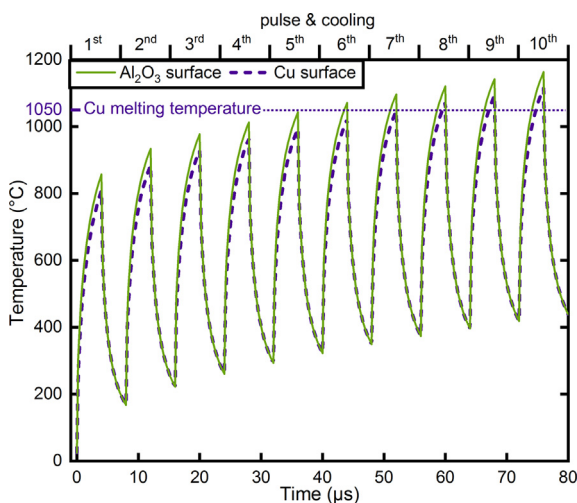
The experimental analysis of  $\text{CO}_2$  laser drilling was conducted on Cu- $\text{Al}_2\text{O}_3$ -FR4 layers. A  $\text{CO}_2$  laser at 10.6  $\mu\text{m}$  wavelength was used with 1.1 mJ power. Three laser pulses were applied for the 4  $\mu\text{s}$  duration with 4  $\mu\text{s}$  dwell time between each pulse to drill 60- $\mu\text{m}$  diameter via-hole (microarray).

The Cu- $\text{Al}_2\text{O}_3$ -FR4 layer stack is represented by cross-section-view in Fig. 4a and 4b. As shown in Fig. 4b, the  $\text{CO}_2$  laser removes the FR4 layer and reaches the surface of  $\text{Al}_2\text{O}_3$  with two possibilities; successful removing of the ALD layer as indicated on the left side or unsuccessful as on the right side. An optical microscopy image after laser drilling of the Cu- $\text{Al}_2\text{O}_3$ -FR4 layer is given in Fig. 4c. The uniform microarrays were obtained on a 5x4 structure. No burr was observed on the entrance and exit of the through-holes, which showed good edge quality. After laser drilling, the microarrays were filled with copper by first depositing a Cu seed layer. Then, using the electroplating technique, vias have been filled utterly to provide a copper-copper connection. Fig. 4d represents the optical microscopy image for the final structure of the Cu- $\text{Al}_2\text{O}_3$ -FR4 layer. The via diameter was measured to be  $\sim 150 \mu\text{m}$ . Moreover, the Cu-FR4 layer (without  $\text{Al}_2\text{O}_3$  thin layer) was additionally investigated using the same laser drilling parameters to ensure the micromachining properties of the FR4. We found that the FR4 layer was successfully removed by  $\text{CO}_2$  laser, given in Figure S3, Supporting Information.





**Fig. 2.** Simulation results for the CO<sub>2</sub> laser drilling. (a) The simulation model includes 100-nm thick Al<sub>2</sub>O<sub>3</sub>, 8-μm thick Cu, and 200-μm thick Si. Gaussian beam distribution was shown on the surface with a 60-μm diameter. (b) A representative 3D temperature distribution for 100-nm thick Al<sub>2</sub>O<sub>3</sub>, 8-μm thick Cu, and 3-μm thick Si after CO<sub>2</sub> laser irradiation with three laser pulses at 1.1 mJ for 20 μs. (c) Variation of the temperature concerning the time along with the Al<sub>2</sub>O<sub>3</sub>, Cu, and Si layers. Each pulse includes 4 μs laser beam irradiation, and 4 μs stop for cooling. Radial distribution of Gaussian beam irradiation on the surface under (d) first laser pulse, (e) second laser pulse, and (f) third laser pulse without cooling steps.

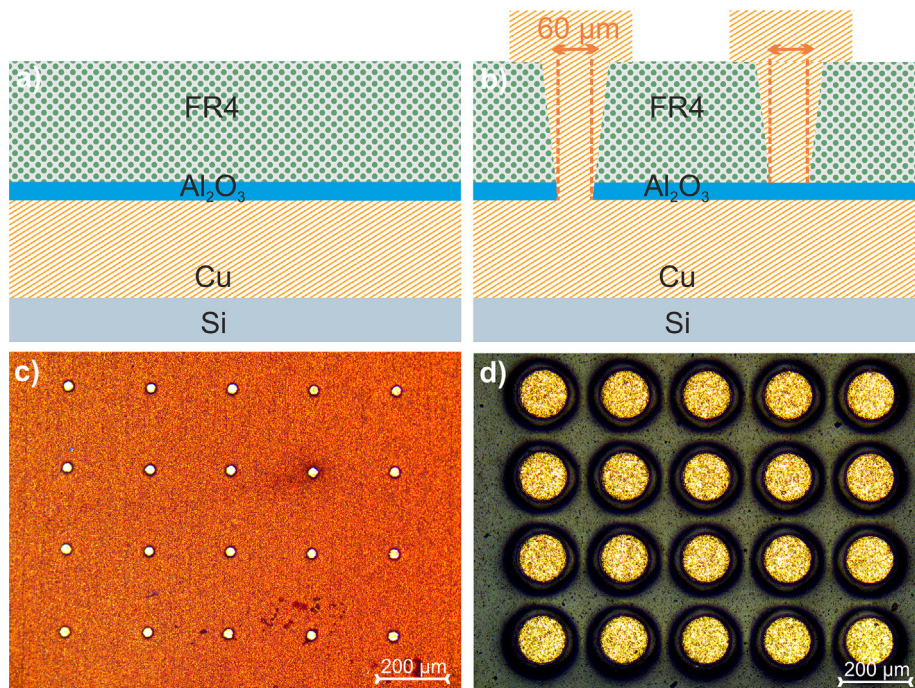


**Fig. 3.** Extended simulation results for the CO<sub>2</sub> laser drilling of 100-nm thick Al<sub>2</sub>O<sub>3</sub> thin film on copper. Temperature distribution on Al<sub>2</sub>O<sub>3</sub> surface and at Cu-Al<sub>2</sub>O<sub>3</sub> interface for ten laser pulses (each pulse includes 4 μs long laser irradiation and 4 μs long cooling).

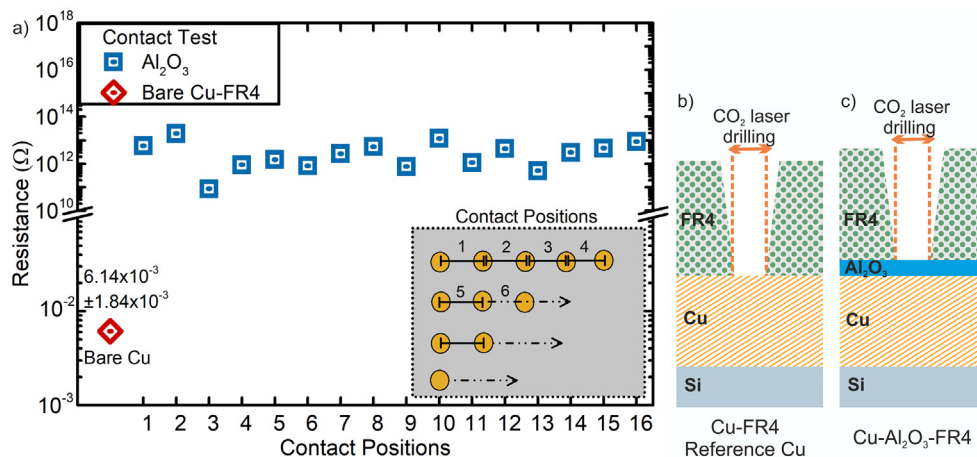
Even though the microarray structure shows the precise structuring, no indication can be predicted about removing the Al<sub>2</sub>O<sub>3</sub> layer by optical microscope image in Fig. 4d. As the FR4 layer was removed by CO<sub>2</sub> laser, the microarrays do only indicate the structuring of the FR4 layer. The electroplating copper filling was followed by the deposition of a seed layer on the via-hole bottom and walls, which results in successful copper filling even if there is no connection to the copper substrate. Therefore, further analysis is necessary to conclude the structuring of the Al<sub>2</sub>O<sub>3</sub> layer.

The electrical resistance of the samples was used as an indicator for the success of micromachining in Cu-Al<sub>2</sub>O<sub>3</sub>-FR4 layers. The electrical resistance of the copper-copper connection through CO<sub>2</sub> laser-drilled microarrays was measured by the four-point probe (FPP) method. For a 5x4-microarray structure, each pad's electrical connection was measured. Fig. 5a represents the resistance results according to contact position, and the inset of the figure schematically explains each contact position of the FPP on the array. The resistance results of the Al<sub>2</sub>O<sub>3</sub> thin film were compared with the bare copper resistance value. The layer systems for the bare copper and Cu-Al<sub>2</sub>O<sub>3</sub>-FR4 layer are schematically explained in Fig. 5b and 5c.

The reference bare copper sample (Cu-FR4) without the ALD-Al<sub>2</sub>O<sub>3</sub> layer showed 6.14x10<sup>-3</sup> Ω resistance, which indicated a reli-



**Fig. 4.** The CO<sub>2</sub> laser drilling of (a) schematic representation of Cu-Al<sub>2</sub>O<sub>3</sub>-FR4 layers on Si (FR4: glass fiber reinforced epoxy). (b) Schematic presentation of micromachining process by CO<sub>2</sub> laser. (c) Optical microscope image of the structured microarrays after micromachining. (d) Optical microscope image of structured microarrays after copper filling.



**Fig. 5.** (a) Electrical resistance of copper vias through CO<sub>2</sub> laser-drilled microarray. Electrical resistance is given according to the contact positions on the microarray. (b) Schematic representation of Si-Cu-FR4 layers, used as a reference sample. (c) Schematic representation of Si-Cu-Al<sub>2</sub>O<sub>3</sub>-FR4 layers.

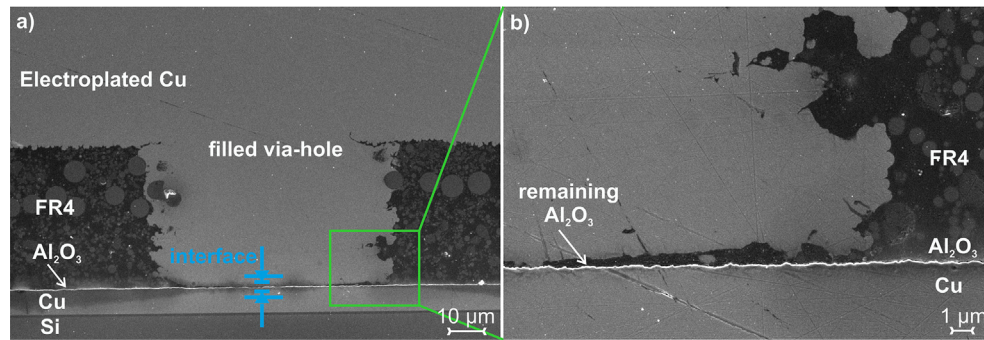
able copper-copper connection and successful structuring of the FR4 layer. However, the Al<sub>2</sub>O<sub>3</sub> protected copper layer showed high resistance in comparison to bare copper. Electrical resistance for all pads was found to be more than 10<sup>11</sup> Ω, indicating that the process was not sufficient for a reliable electrical interconnection. The high resistance values were attributed to the presence of the Al<sub>2</sub>O<sub>3</sub> thin layer on the interface of the copper-copper connection, which was not removed by a CO<sub>2</sub> laser. The cross-section of the filled microarrays was further analyzed by SEM. The cross-section image for one of the copper pads is given in Fig. 6a and higher magnification in 6b.

According to cross-section analysis, the remaining Al<sub>2</sub>O<sub>3</sub> thin layer was found on the interface of the copper-copper interconnection. While copper electroplating successfully filled the via-hole, the grown copper was not in contact with the copper substrate, as shown in Fig. 6b. The interface with the presence of the

Al<sub>2</sub>O<sub>3</sub> layer was further supported by SEM images and confirmed the high electrical resistance results.

The experimental results confirmed that CO<sub>2</sub> laser drilling could not selectively remove the Al<sub>2</sub>O<sub>3</sub> thin films for structuring microarrays. Moreover, the numerical analysis was in line with the experimental results. Few studies reported in the literature for removing the Al<sub>2</sub>O<sub>3</sub> using a CO<sub>2</sub> laser [61,65]. In contrast to this work, those studies were focused on bulk Al<sub>2</sub>O<sub>3</sub> layers with a thickness range of ~ 1 mm. Laser ablation represents the conditions of spatial confinement, and the process is highly dependent on the material properties of the layers. Compared to bulk Al<sub>2</sub>O<sub>3</sub> layers, material properties might show differences for thin films [71]. Additionally, the material below thin Al<sub>2</sub>O<sub>3</sub> layers plays an important role in heat transfer. As copper is a highly conductive material, the heat is directly transferred to the copper layer through Al<sub>2</sub>O<sub>3</sub> layers [72]. In other words, heat is effectively removed by copper in a





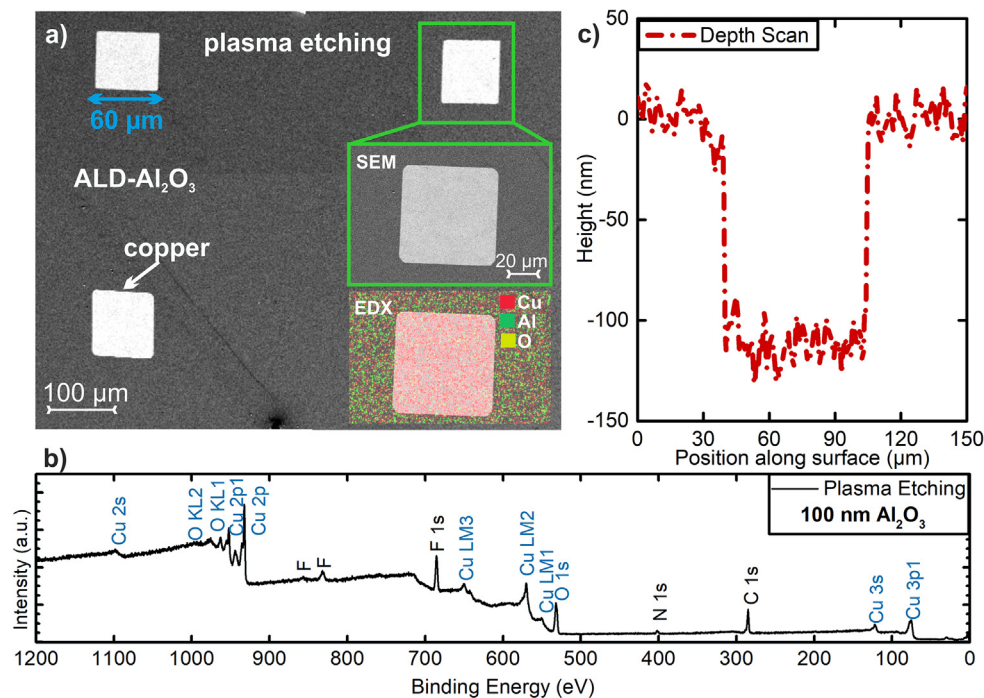
**Fig. 6.** SEM images of copper–copper connection formed in Cu–Al<sub>2</sub>O<sub>3</sub>–FR4 multilayers by CO<sub>2</sub> laser drilling and electroplated copper filling. (a) Cross-section of the copper via (b) with higher magnification.

short time from the thin Al<sub>2</sub>O<sub>3</sub> layer, and the temperature on the surface could not be increased enough to evaporate the Al<sub>2</sub>O<sub>3</sub> layer. Moreover, several other mechanisms are expected to play in 100-nm thick Al<sub>2</sub>O<sub>3</sub> as the layers are thin [21]. Therefore, direct comparison with known literature is not working for such thin ALD-Al<sub>2</sub>O<sub>3</sub> layers, especially on the copper, which acts as a heat sink below the Al<sub>2</sub>O<sub>3</sub>.

### 3.4. Micromachining of Al<sub>2</sub>O<sub>3</sub> by plasma etching

Plasma etching was firstly studied on a Cu–Al<sub>2</sub>O<sub>3</sub> thin film system, where a 100-nm thick Al<sub>2</sub>O<sub>3</sub> film was deposited on copper. Plasma etching was performed by a CHF<sub>3</sub>/O<sub>2</sub> gas mixture and application of RF plasma source. On the Al<sub>2</sub>O<sub>3</sub> layer, the 60-μm structures were patterned. The etching results using SEM, surface profilometer, and XPS analysis are given in Fig. 7.

The plasma etching mechanism between Al<sub>2</sub>O<sub>3</sub> and CHF<sub>3</sub>/O<sub>2</sub> (or CF<sub>4</sub>/O<sub>2</sub>) [73] plasma has been previously proposed [74]. In the CHF<sub>3</sub>/O<sub>2</sub> plasma mixture, the main chemically active species are fluorine atoms ([F<sup>+</sup>]). The presence of O<sub>2</sub> plasma increases [F<sup>+</sup>] species since O or O<sub>2</sub> reacts with CF<sub>x</sub> radicals to form volatile CO. With the absorption of CF<sub>x</sub> radicals on the surface of Al<sub>2</sub>O<sub>3</sub>, AlO<sub>x</sub>F<sub>y</sub> or Al<sub>x</sub>F<sub>y</sub> is formed after a deterioration of the Al–O bond. Ion species stimulate desorption of AlO<sub>x</sub>F<sub>y</sub> or Al<sub>x</sub>F<sub>y</sub> from the surface at the end of the etching process [74]. According to the proposed chemical reactions, the etching of 100-nm thick Al<sub>2</sub>O<sub>3</sub> film was reached in 15.4 min, corresponding to a 6.5 nm/min etching rate. The structuring of Al<sub>2</sub>O<sub>3</sub> film is presented by SEM image in Fig. 7a. As copper has a higher atomic number than both Al and O, the brighter areas are attributed to the copper. No Al atoms were detected inside the structured region according to EDX-elemental mapping, which is in good agreement with the SEM image and indicates the success-



**Fig. 7.** Micromachining of 100-nm thick Al<sub>2</sub>O<sub>3</sub> film on copper by plasma etching. (a) SEM images after plasma etching (60 μm square structures with RF plasma and CHF<sub>3</sub>/O<sub>2</sub> gas mixture). The higher magnification of SEM image and EDX analysis is given in the inset. (b) XPS survey spectra inside the 60-μm structure after plasma etching. (c) Line scan with profilometer along the surface after plasma etching.

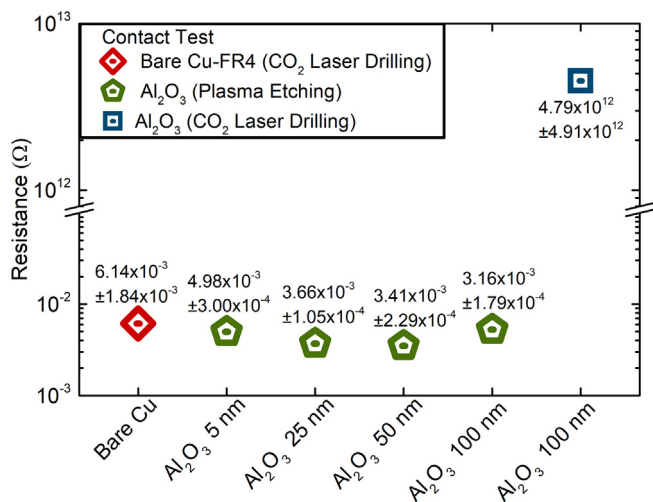
ful structuring of Al<sub>2</sub>O<sub>3</sub> film on copper by plasma etching. This indication was further supported by XPS analysis on the etched region. According to survey spectra given in Fig. 7b, copper and oxygen were detected on the surface without the contribution of aluminum. The O atoms were attributed to the oxidation of copper after etching, additional with C and F, which come from plasma species and environment. The depth of the 60 μm-etched structures was scanned by a profilometer, given in Fig. 7c. The 100-nm depth corresponding to the Al<sub>2</sub>O<sub>3</sub> film thickness was measured. The surface scan further revealed that plasma etching was stopped on the surface of copper.

Plasma etching was secondly studied on the Cu-Al<sub>2</sub>O<sub>3</sub>-FR4 layer system using microwave plasma (Fig. 4a). The micromachining of the Al<sub>2</sub>O<sub>3</sub> layer was investigated using the methods described in the previous section. After removing the FR4 layer by CO<sub>2</sub> laser following the method described above, the CF<sub>4</sub>/O<sub>2</sub> plasma etching was performed by microwave plasma source on Al<sub>2</sub>O<sub>3</sub> films (as CO<sub>2</sub> laser could not remove the Al<sub>2</sub>O<sub>3</sub> films). The microarrays were obtained using two structuring methods with the same structure, 60-μm diameter, defined in Fig. 4c and 4d. After laser drilling and plasma etching, the microarrays were filled with copper by seed layer deposition and followed by electroplating.

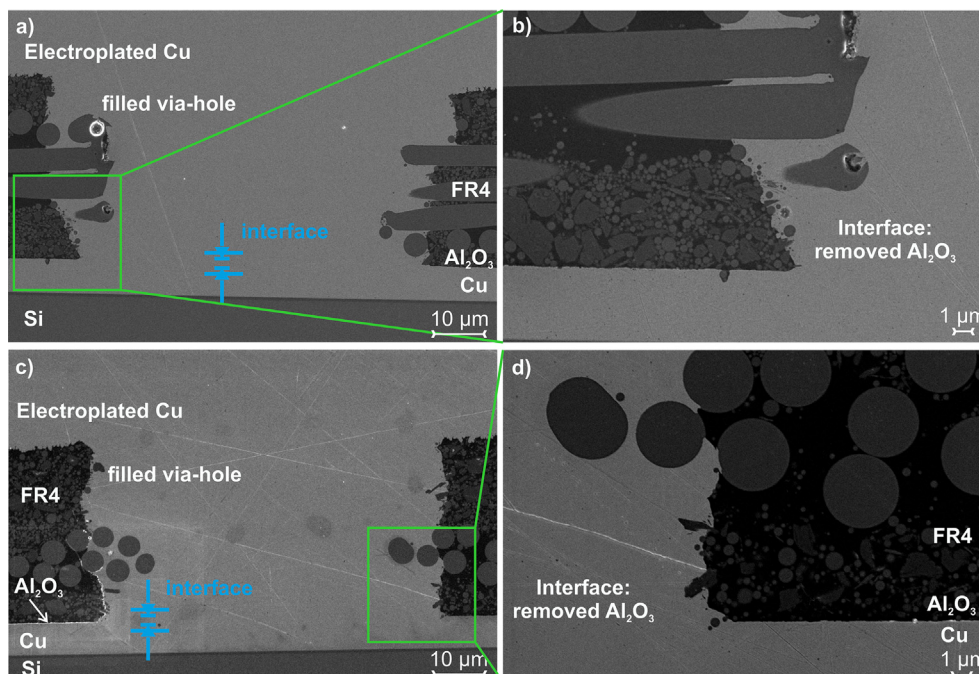
The electrical resistance of the copper-copper connection, measured by the FPP method, is given in Fig. 8. The electrical resistance was given as an average of 16 copper pads. Compared to bare Cu (Cu-FR4 layer), plasma etching of Al<sub>2</sub>O<sub>3</sub> films results in similar contact resistance for the range of 10<sup>-3</sup> Ω. The Al<sub>2</sub>O<sub>3</sub> film was removed entirely from the interface of the copper, indicated by low resistance values. In other words, the same order of magnitude in the resistance for bare Cu and Cu-Al<sub>2</sub>O<sub>3</sub> confirms the high-quality copper-copper connection. Additionally, plasma etching was performed on different thicknesses of Al<sub>2</sub>O<sub>3</sub> films. The thickness variation between 5 nm and 100 nm showed the same order of magnitude contact resistance, representing the reliable copper-copper connection.

The electrical resistance measurement was further supported by cross-section analysis. The cross-section of Cu-via formed on the Cu substrate protected by 5-nm thick Al<sub>2</sub>O<sub>3</sub> film is given in Fig. 9a and higher magnification in 9b. The Al<sub>2</sub>O<sub>3</sub> thin layer was not detected on the interface of copper-copper interconnection. The clean interface of the copper-copper connection, without the residual of Al<sub>2</sub>O<sub>3</sub> film, was also observed on the cross-section of a 100-nm thick Al<sub>2</sub>O<sub>3</sub> film, represented in Fig. 9c and 9d. Even though some glass fibers of the FR4 layer were partially found to overlap into the via-hole, no effect was observed on the electrical connection.

The experimental results showed that plasma etching by RF and microwave sources successfully removed the Al<sub>2</sub>O<sub>3</sub> thin films for

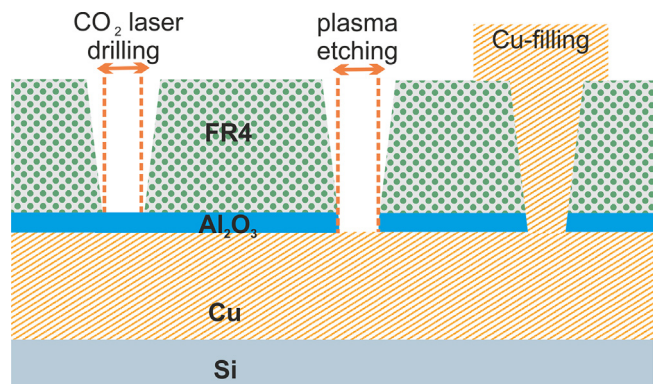


**Fig. 8.** The electrical resistance of copper vias drilled by CO<sub>2</sub> laser and etched by plasma. Electrical resistance is given as an average from 16 contact positions on the microarray. The different thickness variations of Al<sub>2</sub>O<sub>3</sub> film, between 5 nm and 100 nm, are additionally represented. The CO<sub>2</sub> laser drilling result for the 100-nm Al<sub>2</sub>O<sub>3</sub> film is additionally presented.



**Fig. 9.** SEM images of copper-copper connection formed in Cu-Al<sub>2</sub>O<sub>3</sub>-FR4 multilayers by CO<sub>2</sub> laser drilling, plasma etching, and electroplated copper filling. (a) Cross-section of the copper via for 5-nm thick Al<sub>2</sub>O<sub>3</sub> film (b) with higher magnification. (c) Cross-section of the copper via for 100-nm thick Al<sub>2</sub>O<sub>3</sub> film (d) with higher magnification.





**Fig. 10.** Schematic representation of structuring approach for Cu-Al<sub>2</sub>O<sub>3</sub>-FR4 layers on Si by CO<sub>2</sub> laser drilling and plasma etching.

structuring microarrays. Moreover, no mechanical damage was microscopically observed on copper and through the structure, indicating the reliable copper-copper connection. The plasma etching of Cu-Al<sub>2</sub>O<sub>3</sub>-FR4 multilayers was able to structure selectively without using an etching mask. According to the Cu-FR4 layer, the etching rate of FR4 was found 0.7 μm/ 6 min. Therefore, FR4 is thick enough to survive the etching process as a mask. However, we would like to stress that the main removal mechanism for FR4 is laser irradiation. The top layer, ~40-μm thick FR4, was selectively removed by CO<sub>2</sub> laser, and obtained microarray structures acted as a mask for plasma etching, which provides solvent-free structuring. No additional steps for mask preparation and mask etching are necessary for Cu-Al<sub>2</sub>O<sub>3</sub>-FR4 multilayers structuring. The schematic representation of the impact of laser drilling and plasma etching on micromachining is given in Fig. 10. After CO<sub>2</sub> laser drilling, plasma etching was performed and followed by copper filling, allowing multilevel interconnections used for microvias in PCB manufacturing. The quality of the vertically interconnected copper was demonstrated on Cu-Al<sub>2</sub>O<sub>3</sub>-FR4 multilayers without degradation of copper, which can provide 3D design flexibility for large-scale complex metals in semiconductor technology with thinner passivation layers.

#### 4. Conclusions

In summary, we studied the micromachining of ALD-Al<sub>2</sub>O<sub>3</sub> passivation layers by CO<sub>2</sub> laser drilling and plasma etching for establishing a reliable interface for copper-copper interconnects. The Cu-Al<sub>2</sub>O<sub>3</sub>-FR4 layer systems, which were adopted from PCB technology, were investigated to illustrate the applicability of ALD materials in copper interconnection fabrication.

The micromachining of Al<sub>2</sub>O<sub>3</sub> thin films was first analyzed by simulation of a CO<sub>2</sub> laser drilling process. The numerical analysis showed that the temperature on the surface is not sufficient to evaporate a 100-nm thick Al<sub>2</sub>O<sub>3</sub> layer by three CO<sub>2</sub> laser pulses. According to the experimental studies, electrical contact tests, and cross-section analysis confirmed that the CO<sub>2</sub> laser drilling alone is not capable of removing the ALD-Al<sub>2</sub>O<sub>3</sub> thin films without damaging the underlying copper films.

Plasma etching was shown to be effective in the micromachining of Al<sub>2</sub>O<sub>3</sub> layers. A reliable copper-copper connection was supported by electrical contact tests and cross-section analyses. The described CO<sub>2</sub> laser drilling followed by plasma etching successfully removed the encapsulation layers of the Cu-Al<sub>2</sub>O<sub>3</sub>-FR4 multilayer system. The FR4 layer was removed by CO<sub>2</sub> laser drilling and the Al<sub>2</sub>O<sub>3</sub> layer by the plasma etching step that followed.

We believe that the results of this work are essential for the development of complex 3D metal interconnects that require minimization in size and maximization in performance with numerous potential applications ranging from the printed circuit board, microwell arrays, electronic packaging up to semiconductor devices.

#### Declaration of Competing Interest

The authors declare that they have no known competing financial interests or personal relationships that could have appeared to influence the work reported in this paper.

#### Acknowledgments

Authors thank Marion Hagel for plasma etching of Cu-Al<sub>2</sub>O<sub>3</sub> samples, Stephan Schmid for profilometer surface scan, Gerd Maier, Peter Schützendübe and Gunter Richter for GI-XRD and XPS analysis, Felicitas Predel for cross-section preparation, Markus Ost and Alexander Mann for contact test measurements, and Erkan Bektas for simulation analysis. Last but not least, Bernd Ludescher, Umüt T. Sanli, Kay Essig, Lutz Müller, Herbeth Gruhn, Ingo Henkel and Gabriele Ernst are gratefully acknowledged for their kind support.

#### Appendix A. Supplementary material

Supplementary data to this article can be found online at <https://doi.org/10.1016/j.matdes.2021.110114>.

#### References

- [1] S.M. George, Atomic Layer Deposition: An Overview, *Chem. Rev.* 110 (1) (2010) 111–131.
- [2] G.C. Correa, B.o. Bao, N.C. Strandwitz, Chemical Stability of Titania and Alumina Thin Films Formed by Atomic Layer Deposition, *ACS Appl. Mater. Interfaces* 7 (27) (2015) 14816–14821.
- [3] A.I. Abdulagatov, Y. Yan, J.R. Cooper, Y. Zhang, Z.M. Gibbs, A.S. Cavanagh, R.G. Yang, Y.C. Lee, S.M. George, Al<sub>2</sub>O<sub>3</sub> and TiO<sub>2</sub> Atomic Layer Deposition on Copper for Water Corrosion Resistance, *ACS Appl. Mater. Interfaces* 3 (12) (2011) 4593–4601.
- [4] G.e. He, S. Lu, W. Xu, S. Szunerits, R. Boukherroub, H. Zhang, Controllable Growth of Durable Superhydrophobic Coatings on a Copper Substrate via Electrodeposition, *Phys. Chem. Chem. Phys.* 17 (16) (2015) 10871–10880.
- [5] M. Leskela, M. Ritala, Atomic Layer Deposition Chemistry: Recent Developments and Future Challenges, *Angew. Chem. Int. Ed. Engl.* 42 (45) (2003) 5548–5554.
- [6] H. Tiznado, F. Zaera, Surface Chemistry in the Atomic Layer Deposition of TiN Films from TiCl<sub>4</sub> and Ammonia, *J. Phys. Chem. B* 110 (27) (2006) 13491–13498.
- [7] E. Coy, L. Yate, Z. Kabacińska, M. Jancelewicz, S. Jurga, I. Iatsunskiy, Topographic Reconstruction and Mechanical Analysis of Atomic Layer Deposited Al<sub>2</sub>O<sub>3</sub>/TiO<sub>2</sub> Nanolaminates by Nanoindentation, *Mater. Des.* 111 (2016) 584–591.
- [8] M.D. Anderson, B. Aitchison, D.C. Johnson, Corrosion Resistance of Atomic Layer Deposition-Generated Amorphous Thin Films, *ACS Appl. Mater. Interfaces* 8 (44) (2016) 30644–30648.
- [9] A.C. Bronnberg, C. Höhn, R. van de Krol, Probing the Interfacial Chemistry of Ultrathin ALD-Grown TiO<sub>2</sub> Films: An In-Line XPS Study, *J. Phys. Chem. C* 121 (10) (2017) 5531–5538.
- [10] Z. Chai, Y. Liu, J. Li, X. Lu, D. He, Ultra-thin Al<sub>2</sub>O<sub>3</sub> Films Grown by Atomic Layer Deposition for Corrosion Protection of Copper, *RSC Adv.* 4 (92) (2014) 50503–50509.
- [11] V. Cremers, G. Rampelberg, K. Baert, S. Abrahami, N. Claes, T.M. de Oliveira, H. Terryn, S. Bals, J. Dendooven, C. Detavernier, Corrosion Protection of Cu by Atomic Layer Deposition, *J. Vac. Sci. Technol. A* 37 (6) (2019) 060902, <https://doi.org/10.1116/1.5116136>.
- [12] J.S. Daubert, G.T. Hill, H.N. Gotsch, A.P. Gremaud, J.S. Ovental, P.S. Williams, C.J. Oldham, G.N. Parsons, Corrosion Protection of Copper Using Al<sub>2</sub>O<sub>3</sub>, TiO<sub>2</sub>, ZnO, HfO<sub>2</sub>, and ZrO<sub>2</sub> Atomic Layer Deposition, *ACS Appl. Mater. Interfaces* 9 (4) (2017) 4192–4201.
- [13] S. Mirhashemihaghighi, J. Światowska, V. Maurice, A. Seyeux, L.H. Klein, E. Salmi, M. Ritala, P. Marcus, Interfacial Native Oxide Effects on the Corrosion Protection of Copper Coated with ALD Alumina, *Electrochim. Acta* 193 (2016) 7–15.
- [14] S. Mirhashemihaghighi, J. Światowska, V. Maurice, A. Seyeux, L.H. Klein, E. Salmi, M. Ritala, P. Marcus, The Role of Surface Preparation in Corrosion

- Protection of Copper with Nanometer-thick ALD Alumina Coatings, *Appl. Surf. Sci.* 387 (2016) 1054–1061.
- [15] S.E. Potts, L. Schmalz, M. Fenker, B. Díaz, J. Światowska, V. Maurice, A. Seyeux, P. Marcus, G. Radnóczy, L. Tóth, W.M.M. Kessels, Ultra-Thin Aluminium Oxide Films Deposited by Plasma-Enhanced Atomic Layer Deposition for Corrosion Protection, *J. Electrochem. Soc.* 158 (5) (2011) C132–C138.
- [16] S. Mirhashemighighi, J. Światowska, V. Maurice, A. Seyeux, L.H. Klein, E. Härkönen, M. Ritala, P. Marcus, Electrochemical and Surface Analysis of the Corrosion Protection of Copper by Nanometer-Thick Alumina Coatings Prepared by Atomic Layer Deposition, *J. Electrochem. Soc.* 162 (8) (2015) C377–C384.
- [17] Ž.Z. Tasić, M.B. Petrović Mihajlović, M.B. Radovanović, M.M. Antonijević, Milan & Antonijević, New Trends in Corrosion Protection of Copper, *Chem. Pap.* 73 (9) (2019) 2103–2132.
- [18] X.-H. Zhang, X.-X. Li, H. Chen, T.-B. Li, W. Su, S.-D. Guo, Investigation on Microstructure and Properties of Cu–Al<sub>2</sub>O<sub>3</sub> Composites Fabricated by a Novel in-situ Reactive Synthesis, *Mater. Des.* 92 (2016) 58–63.
- [19] R. Schoepner, C. Ferguson, L. Pethö, C. Guerra Nuñez, A.A. Taylor, M. Polyakov, B. Putz, J.M. Breguet, I. Utke, J. Michler, Interfacial Adhesion of Alumina Thin Films Over the Full Compositional Range of Ternary FCC Alloy Films: A Combinatorial Nanoindentation Study, *Mater. Des.* 193 (2020) 108802.
- [20] G. Dogan, U.T. Sanli, K. Hahn, L. Müller, H. Gruhn, C. Silber, G. Schütz, C. Grévent, K. Keskinbora, In Situ X-ray Diffraction and Spectro-Microscopic Study of ALD Protected Copper Films, *ACS Appl. Mater. Interfaces* 12 (29) (2020) 33377–33385.
- [21] R. Bellini, R. Geremia, S. Norval, G. Fichet, D. Karnakis, Laser Thin Film Patterning for Rapid Prototyping and Customised Production of Flexible Electronics Devices, *J. Laser Micro/Nanoeng.* 11 (3) (2016) 388–394.
- [22] S.A. Mastud, M. Garg, R. Singh, S.S. Joshi, Recent Developments in the Reverse Micro-Electrical Discharge Machining in the Fabrication of Arrayed Micro-Features, Proceedings of the Institution of Mechanical Engineers, Part C: Journal of Mechanical Engineering Science 226 (2) (2011) 367–384.
- [23] A.C.M. Peixoto, S.B. Goncalves, A.F.D. Silva, N.S. Dias, J.H. Correia, Neural Electrode Array Based on Aluminum: Fabrication and Characterization, *IEEE Sens. J.* 13 (9) (2013) 3319–3324.
- [24] T. Shibata, S. Yukizono, T. Kawashima, M. Nagai, T. Kubota, M. Mita, Modified Imprinting Process Using Hollow Microneedle Array for Forming Through Holes in Polymers, *Microelectron. Eng.* 88 (8) (2011) 2121–2125.
- [25] G. Wang, E.C. Folk, F. Barlow, A. Elshabini, Fabrication of Microvias for Multilayer LTCC Substrates, *IEEE Trans. Electron. Packag. Manuf.* 29 (1) (2006) 32–41.
- [26] S.S. Zakariyah, P.P. Conway, D.A. Hutt, K. Wang, D.R. Selviah, CO<sub>2</sub> Laser Micromachining of Optical Waveguides for Interconnection on Circuit Boards, *Opt. Lasers Eng.* 50 (12) (2012) 1752–1756.
- [27] M. Zhao, L. Du, L. Qi, Y. Li, Y.u. Li, X. Li, Numerical Simulations and Electrochemical Experiments of the Mass Transfer of Microvias Electroforming under Ultrasonic Agitation, *Ultrason. Sonochem.* 48 (2018) 424–431.
- [28] H.Y. Zheng, D.K.Y. Low, X.C. Wang, G.C. Lim, A Process Study of Laser Micro-Drilling Vias for Wafer-Level Chip Scale Packaging, *Pacific Int. Conf. Appl. Lasers Opt.* (2006) 334–338.
- [29] Z. Lin, Y. Takahashi, T. Murata, M. Takeda, K. Ino, H. Shiku, T. Matsue, Electrochemical Gene-Function Analysis for Single Cells with Addressable Microelectrode/Microwell Arrays, *Angew Chem. Int. Ed Engl.* 48 (11) (2009) 2044–2046.
- [30] J. Yong, F. Chen, Q. Yang, D. Zhang, H. Bian, G. Du, J. Si, X. Meng, X. Hou, Controllable Adhesive Superhydrophobic Surfaces Based on PDMS Microwell Arrays, *Langmuir* 29 (10) (2013) 3274–3279.
- [31] S.S. Iyer, S. Jangam, B. Vaisband, Silicon Interconnect Fabric: A Versatile Heterogeneous Integration Platform for AI Systems, *IBM J. Res. Developm.* 63 (6) (2019) 5:1–5:16.
- [32] E.J.R. Phua, M. Liu, B. Cho, Q. Liu, S. Amini, X. Hu, C.L. Gan, Novel High Temperature Polymeric Encapsulation Material for Extreme Environment Electronics Packaging, *Mater. Des.* 141 (2018) 202–209.
- [33] R. Kaysar, M. Ahsan, A Review on Laser Processing in Electronic and MEMS Packaging, *J. Electron. Packag.* 139(030801) (September) (2017) 1–11.
- [34] H. Yoo, H. Park, S. Yoo, S. On, H. Seong, S.G. Im, J.J. Kim, Highly Stacked 3D Organic Integrated Circuits with via-hole-less Multilevel Metal Interconnects, *Nat. Commun.* 10 (1) (2019) 2424.
- [35] P.-T. Lee, C.-H. Chang, C.-Y. Lee, Y.-S. Wu, C.-H. Yang, C.-E. Ho, High-speed Electrodeposition for Cu Pillar Fabrication and Cu Pillar Adhesion to an Ajinomoto Build-up Film (ABF), *Mater. Des.* 206 (2021) 109830, <https://doi.org/10.1016/j.matdes.2021.109830>.
- [36] F. Liu, C. Nair, G. Khurana, A. Watanabe, B.H. DeProspo, A. Kubo, C.P. Lin, T. Makita, N. Watanabe, R.R. Tummala, in: Next Generation of 2–7 Micron Ultra-Small Microvias for 2.5D Panel Redistribution Layer by Using Laser and Photolithography Technologies, IEEE Las Vegas, NV, USA, 2019, pp. 924–930.
- [37] L. Rihakova, H. Chmelickova, Laser Micromachining of Glass, Silicon, and Ceramics, *Adv. Mater. Sci. Eng.* 2015 (2015) 1–6.
- [38] T. Ge, W. Zhao, X. Wu, Y. Wu, L.u. Shen, X. Ci, Y. He, Design Alternate Epoxy-reduced Graphene Oxide/Epoxy-Zinc Multilayer Coatings for Achieving Long-term Corrosion Resistance for Cu, *Mater. Des.* 186 (2020) 108299, <https://doi.org/10.1016/j.matdes.2019.108299>.
- [39] C.J. Ramirez-an-Juan, J.P. Padilla-Martinez, P. Moran-Zaca, R. Ramos-Garcia, Micro-hole Drilling in Thin Films with CW Low Power Lasers, *Opt. Mater. Exp.* 1 (4) (2011) 598–603.
- [40] M. Miao, Y. Jin, H. Liao, L. Zhaol, Y. Zhu, X. Sun, Y. Guol, Research on Deep RIE-based Through-Si-Via Micromachining for 3-D System-in-package Integration, in: IEEE (Conference of the 2009 4th IEEE International), 2009, pp. 90–93.
- [41] C. Dunsy, H. Matsumoto, G. Simenson, High-speed Microvia Formation with UV Solid State Lasers, RIKEN Review 43(2nd International Symposium on Laser Precision Microfabrication (LPM 2001)) (2002) 80–88.
- [42] Y. Chen, W. He, X. Chen, C. Wang, Z. Tao, S. Wang, G. Zhou, M. Moshrefi-Torbati, Plating Uniformity of Bottom-up Copper Pillars and Patterns for IC Substrates with Additive-assisted Electrodeposition, *Electrochim. Acta* 120 (2014) 293–301.
- [43] Y.L. Cheng, C.Y. Lee, Y.L. Huang, Copper Metal for Semiconductor Interconnects, *IntechOpen* (2018).
- [44] A. Renbi, J. Delsing, A Novel Production Process for 10- $\mu$ m Microvias, *Int. Symposium Microelectron.* 2017 (1) (2017) 468–472.
- [45] Y. Suzuki, R. Furuuya, V. Sundaram, R.R. Tummala, Demonstration of 10- $\mu$ m Microvias in Thin Dry-Film Polymer Dielectrics for High-Density Interposers, *IEEE Trans. Compon. Packag. Manuf. Technol.* 5 (2) (2015) 194–200.
- [46] K.F. Tamrin, S.S. Zakariyah, N.A. Sheikh, Multi-criteria Optimization in CO<sub>2</sub> Laser Ablation of Multimode Polymer Waveguides, *Opt. Lasers Eng.* 75 (2015) 48–56.
- [47] J.-S. Han, Z.-Y. Tan, K. Sato, M. Shikida, Three-Dimensional Interconnect Technology on a Flexible Polyimide Film, *J. Microelectromech. Microeng.* 14 (1) (2004) 38–48.
- [48] K. Murakami, K. Minami, M. Esashi, High Aspect Ratio Fabrication Method Using O<sub>2</sub> RIE and Electroplating, *Microsyst. Technol.* 1 (1995) 137–142.
- [49] T.N.T. Nguyen, N.E. Lee, Deep Reactive Ion Etching of Polyimide for Microfluidic Applications, *J. Korean Phys. Soc.* 51 (3) (2007) 984–1968.
- [50] A. Furuuya, F. Shimokawa, T. Matsuura, R. Sawada, Fabrication of Fluorinated Polyimide Microgrids Using Magnetically Controlled Reactive Ion Etching (MC-RIE) and Their Applications to an Ion Drag Integrated Micropump, *J. Microelectromech. Microeng.* 6 (3) (1996) 310–319.
- [51] G. Turban, M. Rapaux, Dry Etching of Polyimide in O<sub>2</sub>-CF<sub>4</sub> and O<sub>2</sub>-SF<sub>6</sub> Plasmas, *J. Electrochem. Soc.* 130 (1983) 2231–2236.
- [52] F.D. Egitto, Plasma Etching of Organic Materials. I. Polyimide in O<sub>2</sub>-CF<sub>4</sub>, *J. Vac. Sci. Technol. B: Microelectron. Nanometer Struct.* 3 (3) (1985) 893.
- [53] E. Higurashi, O. Ohguchi, T. Tamamura, H. Ukita, R. Sawada, Optically Induced Rotation of Dissymmetrically Shaped Fluorinated Polyimide Micro-objects in Optical Traps, *J. Appl. Phys.* 82 (6) (1997) 2773–2779.
- [54] M.-Q. Liu, C. Wang, Z. Yao, N.-Y. Kim, Dry Etching and Residue Removal of Functional Polymer Mixed with TiO<sub>2</sub> Microparticles via Inductively Coupled CF<sub>4</sub>/O<sub>2</sub> Plasma and Ultrasonic-treated Acetone for Humidity Sensor Application, *RSC Adv.* 6 (47) (2016) 41580–41586.
- [55] J. Pelletier, Y. Arnal, O. Joubert, Etching Mechanisms of Polymers in Oxygen Microwave Multipolar Plasmas, *Appl. Phys. Lett.* 53 (20) (1988) 1914–1916.
- [56] Y. Sun, C.M. Dunsy, H. Matsumoto, G. Simenson, Microvia Formation with Lasers, *Lasers in Material Processing and Manufacturing*, Photonics Asia 2002.
- [57] M. Kato, N. Araki, K. Isaji, H. Karasaki, Concurrent in-line Inspection System for CO<sub>2</sub> Laser Drilling Machine, *Optoelectronics '99 - Integrated Optoelectronic Dev.* (1999) 269–275.
- [58] X. Ruan, R. Wang, J. Luo, Y. Yao, T. Liu, Experimental and Modeling Study of CO<sub>2</sub> Laser Writing Induced Polyimide Carbonization Process, *Mater. Des.* 160 (2018) 1168–1177.
- [59] Y.Z. Hu, W. He, W.D. Xue, Z.H. Tao, Y.X. Huang, H. Xu, W.Q. Lv, A Parameters Optimization of the CO<sub>2</sub> Laser Drilling Process for HDI Microvia Fabrication, *Applied Mechanics and Materials* 214 (2012) 451–454.
- [60] J. Okada, Y. Okamoto, K. Shudo, M. Yorozu, Modeling of Cu Direct Laser Drilling Process, *J. Micro/Nanoeng.* 7 (3) (2012) 369–374.
- [61] A. Bharatish, M.H.N. Narasimha, B. Anand, C.D. Madhusoodana, G.S. Praveena, M. Krishna, Characterization of Hole Circularity and Heat Affected Zone in Pulsed CO<sub>2</sub> Laser Drilling of Alumina Ceramics, *Opt. Laser Technol.* 53 (2013) 22–32.
- [62] M.F. Chen, W.T. Hsiao, M.C. Wang, K.Y. Yang, Y.F. Chen, A Theoretical Analysis and Experimental Verification of a Laser Drilling Process for a Ceramic Substrate, *Int. J. Adv. Manuf. Technol.* 81 (9–12) (2015) 1723–1732.
- [63] W.T. Hsiao, C.C. Yang, S.F. Tseng, D. Chiang, K.C. Huang, K.M. Lin, M.F. Chen, Surface Modification Nanoporous Titanium Oxide Films Using Continuous Wave CO<sub>2</sub> Laser, *Appl. Phys. A* 122 (4) (2016) 1–8.
- [64] N. Krstulović, S. Shannon, R. Stefanuik, C. Fanara, Underwater-Laser Drilling of Aluminum, *Int. J. Adv. Manuf. Technol.* 69 (5–8) (2013) 1765–1773.
- [65] C.J. Moorhouse, F. Villarreal, J.J. Wendland, H.J. Baker, D.R. Hall, D.P. Hand, CO<sub>2</sub> Laser Processing of Alumina (Al<sub>2</sub>O<sub>3</sub>) Printed Circuit Board Substrates, *IEEE Trans. Electron. Packag. Manuf.* 28 (3) (2005) 249–258.
- [66] F. Preusch, B. Adelman, R. Hellmann, Micromachining of AlN and Al<sub>2</sub>O<sub>3</sub> Using Fiber Laser, *Micromachines* 5 (4) (2014) 1051–1060.
- [67] A.N. Samant, N.B. Dahotre, Absorptivity Transition in the 1.06- $\mu$ m Wavelength Laser Machining of Structural Ceramics, *Int. J. Appl. Ceram. Technol.* 8 (1) (2011) 127–139.
- [68] B.H. Zhou, S.M. Mahdavian, Experimental and Theoretical Analyses of Cutting Nonmetallic Materials by Low Power CO<sub>2</sub>-laser, *J. Mater. Process. Technol.* 146 (2) (2004) 188–192.
- [69] S.P.J. Kischkat, B. Gruska, M. Semtsiv, M. Chashnikova, M. Klinsküller, O. Fedosenko, S. Machulik, A. Aleksandrova, G. Monastyrskiy, Y. Flores, W.T. Masselink, Mid-infrared Optical Properties of Thin Films of Aluminum Oxide, Titanium Dioxide, Silicon Dioxide, Aluminum Nitride, and Silicon Nitride, *Appl. Opt.* 51 (2012) 6789–6798.

- [70] MatWeb 2020. <http://www.matweb.com>.
- [71] M. Khelkhal, F. Herlemont, Determination of Effective Optical Constants of Infrared CO<sub>2</sub> Waveguide Laser Materials, *Appl. Opt.* 31 (21) (1992) 4175–4181.
- [72] S.V. Jadhav, P.M. Pawar, S.S. Wangikar, N.N. Bhostekar, S.T. Pawar, Thermal Management Materials for Advanced Heat Sinks used in Modern Microelectronics, *IOP Conference Series: Materials Science and Engineering* 814 (2020) 12044.
- [73] A. Efremov, K.H. Kwon, A. Morgunov, D. Shabadarova, Comparative Study of CF<sub>4</sub>- and CHF<sub>3</sub>-Based Plasmas for Dry Etching Applications, SPIE, 2016.
- [74] J.W. Kim, Y.C. Kim, W.J. Lee, Reactive Ion Etching Mechanism of Plasma Enhanced Chemically Vapor Deposited Aluminum Oxide Film in CF<sub>4</sub>/O<sub>2</sub> Plasma, *J. Appl. Phys.* 78 (3) (1995) 2045–2049.





## 8. Summary

This thesis aims the use and optimize ALD for Cu corrosion protection and investigate proper method for subsequent micromachining.

The excellent corrosion protection performance of 50 nm thick  $\text{Al}_2\text{O}_3/\text{TiO}_2$  and  $\text{Al}_2\text{O}_3/\text{SiO}_2$  bilayer ALD stacks, was demonstrated at high temperatures against oxidation. The oxidation protection performance was carried out by *in situ* XRD measurements, which allowed direct observation and overview of the evaluation of solid-state phases over time and in response to changing temperature. Furthermore, post factum spectro-macroscopic investigations was applied to reveal the interactions of copper with its protection layers, which could not completely captured by XRD measurements. While ALD bilayers showed excellent protection performance against high temperatures under atmospheric conditions, some morphological changes at the surface level was observed an in-depth microstructural evaluation. Copper migration was observed on both layers, albeit more substantially in  $\text{Al}_2\text{O}_3/\text{TiO}_2$  (5.2 at.%) compared to  $\text{Al}_2\text{O}_3/\text{SiO}_2$  (0.7 at.%). Based on the defect density, copper atoms migrated to the films surface through the defects at high temperatures. These investigations demonstrated that the defect density has to be strictly controlled and minimized for better corrosion protection performance, especially such a thin layers. These observations reveal that the correct identification and the tuning of principal ALD parameters are essential to achieve the best corrosion protection with ALD thin films.

Accordingly, the following study focused on a hybrid approach for optimization processes to improve the experimental design process by identifying the principal parameters and optimizing these specified parameters to minimize ALD film' defect density for maximum corrosion protection. The effect of ALD process parameters and copper surface properties on corrosion protection performance was studied with a model-based study of ALD- $\text{Al}_2\text{O}_3$  thin films for various thickness. ALD process parameters such as deposition temperature, pressure, and pulse time were screened together with copper surface properties such as native oxide layer to decrease defect density and improve protection properties. In this work, the Bayesian Optimization (BO), a machine learning method, is reported the first time for the optimization of ALD- $\text{Al}_2\text{O}_3$  films. Compared to the traditional optimization methods, BO efficiently reached the target optimization goal for an ALD process in only a few steps. The optimized ALD- $\text{Al}_2\text{O}_3$  films were achieved four orders of magnitude reduction in defect density as compared to non-optimized films. Optimized parameters of surface pretreatment using Ar/ $\text{H}_2$  plasma, the deposition temperature above 200 °C, and 60 ms pulse time quadruple the corrosion resistance.

Furthermore, this study shows also an example for the application of machine learning methods and highlights the utilization of machine learning based approaches in addressing the challenging problems in material science and engineering.

Following of the protection performance of ALD thin films, the micro- and nano-structuring properties were addressed, which required for many applications such as printed circuit board, electronic packaging, silicon-integrated fabric, etc. The micromachining of ALD- $\text{Al}_2\text{O}_3$  thin films were implemented to the model-based Cu- $\text{Al}_2\text{O}_3$ -FR4 multilayer system, which is adopted from PCB technology. Micromachining was studied using laser drilling and plasma etching, which are most common methods for industrial applications in semiconductor processes. Results have shown that the  $\text{CO}_2$  laser drilling alone is insufficient to remove the  $\text{Al}_2\text{O}_3$  thin films, which total power of 3.3 mJ was used for three shots with 4  $\mu\text{s}$  pulse duration. However, plasma etching, using  $\text{CF}_4/\text{O}_2$  plasma at 2500 W, successfully removes the encapsulation layer, providing a clean interface for conductive vias to interconnect the top layer of copper to the layers below. As ALD offers an attractive route to achieve high quality protective layers, the enabled use of ALD materials in interconnect fabrication supports further flexibility for the design of finer and more complex 3D structures on semiconductor devices. This work highlights that the micromachining of protective ALD layers is essential for the development of complex 3D metal interconnects that require minimization in size and maximization in performance

## 9. Zusammenfassung

Diese Arbeit zeigt, dass der Schnittpunkt von ALD- und Kupferkorrosion den Anwendungsbereich dünner Schichten als Passivierungsschicht ermöglicht hat. Diese Arbeit konzentriert sich hauptsächlich auf die Anwendung der ALD-Technik auf verschiedene dünne Oxidschichten zum Korrosionsschutz von Kupfer.

Die hervorragende Korrosionsschutzleistung von ALD-Oxidschichten wurde bei hohen Temperaturen gegen Oxidation nachgewiesen. Die Oxidationsschutzleistung wurde durch In-situ-XRD-Messungen durchgeführt, die eine direkte Beobachtung und einen Überblick über die Auswertung von Festkörperphasen über die Zeit und als Reaktion auf Temperaturänderungen erlaubten. Des Weiteren wurden Post-factum-spektroskopische Untersuchungen angewendet, um die Wechselwirkungen von Kupfer mit seinen Schutzschichten aufzudecken, die nicht vollständig durch XRD-Messungen erfasst werden konnten. Während ALD-Doppelschichten unter atmosphärischen Bedingungen eine hervorragende Schutzleistung gegen hohe Temperaturen zeigten, wurden einige morphologische Veränderungen auf Oberflächenebene einer tiefgehenden Gefügebeurteilung beobachtet. Basierend auf der Fehlerdichte wanderten Kupferatome durch die Defekte bei hohen Temperaturen an die Oberfläche der Schichten. Diese Untersuchungen haben gezeigt, dass die Fehlerdichte für ein besseres Korrosionsschutzverhalten, insbesondere solche dünnen Schichten, streng kontrolliert und minimiert werden muss. Diese Beobachtungen zeigen, dass die korrekte Identifizierung und die Anpassung der wichtigsten ALD-Parameter essentiell sind, um den besten Korrosionsschutz mit ALD-Dünnschichten zu erreichen.

Die nachfolgende Studie konzentrierte sich daher auf einen hybriden Ansatz für Optimierungsprozesse zur Verbesserung des experimentellen Designprozesses, indem die wichtigsten Parameter identifiziert und diese spezifizierten Parameter optimiert wurden, um die Fehlerdichte der ALD-Folie für maximaler Korrosionsschutz. Der Einfluss von ALD-Prozessparametern und Kupferoberflächeneigenschaften auf die Korrosionsschutzleistung wurde mit einer modellbasierten Studie von ALD- $\text{Al}_2\text{O}_3$ -Dünnschichten untersucht. ALD-Prozessparameter wie Abscheidetemperatur, Druck und Pulszeit wurden zusammen mit Kupferoberflächeneigenschaften wie nativer Oxidschicht gescreent, um die Fehlerdichte zu verringern und die Schutzeigenschaften zu verbessern. In dieser Arbeit wird erstmals über die Bayesian Optimization (BO), eine maschinelle Lernmethode zur Optimierung von ALD- $\text{Al}_2\text{O}_3$ -Filmen berichtet. Im Vergleich zu den klassischen Optimierungsmethoden hat BO das Ziel-Optimierungsziel für einen ALD-Prozess in wenigen Schritten effizient erreicht. Die

optimierten ALD-  $\text{Al}_2\text{O}_3$ -Filme wurden um vier Größenordnungen gegenüber nicht optimierten Filmen in der Fehlerdichte reduziert. Optimierte Parameter der Oberflächenvorbehandlung mittels  $\text{Ar}/\text{H}_2$ -Plasma, die Abscheidetemperatur über  $200\text{ °C}$  und  $60\text{ ms}$  Pulszeit vervierfachen die Korrosionsbeständigkeit. Darüber hinaus zeigt diese Studie auch ein Beispiel für die Anwendung von Methoden des maschinellen Lernens und zeigt die Nutzung von Ansätzen des maschinellen Lernens bei der Lösung der herausfordernden Probleme in Materialwissenschaft und Technik.

Nach der Schutzleistung von ALD-Dünnschichten wurden die mikro- und nanostrukturierenden Eigenschaften adressiert, die für viele Anwendungen wie Leiterplatte, elektronische Verpackung, Silizium-Verbundgewebe, etc. Durch gezieltes und lokales Entfernen der ALD-Dünnschichten wird die obere Kupferschicht mit den darunterliegenden Schichten mittels Laserbohren und Plasmaätzen erfolgreich miteinander verbunden. Diese Arbeit zeigt, dass die Mikrobearbeitung von ALD-Schutzschichten für die Zukunft von feineren und 3D-komplexen Verbindungen auf Halbleiterbauelementen essentiell ist.

## 10. Acknowledgements

There are a number of people whose support over the past three years have made this dissertation possible. First and foremost, I would like to thank my supervisors, Dr. Kahraman Keskinbora and Prof. Dr. Gisela Schütz. Their advice, direction and sheer positivity throughout all aspects of this PhD have been invaluable. I would like especially thank my industrial another supervisor, Dr. Corinnè Grevent for her knowledge, support and guidance throughout this thesis. I want to extend my gratitude to all members of Department of Modern Magnetic Systems at Max Planck Institute for Intelligent Systems and Group of Engineering Integrated Circuits Methods, Tools Technologies (EIM4) at Robert Bosch GmbH, who have all contributed to a valuable experience during the project.

I would like to express my special thanks to Dr. Umut Tunca Sanli for providing me with the opportunity to spend time at ALD-Lab to learn essential deposition and characterization methods. Additionally, several results presented in this thesis would not have been possible without the close collaboration with many groups. I am also grateful to committee members, Prof. Dr. h.c. Guido Schmitz and Prof. Dr. Thomas Schleid for agreeing to review my thesis at this short notice.

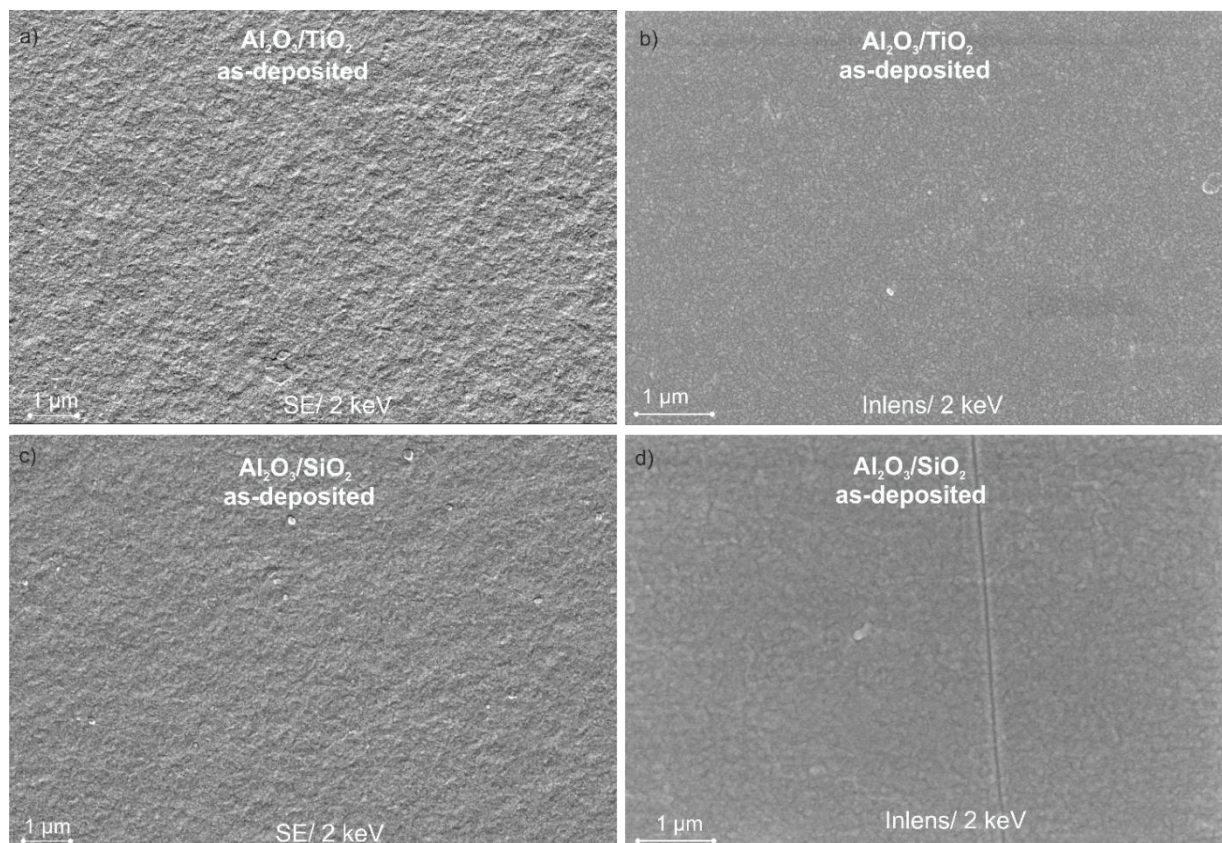
Love and thanks to my sister, Gonca, for her support and encouragement over the years as well as to my parents. Thank you to my friends for the support and encouragement.



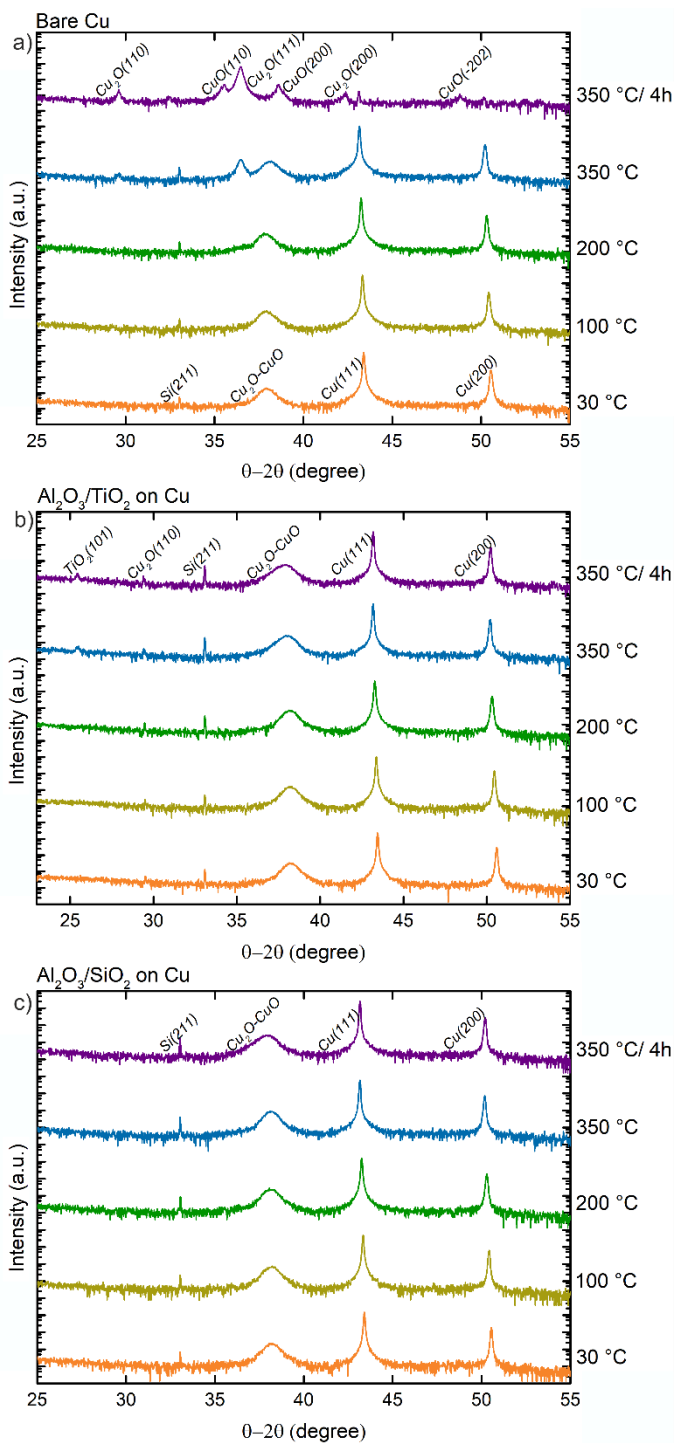


## 11. Appendix

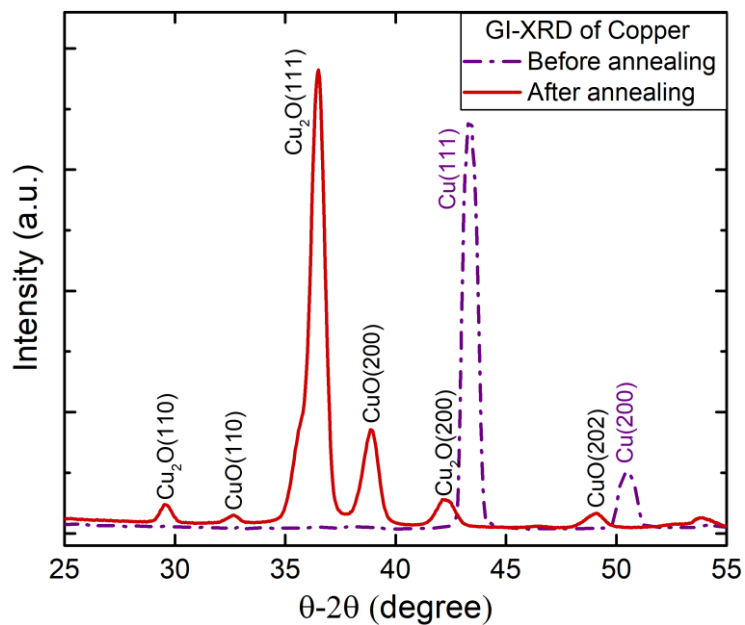
### 11.1. Supporting Information: *In Situ* X-ray Diffraction and Spectro-Microscopic Study of ALD Protected Copper Films



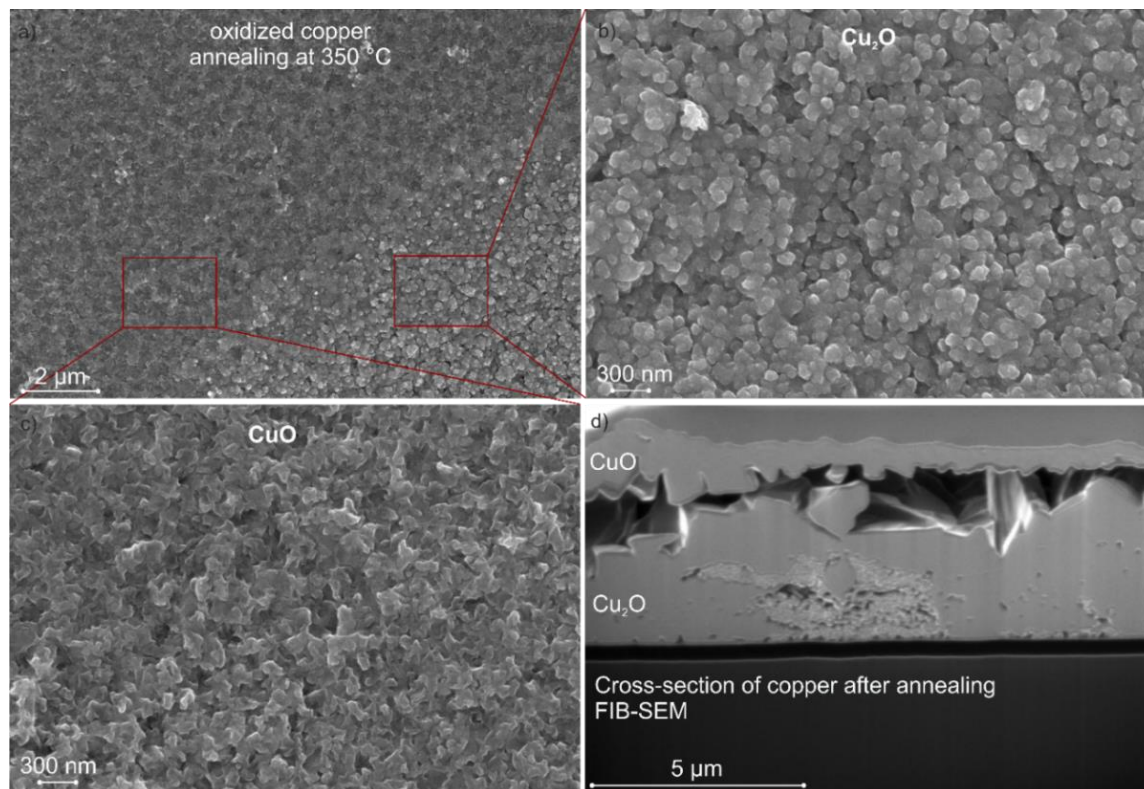
**Figure S1.** Surface properties of a-b)  $\text{Al}_2\text{O}_3/\text{TiO}_2$  and c-d)  $\text{Al}_2\text{O}_3/\text{SiO}_2$  bilayers before annealing. The SEM images were taken in 2 keV with SE (a,c) and Inlens (b,d) detector respectively. The similar morphology observed on the surface for both layers that contributed amorphous ALD layers continued copper' surface properties. Additionally, no void structure is observed on both bilayers.



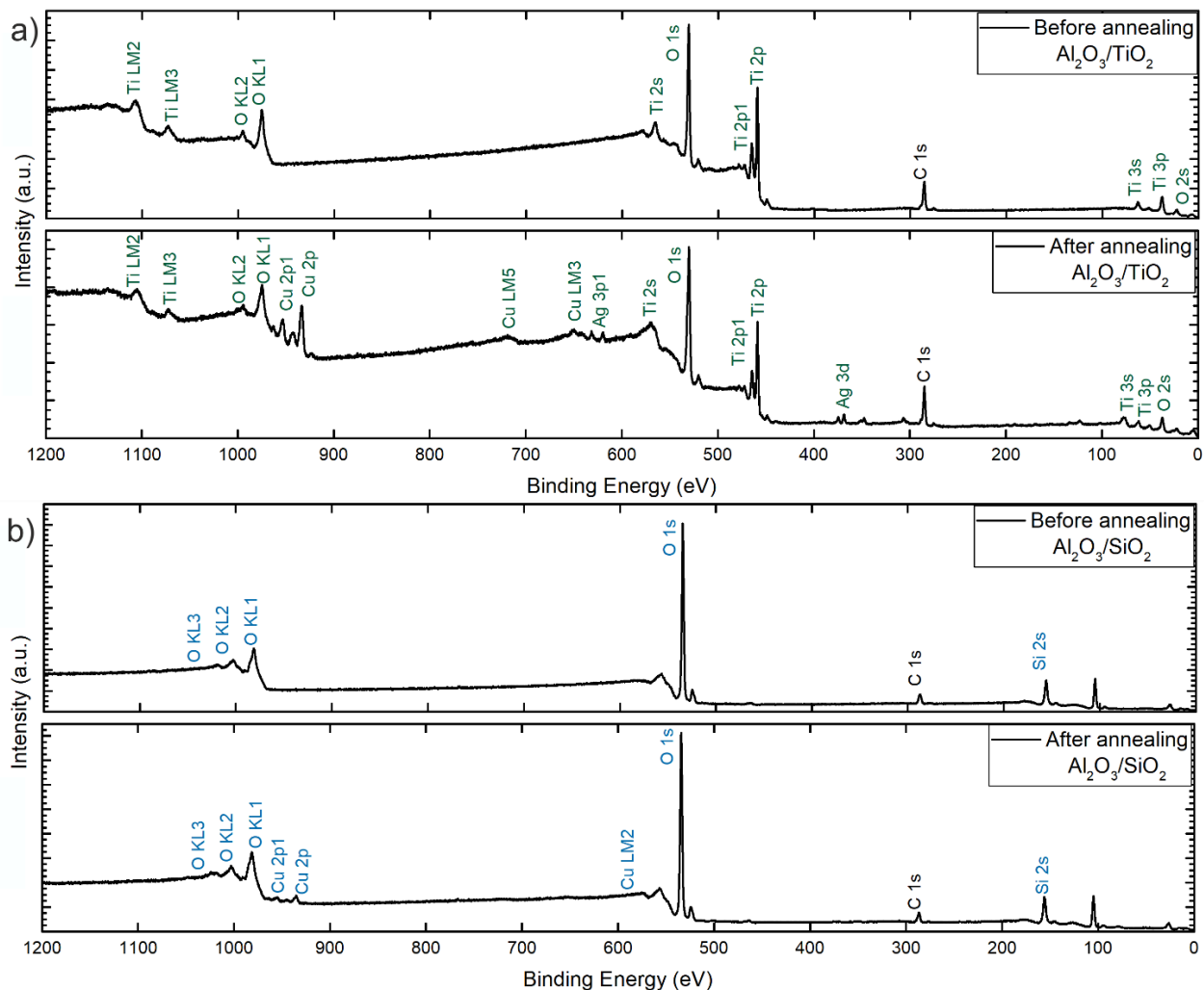
**Figure S2.** Diffraction data of set-point control measurements at 30 °C, 100 °C and 200 °C with additional of annealing at 350 °C. a) Bare copper oxidation started at 350 °C with two main oxide peak separation at  $2\theta=37.5^\circ$  b)  $\text{Al}_2\text{O}_3/\text{TiO}_2$  bilayer showed that amorphous  $\text{TiO}_2$  phase transformed to anatase phase at 350 °C. c)  $\text{Al}_2\text{O}_3/\text{SiO}_2$  diffraction data remained same during heating and annealing



**Figure S3.** GI-XRD of bare copper before annealing and after annealing for 4 hours at 350°C. The copper (111) and (200) peaks completely converted into a mixture of oxide phases.



**Figure S4.** Surface properties of bare copper after 4 hours 350 °C annealing. a) Two different oxide phase of copper were observed in which part b presents the inner part of sample with  $\text{Cu}_2\text{O}$  oxide phase and part c presents the outer part of sample with  $\text{CuO}$  oxide phase. The cross-section of oxidized copper is presented in part d. The huge cavity between the oxide layers was attributed to the thermal stress relaxation during annealing and structural differences in which  $\text{Cu}_2\text{O}$  shows cubic structure ( $\alpha = 4.27 \text{ \AA}$ ) and  $\text{CuO}$  has monoclinic structure ( $a = 0.468 \text{ nm}$ ,  $b = 0.342 \text{ nm}$ ,  $c = 0.512$  and  $\beta = 99.54^\circ$ ).<sup>93</sup> The oxide phases were labeled according to Wan *et al.* observations in “corrosion behavior of copper at elevated temperature” study.<sup>93-94</sup>



**Figure S5.** XPS survey spectra for before and after annealing a) Al<sub>2</sub>O<sub>3</sub>/TiO<sub>2</sub> and b) Al<sub>2</sub>O<sub>3</sub>/SiO<sub>2</sub> bilayers. The atomic percentage of copper for each annealed layer was estimated from the survey spectra over the 50 mm<sup>2</sup> scanned area. The silver (Ag) was detected on Al<sub>2</sub>O<sub>3</sub>/TiO<sub>2</sub> bilayers after annealing due to the using silver paste. According to curve fitting of annealed XPS spectra, the copper was found on both Al<sub>2</sub>O<sub>3</sub>/TiO<sub>2</sub> and Al<sub>2</sub>O<sub>3</sub>/SiO<sub>2</sub> bilayers with 5.2 at.% and 0.7 at.%, respectively.

The energetic electrons penetrate a sample for some distance before they encounter and collide with a specimen atom.<sup>95-98</sup> The penetration depth of electrons largely depends on the accelerating voltage, the material, and the density of the specimen. If the angle of the detector is constant, the penetration depth can be found by Equation S1 where  $\rho$  is the density ( $\text{g/cm}^3$ ) and  $E_0$  is the accelerating voltage (keV).<sup>99</sup> Based on the assumption of 50 nm thick ALD layer, which consists only amorphous  $\text{SiO}_2$  with  $2.2 \text{ g.cm}^3$  density<sup>100</sup>, the penetration depth of electrons was calculated for 5 keV, 2 keV, and 1 keV given in Table S1.

**Equation S1.** The calculation of the penetration depth of electrons ( $x$ )

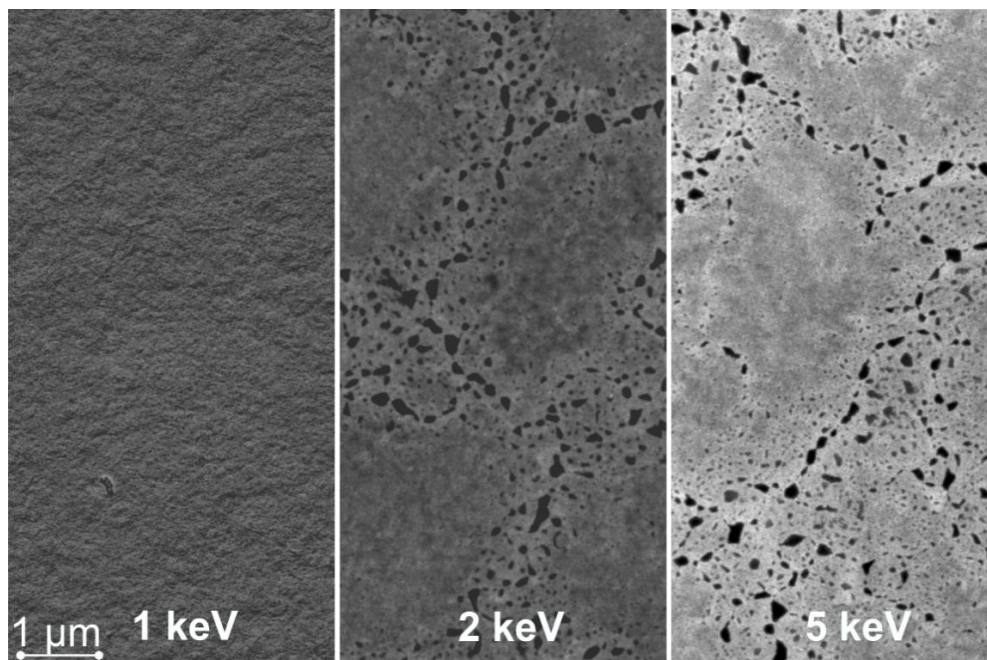
$$x (\mu\text{m}) = \frac{0.1E_0^{1.5}}{\rho}$$

where  $\rho$  is the density ( $\text{g/cm}^3$ ) and  $E_0$  is the accelerating voltage (keV)

**Table S1.** The penetration depth in SEM according to accelerating voltage, calculated for  $\text{Al}_2\text{O}_3/\text{SiO}_2$  layer

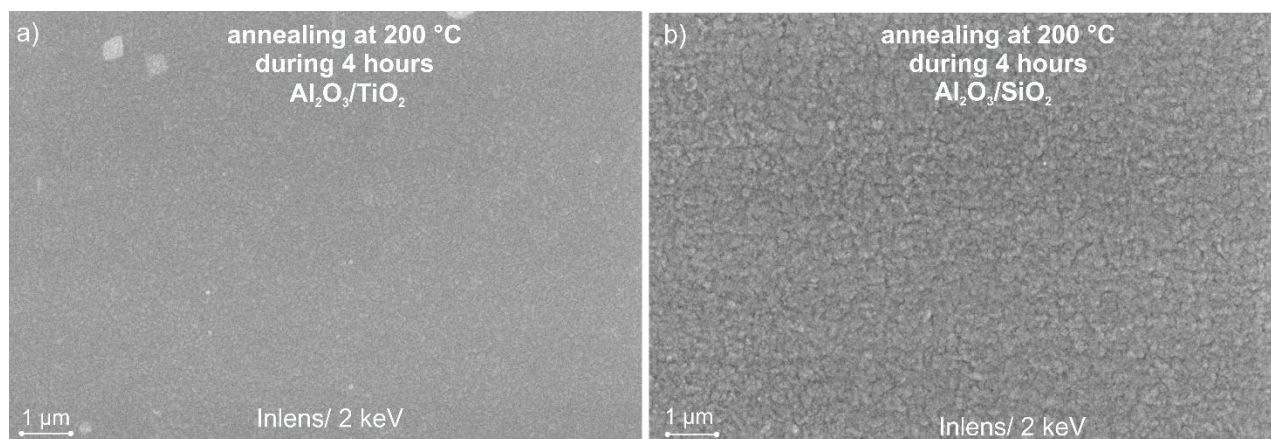
Accelerating Voltage (keV)	Depth of Electron Penetration (nm)
1	46
2	129
5	510



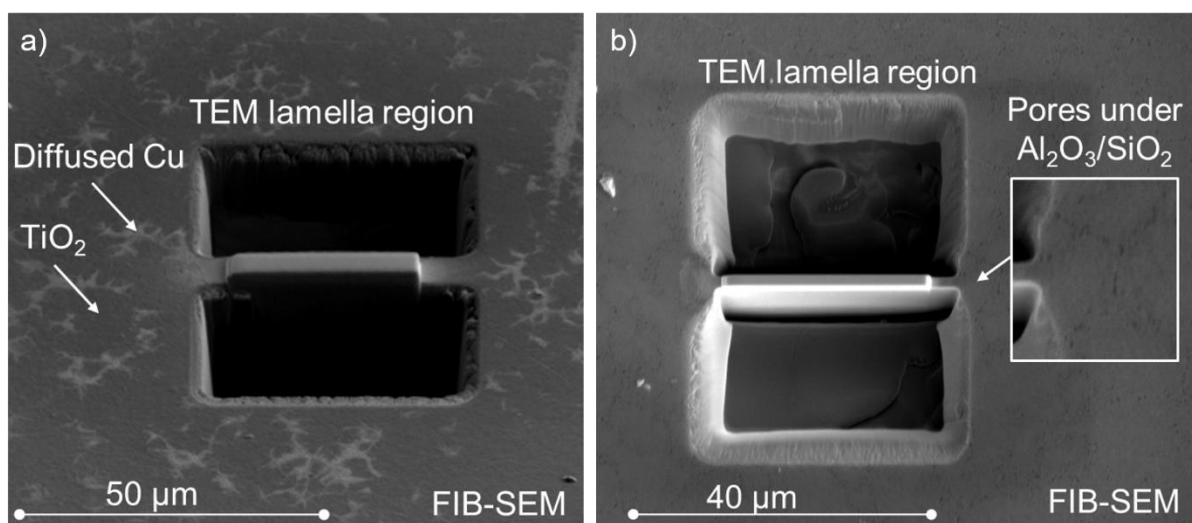


**Figure S6.** The penetration depth of electrons dependency on beam energy for the Al<sub>2</sub>O<sub>3</sub>/SiO<sub>2</sub> bilayer after annealing. The SEM images were taken by InLens detector. While the low beam energy, 1 keV, did not showed the voids, they appeared by increasing the energy to 2 keV and 5 keV. As the penetration depth was increased, it was possible to analyze subsurface that voids were observed.





**Figure S7.** The effect of annealing on the morphology at 200 °C for 4 hours a) Al<sub>2</sub>O<sub>3</sub>/TiO<sub>2</sub> b) Al<sub>2</sub>O<sub>3</sub>/SiO<sub>2</sub>. The ALD samples were annealed at 200 °C for 4 hours under atmospheric conditions as in the case of 350 °C. The SEM analysis revealed that the morphology remained same after annealing at 200 °C as copper was not observed on the surface and voids structures were not formed on the subsurface. While annealing at 350°C leads to morphological changes, at lower temperatures such as 200°C, the whole film stack in both Al<sub>2</sub>O<sub>3</sub>/TiO<sub>2</sub> and Al<sub>2</sub>O<sub>3</sub>/SiO<sub>2</sub> seems to be much more stable based on the SEM analysis.



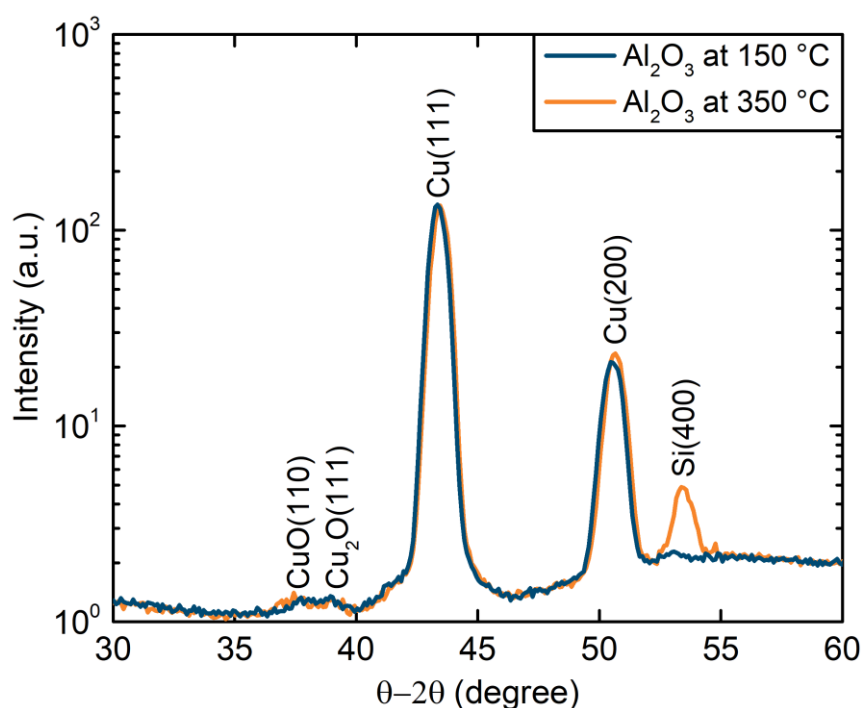
**Figure S8.** TEM lamella preparation for a)  $\text{Al}_2\text{O}_3/\text{TiO}_2$  b)  $\text{Al}_2\text{O}_3/\text{SiO}_2$  The FIB-cut were chosen from the specific regions which includes copper on the surface in  $\text{Al}_2\text{O}_3/\text{TiO}_2$  sample and voids in  $\text{Al}_2\text{O}_3/\text{SiO}_2$  sample

**Table S2.** Effect of annealing on sheet resistance of copper and ALD bilayers

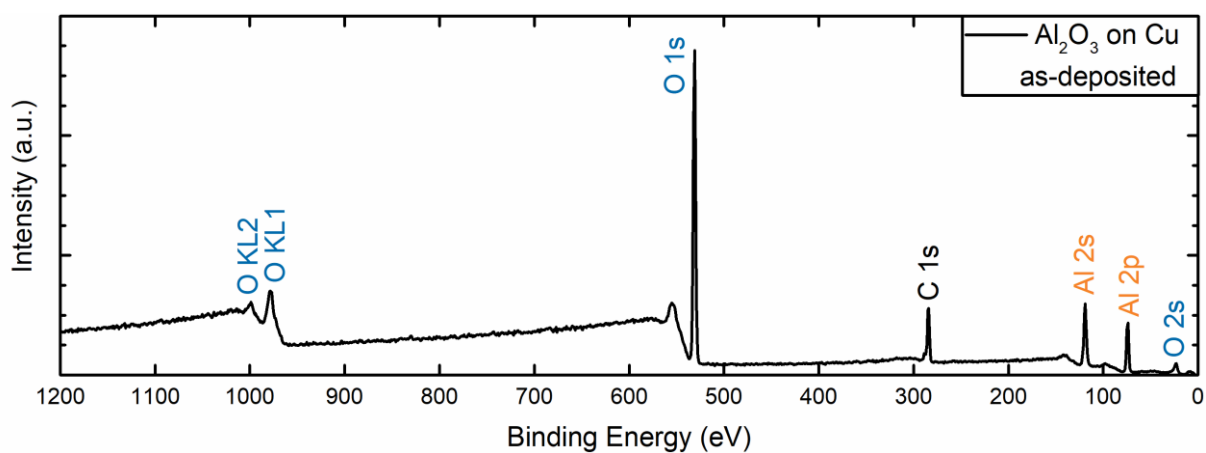
Sample	Sheet Resistance (mohm/□)
bare Copper	14.89 ±0.24
post-annealed Copper	Contact limit-high resistance
as-deposited Al <sub>2</sub> O <sub>3</sub> /TiO <sub>2</sub> on copper	15.03 ±0.59
post-annealed Al <sub>2</sub> O <sub>3</sub> /TiO <sub>2</sub> on copper	15.55 ±0.45
as-deposited Al <sub>2</sub> O <sub>3</sub> /SiO <sub>2</sub> on copper	14.68 ±0.60
post-annealed Al <sub>2</sub> O <sub>3</sub> /SiO <sub>2</sub> on copper	15.14 ±0.29

The resistivity measurements were performed by using four point probe (FFP) by Jandel multiposition wafer probe 8 inch model with 1 mm probe spacing, 100 μm tip radius and 100 g loading (max. current 100 mA and max voltage 100 mV). The correction factor, 4.53, were determined in infinite case according to substrate size and probe spacing.<sup>101</sup> The average sheet resistance and standard deviations were calculated from 3 different sample which include forward and reverse bias on each sample.

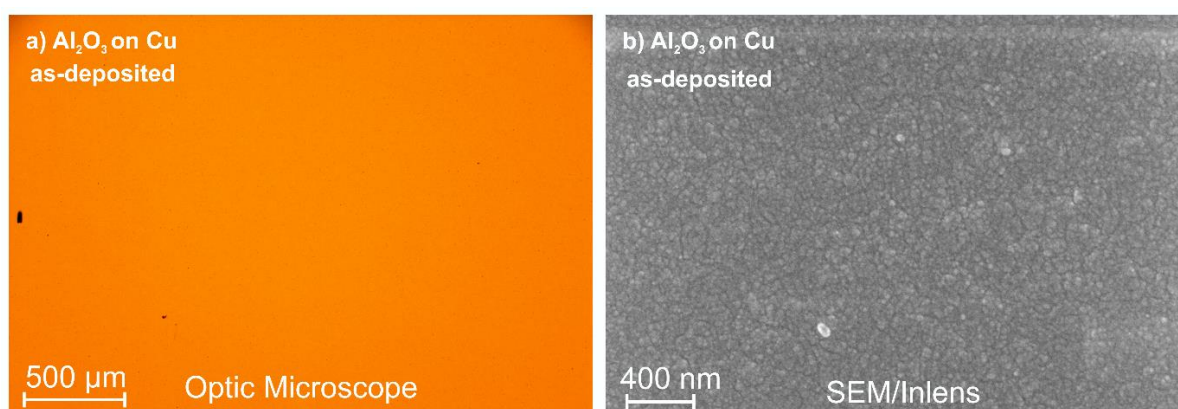
## 11.2. Supporting Information: Bayesian Machine Learning for Efficient Minimization of Defects in ALD Passivation Layers



**Figure S1.** GI-XRD of ALD-Al<sub>2</sub>O<sub>3</sub> on copper for lowest and highest deposition temperatures that used in this work. Both diffraction data showed the amorphous phase of Al<sub>2</sub>O<sub>3</sub>. The Cu (111) and (200) metallic peaks were detected additional of the broad peak at around 38° which was the mixture of copper oxide phase. The Si(400) peak came from the substrate which depends on the relative in-plane orientation of the substrate with respect to the measurement direction. It does not signify a crystallographic change in the structure.

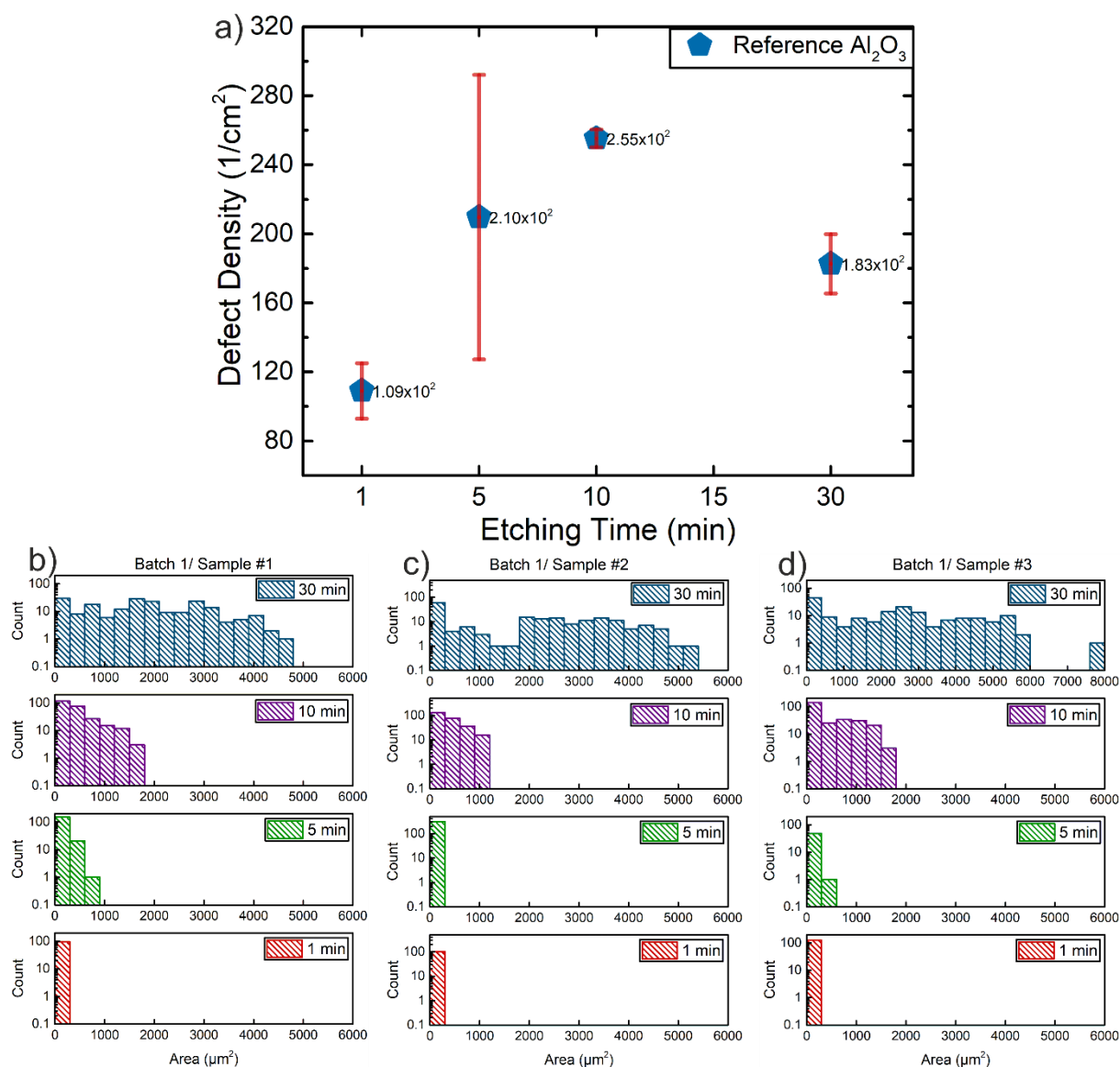


**Figure S2.** XPS survey spectra for as-deposited Al<sub>2</sub>O<sub>3</sub> reference sample. The Al and O atoms were detected on the surface, additional with C which comes from the environment. According to curve fitting of the survey spectra, oxygen was found 47.6 at.% and aluminum was 33.25 at.% which indicates the formation of Al<sub>2</sub>O<sub>3</sub> with [Al:O]: 0.6 atomic ratio.

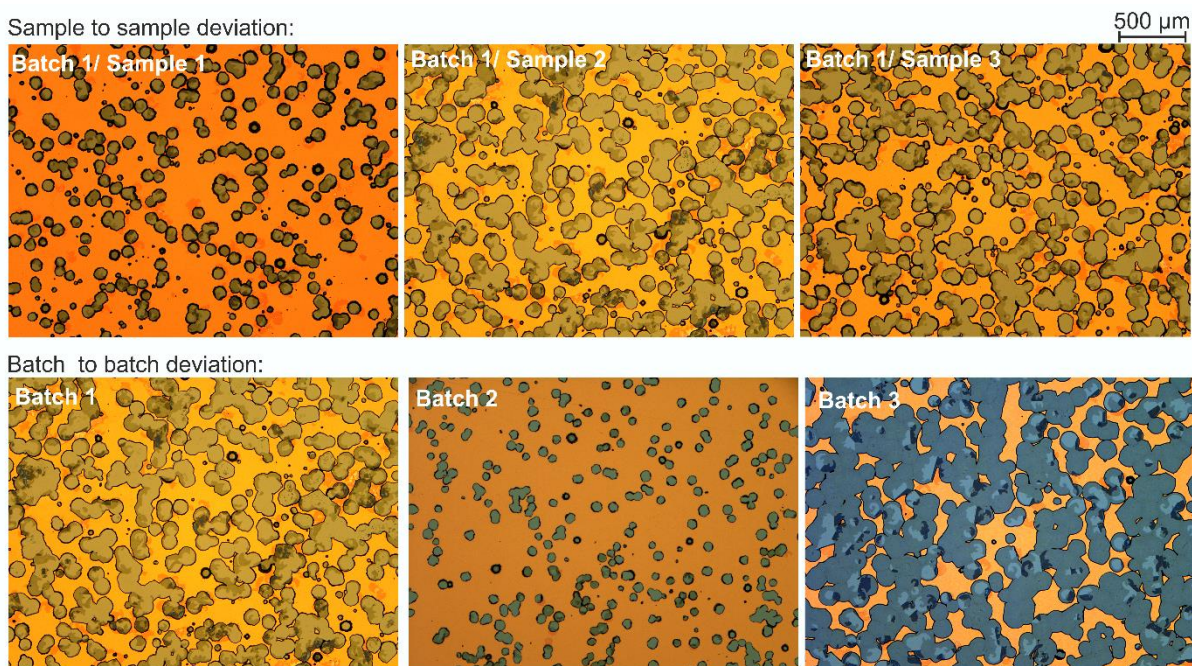


**Figure S3.** Surface properties of Al<sub>2</sub>O<sub>3</sub> (a) optic microscope and (b) SEM before wet etching. The SEM images were taken in 2 keV with an Inlens detector. The reference ALD parameters were used for Al<sub>2</sub>O<sub>3</sub> deposition (150 °C, 20 ms, without plasma pretreatment).

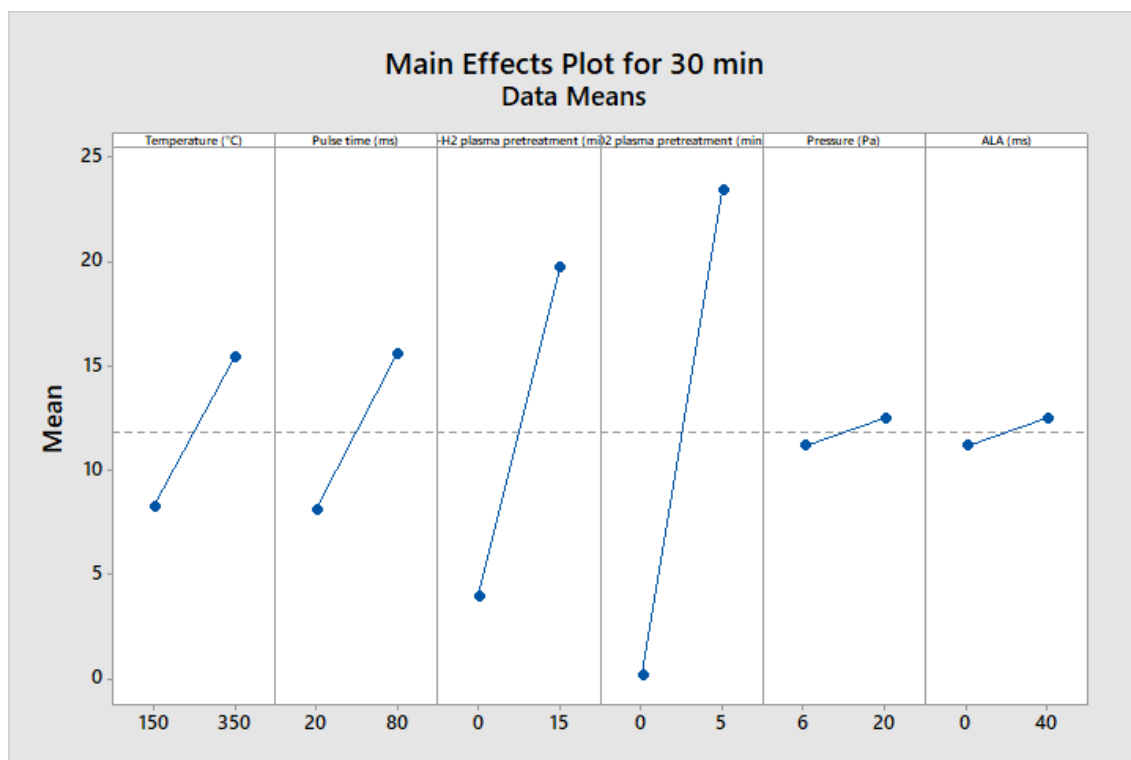




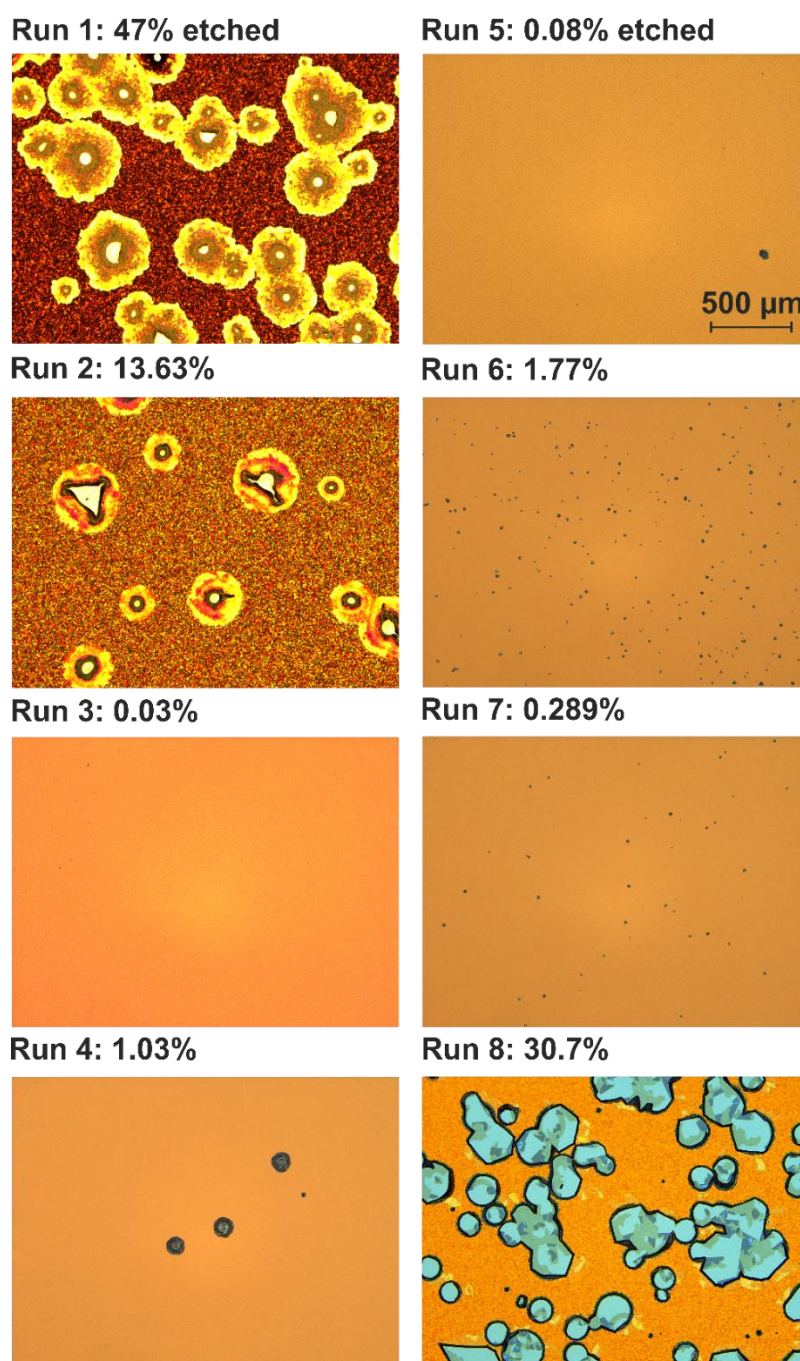
**Figure S4.** Wet etching time dependency of Al<sub>2</sub>O<sub>3</sub> reference sample. (a) Defect density in cm<sup>2</sup> for different etching times. The standard deviations were calculated based on three different samples. The defect size distribution for different etching times is given for (b) sample 1, (c) sample 2, and (d) sample 3. While the defect density was 109 in 1 cm<sup>2</sup>, it was getting similar, around 200 1/cm<sup>2</sup>, for 5 min, 10 min, and 30 min. According to particle distribution, the smaller defects were getting larger with longer penetration but as well new defects started to reveal on the surface. It shows the longer acid penetration provides the overall defect structure with the existence of all types of defect.



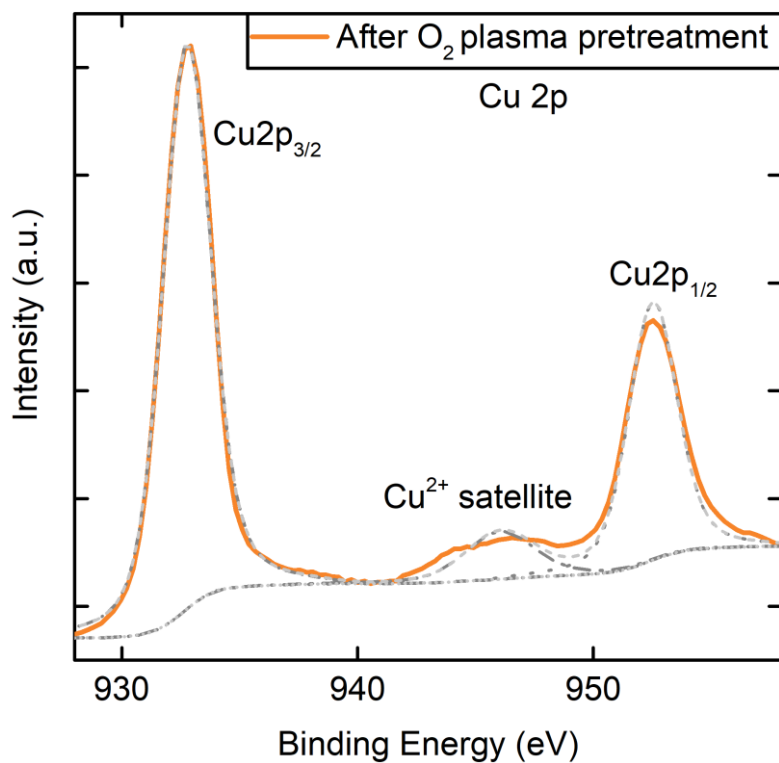
**Figure S5.** The defect density of reference  $\text{Al}_2\text{O}_3$  films after 30 min nitric acid etching. While sample to sample deviation was found  $39.35 \pm 10.51$  for batch 1, it was found  $17.54 \pm 2.02$  and  $77.92 \pm 13.62$  for batch 2 and 3, respectively. The overall etched area and standard deviation for reference  $\text{Al}_2\text{O}_3$  films was found  $44.935 \pm 27.323$ .



**Figure S6.** The main effect plot for defect density of  $\text{Al}_2\text{O}_3$  films according to two-level FFD analysis with six parameters. According to the main effects plot,  $\text{O}_2$  plasma considerably affected the defect density but in an antagonistic manner (negative effect of a parameter). The  $\text{Ar}/\text{H}_2$  plasma pretreatment was also found to have an important effect on defect density. The temperature and pulse time was considered relatively important, and have the same effect magnitude. The pressure and additional waiting time between cycles (ALA) were considered to have a low effect on defect density. While  $\text{O}_2$  was found significant, it was omitted from the optimization step due to its undesired effect on defect density.

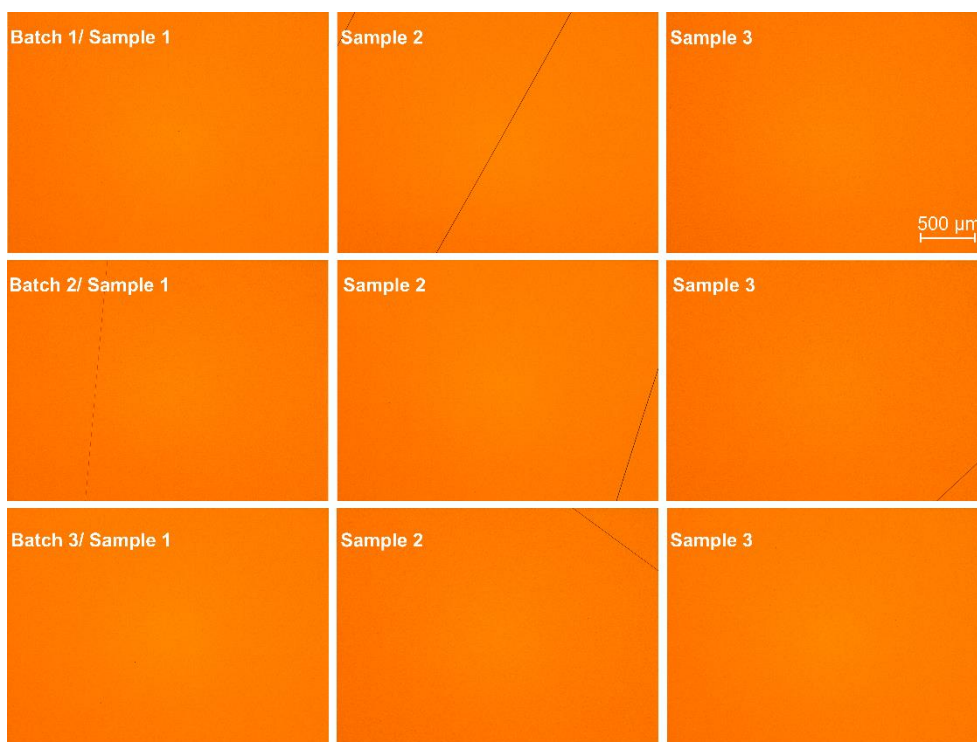


**Figure S7.** The optic microscope images for 30 min wet etching as a result of two-level screening FFD analysis. All optic microscope images were taken with x5 magnification, as indicated in Run5-500  $\mu\text{m}$ .



**Figure S8.** XPS of copper peaks from the surface of O<sub>2</sub> plasma pretreated copper shows the presence of oxide formation. The copper peaks were labeled at 834.5 eV and 954.2 eV and strong Cu<sup>2+</sup> satellite peak at 944.7 eV which were referenced to copper oxide formation. The O<sub>2</sub> plasma pretreatment was applied at 350 °C for 5 min. According to *in situ* spectroscopic ellipsometry measurements, the copper oxide thickness was measured ~2.5 nm before treatment, and ~155 nm after treatment.





**Figure S9.** Optic microscope images for repeatability of optimum process parameters (step 3.6) by 30 min wet etching. The same experimental parameters were applied three times (batch deviation) in which 3 samples were placed in each case (sample deviation). The sample to sample deviation was calculated for each batch and indicated as average value and standard deviation. The batch to batch deviation was calculated based on the average value with error propagation analysis. Table S1 summarized the calculated values.

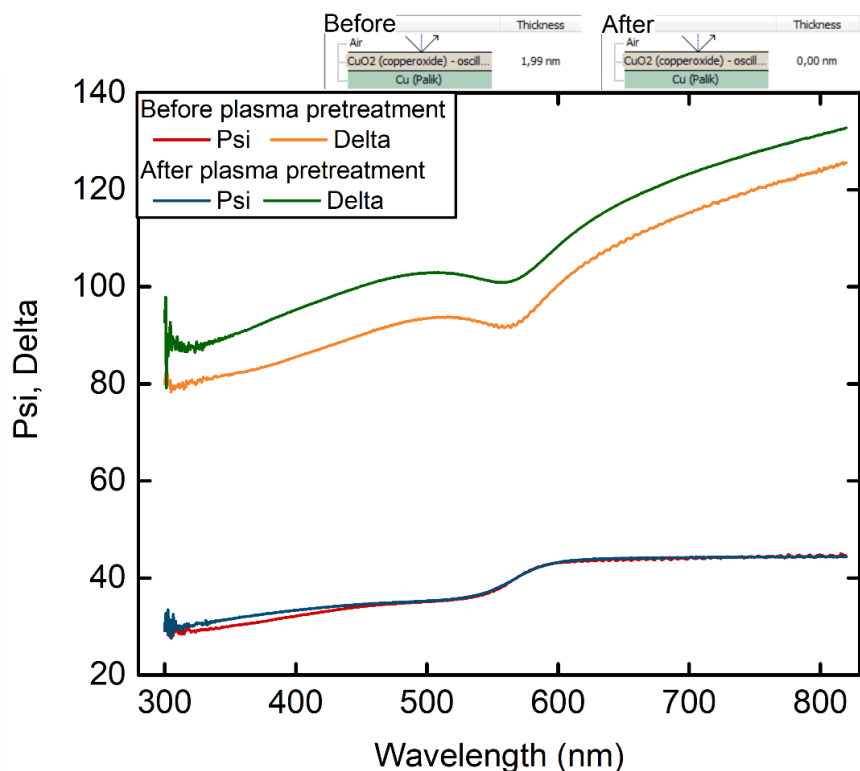
**Table S1.** Repeatability of optimum state defect density for  $\text{Al}_2\text{O}_3$  films

	Defect Density (%)	
Batch 1	0.0027	$\pm 0.0012$
Batch 2	0.0032	$\pm 0.0003$
Batch 3	0.0037	$\pm 0.0017$
Batch to Batch	0.0033	$\pm 0.0011$
Step 3.6	0.0014	$\pm 0.0007$

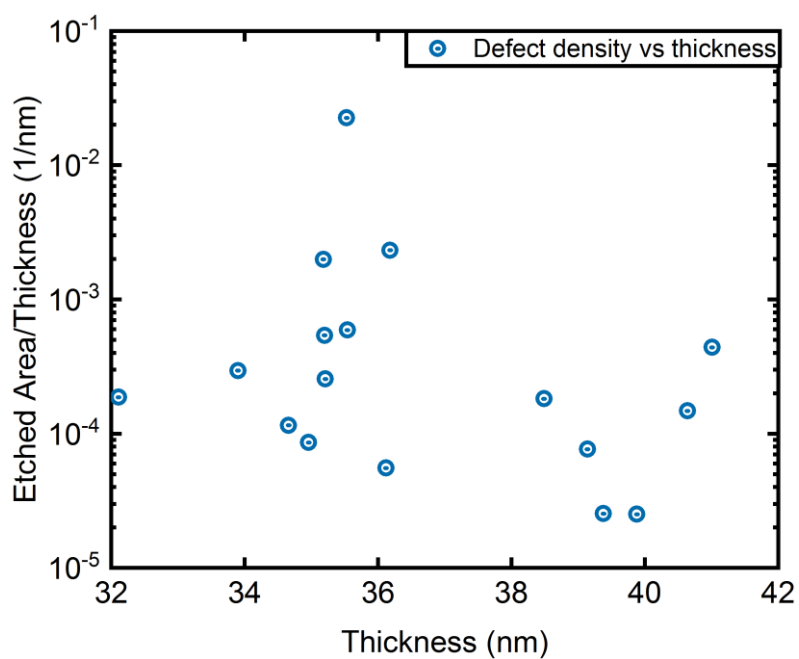


**Table S2.** Additional experiment details that were used during parameters effect analysis in Bayesian Optimization. The experiments were conducted during parameters limit search to identify the low and high levels in FFD analysis. Additionally, Run 3 from FFD analysis was also added as other parameters were in the reference case.

Experiments	Pretreatment	ALD process parameters		Etched Area (%)
	Ar-H <sub>2</sub> plasma (min)	Temperature (°C)	Pulse time (ms)	
1	0	350	80	0.09
2	15	150	20	0.5
3	15	150	80	0.17
4	15	350	80	0.02
Run 3 (FFD)	15	350	20	0.004

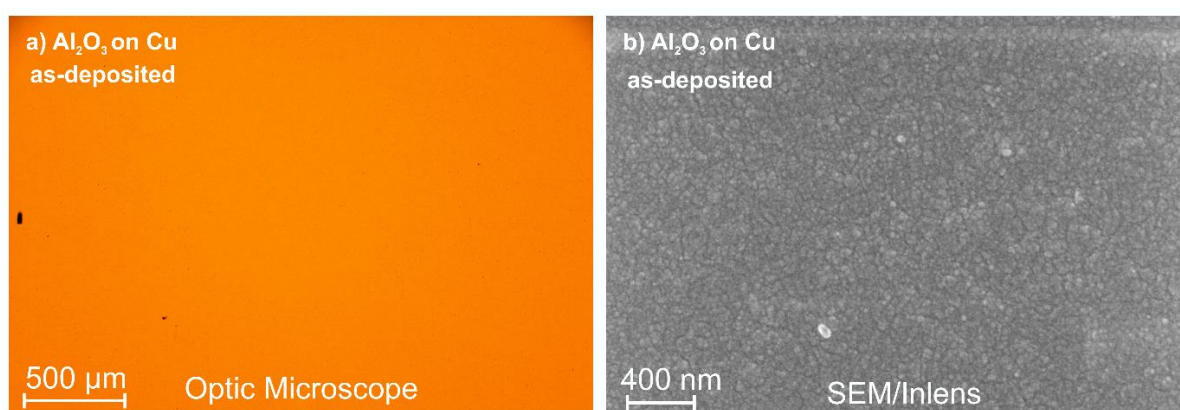


**Figure S10.** By application of the plasma pretreatment, the air-formed oxide layer was removed according to the *in situ* spectroscopic ellipsometry (SE) data. The psi and delta plot is given as a function of wavelength. Before Ar/H<sub>2</sub> plasma pretreatment, *in situ* SE measurement showed 1.99 nm Cu<sub>2</sub>O thickness according to the fitting analysis of psi and delta curves. With the application of 5 min Ar/H<sub>2</sub> plasma pretreatment at 250 °C, the thickness of Cu<sub>2</sub>O found zero, indicated by the change of delta curve. For the optical model, copper was defined as the file layer, and Cu<sub>2</sub>O layer according to Drude and Lorentz oscillator. The model-fitting results are given on the top of the figure for before and after plasma pretreatment with 1.99 nm and 0 nm Cu<sub>2</sub>O thickness, respectively.

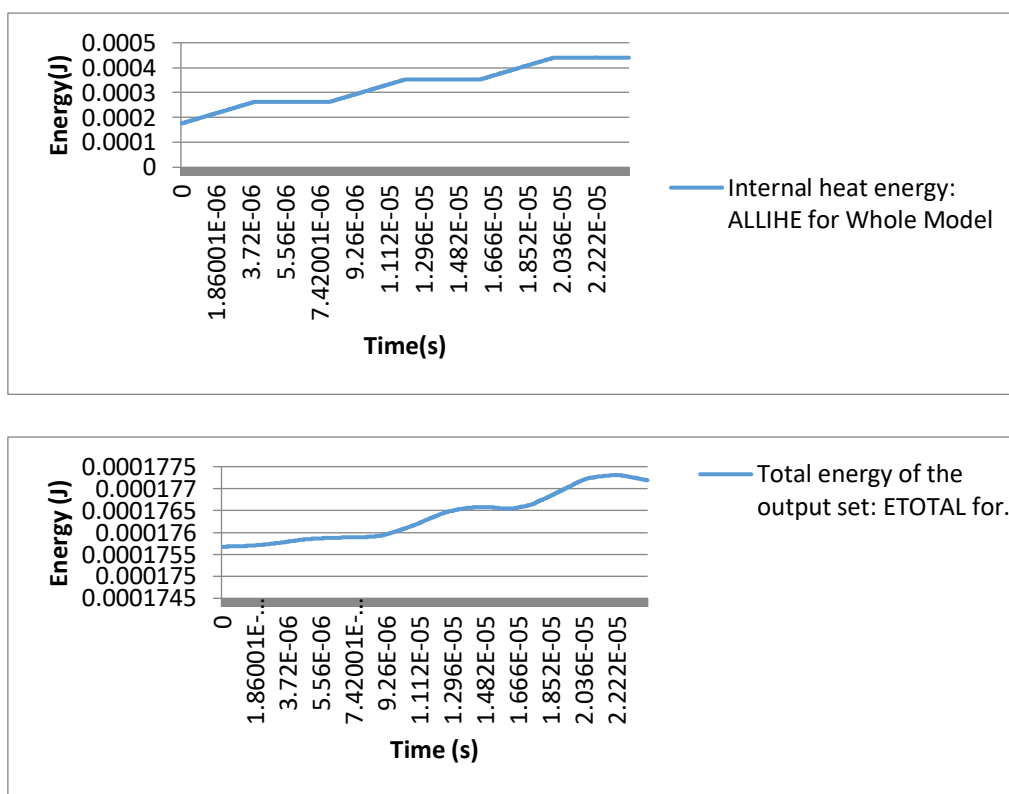


**Figure S11.** Etched area percentage per thickness (1/nm) for optimized  $\text{Al}_2\text{O}_3$  thin films. According to etched area percentage and thickness, the figure shows that independently from the thickness, the corrosion protection properties improved by process optimization (in the range 32 to 42 nm thickness).

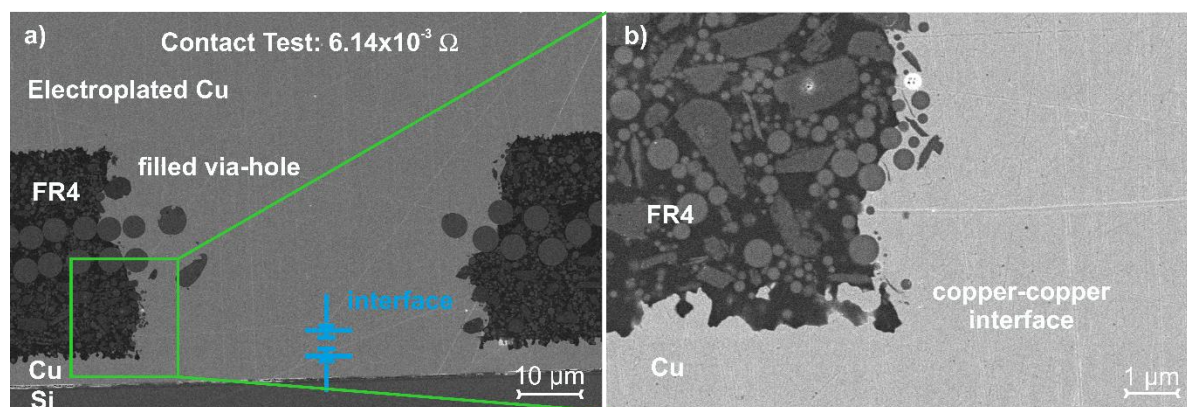
### 11.3. Supporting Information: Micromachining of Al<sub>2</sub>O<sub>3</sub> Thin Films *via* Laser Drilling and Plasma Etching for Interfacing Copper



**Figure S1.** Surface properties of Al<sub>2</sub>O<sub>3</sub> (a) optic microscopy and (b) SEM image. The SEM images were taken in 2 keV with an Inlens detector. The ALD parameters, 150 °C with 20 ms pulse time, were used for Al<sub>2</sub>O<sub>3</sub> deposition.



**Figure S2.** Total energy balance of Al<sub>2</sub>O<sub>3</sub> layer to check the quality of the model. The total internal heat energy of the whole Al<sub>2</sub>O<sub>3</sub> model after the simulation and ALLIHE in the graph are the acronym of internal heat energy of the whole model. (a) By neglecting the effect of convection and radiation, the input energy needs to be equal to the internal heat energy after simulation. The internal heat energy per laser pulse obtained after the simulation is  $88.415 \times 10^{-6}$  J, and the input energy per pulse is  $87.910 \times 10^{-6}$  J. When comparing these energies, the input energy and internal heat energy after the simulation per pulse are found approximately equal. Hence, the quality of the model is proved because of the similar energy. (b) The total energy balance (ETOTAL) of the whole model should be the same from the beginning to the end of the simulation process. The energy at the beginning is  $175.659 \times 10^{-6}$  J, and it should be the same for the whole simulation process. After the simulation, there is a slight increment in energy that occurred that is  $177.193 \times 10^{-6}$  J. Therefore, the model is stable.



**Figure S3.** SEM images of copper-copper connection formed in Cu-FR4 multilayers by CO<sub>2</sub> laser drilling. (a) Cross-section of the copper pad (filled via), (b) with higher magnification. The interface of copper and electroplated copper indicates high quality without any residuals. The electrical resistance by the FPP method was found to be  $6.14 \times 10^{-3} \Omega$ , which showed a reliable copper-copper connection. The electrical resistance result was used as the reference of good contact (low resistance).